The Linear Universe: Geometric Enforcement of Matter, Mass, and Spacetime via the 6-DoF Constraint

Haobo Ma (Auric)*
AELF PTE LTD.
#14-02, Marina Bay Financial Centre Tower 1, 8 Marina Blvd, Singapore 018981

December 30, 2025

Abstract

We adopt a tick-first ontology closed under two declared primitives: *time as tick* (the iteration count along a unitary readout stream) and the *Computational Action Principle (CAP)* as the unique deterministic closure/selection rule on explicit finite candidate families. For reader navigation, we also use the interface-level terms *Wish* (protocol-stable target data/structures) and *Motive* (an auditable objective functional), explicitly marked as [Audit]not used in proofs. Finite observers access only finite windows, hence finite binary words $w \in \Omega_m = \{0,1\}^m$ (Section 2). At the golden branch, a forbidden-word grammar and a cyclic closure predicate define a stable sector $X_m \subset \Omega_m$ with Fibonacci size $|X_m| = F_{m+2}$ and a rigid cyclic/boundary split (Section 4).

To speak about locality, "space" is introduced as a derived *display structure*: an addressing basis folds a finite tick prefix into a locality graph, and distance is the induced graph metric (Section 3 and Section 5). In this paper we use a 2D Hilbert screen for explicit finite diagnostics, while treating any conversion from tick units to physical units (including the measured value of c) as a matching-layer dictionary rather than a theorem-level output.

At the CAP-selected anchor on the chosen screen, $(m,n) = (6,3)$, one has $|\Omega_6| = 64$ and a fully explicit theorem-level folding core $64 \to 21$ with a canonical $18 \oplus 3$ split (Section 4). On the physical identification layer, "particles" are identified with stable readout types, while gauge fields are interpreted as compensating connection data forced by finite projection fibers under cross-site consistency. Mass and energy are treated as time dictionaries: mass scales are expressed in a Fibonacci log-time coordinate and compared to operational delay proxies (Wigner–Smith) and Compton-clock ratios (Section 10 and Appendix Y).

We close several interfaces by bounded-complexity audits with explicit finite candidate families and deterministic tie-break rules, and we record falsifiable predictions in the protocol language. We also record low-complexity rigidity targets for coupling normalization and CP violation, together with explicit log-mismatch factors and reproducible counterfactual baselines generated by deterministic scripts.

Keywords: holographic phase arithmetic; resolution folding; Zeckendorf representation; golden mean shift; Hilbert addressing; dihedral group; chirality; antimatter duality; gauge connections; Weinberg angle; Jarlskog invariant; CP violation.

*Email: auric@aelf.io

Table 1: A compact roadmap of the $m = 1 \dots 12$ resolution spectrum (interface). Under the rigid-frame coarse-lock budget at the anchor (Section 1.3; Proposition 3.7), the bulk dimension is selected as $d = 3$ and the minimal single-window coarse-localization anchor is at $m = 6$, which induces an interface partition into a sub-geometric vacuum ($m < 6$), a geometric ground state ($m = 6$), and hyper-geometric layers ($m > 6$). A quantitative $m = 1 \dots 12$ spectrum template (counts and threshold scales under the minimal calibration) is recorded later in Table 2.

m	1	2	3	4	5	6	7	8	9	10	11	12
regime	pre-geometric				sub-geom. vacuum	anchor	hyper-geometric layers					
marker	–	–	–	–	non-local vacuum	electron/SM	nuclear	QCD	bottom	EW	BSM	deep

Conventions. Unless otherwise stated, log denotes the natural logarithm. We use Fibonacci numbers $F_1 = F_2 = 1$, $F_{k+1} = F_k + F_{k-1}$. For $N \in \mathbb{N}$, the Zeckendorf digits $c_k \in \{0, 1\}$ satisfy $c_k c_{k+1} = 0$ and

$$N = \sum_{k \geq 1} c_k F_{k+1}.$$

We write $w = w_1 \cdots w_m$ for a finite binary word with letters $w_i \in \{0, 1\}$. We reserve m for Zeckendorf window length and reserve n for Hilbert order. We write $t \in \mathbb{Z}$ for the scan iteration count (tick) when an explicit time index is needed. The standard Abel path refers to the limit process $r \uparrow 1$ with $r \in (0, 1)$.

Dimensional language. Throughout the paper we use conventional terms such as "space", "spacetime", "grid", and "dimension" only as shorthand for protocol-level addressing and locality structure induced by the chosen readout basis (e.g. Hilbert addressing at fixed order). No ontic postulate of a pre-existing continuum manifold or a privileged physical dimension is used as a premise for the theorem-level folding statements. References to "4D spacetime" and to the 6-DoF rigid-frame coarse-lock anchor are likewise interface language: time refers to scan iteration count, while the spatial dictionary refers to the chosen locality basis; these identification statements are not used as premises for the folding core.

Data and code availability. All finite constructions, audit tables, and quantitative summaries in this paper are generated by deterministic Python scripts included in the repository under `scripts/`. Generated LaTeX fragments are written to `sections/generated/` and are treated as outputs. The scripts are a reference implementation of the paper's explicit finite constructions and bounded-family audits; they are provided to reproduce tables and to avoid manual transcription errors, not to introduce additional modeling freedom. A single entry point `scripts/run_all.py` regenerates the full set of fragments; see Appendix AJ.

Reader guide and audit contract. The layered audit rule and recommended reading paths are recorded in Part I (Contract).

Contents

Part I
Contract: Wish, Motive, and the Two-Axiom Spine

Reader-facing contract (audit discipline)

Layer tags used in the main text. [Math]marks theorem-level finite constructions and proofs (counts, maps, finite tables). [Interface]marks protocol-to-physics identification statements and operational dictionaries. [Match]marks external comparison conventions (PDG/CODATA targets, unit/scheme choices) that never serve as premises for theorem-level claims. [Audit]marks explicit candidate families/objectives/tie-break rules and other audit/provenance statements (including *not used in proofs* remarks).

Ledger statuses used for dependency tracking. The inference ledger (Appendix K) records dependency status using the five tags [Math], [Prot], [Iface], [CAP], and [Open]. These ledger statuses are not additional main-text layer tags; they are used only for audit and dependency tracking.

Wish and Motive (interface language; not used in proofs). [Interface]We use *Wish* as shorthand for a protocol-stable target datum/structure (a reproducible stable readout type and its associated invariants), and *Motive* as shorthand for an auditable objective functional that combines mismatch certificates with bounded implementation cost. [Audit]These names are organizational and reader-facing: they do not add new axioms, and they are not used as premises in theorem-level proofs. For a compact template definition (reader-facing; not used in proofs), see Appendix C. The only primitives are the tick (Axiom 1.1) and CAP (Axiom 1.5); see also Figure 5 and Appendix G.

No reverse dependence (legend discipline). [Audit]We follow the dependency legend in Figure 5: theorem-level implications flow along solid arrows, while interface dictionaries and audit overlays (dashed/dotted arrows) never serve as premises for theorem-level proofs.

Three channels as the mainline. [Interface]The core finite stability reduction is organized by three channels, denoted φ–π–e: grammar admissibility, cyclic closure, and an analytic stability template. The fully explicit finite reduction at the anchor is recorded in Section 4. [Audit]For a compact checklist of auditable "rigidity bridge" certificate forms and where each mainline step is realized in this paper, see Appendix I.

Reader guide (recommended paths)

This paper supports four complementary reading paths. The main text is organized into eight parts: Contract (Part I), Tick-first (Part II), Periodic Core (Part III), Structure (Part IV), Matter (Part V), Dynamics (Part VI), Validation (Part VII), and Recursive closure (Part VIII).

- **Narrative path (short mainline).** Read the tick dictionary (Section 3), then the folding core at $(m, n) = (6, 3)$ (Section 4), then the SM labeling closure (Section 9), and finally the falsifiability statements (Section 14). If you want one minimal spine: *Section 3* → *Section 4* → *Section 9* → *Section 14.2.1.*
- **Frequency-first dynamical closure (equivalence → action → EOM → thermo).** Read the equivalence semantics and frequency-first dictionary (Appendix AA), then the

CAP closure of a minimal continuum action (Appendix AD.4), then the variational field equations (Appendix AD.5), and finally the thermodynamic closure (Appendix AD.6). For matching-layer delay/redshift templates used as operational proxies, see Appendix Y and Appendix Z.

- **Extended self-contained closures (overhead gravity / quantum / RG / cosmology).** For the overhead-to-gravity closure and the χ reconstruction protocol, see Appendices AD.7 and AD.8. For the quantum readout interface and Born-probability rigidity, see Appendix AD.10. For RG/running couplings in the r coordinate, see Appendix AD.11. For cosmology as resolution flow, see Appendix AD.12.

- **Audit path (what depends on what).** Verify the declared inputs and the dependency hierarchy using Figure 5 and Appendix K, then spot-check representative rigidity certificates (e.g. Tables referenced in Sections 11 and 13).

- **Reproducibility path (run the pipeline).** Use Appendix AJ and run `python3scripts/run_all.py` to regenerate `sections/generated/` and the figures. The paper's definitions and candidate-family specifications are the logical source of truth; the scripts are the deterministic reproducer.

1 Introduction: from tick-only readout to stable sectors

The Standard Model (SM) organizes known non-gravitational interactions into the gauge structure

$$SU(3) \times SU(2) \times U(1),$$

with chiral matter content and experimentally established parity violation and CP violation; see, e.g., [1, 2]. Despite its predictive success, several structural features remain "input-like" at the microscopic explanatory level: the origin of chirality, the meaning of gauge redundancy, and the origin of small CP-odd invariants.

This paper adopts the HPA–Ω viewpoint: observability is not the presence of continuous fields *a priori*, but the output of a finite-resolution protocol produced by unitary scanning and window projection (Section 2). In this view, a "particle" is first a *stable readout type*, and "forces" arise from the constraints required to keep readout consistent across space.

The present paper is written to be closed under its declared input set (Table 25 and Appendix K): the only primitives are the tick (Axiom 1.1) and CAP (Axiom 1.5). All other ingredients (addressing basis, anchor choice, orientation-bit convention, phase-register dictionary, and quantitative normalization targets) are outputs of explicit finite definitions and CAP-closures with deterministic tie-breaks and reproducible scripts. Companion manuscripts in the same `docs/papers` repository provide extended context and alternative presentations [3–11], but they are not required to follow the present paper's definitions, proofs, and audits.

Audit note. [Audit]**Status:** [Audit]. **Depends on:** the reader-facing audit contract (Table 25) and the bounded-closure template (Appendix H). **If:** any quantitative interface component is reported, it is either a finite theorem-level statement or a CAP-closure over an explicitly declared finite family with deterministic tie-breaks; external PDG/CODATA values enter only as matching-layer reference conventions.

For reader navigation, Table 2 provides the global map of the resolution axis under the minimal calibration. In the tick-first spine used here, the only primitive physical input is *time as tick* (scan iteration count), and the only primitive selection law is CAP. Accordingly, all physical-language notions (space, distance, velocity, gauge connections, mass/energy scales) are treated as derived protocol structures and/or CAP-closed interface components. Section 3 records the corresponding dictionary and fixes the time-first dependency order used throughout.

Table 2: The holographic resolution spectrum under the minimal calibration $r_{\text{step}} = 2\pi$ (Section 14.2.1). Under the rigid-frame coarse-lock budget at the anchor (Section 1.3; Proposition 3.7), the bulk dimension is selected as $d = 3$ and the minimal single-window coarse-localization anchor is at $m = 6$, inducing an interface partition into a sub-geometric vacuum ($m < 6$), a geometric ground state ($m = 6$), and hyper-geometric layers ($m > 6$). Stable-type counts obey $|X_m| = F_{m+2}$ (Lemma 4.5); threshold energies use the $\mu_{\text{th}}(m)$ rule defined in Section 14.2.1.

m	$\lvert X_m\rvert$	$\mu_{\text{th}}(m)$	physical correspondence (interface)	mechanism (protocol language)
			Phase I: Sub-geometric (the vacuum)	
1–4	2–8	–	pre-geometric logic	finite bits, causality, addressability
5	13	$\sim 25\,\text{keV}$	sub-geometric vacuum (non-local)	coarse-lock deficit: one bit short of the $m = 6$ anchor
			Phase II: Geometric ground state (matter)	
6	21	$0.511\,\text{MeV}$	electron / minimal SM anchor	coarse-lock anchor: minimal localized rigid-frame display
			Phase III: Hyper-geometric (mass & thresholds)	
7	34	$\sim 10\,\text{MeV}$	nuclear binding scale	binding bridge between $m = 6$ matter and hadronic confinement
8	55	$\sim 0.2\,\text{GeV}$	QCD onset	confinement-scale template at the protocol interface
9	89	$\sim 4.4\,\text{GeV}$	bottom threshold	heavy-flavor onset in the staircase
10	144	$\sim 91\,\text{GeV}$	electroweak (Z/H) layer	uplift/coarse graining: protocol-level mass generation
11	233	$\sim 1.9\,\text{TeV}$	BSM frontier	first hyper-compressed layer; constrained topological capacity
12	377	$\sim 38\,\text{TeV}$	deep structure	candidate scale for further refinement (preons/extra dimensions)

Appendix G records the complete tick + CAP derivation spine (explicit candidate families, objectives, and deterministic tie-breaks for each closed interface component). Appendix R records short "forced-by-rigidity" interface lemmas (minimal coarse locking, compactness of probability-preserving redundancy, channelwise factorization, and minimal anomaly-neutral closures) that are repeatedly used as audit-level justifications in the main text.

1.1 Axiom 0: the tick (sequential readout) as the only primitive input (interface)

Axiom 1.1 (Readout sequentiality (interface))**.** *The microscopic description is* sequential. *An observer couples to a single unitary scan order that produces a one-dimensional readout stream, and finite observability appears through window projection (Section 2). Multi-dimensional language enters only through a choice of* addressing basis *that folds the scan order into a locality structure (Section 5); throughout, we use "space" and "spacetime" only in this protocol-level addressing sense (Conventions).*

Time, signal rate, and matching dictionaries. Under Axiom 1.1, "time" is operationally the iteration count along the scan. Any conversion from the dimensionless scan rate to physical units is therefore a matching-layer and units dictionary: once a locality basis is fixed, a constant step advance defines a maximal protocol signal rate, while the measured constant c appears only after choosing a physical calibration. We do not treat c as a theorem-level output of the folding core.

Matter as recurrent patterns and mass as protocol cost. In a linear ontology, stable excitations are not points placed in an ontic background, but persistent patterns in the readout

stream that are stable under the chosen channels. On the physical identification layer, we adopt the interface identification that an observed mass scale corresponds to protocol overhead required to resolve and stabilize a pattern at a given resolution (e.g. increased local scan density, deeper matching shifts, or larger folding-degeneracy costs in the finite invariants). This paper makes this identification auditable by a closed depth coordinate and a reproducible mass-spectrum template (Section 13).

Remark 1.2 (Static ontology vs. sequential readout (interface))**.** *Although the paper is written in the scan-first language of Axiom 1.1, one may also adopt a complementary interface dictionary: the scan order together with the chosen addressing dictionary can be regarded as a fixed (already-defined) structure, while "time" is the ordered traversal experienced by a coupled observer. In this reading, dynamical episodes are a playback effect of sequential readout on a static protocol substrate (a block-universe style viewpoint), not the construction of that substrate. We record this only as an interface dictionary viewpoint; none of the theorem-level finite folding statements depends on it as a premise.*

Remark 1.3 (A historical analogy: Wheeler's one-electron universe)**.** *As a historical analogy, Wheeler suggested to Feynman that the identity of electrons might admit a radical kinematic explanation: a single electron world-line could thread the observed phenomenology, with positrons interpreted as the same object propagating backward in time in the spacetime picture. We use this only as an analogy for the present linear-ontology interface: a sequential primitive can generate rich multi-body effective structure once it is read through an addressing basis and a matching dictionary, without promoting the analogy to a premise of the mathematical layer. See, e.g., [12, 13].*

The key inversion relative to conventional field-first narratives is methodological: we treat the problem of "what particles and forces exist" as a problem of *which readout types are stable under a fixed protocol*. Finite windows induce symbolic compression; stability constraints induce further compression; and the effective "spectrum" is the surviving stable sector. From this viewpoint, discreteness is not a postulate but a consequence of finite-resolution projection.

Stability and agency as dual interface viewpoints. The stable-sector viewpoint used in this paper admits a control-theoretic dual dictionary: in open systems, long-lived low-entropy structure can be modeled as *predictive active error correction* (AEC) that suppresses protocol-level mismatch relative to a passive baseline while paying dissipation and implementation costs [14, 15]. Appendix U records a protocol-level dictionary that aligns stable-sector objects (alphabets, stability channels, degeneracies) with AEC objects (mismatch certificates, feedback, and audit constraints) without mixing mathematical-layer premises with physical identification claims.

1.2 From scan to knot: an interface picture

Figure 1 provides a narrative visualization of the interface picture used throughout this paper. The primitive description is a single sequential readout stream (Axiom 1.1), while spatial language enters only after choosing an addressing basis that folds the stream into locality neighborhoods (Section 5). Under the rigid-frame coarse-lock budget at the anchor, CAP selects bulk dimension $d = 3$, and $m = 6$ is the smallest *single-window* anchor for localized display (Section 1.3).

The scan (1D). One may picture the readout as an extremely thin "luminous thread" whose order is fixed by the unitary scan: the observer sees only a time-ordered sequence of windowed binary words.

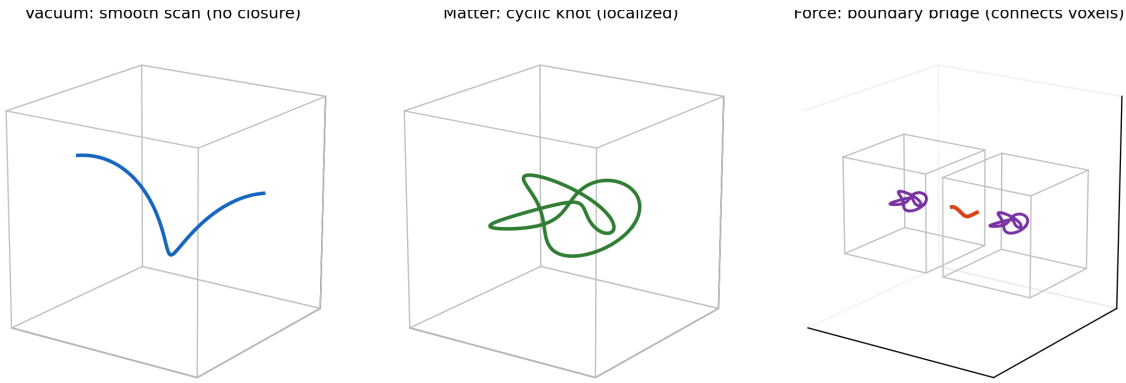

Figure 1: Conceptual triptych (interface picture). *Left: Vacuum.* Below the 6-DoF anchor, a scan segment can be stable as a symbolic word yet remains sub-admissible for localized rigid-frame display; it is therefore treated as a non-local background (sub-geometric vacuum). *Middle: Matter (cyclic).* At the $m = 6$ anchor, stability can self-close into localized recurrent patterns; at the minimal anchor $(m, n) = (6, 3)$ the stable sector obeys $64 \to 21$ with a canonical cyclic/boundary split $21 = 18 \oplus 3$. *Right: Force (boundary).* Boundary-type patterns connect neighboring voxels/sites and are interpreted as interaction carriers enforcing cross-site consistency. This figure is a schematic interface picture and does not enter the theorem-level folding statements, which are formulated in finite readout language.

The fold (local compression). Once a locality dictionary is chosen, a single window must encode enough independent distinctions to be displayed as a localized object in that dictionary. Under the minimal two-bin-per-DoF convention, this creates a geometric bottleneck at $m = 6$ in the derived $d = 3$ dictionary: the readout must fold its local patterning to supply a coarse position–orientation frame.

The lock (closure vs. bridge). At the interface level, cyclic closure (a local recurrence) is interpreted as a fermion-like localized excitation, while boundary-type connectivity between neighboring sites is interpreted as a boson-like carrier that transmits readout constraints across space. The subsequent sections make these statements auditable by fully explicit finite constructions at $(m, n) = (6, 3)$ and by closed protocol-level interfaces.

1.3 Derived bulk dimension: rigid-frame display budget at the anchor (interface)

While Axiom 1.1 fixes only sequentiality, any physical identification must specify what it means to *display* a localized object. In the tick-first dictionary of Section 3, locality is a derived addressing graph, and a "localized rigid frame" is an interface notion tied to coarse pose distinguishability. Let d denote a candidate bulk dimension of such a rigid-frame display dictionary. A local rigid frame carries d translational degrees of freedom and $d(d-1)/2$ rotational degrees of freedom, hence

$$\dim SE(d) = d + \frac{d(d-1)}{2} = \frac{d(d+1)}{2}.$$

We now state explicitly what the "bit-per-DoF" language means in this paper. The claim is *not* that m bits can encode a continuous pose in $SE(d)$ with arbitrary precision. Rather, it is the minimal nontrivial coarse-lock convention at the protocol interface (Lemma R.1): a length-m window yields at most 2^m distinct binary readout classes, and to display a local rigid frame the protocol must be able to distinguish at least two coarse bins along each independent parameter

of $SE(d)$. In this minimal two-bin-per-parameter convention, a sufficient single-window coarse-admissibility condition is

$$2^m \;\geq\; 2^{\dim SE(d)} \qquad \Longleftrightarrow \qquad m \;\geq\; \dim SE(d) = \frac{d(d+1)}{2}.$$

More generally, if one asks to specify an element of a k-dimensional Lie group up to an ε-scale resolution, the required number of bits scales as $m \gtrsim k \log(1/\varepsilon)$ (metric-entropy / quantization scaling) [16, 17]. In the present paper we use only the minimal two-bin-per-parameter anchor, and we keep the rigid-frame lock on the physical identification layer.

Remark 1.4 (What the 6-DoF "lock" does and does not assert)**.** *The 6-DoF coarse-lock is an* interface *convention, not a theorem about continuous pose estimation. It does not claim that $m = 6$ is sufficient to "lock" a pose in $SE(3)$ at any fixed accuracy; continuous pose locking at accuracy ε requires a bit budget scaling as $m \gtrsim 6 \log(1/\varepsilon)$ in the standard quantization sense [16,17]. It also does not claim that $m \geq 6$ is necessary for localization under all possible protocols: multi-window temporal integration, analog readout features, or additional structure/constraints can reduce the effective information required at a given task. The role of the lock in this paper is narrower: given the CAP-selected anchor bit budget $m = 6$ and the minimal two-bin-per-parameter convention, CAP selects the bulk dimension $d = 3$ (Proposition 3.7) and thereby identifies $m = 6$ as the minimal* single-window *coarse rigid-frame display budget in that derived dictionary. Once a $\mu \leftrightarrow m$ selection rule is fixed at the protocol layer (Corollary 14.2), the protocol uses the smallest admissible m throughout the corresponding energy band until an uplift threshold is crossed.*

At the anchor $m = 6$, CAP selects the maximal bulk dimension compatible with the rigid-frame budget, namely $d = 3$ (Proposition 3.7). Empirically, the observed locality structure is three-dimensional to high precision on laboratory and astrophysical scales, providing an external consistency check.

Audit note. [Audit]**Status:** [Interface] + CAP. **Depends on:** the minimal coarse-lock criterion (Lemma R.1) and Proposition 3.7. **If:** the coarse-lock is interpreted in the minimal two-bin-per-parameter sense and applied as a single-window admissibility criterion; the resulting d is a protocol-interface output and is not used as a premise for the folding core.

At $d = 3$, a local rigid frame is modeled by the Euclidean group

$$SE(3) \cong \mathbb{R}^3 \rtimes SO(3),$$

as a semidirect product; see, e.g., [18]. It is specified by a position $x \in \mathbb{R}^3$ and an orientation $R \in SO(3)$. Hence the minimal kinematic description carries six independent parameters: three translational plus three rotational degrees of freedom.

We treat this as a geometric coarse-lock on the physical identification layer: a fundamental readout window supplies one bit per kinematic degree of freedom of a local frame. In 3D this locks the minimal window to six bits, $\Omega_6 = \{0, 1\}^6$. This statement belongs to the physical identification layer: it fixes the preferred anchor scale under the minimal nontrivial coarse-lock convention but is not used as a premise for any theorem-level folding statement.

To make the geometric exclusivity explicit, compare the first few balanced candidates $m \in \{4, 6, 8, \dots\}$ against the rigid-frame degree count $\frac{d(d+1)}{2}$ [18]: in 2D one has 3 DoF, so the balanced code length $m = 4$ overspecifies the kinematics ($4 > 3$); in 4D one has 10 DoF, so the next balanced length $m = 8$ underspecifies it ($8 < 10$). Only at $d = 3$ does the balanced length $m = 6$ match exactly ($6 = 3 + 3$), yielding a unique geometric lock at the anchor that selects the bulk dimension.

Once a locality-preserving addressing basis is fixed (e.g. Hilbert addressing on a chosen readout screen), one may adopt a balanced coupling convention that matches the m-bit readout

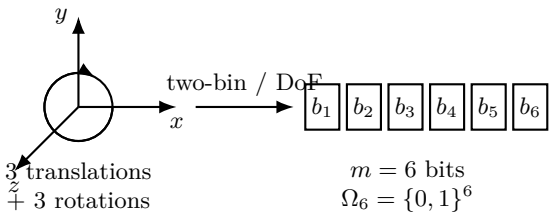

Figure 2: The 6-DoF coarse-lock (interface language): at the anchor $m = 6$, CAP selects bulk dimension $d = 3$ under the minimal coarse-lock convention (Proposition 3.7), so a local rigid frame has six degrees of freedom (three positional plus three orientational).

alphabet size 2^m with the number of sites at Hilbert order n (Lemma 4.1). Throughout this paper we use the classical 2D Hilbert addressing (a square grid), so the matched site count is $4^n = (2^2)^n$ and the balanced relation takes the form $m = 2n$; other addressing dimensions would change this arithmetic match (Remark 4.2 and Remark 5.1). Balanced coupling is used only to attach spatial diagnostics and is not a theorem-level necessity for the folding core (Remark 4.3). At the chosen anchor $m = 6$ on the 2D screen, balanced coupling yields $n = 3$ and $2^6 = 4^3 = 64$.

1.3.1 The geometric vacuum and protocol rejection

The rigid-frame coarse-lock has an immediate consequence: in the derived $d = 3$ locality dictionary, any readout pattern that is to be displayed as a localized object must supply enough independent information to fix a local position–orientation frame. Under the minimal coarse-lock hypothesis stated above (two bins per independent parameter), a single-window coarse display requires at least $m \geq 6$ binary distinctions; in this sense $m = 6$ is the minimal interface anchor for matter-like localization in the derived dictionary.

For $m < 6$, stable symbolic types still exist at the mathematical layer—indeed the golden-mean admissible set has size $|X_m| = F_{m+2}$ (Section 4.3)—but they are sub-geometric for a $d = 3$ readout: they underdetermine the kinematic frame and cannot be consistently assigned to a unique local site-and-frame configuration. We therefore treat these modes as *protocol-rejected as matter*: they do not appear as stable localized particles, but persist as a non-local background that can seed transient fluctuations when coupled to higher-resolution readout. [Interface]Below the anchor, these modes are treated as sub-geometric vacuum/ghost-sector degrees of freedom; diagnostic sweeps are recorded in Appendix P.

Roadmap: the $m = 1 \ldots 12$ spectrum. Although the technical core of this paper is anchored at the CAP-minimal holonomy instance $(m, n) = (6, 3)$ on the chosen 2D screen, the derived $d = 3$ rigid-frame coarse-lock dictionary induces a canonical interface partition of the resolution axis into three regimes: the sub-geometric vacuum ($m < 6$), the geometric ground state ($m = 6$), and hyper-geometric layers ($m > 6$). We use this dictionary-induced partition as the global narrative spine, and we summarize a compact $m = 1 \ldots 12$ spectrum template (counts and threshold scales under the minimal calibration) in Table 2; the detailed falsifiability statement is then formulated in the protocol language in Section 14.2.1.

1.4 Methodological note: auditable layering

No-hidden-knobs contract (reader-facing). [Audit]Whenever a quantitative claim is reported, it is either a finite theorem-level statement or an audited interface closure within an explicitly declared finite candidate family with deterministic tie-break rules (Definition H.1; Appendix AE and Appendix AJ). [Match]External reference targets (PDG/CODATA, scheme/scale conventions) enter only as comparison inputs and are not fit parameters. The compact audit contract table is recorded in Appendix H (Table 24).

Audit-facing contract and inference map (supplement). [Audit]The reader-facing audit contract and the dependency map are recorded compactly in Appendix J (Table 25 and Figure 5).

Layer separation. [Math]The finite folding statements constrain [Interface]the falsifiable mapping/identification layer; Appendix K records the dependency status in compact form.

Inference map (what depends on what). Figure 5 is recorded in Appendix J; we use its legend throughout: solid arrows are theorem-level dependencies, dashed arrows are interface dictionaries, and dotted arrows indicate CAP-audited selections within explicit finite families.

Dependency checklist. Appendix K provides the compact checklist of which statements are [Math]theorem-level, which are [Interface]interface dictionaries/closures, and which are [Match]matching conventions.

1.5 Research questions (summary)

[Interface]The paper closes (i) minimal stable-sector structure at the anchor, (ii) a deterministic SM labeling map consistent with anomaly constraints, and (iii) protocol-level falsifiability routes; the compact dependency status is recorded in Appendix K.

1.6 Audit protocol: bounded-complexity closure and rigidity certificates

Several quantitative interface statements in this paper take the form of a *bounded-complexity closure*: we specify a small, discrete candidate family for a target observable and select a unique minimizer by a deterministic rule under an explicit finite complexity bound. This is designed to address a standard audit concern in speculative constant/parameter matching: post-hoc freedom.

Axiom 1.5 (Computational Action Principle (CAP; interface))**.** *Within a fixed protocol class, realized effective structures are selected by minimizing accumulated readout mismatch (discrepancy) and implementation overhead subject to protocol constraints. In the finite audited setting of this paper, CAP is instantiated by explicit bounded candidate families and deterministic selection rules: given a declared finite complexity budget and an explicit objective measuring mismatch to reference targets, select the unique minimizer with a fully specified tie-break rule (Definition H.1).*

Audit form (supplement). [Audit]The formal closure definition, log-mismatch rationale, rigidity certificate, and audit-output conventions are recorded in Appendix H and Appendix AE.

1.7 A minimal falsifiable anchor: $64 \to 21$ stability at $(m, n) = (6, 3)$

[Math]We work at the fully explicit finite anchor $(m, n) = (6, 3)$ on the chosen 2D Hilbert screen (Table 30). At $m = 6$ the folding core yields $64 \to 21$ and the canonical split $21 = 18 \oplus 3$ (Section 4).

1.8 $\mathbb{Z}_{128}$ as a phase-register label

[Interface]We represent internal phases by a finite dyadic register $\mathbb{Z}_{2^p}$ (Appendix B). At the anchor window $m = 6$, the baseline choice is $p = m + 1 = 7$, i.e. $\mathbb{Z}_{128}$. The remaining bounded phase-lift freedom (denominators and low-complexity phase maps) is audited by deterministic sweeps (Appendix AE and Appendix AF).

1.9 Main interface closures

Building on the provable $64 \to 21$ folding core, we record three interface closures: [Interface]gauge as compensation (Section 8.1), [Interface]chirality as protocol selection (Section 7), and [Interface]antimatter as conjugate readout (Section 7).

We emphasize the audit separation: the folding counts and tables are mathematical-layer facts, while the SM identifications are recorded as falsifiable mapping problems.

Quantitative anchor. The closed-theory rigidity targets and their CODATA/PDG deviations are summarized in Table 16.

Closure deliverables at (m,n)=(6,3). [Math]the folding core $64 \to 21$ and $18 \oplus 3$ (Section 4); [Interface]a unique SM labeling map (Section 9); [Interface]a closed mass-depth template (Section 13).

Rigidity doctrine (interface). [Interface]Once one commits to finite readout primitives and CAP-style bounded closure, many interface components become sharply constrained at the anchor; Appendix K records the compact dependency status.

Reader guide: rigidity checkpoints (supplement). [Audit]A compact checkpoint list is recorded in Appendix K.

Part II
Tick-first: From Scan to Finite Observables

2 HPA readout dynamics: from unitary scan to Zeckendorf windows

2.1 Unitary scan and a Weyl pair: time as iteration count

In HPA, microscopic dynamics is modeled as a unitary scan with a Weyl-pair structure [19]. Abstractly, one may encode noncommutativity by operators (U, V) satisfying

$$UV = \mathrm{e}^{2\pi \mathrm{i}\alpha} VU, \tag{1}$$

with an irrational slope α. At the level of a circle rotation model, let $x_0 \in \mathbb{R}/\mathbb{Z}$ and define the orbit

$$x_n := x_0 + n\alpha \pmod 1, \qquad z_n := \mathrm{e}^{2\pi \mathrm{i} x_n} \in \mathbb{T}. \tag{2}$$

Time is not imposed as an external parameter; it is realized as the iteration count $n \in \mathbb{Z}$ along the scan.

Remark 2.1 (Scan rate, units, and the speed-of-light dictionary)**.** *The scan iteration count n is dimensionless. In this paper, we treat any conversion between "one step per iteration" and a physical time unit, and therefore any identification of an effective maximal signal speed with the measured constant c, as part of a matching-layer and units dictionary rather than as a theorem-level output of the finite folding core. Once a locality basis is fixed (e.g. via Hilbert addressing), a constant step advance induces a protocol-invariant notion of maximal propagation rate on the associated locality graph; the physical value of c enters only after calibration.*

Remark 2.2 (Delay observables as an operational time dictionary)**.** *When the protocol is matched to an experimental platform, "time per update" can be accessed through standard delay observables. In scattering settings where a unitary S-matrix $S(\omega)$ is measured as a function of frequency, the Wigner–Smith time delay provides an operational proxy for additional overhead via $\tau_{\mathrm{WS}}(\omega) = \mathrm{Tr}(-\mathrm{i}S^{\dagger}\mathrm{d}S/\mathrm{d}\omega)$ [20, 21]. We record this dictionary (and its relation to relativistic lapse/redshift templates) as an interface section (Section Y).*

2.2 Window projection and symbolic words: finite observability

Let $W \subset \mathbb{T}$ be a measurable "readout window". Define the binary readout word by thresholding the scan orbit:

$$w_n := \mathbf{1}\{z_n \in W\} \in \{0, 1\}. \tag{3}$$

The resulting sequence $w = (w_n)_{n\in\mathbb{Z}}$ is a symbolic coding of the orbit (mechanical/Sturmian in classical settings; see, e.g., [22, 23]). Finite observers access only finite windows, hence finite words $w_1 \cdots w_m \in \Omega_m$. In operational quantum language, such coarse readout corresponds to a POVM-like description, where the "particle spectrum" is readout-induced discreteness rather than an *a priori* field continuum; see, e.g., [24] for standard measurement and POVM formalism. In particular, what is experimentally accessible is not the underlying continuous orbit, but the empirical statistics of finite window words. The finite readout alphabet Ω_m and its stability-filtered subsets therefore serve as the primary objects for any auditable finite-resolution model.

Remark 2.3 (Irrational rotations and Sturmian minimal complexity)**.** *For the canonical two-interval partition induced by an irrational rotation (equivalently, for the length-α window $W_\alpha = [1-\alpha, 1)$ or its complement), the resulting binary coding is Sturmian (a mechanical word): it is aperiodic and has minimal factor complexity among aperiodic binary sequences, namely $p(\ell) = \ell + 1$ distinct length-ℓ subwords for each $\ell \geq 1$. Appendix L gives a self-contained proof of the complexity formula and the resulting zero entropy-rate bound.*

2.3 The golden branch and Zeckendorf/Ostrowski coding

At the golden branch $\alpha = \varphi^{-1}$, the symbolic language is constrained by Fibonacci/Sturmian structure and connects naturally to Ostrowski and Zeckendorf numeration [22, 25, 26]. In particular, every $N \in \mathbb{N}$ admits a unique Zeckendorf expansion

$$N = \sum_{k\geq 1} c_k F_{k+1}, \qquad c_k \in \{0, 1\}, \qquad c_k c_{k+1} = 0, \tag{4}$$

which is a forbidden-word grammar (no adjacent ones) on the digit string (c_k). This grammar is the mathematical origin of the φ-channel in the folding model: it selects a stable type set $X_m \subset \Omega_m$ by excluding the forbidden substring "11" at finite window length (Section 4).

A coding bridge (symbol $\leftrightarrow$ arithmetic). At the golden branch, Fibonacci weights provide a canonical arithmetic bridge between symbolic digits and integers. Given a binary digit sequence (c_k) satisfying the Zeckendorf grammar, the value map is

$$V(c) := \sum_{k\geq 1} c_k F_{k+1}.$$

Conversely, given a binary readout word (w_k) produced by a window protocol, one may form a Fibonacci-weighted observable

$$Z := \sum_{k\geq 1} w_k F_k, \tag{5}$$

which makes explicit the "arithmetic–symbol–geometry" loop emphasized in the HPA program: window projection induces symbolic words; the golden branch constrains them by a forbidden grammar; and Fibonacci weights convert the resulting digits into arithmetic invariants.

Audit note (finite coordinate bridge). [Audit]**Status:** [Math] (numeration/grammar) → [Interface] (protocol identification). **Depends on:** the golden-branch choice $\alpha = \varphi^{-1}$ and its induced Zeckendorf/Ostrowski numeration (Section 2.3). **If:** one represents a finite microstate register dyadically while reading stable types in Zeckendorf digits, the explicit bridge between these coordinates is fixed by the folding map Fold_m in Section 4; a bounded counterfactual family of alternative bridges at $m = 6$ is audited in Appendix Q.

Remark 2.4 (Why the golden branch is singled out among irrational slopes)**.** *For a general irrational slope α, interval codings of the rotation* (2) *are Sturmian and admit an Ostrowski numeration determined by the continued-fraction expansion of α [22, 26]. The choice $\alpha = \varphi^{-1} = [0; 1, 1, 1, \dots]$ is distinguished by its extremal Diophantine property: among irrationals it is "most poorly approximable" by rationals (all continued-fraction digits are minimal), yielding a canonical and maximally rigid substitution structure (the Fibonacci word) and therefore a canonical digit grammar that closes to Zeckendorf/Fibonacci weights [22, 27]. This is the mathematical sense in which the golden branch is the minimal nontrivial symbolic/arithmetic bridge: it is the unique slope whose Ostrowski system reduces to the Fibonacci/Zeckendorf system used throughout the folding layer.*

Tick-only reading: the base φ as the intrinsic clock-ratio. In a tick-first ontology, the scan index n is the only primitive time variable. Choosing a slope α therefore fixes, at finite depth, how the tick stream distributes symbols under window projection and how mismatch accumulates along time. Proposition 2.5 makes this selection auditable: at every finite depth, the golden branch is the unique minimizer of a finite-depth continued-fraction complexity proxy and therefore the unique choice that closes the symbolic/arithmetic bridge to a canonical digit grammar. This is why the Fibonacci growth rate $\log \varphi$ becomes the intrinsic normalization constant for scale and time dictionaries downstream: it is the topological entropy (capacity) of the Zeckendorf-admissible stable-type language X_m on the golden branch (cf. Remark 10.2 and Remark 4.4). This should not be confused with the entropy *rate* of the Sturmian time-series readout, which vanishes (Appendix L). Accordingly, the resolution coordinate $r(\mu) = \log(\mu/m_e)/\log \varphi$ used later is simultaneously a log-frequency and (up to sign) a log-time coordinate (Appendix Y), providing a unified tick-derived scale language.

Proposition 2.5 (Finite-depth least-discrepancy rigidity of the golden branch)**.** *Let $\alpha = [0; a_1, a_2, \dots] \in (0, 1) \setminus \mathbb{Q}$ and fix a depth $m \geq 0$. Define the finite-depth continued-fraction proxy*

$$C_m(\alpha) := \sum_{k=0}^{m} a_{k+1}.$$

Then $C_m(\alpha) \geq m + 1$, with equality if and only if $a_1 = \cdots = a_{m+1} = 1$. In particular, $\alpha = \varphi^{-1} = [0; 1, 1, 1, \dots]$ uniquely minimizes $C_m(\alpha)$ at every depth.

Proof. Since $a_i \in \mathbb{N}$ for all i, one has $a_i \geq 1$, hence $C_m(\alpha) \geq m + 1$. Equality holds if and only if each term satisfies $a_{k+1} = 1$ for $k = 0, \dots, m$, i.e. $a_1 = \cdots = a_{m+1} = 1$. □

The CAP reading is that, among irrational scan slopes, the golden branch is rigidly selected as the unique minimizer of a finite-depth complexity/discrepancy proxy, and it is the unique choice that closes the Ostrowski numeration to Zeckendorf/Fibonacci ticks used throughout the folding layer.

2.3.1 Accumulated mismatch and discrepancy certificates (interface)

Beyond finite-depth proxies, mismatch accumulation along scan time admits a standard certificate formulation in terms of discrepancy. For the orbit $x_n = x_0 + n\alpha \pmod 1$ (Section 2.1),

define the star discrepancy of the length-N prefix by [28]

$$D_N^* := \sup_{a\in[0,1]} \left| \frac{1}{N} \sum_{n=0}^{N-1} \mathbf{1}_{[0,a)}(x_n) - a \right|, \tag{6}$$

and the accumulated mismatch by

$$E_N := N\, D_N^*. \tag{7}$$

In this language, sustainable readout corresponds to keeping E_N controlled over long horizons, while phase locking corresponds to linear growth in E_N for rational (or effectively rational) slopes. For bounded-type irrational slopes (notably the golden branch), E_N admits explicit logarithmic upper bounds tied to continued-fraction data [28, 29]; in the HPA–Ω program this provides a quantitative mismatch dynamic that complements the symbolic/grammar viewpoint and supports least-discrepancy selection principles [4, 7].

Remark 2.6 (An explicit bounded-type certificate (self-contained))**.** *Appendix N records a self-contained derivation of a continued-fraction/Ostrowski bound for the Kronecker scan: if $\alpha = [0; a_1, a_2, \ldots]$ has bounded partial quotients $a_k \le A$, then*

$$D_N^*(P_N(\alpha)) \le \frac{8A}{N}(4 + \log_\varphi N), \qquad E_N \le 8A(4 + \log_\varphi N),$$

and the golden branch $a_k \equiv 1$ is the minimax choice within this audited certificate family (Remark N.7).

Remark 2.7 (What changes if α is varied)**.** *If one replaces $\alpha = \varphi^{-1}$ by another irrational, the theorem-level Sturmian minimal-complexity property remains (Remark 2.3), but the canonical digit system changes: the induced numeration becomes the Ostrowski system associated to the continued fraction of α rather than Zeckendorf/Fibonacci [22, 26]. Accordingly, the specific Fibonacci counts and φ-based depth coordinates used in later sections are tied to the golden branch choice; a generalized program would replace Fibonacci weights by the corresponding Ostrowski weights and would induce a different admissibility grammar. In the present paper we therefore fix $\alpha = \varphi^{-1}$ as the CAP-minimal choice within this audited class (Proposition 2.5), and we audit robustness primarily under window-length uplift $m \mapsto m'$ and balanced refinement $m = 2n$ (Appendix AE), rather than under arbitrary irrational-slope substitution.*

Golden-angle scan on a planar screen (phyllotaxis overlay; not used in proofs)

[Interface]For reader intuition, one may visualize the golden-branch scan as a planar point set (a phyllotaxis/sunflower disk) obtained by a deterministic map from the one-dimensional rotation orbit. [Audit]This construction is an interpretation-layer overlay: it introduces no new axiom and is not used as a premise in theorem-level proofs. The quantitative auditable proxy remains the mismatch/discrepancy certificates of Subsubsection 2.3.1 and Appendix N.

Let $\alpha = \varphi^{-1}$ be the golden-branch slope in (2). Writing the same orbit with the complementary step

$$\beta := 1 - \alpha = \varphi^{-2},$$

the corresponding planar "golden angle" increment is $\gamma := 2\pi\beta \approx 137.5°$. Given a horizon $N \ge 1$, define the tick-indexed planar points by

$$\theta_k := 2\pi k\beta, \qquad \rho_k := \sqrt{\frac{k}{N}}, \qquad z_k := \rho_k\, \mathrm{e}^{\mathrm{i}\theta_k} \in \mathbb{C}, \qquad k = 0, 1, \ldots, N-1.$$

The set $\{z_k\}$ is the classical phyllotaxis disk. Its role here is organizational: it turns the slope selection at the golden branch into a planar "screen" picture that helps connect three interface dictionaries used elsewhere in the paper: (i) uniform coverage / isotropy proxies (quantified by discrepancy, i.e. E_N in (7)), (ii) distance as addressing steps on a chosen display graph (Section 5 and Definition 3.3), and (iii) local density/revisit as a visualization proxy for overhead/latency dictionaries (Section 10 and Appendix Y).

[Match]The value 137.5° is an angle reported in a chosen unit system, while $1/\alpha_{\mathrm{em}}$ is a dimensionless ratio; any numerical comparison belongs to matching/interpretation and is not used as a premise for closure.

3 Tick calculus: deriving observables, space, gauge, and scale from sequential readout

Aim. This section fixes the time-first spine used throughout the paper. We treat the tick (scan iteration count) as the only primitive input and CAP as the only primitive closure/selection rule, and we define all physical-language quantities as derived protocol structures. Mathematical-layer statements (counts, maps, and finite tables) remain as in Sections 2 and 4; the additional content here is a dictionary that maps each physical concept to an explicit mathematical object.

3.1 The tick as the only primitive input

Definition 3.1 (Tick (scan time))**.** *The* tick *is the scan iteration index $t \in \mathbb{Z}$. The direction $t \mapsto t+1$ is the operational notion of forward time within the protocol.*

Audit note. [Audit]**Status:** [Interface]. **Depends on:** Axiom 1.1. **If:** time is identified with the executed update order (a definitional convention; no additional dynamical assumption).

3.2 Time orientation and initialization: the arrow of time in tick-only language

Orientation is part of sequential execution. [Interface]At the mathematical layer, the scan orbit can be indexed by $\mathbb{Z}$ and is formally symmetric under reversal $t \mapsto -t$. In the executed protocol, "time" is the operational update order (Definition 3.1), so $t \mapsto t+1$ is the forward direction by definition.

Origin choice. [Interface]Protocol observables depend only on tick differences (e.g. Definition 3.4), so shifting $t \mapsto t + t_0$ is a coordinate convention away from boundary conditions.

Irreversibility from finite observability (no new axiom). [Interface]The arrow is not postulated as an extra dynamical law: it arises because "physics" here is the finite record after window projection and stability folding, both many-to-one. Consequently, observable word histories are not invertible to unique microstate histories, and reversal corresponds to a different protocol/run (Section 7.1).

3.3 From ticks to finite observables: windows and words

Observable records are finite. Fix a window length $m \geq 1$. Finite readout is represented by length-m binary words

$$\Omega_m := \{0,1\}^m, \qquad |\Omega_m| = 2^m,$$

obtained by window projection of the scan stream (Section 2.2). [Math]At resolution m, an elementary record is the pair *(tick, word)*.

3.4 Stability as an intrinsic grammar: admissible types and folding

Stability is a predicate on words. At the golden branch, the φ-channel selects the admissible set $X_m \subset \Omega_m$ by a forbidden-word grammar (no adjacent ones), and one has the Fibonacci count $|X_m| = F_{m+2}$ (Lemma 4.5). The π-channel induces the cyclic/boundary split (Proposition 4.8).

Microstates and projection. [Math]The folding map Fold_m (Definition (14)) deterministically projects microstate indices in Ω_m to stable types in X_m; it is surjective for all m (Proposition 4.20).

Audit note. [Audit]**Status:** [Math]. **Depends on:** the admissible grammar defining X_m and the explicit truncation map Fold_m (Section 4). **If:** Fold_m is the Zeckendorf-truncation projection adopted in this paper (theorems apply to the map as defined).

3.5 Space as addressing: display graphs, distance, and velocity

Space is a derived display structure. To speak about locality, the protocol must choose an addressing basis that embeds a finite tick prefix into a neighborhood graph. At Hilbert order n, the canonical finite prefix is $t \in \{0, \ldots, 4^n - 1\}$ and the Hilbert addressing map is a bijection

$$H_n : \{0, 1, \ldots, 4^n - 1\} \to \{0, 1, \ldots, 2^n - 1\}^2$$

(Section 5).

Definition 3.2 (Addressing map and display graph)**.** *Fix an order n and an addressing map A_n from indices to sites. For the Hilbert screen, $A_n := H_n$. Define the* display graph *G_n as the nearest-neighbor graph on the site set $A_n(\{0, \ldots, 4^n - 1\})$, with edges given by unit Manhattan adjacency on the grid.*

Definition 3.3 (Protocol distance)**.** *For sites x, y in the display graph G_n, define the protocol distance*

$$d_n(x, y) := \textit{shortest-path distance between } x \textit{ and } y \textit{ in } G_n.$$

Tick-distance relation. [Interface]Distance is a tick-count proxy once a per-move tick budget is fixed (Definition 3.3).

Definition 3.4 (Protocol velocity and maximal signal rate (tick units))**.** *Given a tick-indexed site trajectory $x(t) \in G_n$, define the protocol velocity (in sites per tick) by*

$$v(t_1, t_2) := \frac{d_n(x(t_1), x(t_2))}{|t_2 - t_1|} \qquad (t_1 \neq t_2).$$

The maximal protocol signal rate on G_n is the supremum of v over admissible update rules.

Remark 3.5 (Physical units and the speed-of-light dictionary)**.** *The quantities in Definitions 3.3 and 3.4 are dimensionless (graph units per tick). Any identification with meters/seconds, and hence any identification with the measured constant c, is a matching-layer calibration (Remark 2.1).*

3.6 Bulk dimension as a CAP output from the anchor bit budget

Screen versus bulk. The addressing screen used for finite diagnostics is a protocol-level readout basis (Section 5). By contrast, the *bulk dimension* d is an interface parameter that enters when one asks what it means to *display* a localized rigid object and to compare its pose across sites. In the tick-only language, d is not taken as a primitive input: it is selected from a finite candidate set by CAP at the chosen anchor scale.

Definition 3.6 (Rigid-frame coarse-lock budget (tick-only interface))**.** *Let $d \geq 1$ be a candidate bulk dimension. A local rigid frame has d translational degrees of freedom and $d(d-1)/2$ rotational degrees of freedom, hence* $\dim SE(d) = d(d+1)/2$. *Under the minimal nontrivial coarse-lock convention (two bins per independent parameter), a single binary window of length m can coarse-lock a rigid frame only if*

$$m \;\geq\; \dim SE(d) = \frac{d(d+1)}{2}.$$

Proposition 3.7 (CAP-maximal bulk dimension at the anchor)**.** *At the chosen anchor window length $m = 6$, CAP selects the maximal bulk dimension compatible with the coarse-lock budget in Definition 3.6, namely $d = 3$. Equivalently,* $\dim SE(3) = 6$ *matches the anchor bit budget.*

Proof. For $d = 4$ one has $\dim SE(4) = 10 > 6$, so a single $m = 6$ window cannot coarse-lock a 4D rigid frame under the minimal two-bin convention. For $d = 3$ one has $\dim SE(3) = 6$, so $d = 3$ is admissible and saturates the budget. Thus the maximal admissible d is 3. □

Audit note. [Audit]**Status:** [Interface] + CAP. **Depends on:** Definition 3.6 and the anchor choice $m = 6$. **If:** the single-window coarse-lock criterion uses the minimal two-bin-per-parameter convention; this selection does not enter the theorem-level folding statements.

3.7 Gauge data as fiber compensation

Why connections are forced. At fixed m, stable labels $w \in X_m$ carry finite microstate fibers $P(w) = \mathrm{Fold}_m^{-1}(w)$. Once the protocol demands cross-site consistency on the display graph, stable labels alone are insufficient: one must also specify how fibers are matched between neighbors (Proposition 8.1). This is the finite origin of compensating connection data and gauge redundancy.

3.8 Overhead, delay, and scale: mass and energy as time dictionaries

Overhead as time-lag. In a tick-first ontology, "mass as depth" is an operational statement about overhead: stabilizing a pattern consumes additional local protocol resources. At the matching layer, this overhead can be accessed through delay observables (Wigner–Smith; Appendix Y) and compared to clock-rate/lapse dictionaries.

A single log-time coordinate. Fix the electron reference $\mu_0 = m_e$ and define the resolution coordinate

$$r(\mu) := \frac{\log(\mu/m_e)}{\log \varphi}.$$

By the Compton-clock dictionary (Appendix Y), r is simultaneously a log-frequency and (up to a sign) a log-time coordinate. This is the sense in which mass and energy are derived from time in the present protocol language: they are calibrated re-expressions of time-scale ratios relative to the $m = 6$ anchor.

protocol concept	mathematical object	where fixed in this paper	operational proxy (matching layer)
time (tick)	$t \in \mathbb{Z}$ (Definition 3.1)	Axiom 1.1; Section 3	laboratory clock ticks after calibration
finite observables	$w \in \Omega_m = \{0,1\}^m$	Section 2.2	binary readout stream / bit records
stability (types)	$X_m \subset \Omega_m$	Section 4	persistent readout classes
projection	$\mathrm{Fold}_m : \{0,\dots,2^m-1\} \twoheadrightarrow X_m$	Section 4.7	coarse graining / equivalence classes
space (display)	addressing map A_n and graph G_n	Section 5; Definition 3.2	locality graph used for audits
distance	d_n (graph metric)	Definition 3.3	hop count / minimal transport steps
velocity (tick units)	$v = \Delta d/\Delta t$	Definition 3.4	propagation rate; c after calibration
phase	dyadic register $\mathbb{Z}_{2^p}$ and $\mathrm{e}^{\mathrm{i}\theta}$	Appendix B; Section 1.8	phase readout / interferometry
frequency	$\omega = \Delta\theta/\Delta t$ (tick units)	Appendix AA	spectral peaks; clock ratios; redshift
gauge data	fiber matchings / holonomy	Section 6	plaquette holonomy statistics
curvature (finite)	holonomy conjugacy invariants	Section 6; Appendix AA	loop/plaquette statistics
overhead / lapse	$\kappa, \chi = \log(\kappa/\kappa_0)$, $N = \mathrm{e}^{-\gamma\chi}$	Appendices Y, AD.7	clock slowdown; redshift; time delay
mass (overhead)	depth / delay dictionary	Sections 10, 13	Compton time; Wigner–Smith delay
energy/scale	$r(\mu) = \log_\varphi(\mu/m_e)$	Section 10.1	frequency/energy conventions
dynamics (continuum closure)	CAP-selected action class $[S]$ and its EOM	Appendices AD.4–AD.5	weak-field tests; effective-field fits
entropy/temperature	state-count and conjugate scale	Appendix AD.6	thermodynamic entropy; noise spectra
force	response functional (action/free energy gradient)	Appendices AD.5, AD.6	acceleration; pressure/gradient forces
Born probabilities	POVM probabilities $P_k = \mathrm{Tr}(\rho E_k)$	Appendix AD.10	measurement frequencies
RG / running	$\mathrm{d}g/\mathrm{d}r = (\log\varphi)\beta(g)$	Appendix AD.11	scale dependence of couplings
cosmology (interface)	$f_{\mathrm{stab}}(m) = F_{m+2}/2^m$, $d_m = 2^m/F_{m+2}$	Appendix AD.12	energy budget / clustering proxies

Table 3: Tick-first dictionary: each physical-language concept used in this paper is identified with an explicit mathematical object derived from sequential readout.

3.9 Dictionary summary: physical concepts as mathematical objects

Full derivation spine (supplement). [Audit]Appendix G records the full tick + CAP derivation spine (candidate families, objectives, and deterministic tie-breaks) behind the interface components summarized here.

Part III
Periodic Core: the $(\varphi, \pi, \mathrm{e})$ channels and the anchor

4 Resolution folding core: $\Omega_6 \to X_6$ and the $64 \to 21$ stable sector

This section records the finite-resolution mathematical layer of the construction with fully explicit definitions and proofs. The broader resolution-folding and recursive uplift program (beyond the $m = 6$ anchor emphasized here) is developed in the companion manuscript [9].

4.1 Microstate readout space and balanced coupling

Fix a window length $m \geq 1$ and define the microstate readout space

$$\Omega_m := \{0,1\}^m, \qquad |\Omega_m| = 2^m,$$

with linearization $\mathcal{H}_m := \ell^2(\Omega_m)$. To attach explicit spatial diagnostics later (Hilbert addressing, chirality, holonomy), we use an addressing basis as a readout screen (Section 5); at the minimal anchor this choice is made explicit and auditable (Table 5). We adopt the classical 2D Hilbert addressing and a balanced cardinality match on that screen, $2^m = 4^n$ (equivalently $m = 2n$). We focus on the minimal instance used in this paper, $n = 3$ and hence $m = 6$:

$$\Omega_6 = \{0,1\}^6, \qquad |\Omega_6| = 64.$$

At the same order $n = 3$, the 2D Hilbert-addressed grid has $4^n = 64$ sites, matching the local readout cardinality.

Lemma 4.1 (Balanced coupling equivalences)**.** *For integers $m, n \geq 1$, the following are equivalent:*

$$2^m = 4^n, \qquad m = 2n.$$

Equivalently, an order-n Hilbert grid has the same number of sites as the m-bit readout alphabet Ω_m if and only if $m = 2n$.

Proof. Since $4^n = (2^2)^n = 2^{2n}$, the equality $2^m = 4^n$ holds if and only if $m = 2n$. □

Remark 4.2 (Balanced coupling and addressing dimension)**.** *Lemma 4.1 is the cardinality match specialized to the 2D Hilbert addressing used for the explicit finite diagnostics in this paper: an order-n square grid has $4^n = (2^2)^n$ sites, hence $2^m = 4^n \iff m = 2n$. More generally, a d-dimensional hypercubic addressing basis at side length 2^n has $(2^n)^d = 2^{dn}$ sites, and matching $|\Omega_m| = 2^m$ corresponds to $m = dn$. We use the 2D Hilbert grid as an explicit readout screen for the diagnostics below; see Remark 5.1 for the rationale, Table 5 for the bounded counterfactual audit, and the 3D comparison in Remark 5.1.*

Operational forcing rationale for $m = 2n$ (2D screen) and for the "minimal" instance. At Hilbert order n, the scan index ranges over $\{0, \ldots, 4^n - 1\}$ and therefore carries exactly $2n$ bits of information. The balanced rule $m = 2n$ identifies a readout window length with this canonical bit budget and yields a simple one-to-one site labeling on the chosen 2D screen (Lemma 4.1).

Remark 4.3 (Balanced coupling is a diagnostic convention)**.** *Balanced coupling is not a theorem-level requirement of the folding core. All folding maps, admissible sets, and counting statements in this section are defined for every m. The balanced relation $2^m = 4^n$ is adopted only when we attach spatial diagnostics by placing window words (or stable types) on an order-n addressing grid with matched cardinality so that each site carries exactly one m-bit microstate label. Within the tick-only interface of this paper, this choice is CAP-minimal among couplings on a fixed screen: a bijective site↔window assignment avoids additional protocol conventions and mapping overhead. Other couplings $2^m \neq 4^n$ correspond to non-bijective site↔window assignments and would require additional protocol conventions; they are not pursued here.*

Why (m,n)=(6,3)? A minimal holonomy anchor (CAP). The algebra permits any m and any addressing basis; attaching locality and transport diagnostics requires additional protocol structure. A closed-loop holonomy diagnostic requires at least a two-dimensional display graph, so we use a 2D screen (Section 5). Given a fixed 2D screen and an addressing basis, balanced coupling $2^m = 4^n$ is CAP-minimal because it yields a bijective site↔microstate assignment and avoids additional mapping overhead (Remark 4.3). Among balanced pairs, CAP then

channel	explicit finite-m definition and derived output at $m = 6$
φ (grammar)	Forbidden-word legality: $X_m := \{w \in \{0,1\}^m : w_i w_{i+1} = 0\}$, equivalently $D_\varphi(w) = \mathbf{1}\{w \text{ contains } 11\}$ and φ-stability is $D_\varphi(w) = 0$ (Equation (8)). Then $\lvert X_m\rvert = F_{m+2}$ and in particular $\lvert X_6\rvert = F_8 = 21$ (Lemma 4.5).
π (wrap-around)	Cyclic closure at finite window length: $D_\pi(w) = \mathbf{1}\{w_1 = w_m = 1\}$ and $X_m = X_m^{\mathrm{cyc}} \sqcup X_m^{\mathrm{bdry}}$ with $X_m^{\mathrm{cyc}} = \{w \in X_m : w_1 w_m = 0\}$ and $X_m^{\mathrm{bdry}} = \{w \in X_m : w_1 = w_m = 1\}$ (Section 4.4). Then $\lvert X_m^{\mathrm{bdry}}\rvert = F_{m-2}$ and at $m = 6$ one has the canonical split $21 = 18 \oplus 3$ with explicit boundary words (Proposition 4.8 and Corollary 4.9).
e (analytic)	Analytic stability template: Artin–Mazur zeta and Abel normalization for the golden mean shift, yielding $\zeta(z) = 1/(1-z-z^2)$ and the Abel pole barrier at $r = 1$ under $z = r/\varphi$ (Section 4.5). At $m = 6$ this channel is used as an interpretation layer rather than to further reduce X_6 (Remark 4.12).

Table 4: The three stability channels as explicit finite constructions. The reduction $64 \to 21$ at $m = 6$ is enforced by the φ-grammar (admissible words), while the π-channel induces the canonical $18 \oplus 3$ cyclic/boundary split; the e-channel supplies an analytic stability template used for interpretation and for higher-resolution variants.

selects the smallest n for which the deterministic finite connection yields nontrivial plaquette holonomies (3/4 cycles) and a nonzero phase-lift signal; the balanced-chain sweep in Table 30 shows that $n = 1, 2$ produce only trivial holonomy while $n = 3$ is the first scale with nontrivial 3/4-cycle content. Thus the minimal anchor on this screen is $(n, m) = (3, 6)$. We treat $(m, n) = (6, 3)$ as a concrete anchor for fully explicit finite diagnostics; higher balanced pairs such as $(m, n) = (8, 4)$ and $(10, 5)$ are addressed uniformly by the same definitions and by the uplift sweeps recorded in Appendix AE. In particular, the Fibonacci admissible sizes and the π-channel split persist for all m (Lemma 4.5 and Proposition 4.8): for example,

$$2^8 \to |X_8| = 55, \qquad 55 = 47 \oplus 8,$$

and

$$2^{10} \to |X_{10}| = 144, \qquad 144 = 123 \oplus 21,$$

as recorded in Table 66.

4.2 Three stability channels (summary)

At finite window length, stability is organized by three channels, denoted φ–π–e. For the mainline narrative we treat them as explicit predicates/definitions on finite words. An equivalent defect-operator viewpoint and an optional relaxation dynamics are recorded in Appendix O.

Three stability channels (fully explicit at finite window length). The $64 \to 21$ claim at $m = 6$ is not obtained by fitting or post-hoc filtering: it follows deterministically from explicit defect predicates on finite words (the φ and π channels) together with a standard analytic template (the e channel). For reader convenience, Table 4 summarizes the precise channel definitions used in this paper and points to the theorem-level count statements that follow.

4.3 The φ-channel: Zeckendorf grammar and $|X_6| = 21$

Define the golden-mean admissible set (forbidden substring "11")

$$X_m := \{w \in \{0,1\}^m : \ w_i w_{i+1} = 0 \text{ for all } i = 1, \ldots, m-1\}. \tag{8}$$

Equivalently, define the defect function

$$D_\varphi(w) := \mathbf{1}\{w \text{ contains the substring } 11\},$$

so that φ-stability is $D_\varphi(w) = 0$ and the φ-stable sector is exactly X_m.

Remark 4.4 (Sturmian readout language vs. golden-mean admissible language)**.** *The set X_m is the length-m* block language *of the golden-mean shift (the shift of finite type forbidding the word* 11*), hence $|X_m| = F_{m+2}$ and its associated topological entropy is* $\log\varphi$ *(Lemma 4.5 and Remark 10.2). This should not be confused with the factor language of the* Sturmian *time-series readout produced by an irrational scan and a canonical two-interval window partition, which has factor complexity $p(m) = m + 1$ and zero entropy rate (Appendix L). The two notions are compatible because the Sturmian language is a strict subset of the golden-mean admissible block language (Appendix M).*

Lemma 4.5 (Fibonacci count of admissible words)**.** *For all $m \geq 1$, one has $|X_m| = F_{m+2}$. In particular, $|X_6| = F_8 = 21$.*

Proof. Let $a_m := |X_m|$. An admissible length-m word either starts with 0 followed by an admissible length-$(m-1)$ word, or starts with 10 followed by an admissible length-$(m-2)$ word. Thus $a_m = a_{m-1} + a_{m-2}$ with initial values $a_1 = 2$, $a_2 = 3$, hence $a_m = F_{m+2}$. □

Remark 4.6 (Sub-geometric stable types at $m < 6$ (interface))**.** *Lemma 4.5 shows that admissible stable types exist at every window length, including the near-threshold case $m = 5$ with $|X_5| = F_7 = 13$. Under the rigid-frame coarse-lock budget at the anchor (Section 1.3; Proposition 3.7), $m = 6$ is the minimal* single-window *anchor compatible with coarse localized rigid-frame display at the protocol interface, so $m < 6$ admissible types are* sub-geometric *in this interface sense (cf. Remark 1.4). We refer to Section 1.3.1 and Section P for the complementary protocol interpretations of the vacuum sector (sub-geometric admissibility versus protocol-unstable microstates).*

Remark 4.7 (The ghost sector: protocol-unstable microstates (interface))**.** *In the HPA scan–projection paradigm, a vacuum is not the absence of microstates but the absence of* stable localized outputs *under a fixed finite-resolution protocol. In addition to sub-geometric admissible types at $m < 6$ (Section 1.3.1), a second contribution is present already at fixed m: the protocol-unstable complement $\Omega_m \setminus X_m$ consisting of readout words that violate the admissibility grammar. We refer to $\Omega_m \setminus X_m$ as the* ghost sector*.*

At the anchor $m = 6$, one has $|\Omega_6| = 64$ and $|X_6| = 21$, hence $|\Omega_6 \setminus X_6| = 64 - 21 = 43$. This same count also appears as projection redundancy in the many-to-one folding map Fold_6 *(Section 4.6): stable readout labels retain* 21 *degrees of freedom while* 43 *microscopic degrees of freedom are suppressed by projection.*

A minimal instability witness. *Define the adjacent-ones count*

$$N_{11}(w) := \#\{\, i \in \{1, \ldots, m-1\} \;:\; w_i = w_{i+1} = 1 \,\}.$$

Then $X_m = \{w \in \Omega_m : \; N_{11}(w) = 0\}$ and the ghost sector is $\Omega_m \setminus X_m = \{w \in \Omega_m : \; N_{11}(w) \geq 1\}$. Section P records diagnostic m-sweeps for the ghost sector (violation distributions and minimal repair costs) generated by deterministic scripts.

Define the φ-stable projection $P_\varphi : \mathcal{H}_m \to \mathcal{H}_m$ as the orthogonal projection onto $\ell^2(X_m)$. At $m = 6$, this is the first rigid compression:

$$\mathrm{rank}(P_\varphi) = |X_6| = 21.$$

4.4 The π-channel: cyclic closure and the $18 \oplus 3$ split

At finite window length, the π-channel refines stability by imposing a cyclic wrap-around admissibility. Define the wrap-around defect

$$D_\pi(w) := \mathbf{1}\{w_1 = w_m = 1\}.$$

For a window length $m \geq 4$, define

$$X_m^{\mathrm{cyc}} := \{w \in X_m : \ w_1 w_m = 0\}, \qquad X_m^{\mathrm{bdry}} := \{w \in X_m : \ w_1 = w_m = 1\}.$$

Proposition 4.8 (Cyclic/boundary split size for the π-channel)**.** *For every $m \geq 4$, the boundary set has Fibonacci size*

$$|X_m^{\mathrm{bdry}}| = F_{m-2},$$

and therefore, using Lemma 4.5,

$$|X_m^{\mathrm{cyc}}| = |X_m| - |X_m^{\mathrm{bdry}}| = F_{m+2} - F_{m-2}.$$

Proof. If $w \in X_m^{\mathrm{bdry}}$, then $w_1 = w_m = 1$ and Zeckendorf admissibility forces $w_2 = w_{m-1} = 0$. Thus the middle substring $w_3 \cdots w_{m-2}$ is an admissible word of length $m-4$ with no adjacent ones, i.e. an element of X_{m-4}. Conversely, any $u \in X_{m-4}$ yields a boundary word $w = 10\,u\,01 \in X_m^{\mathrm{bdry}}$. This gives a bijection $X_m^{\mathrm{bdry}} \cong X_{m-4}$, hence

$$|X_m^{\mathrm{bdry}}| = |X_{m-4}| = F_{(m-4)+2} = F_{m-2}$$

by Lemma 4.5. □

Corollary 4.9 (Canonical $18 \oplus 3$ split at $m = 6$)**.** *At $m = 6$, one has $|X_6^{\mathrm{cyc}}| = 18$ and $|X_6^{\mathrm{bdry}}| = 3$, and*

$$X_6^{\mathrm{bdry}} = \{100001,\ 100101,\ 101001\}.$$

Proof. The sizes follow from Proposition 4.8 and Lemma 4.5. For the explicit list, use the bijection in the proof of Proposition 4.8: every boundary word at $m = 6$ has the form $w = 10\,u\,01$ with $u \in X_2$. Now $X_2 = \{00, 01, 10\}$, hence $X_6^{\mathrm{bdry}} = \{10\,00\,01,\ 10\,01\,01,\ 10\,10\,01\} = \{100001, 100101, 101001\}$. □

4.5 The e-channel: Artin–Mazur zeta and Abel pole barrier

The e-channel expresses analytic stability through zeta functions and Abel normalization [30–32]. For a compact, self-contained summary of the Abel-path and pole-barrier viewpoint used in this channel, see Appendix B. For a dynamical system (X, f), the Artin–Mazur zeta function is defined by the periodic-point counts

$$\zeta_f(z) := \exp\left(\sum_{n \geq 1} \frac{\#\mathrm{Fix}(f^n)}{n}\, z^n\right), \tag{9}$$

whenever the series is well-defined [30,31]. For shifts of finite type with transition matrix A, the Artin–Mazur zeta function admits the standard rational form $\zeta(z) = 1/\det(I - zA)$ [23,31,32]. For the golden mean shift, one can make A explicit:

Lemma 4.10 (Golden mean shift: transition matrix and zeta)**.** *Let $X \subset \{0,1\}^{\mathbb{Z}}$ be the shift of finite type defined by the forbidden word 11. With state space $\{0,1\}$ and allowed transitions $0 \to 0$, $0 \to 1$, $1 \to 0$, the transition matrix is*

$$A = \begin{pmatrix} 1 & 1 \\ 1 & 0 \end{pmatrix}.$$

Consequently,

$$\zeta(z) = \frac{1}{\det(I - zA)} = \frac{1}{1 - z - z^2}. \tag{10}$$

Proof. The transition rule encodes the forbidden substring "11", hence the stated adjacency matrix. Then

$$I - zA = \begin{pmatrix} 1-z & -z \\ -z & 1 \end{pmatrix}, \qquad \det(I - zA) = (1-z)\cdot 1 - z^2 = 1 - z - z^2,$$

which gives (10). □

Let φ be the golden ratio and apply spectral normalization $z = r/\varphi$. Then

$$\zeta_{\mathrm{e}}(r) := \zeta(r/\varphi) = \frac{1}{1 - \frac{r}{\varphi} - \frac{r^2}{\varphi^2}} = \frac{1}{(1-r)(1+\frac{r}{\varphi^2})}. \tag{11}$$

The principal pole at $r = 1$ lies on the boundary of the unit disk and plays the role of an analytic "pole barrier" for Abel-type limits.

Lemma 4.11 (Golden normalization factorization)**.** *One has the identity*

$$1 - \frac{r}{\varphi} - \frac{r^2}{\varphi^2} = (1-r)(1+\frac{r}{\varphi^2}),$$

so the poles of ζ_{e} are located at $r = 1$ and $r = -\varphi^2$.

Proof. Using $1 - \varphi^{-2} = \varphi^{-1}$ (equivalently $\varphi^2 = \varphi + 1$), expand

$$(1-r)(1+\frac{r}{\varphi^2}) = 1 - r + \frac{r}{\varphi^2} - \frac{r^2}{\varphi^2} = 1 - \Big(1 - \frac{1}{\varphi^2}\Big)r - \frac{r^2}{\varphi^2} = 1 - \frac{r}{\varphi} - \frac{r^2}{\varphi^2}.$$

□

Remark 4.12 (Finite window vs. higher-resolution distinction)**.** *At the minimal window length $m = 6$, the analytic channel is used here primarily as an* interpretation layer *for stability (holomorphy domain and boundary pole), while the admissible-word selection is already enforced by the φ-grammar. At higher resolution, weighted/pressure-like variants can make* e *genuinely distinct from a single forbidden-word predicate.*

4.6 The folding map Fold_6: from 64 indices to 21 stable types

Index the microstate words by integers $\{0, \dots, 2^m - 1\}$ via the usual binary identification. For $N \in \{0, \dots, 63\}$, let (c_k) be the Zeckendorf digits of N as in (4). Define the length-6 folding map by truncation:

$$\mathrm{Fold}_6(N) := (c_1, \dots, c_6) \in X_6, \tag{12}$$

padding by zeros if the expansion length is < 6.

Remark 4.13 (Dyadic microstates versus Zeckendorf digits)**.** *At fixed window length m, there are two distinct binary coordinate systems in play. The microstate register $\{0, \dots, 2^m - 1\}$ is dyadic (a size-2^m index set), while the stable sector X_m is defined as a Zeckendorf-admissible digit language (no adjacent ones) on the golden branch. The folding map Fold_m used in this paper is the explicit deterministic bridge between these coordinates: it converts a dyadic index N to its Zeckendorf digits and then takes a length-m prefix (Definition (14)). This is a [Math]definition of the finite folding layer. Other deterministic base-change/repair conventions from $\{0, \dots, 2^m - 1\}$ to X_m are possible and would, in general, induce different fiber statistics. To make this dependence auditable, Appendix Q records a bounded counterfactual family of alternative maps at $m = 6$ and summarizes the resulting finite invariants. Within that bounded family, the additional natural fixed-point constraint $F(V(w)) = w$ for all $w \in X_6$ (Definition Q.1) selects the Zeckendorf-truncation map uniquely (Proposition Q.2).*

Definition 4.14 (Zeckendorf value of a stable word)**.** *For $w = w_1 \cdots w_6 \in X_6$, define its Zeckendorf value*

$$V(w) := \sum_{k=1}^{6} w_k F_{k+1} = w_1 \cdot 1 + w_2 \cdot 2 + w_3 \cdot 3 + w_4 \cdot 5 + w_5 \cdot 8 + w_6 \cdot 13. \tag{13}$$

Proposition 4.15 (Value labeling of the 21 stable types)**.** *The map $V : X_6 \to \{0, 1, \ldots, 20\}$ is a bijection.*

Proof. **Step 1 (range).** Since $w \in X_6$ has no adjacent ones, the maximal value is attained by the admissible choice $w = 010101$, giving

$$V(w) = 2 + 5 + 13 = 20.$$

Thus $0 \le V(w) \le 20$ for all $w \in X_6$, so V maps into $\{0, \ldots, 20\}$.

Step 2 (injectivity). Let $w, w' \in X_6$ and suppose $V(w) = V(w') =: N$. By Step 1, $N \le 20 < 21 = F_8$, so the Zeckendorf expansion of N uses only Fibonacci weights up to $F_7 = 13$ and has zero digits beyond position 6. Therefore the length-6 Zeckendorf digit vector of N is uniquely defined. Since w and w' are both admissible digit vectors yielding the same value N, Zeckendorf uniqueness forces $w = w'$. Hence V is injective.

Step 3 (bijectivity). By Lemma 4.5, $|X_6| = 21$, and $|\{0, \ldots, 20\}| = 21$. An injective map between two finite sets of equal size is bijective. □

Lemma 4.16 (Surjectivity of Fold_6)**.** *For every stable word $w \in X_6$, one has*

$$\mathrm{Fold}_6(V(w)) = w.$$

In particular, $\mathrm{Fold}_6 : \{0, \ldots, 63\} \twoheadrightarrow X_6$ *is surjective.*

Proof. Fix $w = w_1 \cdots w_6 \in X_6$ and set $M := V(w)$. By Proposition 4.15, $0 \le M \le 20 < 21 = F_8$, so the Zeckendorf expansion of M uses only Fibonacci weights up to $F_7 = 13$ and has zero digits beyond c_6. Moreover, by construction of $V(w)$, the digit vector $(c_1, \ldots, c_6)$ of this Zeckendorf expansion equals $(w_1, \ldots, w_6)$. Therefore, by the definition (12), $\mathrm{Fold}_6(M) = (c_1, \ldots, c_6) = w$. □

Lemma 4.17 (Explicit fiber description of Fold_6)**.** *Let $w \in X_6$ and write $v := V(w) \in \{0, \ldots, 20\}$. Then $\mathrm{Fold}_6^{-1}(w)$ is given explicitly by:*

- *If $w_6 = 1$, then $\mathrm{Fold}_6^{-1}(w) = \{v,\ v + 34\}$.*
- *If $w_6 = 0$ and $v \le 8$, then $\mathrm{Fold}_6^{-1}(w) = \{v,\ v + 21,\ v + 34,\ v + 55\}$.*
- *If $w_6 = 0$ and $9 \le v \le 12$, then $\mathrm{Fold}_6^{-1}(w) = \{v,\ v + 21,\ v + 34\}$.*

In particular, every stable type has preimage size in $\{2, 3, 4\}$.

Proof. Fix $w \in X_6$ and write $v := V(w)$. By definition, $\mathrm{Fold}_6(N) = w$ iff the Zeckendorf digit string of N begins with $(c_1, \ldots, c_6) = w$. Write the Zeckendorf expansion of N as

$$N = v + \sum_{k \ge 7} c_k F_{k+1} = v + 21c_7 + 34c_8 + 55c_9 + \sum_{k \ge 10} c_k F_{k+1},$$

using $F_8 = 21$, $F_9 = 34$, $F_{10} = 55$. Since $0 \le N \le 63$, one must have $c_k = 0$ for all $k \ge 10$ because $F_{11} = 89 > 63$. Hence

$$N = v + 21c_7 + 34c_8 + 55c_9, \qquad c_7, c_8, c_9 \in \{0, 1\},$$

with Zeckendorf admissibility constraints

$$w_6c_7 = 0, \qquad c_7c_8 = 0, \qquad c_8c_9 = 0.$$

We now enumerate admissible (c_7, c_8, c_9) and enforce $N \le 63$.

Case 1: $w_6 = 1$**.** Then $c_7 = 0$. If $c_8 = 1$ then $c_9 = 0$ and $N = v + 34$. If $c_8 = 0$, then either $c_9 = 0$ giving $N = v$, or $c_9 = 1$ giving $N = v + 55$. But when $w_6 = 1$ one has $v \ge 13$, hence $v + 55 \ge 68 > 63$, so $c_9 = 1$ is impossible. Thus $\mathrm{Fold}_6^{-1}(w) = \{v, v + 34\}$.

Case 2: $w_6 = 0$**.** Now c_7 may be 0 or 1. If $c_7 = 1$ then $c_8 = 0$, and c_9 may be 0 or 1: this yields $N = v + 21$ or $N = v + 76$. The latter exceeds 63, so only $N = v + 21$ remains. If $c_7 = 0$, then c_8 may be 0 or 1. If $c_8 = 1$ then $c_9 = 0$ and $N = v + 34$. If $c_8 = 0$ then c_9 may be 0 or 1, yielding $N = v$ or $N = v + 55$. The option $N = v + 55$ is admissible iff $v \le 8$. Finally, note that for $w_6 = 0$ one always has $v \le 12$ (the maximal value without the $F_7 = 13$ digit). Therefore:

- if $v \le 8$, all three values v, $v + 21$, $v + 34$, $v + 55$ lie in $[0, 63]$;
- if $9 \le v \le 12$, $v + 55 > 63$ and the preimage reduces to $\{v, v + 21, v + 34\}$.

This proves the stated cases and the preimage-size set $\{2, 3, 4\}$. □

Theorem 4.18 (Finite folding statistics at $m = 6$)**.** *The map* $\mathrm{Fold}_6 : \{0, \dots, 63\} \twoheadrightarrow X_6$ *is surjective. Every stable type has preimage size* 2*,* 3*, or* 4*, with degeneracy histogram*

$$(|V_2|, |V_3|, |V_4|) = (8, 4, 9),$$

where $V_k := \{w \in X_6 : \ |\mathrm{Fold}_6^{-1}(w)| = k\}$*. Moreover, the boundary-sector preimages are*

$$\mathrm{Fold}_6^{-1}(100001) = \{14, 48\}, \quad \mathrm{Fold}_6^{-1}(100101) = \{19, 53\}, \quad \mathrm{Fold}_6^{-1}(101001) = \{17, 51\}.$$

Proof. Surjectivity is Lemma 4.16. Lemma 4.17 gives $|\mathrm{Fold}_6^{-1}(w)| \in \{2, 3, 4\}$.

Histogram. First count words with $w_6 = 1$. Such words satisfy $w_5 = 0$ and the prefix $w_1 \cdots w_4$ is any admissible word in X_4, hence there are $|X_4| = F_6 = 8$ such words. By Lemma 4.17 (case $w_6 = 1$) they have fiber size 2, so $|V_2| = 8$.

Now consider words with $w_6 = 0$. Then $w_1 \cdots w_5 \in X_5$, so there are $|X_5| = F_7 = 13$ such words. Among them, those with $w_5 = 1$ have $w_4 = 0$ and the remaining triple (w_1, w_2, w_3) can be any admissible length-3 word not equal to 000. Indeed, if $(w_1, w_2, w_3) = 000$ then $v = 8$, while any other admissible triple adds at least 1 to the value, giving $v \in \{9, 10, 11, 12\}$. There are exactly 4 admissible triples with sum ≥ 1, namely $100, 010, 001, 101$. Hence there are 4 words in X_6 with $w_6 = 0$ and $v \in \{9, 10, 11, 12\}$, and by Lemma 4.17 they have fiber size 3. Thus $|V_3| = 4$. The remaining $13 - 4 = 9$ words with $w_6 = 0$ have $v \le 8$ and therefore fiber size 4, so $|V_4| = 9$. This yields $(|V_2|, |V_3|, |V_4|) = (8, 4, 9)$.

Boundary-sector preimages. Using Definition 4.14, compute the boundary values:

$$V(100001) = 1 + 13 = 14, \quad V(100101) = 1 + 5 + 13 = 19, \quad V(101001) = 1 + 3 + 13 = 17.$$

All three have $w_6 = 1$, so Lemma 4.17 gives $\mathrm{Fold}_6^{-1}(w) = \{V(w), V(w) + 34\}$, yielding the displayed pairs. □

Degeneracy histogram (supplement). The rigid $(2, 3, 4)$ degeneracy histogram is recorded in Appendix O.

Summary at minimal resolution. At $(m, n) = (6, 3)$, the three-channel stability mechanism yields an explicit, auditable chain:

$$\Omega_6 \text{ (64 microstates)} \xrightarrow[\varphi\text{-projection}]{\text{forbidden grammar}} X_6 \text{ (21 stable types)} \xrightarrow[\pi\text{-split}]{\text{cyclic closure}} X_6^{\mathrm{cyc}} \oplus X_6^{\mathrm{bdry}} \ (18 \oplus 3).$$

This $64 \to 21$ and $18 \oplus 3$ structure is not a metaphor but a finite combinatorial theorem with explicit tables. The remainder of the paper treats this rigid finite skeleton as the stable-sector substrate for Standard Model interface hypotheses.

4.7 Uplift: Fold_m and persistence across m

The $m = 6$ map Fold_6 is the first nontrivial instance of a general truncation map at arbitrary window length. For $m \geq 1$ and $N \in \{0, \ldots, 2^m - 1\}$, let $(c_k)_{k \geq 1}$ be the Zeckendorf digits of N (no adjacent ones) and define

$$\mathrm{Fold}_m(N) := (c_1, \ldots, c_m) \in X_m, \tag{14}$$

padding by zeros if the digit vector length is $< m$.

Lemma 4.19 (Dyadic bound for Fibonacci growth)**.** *For all $m \geq 1$, one has $F_{m+2} \leq 2^m$.*

Proof. At $m = 1$, $F_3 = 2 = 2^1$. Assume $F_{m+2} \leq 2^m$ and $F_{m+1} \leq 2^{m-1}$ for some $m \geq 2$ (the second inequality holds by the induction hypothesis at $m - 1$). Then

$$F_{m+3} = F_{m+2} + F_{m+1} \leq 2^m + 2^{m-1} < 2^{m+1}.$$

Thus $F_{m+3} \leq 2^{m+1}$, completing the induction. □

Proposition 4.20 (Surjectivity of Fold_m onto X_m)**.** *For every $m \geq 1$, the map $\mathrm{Fold}_m : \{0, \ldots, 2^m - 1\} \twoheadrightarrow X_m$ is surjective.*

Proof. Let $w \in X_m$ and define its Zeckendorf value

$$V_m(w) := \sum_{k=1}^{m} w_k F_{k+1}.$$

It is standard that the admissible digit set X_m has size F_{m+2} and represents exactly the integers $\{0, \ldots, F_{m+2} - 1\}$ under V_m (Lemma 4.5; see also [25, 26, 33–35]). In particular, $V_m(w) \leq F_{m+2} - 1$. By Lemma 4.19, $F_{m+2} \leq 2^m$ for all $m \geq 1$, hence $V_m(w) \in \{0, \ldots, 2^m - 1\}$. Moreover, the Zeckendorf expansion of $V_m(w)$ uses no Fibonacci weights beyond F_{m+1}, hence its digits beyond c_m are zero and its first m digits equal w. Therefore $\mathrm{Fold}_m(V_m(w)) = w$. □

A canonicality criterion for the digit window. Beyond surjectivity, one may ask whether the choice of the *digit window* $(c_1, \ldots, c_m)$ in (14) is forced within natural nearby variants. The following simple fixed-point condition rules out "shifted" Zeckendorf digit windows.

Definition 4.21 (Shifted Zeckendorf-window maps)**.** *For $m \geq 1$ and an integer shift $s \geq 0$, define the shifted map*

$$\mathrm{Fold}_m^{(s)}(N) := (c_{1+s}, c_{2+s}, \ldots, c_{m+s}) \in X_m,$$

where $(c_k)_{k \geq 1}$ are the Zeckendorf digits of N (padding by zeros for indices beyond the expansion length). Thus $\mathrm{Fold}_m^{(0)} = \mathrm{Fold}_m$ and $s = 1$ is the "FoldZ-shift" counterfactual at $m = 6$ (Appendix Q).

Definition 4.22 (Value consistency at window length m)**.** *A deterministic map* $F : \{0, \dots, 2^m - 1\} \to X_m$ *is* value-consistent *if*

$$F(V_m(w)) = w \qquad \text{for all } w \in X_m,$$

where $V_m(w) = \sum_{k=1}^{m} w_k F_{k+1}$ *is the Zeckendorf value used above.*

Proposition 4.23 (Value consistency forbids Zeckendorf window shifts)**.** *Fix* $m \geq 1$*. Within the shifted Zeckendorf-window family* $\{\mathrm{Fold}_m^{(s)} : s \geq 0\}$*, the only value-consistent map (Definition 4.22) is the unshifted map* $\mathrm{Fold}_m^{(0)} = \mathrm{Fold}_m$*.*

Proof. Let $w = 10 \cdots 0 \in X_m$ (a single 1 followed by zeros). Then $V_m(w) = F_2 = 1$. The Zeckendorf digits of 1 satisfy $c_1 = 1$ and $c_k = 0$ for all $k \geq 2$. Therefore, for any shift $s \geq 1$,

$$\mathrm{Fold}_m^{(s)}(V_m(w)) = (c_{1+s}, \dots, c_{m+s}) = (0, \dots, 0) \neq w,$$

so $\mathrm{Fold}_m^{(s)}$ is not value-consistent. On the other hand, $\mathrm{Fold}_m^{(0)}(V_m(w)) = \mathrm{Fold}_m(1) = w$ by the definition of Fold_m and Zeckendorf uniqueness. □

Degeneracy as truncated Zeckendorf tails. For a fixed $w \in X_m$, the preimage size $g_m(w) := |\mathrm{Fold}_m^{-1}(w)|$ counts how many Zeckendorf expansions of numbers $N \in \{0, \dots, 2^m - 1\}$ share the same first m digits. Equivalently, writing

$$N = V_m(w) + \sum_{k \geq m+1} c_k F_{k+1},$$

the fiber size is the number of admissible tail digit strings $(c_{m+1}, c_{m+2}, \dots)$ (with $c_m = w_m$ enforcing $c_m c_{m+1} = 0$) whose tail value keeps N in the finite domain. Thus finite preimage degeneracy is a direct consequence of Zeckendorf truncation at finite window length and the cutoff $N < 2^m$; it is not an artifact of the $m = 6$ case.

Uplift evidence. Appendix AE records an m-sweep (generated by `scripts/exp_foldm_stats.py`) that verifies $\mathrm{Im}(\mathrm{Fold}_m) = X_m$ and reports the full degeneracy histograms for $m = 6, \dots, 16$ (Table 68). In particular, the support $\{2, 3, 4\}$ at $m = 6$ uplifts to larger, still highly structured degeneracy values at $m = 8$ and $m = 10$ (Table 68), consistent with the tail-count interpretation above.

Vacuum / ghost-sector diagnostics (supplement). [Interface]The protocol-unstable complement $\Omega_m \setminus X_m$ (the ghost sector) and its diagnostic sweeps are recorded in Appendix P.

Part IV
Structure: Locality, Gauge, Chirality, and Antimatter

Planar holographic screen as a chart (stereographic projection; interface)

[Interface]When we speak of a "screen" in this paper, the concrete object is a finite display graph induced by an addressing basis (Section 5). The 2D Hilbert grid is used for fully explicit finite diagnostics at the anchor, and it may also be viewed as a discrete sampling of a planar chart.

[Interface]A standard continuous display chart that connects bearing/boundary language to planar coordinates is the stereographic projection of the unit sphere $S^2 \subset \mathbb{R}^3$ to the complex plane. For a direction $\omega = (\omega_1, \omega_2, \omega_3) \in S^2$ (away from the projection pole), define

$$z(\omega) := \frac{\omega_1 + \mathrm{i}\omega_2}{1 - \omega_3} \in \mathbb{C}.$$

Conversely, for $z \in \mathbb{C}$ define the inverse map

$$\omega(z) := \left(\frac{2\,\mathrm{Re}\, z}{1 + |z|^2}, \frac{2\,\mathrm{Im}\, z}{1 + |z|^2}, \frac{|z|^2 - 1}{1 + |z|^2} \right) \in S^2.$$

In this chart, planar distance and density are display-dependent quantities; the protocol distance used for operational statements in this paper remains the graph metric on the chosen display graph (Definition 3.3).

[Audit]This stereographic chart is a display convention (interface dictionary) and is not used as a premise for theorem-level folding statements or for CAP minimality audits; it provides a compact coordinate language for "planar screen" discussions when a continuum chart is convenient.

5 Hilbert addressing and dihedral layout families

5.1 Hilbert addressing as a locality-preserving embedding

Under the linear-ontology interface of this paper (Axiom 1.1), the primitive object is a one-dimensional scan order (tick stream). To represent locality at finite resolution, we introduce *space* as a derived display structure: an addressing basis folds a finite tick prefix into a neighborhood graph (Section 3). Hilbert addressing provides a classical locality-preserving bijection

$$H_n : \{0, 1, \ldots, 4^n - 1\} \to \{0, 1, \ldots, 2^n - 1\}^2$$

with bounded jump statistics relative to the Euclidean metric; see [36–38]. At $n = 3$, the grid has $4^3 = 64$ sites, matching the 64 microstates of Ω_6 for the chosen 2D balanced coupling $(m, n) = (6, 3)$.

5.1.1 Space from ticks: display graph, distance, and velocity (dictionary)

Fix an order n and view tick indices as embedded on the grid by H_n. We treat the resulting nearest-neighbor grid graph as the *display graph* and use its graph metric as the protocol notion of distance (Definition 3.3). Accordingly, a tick-indexed trajectory $x(t)$ on the display graph has a protocol velocity in sites per tick given by

$$v(t_1, t_2) = \frac{d_n(x(t_1), x(t_2))}{|t_2 - t_1|},$$

as in Definition 3.4. Any conversion of this dimensionless rate to physical units, and therefore any identification with the measured constant c, is a matching-layer calibration (Remark 2.1).

Remark 5.1 (Why the 2D Hilbert grid is used in this paper)**.** *Higher-dimensional locality-preserving space-filling curves (including 3D Hilbert variants) exist. Other 2D space-filling curves can likewise be used as alternative addressing bases; we do not claim they fail. At the minimal anchor used in this paper, the choice of addressing basis is made explicit and auditable by a bounded counterfactual comparison, in which Hilbert addressing is selected as CAP-minimal within the stated finite family (Table 5). Independently of this audit, Hilbert addressing provides*

addressing	jump q90	jump q99	edge q90	edge q99	failures/total	failure frac	status
`hilbert`	1.000	1.000	12.000	17.000	0/5	0.000	**selected**
`row-major`	8.000	8.000	10.000	12.000	0/3	0.000	

Table 5: Addressing-basis audit at the minimal anchor $(m, n) = (6, 3)$: Hilbert vs. a row-major counterfactual on the 8×8 screen. "jump" is the Manhattan step length along the scan path (tick order) on the screen; "edge" is the 0.90/0.99 quantile of the minimum fiber-matching cost across nearest-neighbor edges (Hamming cost on 6-bit microstates); "failures" counts Gram–Schmidt failures when projecting phase-lifted holonomies (denom = 64) on nontrivial (3/4-cycle) plaquettes. Rows are reproduced by the deterministic script `scripts/exp_addressing_selection.py`.

a concrete locality-preserving representative with a fully explicit symmetry structure [37]. In particular, one may use a 3D Hilbert-type addressing map

$$H_n^{(3)} : \{0, 1, \ldots, 2^{3n} - 1\} \to \{0, 1, \ldots, 2^n - 1\}^3,$$

so that the order-n hypercubic grid has $(2^n)^3 = 2^{3n}$ sites. At window length $m = 6$, the balanced cardinality match for 3D addressing is $m = 3n$, hence $n = 2$ and $2^6 = 2^{3\cdot 2} = 64$; equivalently, a $4 \times 4 \times 4$ grid carries the same 64 sites as Ω_6. We use the classical 2D Hilbert grid for three complementary reasons. First, it is the minimal screen dimension that admits closed loops (plaquettes) and therefore supports the holonomy diagnostics used later (Section 6); in one dimension there are no cycles. Second, it yields an explicit dihedral layout family with a transparent orientation-preserving vs. orientation-reversing split (Section 5.2), making the parity/chirality protocol audits fully explicit at the 64-site anchor [37]. Third, the 2D grid can be read as a minimal finite "screen" on which the linear scan is rendered, consistent with a boundary-first (holographic) viewpoint in which observable data live on a readout boundary while bulk locality is an interface dictionary [39–41]. Nothing in the folding statements depends on the addressing dimension; changing the addressing basis changes only which spatially organized diagnostics (e.g. chirality/holonomy histograms) are attached to the same theorem-level stable types.

A bounded counterfactual and a CAP-minimality audit. *To make the addressing choice auditable in the tick-first language, we compare Hilbert addressing to a bounded counterfactual of equal description complexity: a row-major scan order on the same 8×8 screen. We score each candidate by protocol-internal locality metrics (no external targets): (i) high-quantile scan-path jump length (Manhattan distance) per tick, and (ii) neighbor-fiber matching overhead and a phase-lift computability diagnostic on nontrivial plaquettes. Table 5 reports the resulting comparison and records the CAP-style deterministic selection within this explicit finite candidate family.*

Remark 5.2 (Addressing geometry versus ontic dimension)**.** *The square grid and its Euclidean metric are used here as part of a protocol-level readout basis that makes locality auditable at finite resolution. They do not serve as premises about an underlying ontic manifold; the theorem-level folding statements depend only on word combinatorics, while addressing enters only through controlled families of readout bases (Section 5.2).*

5.2 The D_4 layout family and non-canonicity

Hilbert recursion is not unique: there are 8 global layout variants related by the dihedral group D_4 acting on the square by rotations and reflections. These correspond to different address fami-

lies (different orientation and reflection choices at recursion seed), and can be treated as different readout bases. Rotation elements preserve orientation; reflection elements reverse orientation.

Lemma 5.3 (D_4 layouts and orientation classes (standard))**.** *The symmetry group of the square is the dihedral group D_4 with $|D_4| = 8$ elements. Composing a fixed order-n Hilbert addressing map H_n with any $g \in D_4$ yields another valid global layout with the same locality-preserving recursion statistics. Moreover, D_4 splits into 4 orientation-preserving rotations and 4 orientation-reversing reflections.*

Proof. The symmetry group of the square is classical and has 8 elements. Since each $g \in D_4$ is an isometry of the grid, the composition $g \circ H_n$ is again a bijection $\{0, \ldots, 4^n - 1\} \to \{0, \ldots, 2^n - 1\}^2$. The rotation subgroup has order 4 and preserves orientation; the remaining coset consists of reflections and reverses orientation [37]. □

This non-canonicity is the geometric entrance for chirality in the readout protocol: fixing an orientation class at initialization selects a handedness for the address recursion. In the physical identification layer, we elevate this to a *protocol choice* whose mirror is not a symmetry within the same protocol (Section 7).

Non-canonicity as protocol, not gauge. Changing Hilbert layout changes the address mapping and therefore changes certain finite statistics of neighborhood patterns. At the same time, the folding core of Section 4 is protocol-stable: the $64 \to 21$ and $18 \oplus 3$ statements are invariant as combinatorics of words, independent of the spatial embedding. The role of D_4 is therefore not to modify the folding theorem, but to provide a controlled family of readout bases in which chirality can be defined and tested.

5.3 A discrete Hilbert chirality index

Let $p_0, p_1, \ldots, p_{4^n-1} \in \mathbb{Z}^2$ be the Hilbert path points, with $p_k = H_n(k)$. Define the discrete chirality index

$$\chi := \sum_{k=1}^{4^n-2} \operatorname{sgn}((p_k - p_{k-1}) \times (p_{k+1} - p_k)), \tag{15}$$

where the 2D cross product is the scalar $(a_x, a_y) \times (b_x, b_y) := a_x b_y - a_y b_x$ and $\operatorname{sgn}(t) \in \{-1, 0, +1\}$. Intuitively, χ is the net excess of left turns over right turns along the discrete path. We take $\operatorname{sgn}(0) = 0$, so collinear triples contribute 0; thus χ counts signed turns and ignores straight steps.

Proposition 5.4 (Parity and traversal reversal flip χ)**.** *Let P be any reflection of the grid and let T be traversal reversal (path reversal). Then*

$$\chi(P \cdot p) = -\chi(p), \qquad \chi(T \cdot p) = -\chi(p),$$

while orientation-preserving rigid motions (rotations and translations) preserve χ.

Proof. Reflections reverse orientation, hence reverse the sign of the scalar cross product at every non-collinear local turn. Traversal reversal swaps the order of each local triple (p_{k-1}, p_k, p_{k+1}), which also flips the cross-product sign. Rotations preserve orientation and therefore preserve cross-product signs. Translations cancel in the differences $p_k - p_{k-1}$ and $p_{k+1} - p_k$, hence leave every cross product unchanged. □

Appendix AE records a reproducible $n = 3$ check (generated by `scripts/exp_hilbert_chirality_index.py`): the canonical Hilbert path has $\chi = -2$, while both reflection and traversal reversal yield $\chi = +2$.

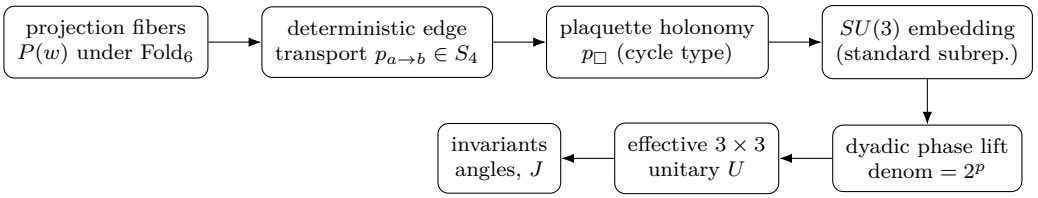

Figure 3: Holonomy diagnostic pipeline (finite, auditable): deterministic edge matching induces an S_4 connection on the Hilbert grid; plaquette holonomies are embedded into an $SU(3)$ skeleton and optionally phase-lifted to yield effective unitary matrices and rephasing-invariant summaries.

6 Protocol connections and finite holonomy diagnostics on a tick-addressed grid

This section records a minimal, auditable connection model that makes the slogan "gauge fields as compensating connections" concrete at finite resolution. The construction is discrete, finite, and fully computable at the chosen anchor scale $(m, n) = (6, 3)$. It is used here as a protocol-level diagnostic: every choice is explicit, every search domain is finite, and the reported fit objectives reuse the same log-mismatch norms as in Definition H.1. No continuum limit is assumed in the computations below; any continuum interpretation is an interface dictionary (see Proposition 8.2). As an audit-oriented look-elsewhere check, Appendix AE includes counterfactual baselines for selected holonomy fits (e.g. Hilbert vs. row-major addressing) in Table 74. In the tick-first spine, the addressing basis is part of the display dictionary (Section 3); its minimality at the anchor is made explicit by the addressing audit in Table 5.

Non-circular diagnostic contract. The holonomy outputs in this section are *diagnostics* and are not used as premises for the CKM/PMNS closures in Sections AF.4 and 12. Whenever PDG/global-fit targets appear, they enter only as external comparison values to score a finite family of protocol outputs under the shared audit norm (Definition H.1).

Fit objective and deterministic tie-breaks (audit rule). Whenever we report a "best fit" of a finite holonomy construction to a target triple of mixing sines (s_{12}, s_{23}, s_{13}) in PDG conventions, we use the same audit norm as elsewhere in the paper: for each component s_i with reference $s_i^{\mathrm{ref}} > 0$ we set $e_i := |\log(s_i/s_i^{\mathrm{ref}})|$, then summarize by

$$E_\infty := \max_i e_i, \qquad E_1 := \sum_i e_i.$$

Candidates are selected by lexicographic minimization of (E_∞, E_1), followed by an explicitly stated deterministic complexity tie-break (e.g. phase-denominator exponent p, discrete phase map family, loop indices, and global $S_3 \times S_3$ relabelings), so that reported best fits are unique within the declared finite search domains.

Remark 6.1 (Diagnostic status and non-circular use of mixing targets)**.** *The holonomy constructions in this section are* diagnostics*: they do not supply premises for the CKM/PMNS closures in Sections AF.4 and 12. Whenever PDG/global-fit targets appear here, they enter only as external comparison values used to score a finite family of protocol outputs under the audit norm. In particular, we do not tune the connection rule, the phase-map family, or the phase denominator by importing Standard Model targets into the folding core; we instead report bounded sweeps over these explicit finite protocol parameters and record uniqueness/gap information within each declared search domain.*

6.1 Fibers under projection: stable types with finite degeneracy

At $m = 6$, the folding map $\mathrm{Fold}_6 : \{0, \ldots, 63\} \to X_6$ is surjective and each stable type $w \in X_6$ has a finite preimage

$$P(w) := \mathrm{Fold}_6^{-1}(w) \subset \{0, \ldots, 63\}, \qquad |P(w)| \in \{2, 3, 4\}.$$

From the protocol viewpoint, $P(w)$ is a finite *fiber* of microstates that project to the same stable readout label. Comparing stable labels across space requires a convention for how these fibers are identified, which is the discrete origin of a compensating connection.

6.2 A deterministic discrete connection on grid edges

Fix Hilbert order $n = 3$ and embed indices $k \in \{0, \ldots, 63\}$ into an 8×8 grid via Hilbert addressing (Section 5). Label each site by its stable type $w = \mathrm{Fold}_6(k)$. For each undirected nearest-neighbor grid edge $\{a, b\}$, we define a deterministic transport map between the two endpoint fibers by the following rule:

- For each stable type w, list its fiber $P(w)$ in increasing order and pad it deterministically to length 4 (the maximal degeneracy at $m = 6$) by repeating its last element.
- Define a cost between microstates by Hamming distance on their 6-bit binary words.
- Choose the minimum-cost bijection between the two length-4 padded fibers; if multiple bijections attain the same minimum cost, select the lexicographically smallest permutation. This yields a well-defined permutation in S_4.
- For the reverse orientation, use the inverse permutation.

This produces a discrete, non-abelian edge connection on edges, designed to be auditable and fully reproducible by a finite exhaustive search over 4! matchings per edge.

Remark 6.2 (Why we pad fibers to 4 and use Hamming cost)**.** *At $(m, n) = (6, 3)$ the $Fold_6$ preimage sizes satisfy $|P(w)| \in \{2, 3, 4\}$ (Theorem 4.18), so rank-4 padding is the unique smallest uniform slot count that accommodates every fiber without truncation. Repeating the last element is a deterministic minimal padding that does not introduce any new microstate index beyond the true fiber. For the cost, Hamming distance on $\{0, 1\}^6$ is the canonical bit-flip metric induced by the readout alphabet itself; it measures the minimal number of elementary bit changes between microstates and is independent of any external geometric scale.*

Definition 6.3 (Hamming distance on microstates)**.** *Let $u, v \in \Omega_6 = \{0, 1\}^6$. Define the Hamming distance*

$$d_H(u, v) := \sum_{i=1}^{6} |u_i - v_i|.$$

For indices $k, \ell \in \{0, \ldots, 63\}$, write $\mathrm{bin}(k) \in \{0, 1\}^6$ for the 6-bit binary word of k and set $d_H(k, \ell) := d_H(\mathrm{bin}(k), \mathrm{bin}(\ell))$.

Lemma 6.4 (Well-defined edge transport in S_4)**.** *For any oriented neighbor edge $a \to b$, the above rule produces a unique permutation $p_{a\to b} \in S_4$. Moreover, the reverse-edge rule $p_{b\to a} := p_{a\to b}^{-1}$ makes the transport involutive under orientation reversal.*

Proof. Each endpoint has a padded fiber list of length 4. There are finitely many bijections between two 4-element index sets, namely 4! permutations. The cost of a permutation is a finite sum of Hamming distances (Definition 6.3), hence each cost is well-defined and real-valued. Therefore a minimum-cost permutation exists. If the minimum is attained by more than one permutation, the fixed lexicographic tie-break selects a unique one, giving a unique $p_{a\to b} \in S_4$. Defining the reverse-edge transport as the inverse permutation is then deterministic and satisfies $(p_{a\to b})^{-1} = p_{b\to a}$ by construction. □

degeneracy pair $(\lvert P(w_a)\rvert, \lvert P(w_b)\rvert)$	count	fraction
$(2, 2)$	16	0.143
$(2, 3)$	11	0.098
$(2, 4)$	13	0.116
$(3, 3)$	12	0.107
$(3, 4)$	11	0.098
$(4, 4)$	49	0.438

Table 6: Distribution of preimage-size (fiber degeneracy) pairs across nearest-neighbor edges on the 8×8 grid at $n = 3$. Rows are reproduced by the deterministic script `scripts/exp_edge_mismatch_decomposition.py`.

quantile q	min-match cost quantile
0.00	0.000
0.50	8.000
0.90	12.000
0.99	17.000
1.00	17.000

Table 7: Quantiles of the minimum matching cost (sum of Hamming distances under the chosen optimal bijection) across all nearest-neighbor edges. Rows are reproduced by the deterministic script `scripts/exp_edge_mismatch_decomposition.py`.

Definition 6.5 (Vertex relabelings and cycle-type invariance)**.** *At a vertex x, relabeling the padded fiber positions is modeled by a permutation $g_x \in S_4$ acting on the local index $i \in \{0, 1, 2, 3\}$. Under such a local relabeling field g : vertices $\to S_4$, the edge transport transforms as*

$$p_{a\to b} \;\mapsto\; p'_{a\to b} := g_b \, p_{a\to b} \, g_a^{-1}.$$

Proposition 6.6 (Plaquette cycle type is invariant under local relabelings)**.** *Let $p_\square$ be the plaquette holonomy obtained by composing the four oriented edge permutations around a unit square. Under the local relabeling action of Definition 6.5, the holonomy transforms by conjugation, hence its S_4 cycle type is invariant.*

Proof. This is the standard lattice-gauge transformation law: edge transports change by left/right multiplication at endpoints, so the ordered product around a closed loop changes by conjugation by the vertex relabeling at the basepoint [42, 43]. Conjugation preserves cycle type in S_4, so the cycle-type summary in Table 8 is gauge invariant under local fiber relabelings. □

6.3 Elementary plaquette holonomy

Given an S_4-valued edge transport rule, we define the holonomy of a unit-square plaquette by composing the four oriented edge permutations around its boundary. Because the connection takes values in a non-abelian group, holonomy can be nontrivial even in a fully finite setting. This is the standard lattice-gauge notion of plaquette holonomy as a minimal loop observable [42, 43]. We summarize holonomy values by S_4 cycle type.

Remark 6.7 (Why we emphasize 3/4-cycle holonomies)**.** *In the standard S_4 action on four fiber slots,* 3- *and* 4*-cycles are the simplest nontrivial cycle types that move at least three slots.*

cycle type	count	fraction
`1`	24	0.490
`2`	19	0.388
`2x2`	1	0.020
`3`	3	0.061
`4`	2	0.041
`other`	0	0.000

Table 8: Holonomy distribution on the 7×7 family of unit-square plaquettes in the 8×8 grid at $n = 3$, under the deterministic S_4 edge transport rule. Rows are reproduced by the deterministic script `scripts/exp_holonomy_loops.py`.

Under the 3-dimensional sum-zero (standard) representation used below, these cycle types induce genuine rotations in $SO(3)$ with nonzero angles, providing the minimal finite skeleton for later 3×3 mixing-matrix diagnostics [44].

6.4 A minimal $SO(3) \subset SU(3)$ representation bridge

To connect the discrete S_4 holonomy values to a continuous group action (as a skeleton for later mixing-matrix work), we use the standard permutation representation and its 3-dimensional "standard" subrepresentation [44]. Concretely, let $\rho : S_4 \to O(4)$ act by permutation matrices on $\mathbb{R}^4$, and let

$$H := \Big\{ x \in \mathbb{R}^4 : \sum_{i=1}^{4} x_i = 0 \Big\},$$

the sum-zero subspace. Then H is ρ-invariant and $\dim H = 3$.

Remark 6.8 (Why the sum-zero subspace is canonical)**.** *The permutation representation of S_4 on $\mathbb{R}^4$ contains a trivial one-dimensional invariant subspace spanned by $(1, 1, 1, 1)$. Restricting to H removes this trivial mode and yields the standard 3-dimensional representation that captures the nontrivial mixing of slots; see, e.g., [44].*

Lemma 6.9 (Sign-twisted standard representation $S_4 \to SO(3)$)**.** *Let $\rho_H : S_4 \to O(H) \cong O(3)$ be the restriction of the permutation representation to H. Then $\det(\rho_H(\sigma)) = \operatorname{sgn}(\sigma)$. Consequently the twisted representation*

$$\widetilde{\rho}(\sigma) := \operatorname{sgn}(\sigma)\, \rho_H(\sigma)$$

lands in $SO(3)$. Viewing $SO(3)$ matrices as real unitary matrices gives an inclusion $SO(3) \subset SU(3)$.

Proof. Permutation matrices satisfy $\det(\rho(\sigma)) = \operatorname{sgn}(\sigma)$. Moreover $\mathbb{R}^4$ decomposes as an orthogonal direct sum

$$\mathbb{R}^4 = \operatorname{span}\{(1, 1, 1, 1)\} \ \oplus \ H,$$

and $\rho(\sigma)$ fixes $(1, 1, 1, 1)$. Thus $\det(\rho(\sigma)) = \det(\rho(\sigma)|_{\operatorname{span}\{(1,1,1,1)\}}) \cdot \det(\rho_H(\sigma)) = 1 \cdot \det(\rho_H(\sigma))$, proving $\det(\rho_H(\sigma)) = \operatorname{sgn}(\sigma)$. Finally, on the 3-dimensional space H, multiplication by the scalar $\operatorname{sgn}(\sigma) \in \{\pm 1\}$ contributes determinant $\operatorname{sgn}(\sigma)^3 = \operatorname{sgn}(\sigma)$, hence

$$\det(\widetilde{\rho}(\sigma)) = \det(\operatorname{sgn}(\sigma)\, I_3)\ \det(\rho_H(\sigma)) = \operatorname{sgn}(\sigma) \cdot \operatorname{sgn}(\sigma) = 1,$$

so $\widetilde{\rho}(\sigma) \in SO(3)$. The inclusion $SO(3) \subset SU(3)$ follows because a real orthogonal 3×3 matrix is unitary over $\mathbb{C}$, and determinant 1 is preserved. □

Table 9 summarizes the induced rotation angles (in degrees) by S_4 cycle type for the plaquette holonomies at $n = 3$.

cycle type	count	mean angle [deg]	min [deg]	max [deg]
1	24	0.000	0.000	0.000
2	19	180.000	180.000	180.000
2x2	1	180.000	180.000	180.000
3	3	120.000	120.000	120.000
4	2	90.000	90.000	90.000
other	0	–	–	–

Table 9: Rotation-angle summary for the sign-twisted standard $SO(3) \subset SU(3)$ representation of plaquette holonomies at $n = 3$. Rows are reproduced by the deterministic script `scripts/exp_holonomy_su3_representation.py`.

6.5 A phase-register lift and a CP-odd invariant

To allow CP-odd signatures in a holonomy-based description, one must go beyond purely real orthogonal representations. As a minimal protocol-level bridge consistent with the $\mathbb{Z}_{128}$ phase-register stance, we can attach a deterministic discrete phase to each microstate and lift the edge transport to a unitary (phase-weighted) transport. We make this lift fully explicit. Fix a dyadic denominator $\mathrm{denom} = 2^p$ and a low-complexity index map $\tau : \{0, \dots, 63\} \to \{0, \dots, 63\}$ chosen from the family

$$\tau_{\mathrm{id}}(k) = k, \qquad \tau_{\mathrm{gray}}(k) = k \oplus (k \gg 1), \qquad \tau_{\mathrm{bitrev}}(k) = \mathrm{bitreverse}_6(k), \qquad \tau_{\mathrm{not}}(k) = 63 - k.$$

Here $\oplus$ and $\gg$ denote bitwise XOR and right shift on 6-bit integers, and $\mathrm{bitreverse}_6$ reverses the 6-bit binary expansion.

Remark 6.10 (Why the phase-map family is bounded)**.** *The map τ is a pure indexing convention for attaching phases to the finite microstate set $\{0, \dots, 63\}$. To bound look-elsewhere freedom, we restrict to a small explicit family of invertible, bit-level transforms of minimal description complexity (identity, Gray map, bit reversal, and complement). Within this bounded family, the protocol adopts a canonical representative by CAP tie-break (Axiom 1.5): the baseline choice is $\tau = \tau_{\mathrm{id}}$ unless an explicitly stated bounded-complexity closure selects otherwise. This keeps the phase attachment auditable and makes any refinement of the map family an explicit change of the finite candidate set rather than an implicit tuning knob.*

Remark 6.11 (Dyadic phase registers and $\mathbb{Z}_{128}$)**.** *The choice* $\mathrm{denom} = 2^p$ *matches the finite-ring phase-register stance in which phases are represented in $\mathbb{Z}_{2^p}$ rather than as continuous angles. In particular, $p = 7$ corresponds to a $\mathbb{Z}_{128}$ register. At the minimal window $m = 6$, the default choice* $\mathrm{denom} = 2^m = 64$ *used in several tables is equivalently a $\mathbb{Z}_{128}$ register restricted to even residues, since $2\pi\,\tau(k)/64 = 2\pi\,(2\tau(k))/128$. Smaller p coarsen the phase resolution, while larger p refine it; the dyadic family provides a nested, auditable refinement chain. In CAP audit language, denominators of the form* $\mathrm{denom} = 2^p$ *are treated as an explicit bounded candidate family: the baseline uses the anchor-coherent choice* $\mathrm{denom} = 2^m$ *and the bounded sweeps record sensitivity and counterfactuals (Appendix AE and Appendix S). This is consistent with standard dyadic phase encodings used in finite-register quantum information models; see, e.g., [24].*

Define the phase register embedding

$$\phi(k) := 2\pi\,\frac{\tau(k)}{\mathrm{denom}}. \tag{16}$$

For an oriented edge $a \to b$ with padded fibers $f_a(i)$ and $f_b(i)$ $(i = 0, 1, 2, 3)$ and transport permutation $p \in S_4$ (Section 6.2), define the phase-lifted edge transport $U_{a\to b} \in U(4)$ by

$$(U_{a\to b})_{p(i),i} := \exp\Big(\mathrm{i}\big(\phi(f_b(p(i))) - \phi(f_a(i))\big)\Big), \qquad i = 0, 1, 2, 3, \tag{17}$$

cycle type	count	mean $\lvert J\rvert$	max $\lvert J\rvert$	mean J
1	24	1.25398e-50	8.55285e-50	+1.00603e-50
2	19	1.05674e-17	6.04883e-17	+3.42678e-18
2x2	1	0	0	+0
3	3	0.0634247	0.0772868	+0.0396244
4	2	0.0225747	0.030227	-0.00765223
other	0	–	–	–

Table 10: Phase-register lifted holonomy and a CP-odd invariant in a finite projection/renormalization model at $n = 3$. The baseline CAP choice here is $\tau = \tau_{\mathrm{id}}$ and denom $= 64$ (equivalently a $\mathbb{Z}_{128}$ register restricted to even residues; Remark 6.11). Rows are reproduced by the deterministic script `scripts/exp_holonomy_phase_lift_cp_invariant.py`.

with all other entries equal to 0.

Lemma 6.12 (Phase-lifted edge transport is unitary)**.** *For each oriented edge $a \to b$, the matrix $U_{a\to b}$ defined in* (17) *is unitary.*

Proof. Each column i has exactly one nonzero entry, located at row $p(i)$, and this entry has modulus 1. Since p is a permutation, distinct columns have disjoint nonzero rows, hence the columns are orthonormal. Therefore $U^*_{a\to b}U_{a\to b} = I_4$, so $U_{a\to b} \in U(4)$. □

Projecting the resulting 4×4 unitary plaquette holonomy to the 3-dimensional sum-zero subspace and renormalizing by a deterministic Gram–Schmidt procedure yields an effective 3×3 unitary matrix.

Remark 6.13 (When projection/renormalization can fail)**.** *The projection to the sum-zero subspace can produce a rank-deficient 3×3 matrix for certain degenerate holonomies or phase choices. In that case Gram–Schmidt cannot produce a full orthonormal basis and the effective unitary is undefined. Our scripts treat such cases as deterministic failures and record the failure counts explicitly in the relevant tables (e.g. Tables 11 and 30).*

From this effective unitary one can compute a rephasing-invariant CP-odd quantity, e.g. the Jarlskog-type invariant

$$J := \Im(U_{11}U_{22}U^*_{12}U^*_{21}).$$

This is the standard rephasing-invariant combination for 3×3 unitary mixing matrices [2, 45]. Table 10 summarizes the induced values by underlying S_4 cycle type for the $n = 3$ plaquettes.

A bounded family sweep over the phase denominator. To make the phase-lift choice auditable, we can sweep a bounded candidate family for the phase denominator denom $= 2^p$ and record the induced mean $|J|$ on the nontrivial plaquettes (3- and 4-cycles). Table 11 reports the resulting values and the log mismatch to the constant-geometry target $J_{\mathrm{geo}} = 1/(11\pi^7)$.

Angle extraction (PDG convention, diagnostic). From a 3×3 unitary matrix U in the PDG standard parameterization [2], one can extract mixing sines by the identities

$$s_{13} = |U_{13}|, \qquad c_{13} = \sqrt{1 - s^2_{13}}, \qquad s_{12} = \frac{|U_{12}|}{c_{13}}, \qquad s_{23} = \frac{|U_{23}|}{c_{13}},$$

and obtain a principal Dirac phase δ from the Jarlskog invariant via

$$\sin\delta = \frac{J}{s_{12}s_{23}s_{13}c_{12}c_{23}c^2_{13}}, \qquad c_{ij} = \sqrt{1 - s^2_{ij}}.$$

denom	p	mean $\|J\|$ (3)	mean $\|J\|$ (4)	mean $\|J\|$ (3/4)	$\log(\text{mean}/J_{\text{geo}})$	$\|\cdot\|$	failures
64	6	0.0634247	0.0225747	0.0470847	+7.355	7.355	0
128	7	0.0253985	0.0480647	0.034465	+7.043	7.043	0
256	8	0.0096841	0.0408178	0.0221376	+6.601	6.601	0
512	9	0.0045296	0.0192532	0.010419	+5.847	5.847	0
1024	10	0.00222787	0.00943926	0.00511243	+5.135	5.135	0
2048	11	0.00110939	0.00469533	0.00254376	+4.437	4.437	0
4096	12	0.000554126	0.0023446	0.00127032	+3.743	3.743	0
8192	13	0.000276992	0.00117192	0.000634963	+3.049	3.049	0
16384	14	0.000138487	0.000585911	0.000317457	+2.356	2.356	0
32768	15	6.92426e-05	0.00029295	0.000158725	+1.663	1.663	0
65536	16	3.46211e-05	0.000146474	7.93623e-05	+0.970	0.970	0
131072	17	1.73106e-05	7.3237e-05	**3.96811e-05**	**+0.276**	**0.276**	0
262144	18	8.65527e-06	3.66185e-05	1.98406e-05	-0.417	0.417	0

Table 11: Phase-denominator sweep for the phase-lifted holonomy CP invariant at $n = 3$, over denom $= 2^p$ for a bounded range of p. Rows are reproduced by the deterministic script `scripts/exp_holonomy_phase_lift_family_sweep.py`.

cycle type	count	mean s_{12}	mean s_{23}	mean s_{13}	mean δ [deg]	mean $\|J\|$
`1`	24	0.0000	0.0000	0.0000	38.77	1.25398e-50
`2`	19	0.4569	0.7719	0.3407	14.01	1.05674e-17
`2x2`	1	1.0000	0.8165	0.8112	nan	0
`3`	3	0.6434	0.8005	0.4966	59.46	0.0634247
`4`	2	0.7439	0.8485	0.4548	47.03	0.0225747
`other`	0	–	–	–	–	–

Table 12: PDG-style angle extraction from phase-lifted effective holonomy matrices at $n = 3$ (finite diagnostic). The default choice here is $\tau = \tau_{\text{id}}$ and denom $= 64$ (the same choice as Table 10). Rows are reproduced by the deterministic script `scripts/exp_holonomy_phase_lift_angles.py`.

In the holonomy diagnostics below, because row/column identifications are not fixed *a priori*, we also allow a global relabeling (a pair of permutations in $S_3 \times S_3$) when comparing to PMNS/CKM targets. Table 12 reports cycle-type aggregated mean values at the default phase denominator used in Table 10.

Extended sweeps and robustness diagnostics (supplement). The balanced-chain sweep across higher balanced pairs, loop-scale/denominator scans, phase-map family sweeps, and the soft-transport variant are recorded in Appendix S.

Protocol EFT embedding (supplement). [Interface]A standard local gauge-invariant EFT embedding consistent with the closed labeling is recorded in Appendix T.

7 Chirality, antimatter, and CPT as protocol geometry

7.1 Protocol-level P, T, C: definitions

Definition 7.1 (Protocol-level discrete symmetries)**.** *Fix a Hilbert order n and a window length m. We define:*

- P_{prot}*: a spatial reflection (an orientation-reversing element of the* D_4 *layout family acting on the Hilbert-addressed grid);*
- T_{prot}*: scan traversal reversal (replacing the scan index order* $k \mapsto 4^n - 1 - k$ *on the Hilbert path);*
- C_{prot}*: phase conjugation on the scan orbit,* $z_n \mapsto \overline{z_n}$*, with window conjugation chosen so that admissible readout is compared within matched protocols.*

These are protocol transformations; they need not coincide with the continuum-field definitions of P, T, C *in standard QFT, but are designed to be auditable at finite resolution. In particular,* T_{prot} *reverses the execution orientation of a finite tick prefix, and is therefore a protocol change relative to a given initialized run in the tick-only language (Section 3.2).*

7.2 Scan–chirality locking

Hilbert addressing admits both orientation-preserving and orientation-reversing layout families (Section 5). The D_4 layout family therefore splits into two orientation classes exchanged by reflection, and this exchange flips the sign of the discrete chirality index χ (Proposition 5.4).

Definition 7.2 (Orientation class bit and canonical representative (CAP tie-break))**.** *The orientation class is a one-bit protocol datum: it specifies whether the initialized addressing layout lies in the orientation-preserving or orientation-reversing class. Since the two classes are cost-degenerate under the tick-only locality diagnostics of Section 5, we fix a canonical representative by the deterministic tie-break rule of CAP (Axiom 1.5): at the* $n = 3$ *anchor, use the standard Hilbert layout for which the forward-traversal chirality index satisfies* $\chi < 0$ *(Appendix AE). The reflected layout defines the mirror protocol and has* $\chi > 0$*. Accordingly, protocol-level parity is implemented as a protocol swap to the mirror layout rather than as a symmetry within a fixed protocol.*

Which D_4 choices are physically distinguishable. The D_4 family consists of 4 rotations and 4 reflections (Lemma 5.3). In an isotropic setting, a global rotation of the spatial grid is a coordinate convention and does not define a distinct physical protocol once the observer's coordinate frame is fixed. The nontrivial discrete choice is therefore the *orientation class* (rotation vs. reflection), which is detected by the sign of the discrete chirality index χ (Proposition 5.4). This is why SCL is formulated as an orientation-class selection rather than as a choice among all eight layouts.

Proposition 7.3 (Orientation class as the minimal discrete protocol datum)**.** *Fix a Hilbert order* n *and an observer coordinate frame. Within the* D_4 *layout family, orientation-preserving layouts are related by rigid motions of the grid and are coordinate conventions, while orientation-reversing layouts flip the sign of the discrete chirality index* χ*. Consequently, modulo orientation-preserving conventions, the only physically distinguishable discrete choice is the orientation class, and it is detected by* $\mathrm{sgn}(\chi)$*.*

Proof. Lemma 5.3 gives the D_4 split into rotations and reflections. Proposition 5.4 shows that rotations preserve χ while reflections flip its sign. □

In this view, parity violation in the weak sector is a protocol statement: the weak compensation connection is defined within a chosen protocol class, while its mirror requires a protocol swap (it changes the readout basis).

Proposition 7.4 (A minimal parity-odd sign datum at finite resolution)**.** *Fix a Hilbert order* n *and any Hilbert layout within a chosen orientation class. Let* χ *be the discrete chirality index of the associated path, defined in* (15)*. Then* P_{prot} *flips the sign of* χ *(Proposition 5.4), while*

any orientation-preserving protocol change leaves χ invariant. Consequently, any protocol-level observable that is a deterministic function of χ is parity-odd in the sense that it changes sign under P_{prot}.

Proof. This is immediate from Proposition 5.4. □

Why this targets the weak sector. Within the three-channel template, the π-channel is the closure/topology channel, and the weak sector is the minimal non-abelian gauge sector $SU(2)$. If the corresponding compensation connection is implemented by protocol-local consistency rules that depend on Hilbert layout orientation, then the mirror layout is not a symmetry but a different protocol. This provides a readout-geometric route to parity asymmetry: the "right-handed" copy is not an internal symmetry operation within the fixed protocol.

Observable consequences of different orientation classes. If different orientation classes occur in different spacetime domains (different initializations), then parity-odd observables tied to χ should flip sign between domains while remaining invariant under orientation-preserving layout changes; see Prediction P2 in Section 14.1.2. Conversely, if a single global protocol class is selected, then all parity-odd statistics should be coherent with a fixed sign of χ at a given scale.

7.3 Time reversal and discrete chirality

The chirality index χ in (15) flips sign under traversal reversal (Proposition 5.4). Since traversal reversal is the discrete operational avatar of time reversal in a scan process, this provides an auditable finite-resolution coupling:

$$T \text{ reversal} \quad \Longleftrightarrow \quad \chi \mapsto -\chi.$$

Appendix AE records the $n = 3$ computation (generated by `scripts/exp_hilbert_chirality_index.py`) that $\chi(\text{path}) = -2$ and $\chi(\text{reversed path}) = +2$.

A discrete proxy for geometric phase. The index χ counts the signed turning of a locality-preserving address curve. In continuous settings, signed turning and orientation couple naturally to geometric phase (Berry phase) and to spinorial sign structures [46, 47]. The finite $n = 3$ computation therefore provides a minimal auditable finite-resolution model for the statement

$$T \text{ reversal} \iff \text{chirality/spin sign flip},$$

at the protocol layer: both traversal reversal (time reversal) and reflection (parity) flip the same discrete sign datum.

7.4 Antimatter as conjugate readout

Consider the scan orbit $z_n = \mathrm{e}^{2\pi\mathrm{i}(x_0+n\alpha)}$. Complex conjugation yields

$$\overline{z_n} = \mathrm{e}^{-2\pi\mathrm{i}(x_0+n\alpha)} = \mathrm{e}^{2\pi\mathrm{i}((-x_0)+(-n)\alpha)}.$$

Thus phase conjugation is equivalent to scan reversal $n \mapsto -n$ up to a phase shift. Formally:

Lemma 7.5 (Conjugation equals reversal up to an initial-phase flip)**.** *Let $z_n = \mathrm{e}^{2\pi\mathrm{i}(x_0+n\alpha)}$ and define $z'_n := \mathrm{e}^{2\pi\mathrm{i}(x'_0+n\alpha)}$ with $x'_0 = -x_0$. Then $\overline{z_n} = z'_{-n}$ for all $n \in \mathbb{Z}$.*

Proof. This is the displayed computation. □

Lemma 7.6 (Matched-window readout conjugation induces scan reversal)**.** *Let $W \subset \mathbb{T}$ be a measurable readout window and write $\overline{W} := \{\overline{z} : z \in W\}$. Let (z_n) and (z'_n) be as in Lemma 7.5. Define readout sequences by*

$$w_n := \mathbf{1}\{z_n \in W\}, \qquad w'_n := \mathbf{1}\{z'_n \in \overline{W}\}.$$

Then $w'_n = w_{-n}$ for all $n \in \mathbb{Z}$.

Proof. By Lemma 7.5, $z'_n = \overline{z_{-n}}$. Therefore $z'_n \in \overline{W}$ if and only if $z_{-n} \in W$, hence $w'_n = \mathbf{1}\{z_{-n} \in W\} = w_{-n}$. □

Consequently, in the rotation model the protocol operation C_{prot} is realized by traversal reversal together with an initial-phase flip, hence it is tied to the same discrete chirality sign datum as T_{prot}:

$$C_{\mathrm{prot}} \implies \chi \mapsto -\chi.$$

A CP-sign anchor from chirality. Complex conjugation flips the sign of any conjugation-odd (hence CP-odd) holonomy residue. Since C_{prot} is realized at the scan layer by conjugation-as-reversal, the protocol already contains a canonical orientation sign datum, $\mathrm{sgn}(\chi)$, that can be used to fix the CP-odd sign convention within a chosen protocol class. We record the resulting interface rule:

Definition 7.7 (Chirality-anchored CP-odd sign convention (interface))**.** *Let J_{CP} be a CP-odd rephasing-invariant holonomy residue (e.g. a Jarlskog invariant) expressed in a fixed PDG convention. Within a fixed protocol class, its sign is anchored by the chirality sign datum:*

$$\mathrm{sgn}(J_{\mathrm{CP}}) = \mathrm{sgn}(\chi).$$

Switching to the mirror protocol (reflection) flips χ and therefore flips the anchored sign.

Remark 7.8 (Convention dependence of CP-odd signs)**.** *The sign of a CP-odd invariant depends on phase conventions and on bookkeeping conventions (e.g. generation ordering and parameterization), even when the magnitude is rephasing invariant. In this paper, whenever a CP-odd sign is used, we keep the PDG parameterization fixed and treat the chirality sign* $\mathrm{sgn}(\chi)$ *as a protocol-internal orientation datum that removes the remaining quadrant ambiguity in a deterministic way (cf. the PMNS phase closure in Section 12.2). Observable consequences are therefore phrased at the protocol level as parity-sensitive statistical contrasts (Prediction P2), rather than as a standalone claim about a convention-free sign.*

At the level of finite readout words, Lemma 7.6 yields a concrete antimatter dual:

Definition 7.9 (Scan-reversal dual of a finite word)**.** *For a finite binary word $w = w_1 \cdots w_m$, define its scan-reversal dual by*

$$\overline{w} := w_m \cdots w_1.$$

Lemma 7.10 (Reversal preserves admissibility and the π-tag)**.** *If $w \in X_m$ (no adjacent ones), then $\overline{w} \in X_m$. Moreover, the π-channel boundary tag is preserved: $D_\pi(\overline{w}) = D_\pi(w)$.*

Proof. The forbidden substring "11" occurs in w if and only if it occurs in the reversed word $\overline{w}$, so Zeckendorf admissibility is preserved. For the boundary tag, $D_\pi(w) = \mathbf{1}\{w_1 = w_m = 1\}$ and reversal swaps endpoints, hence $D_\pi(\overline{w}) = \mathbf{1}\{\overline{w}_1 = \overline{w}_m = 1\} = D_\pi(w)$. □

Massless-limit matching dictionary (consistency check). In the relativistic massless limit, chirality coincides with helicity [1,48]. Under conjugation-as-reversal, a left-handed particle maps to a right-handed antiparticle, matching the standard massless-limit dictionary between chirality and helicity when combined with scan-direction reversal. *Remark:* we record this only as a matching-layer consistency check with standard QFT kinematics, not as a premise of the folding layer.

7.5 CPT at the scan layer vs. symmetry breaking at the protocol layer

The scan layer is unitary and reversible by construction, so combined transformations can remain valid at the microscopic level. However, once a readout protocol is fixed (window choice plus Hilbert orientation class), P and T may no longer be symmetries within the same protocol: they change the readout basis. This provides a protocol-geometric route to understanding why effective theories may violate P (and CP) while preserving CPT. *Remark:* in standard local Lorentz-invariant quantum field theory under the usual assumptions (locality, a Hermitian Hamiltonian, and the spectrum condition), CPT invariance is enforced by the CPT theorem; see, e.g., [48, 49]. Here we use the CPT theorem only as a consistency reference point: $P_{\mathrm{prot}}, T_{\mathrm{prot}}, C_{\mathrm{prot}}$ are explicitly defined finite-resolution protocol operations, and no continuum-field axioms are used as premises in the folding layer.

7.6 Mirror protocols and a "right-handed" universe

If the initialization at $t = 0$ selects the opposite Hilbert orientation class, then the protocol-level chirality sign flips globally. In such a mirror protocol, the weak sector would appear right-handed rather than left-handed. This provides a precise sense in which a "mirror universe" is not a different Lagrangian, but a different readout protocol (Hilbert layout class). If protocol domains existed in the early universe, their boundaries would be protocol defects, yielding the domain-wall prediction in Section 14.1.2.

Part V
Matter: Standard Model interface closures at the anchor

8 A φ–π–e template for the Standard Model interface

This section records the physical identification layer: falsifiable mapping hypotheses that connect the three-channel folding template to Standard Model structures.

8.1 Three channels as three compensation classes

The folding framework isolates three commuting stability channels:

- (φ) **syntactic legality.** A forbidden-word grammar (Zeckendorf admissibility).
- (π) **topological closure.** A cyclic monodromy / wrap-around admissibility condition.
- (e) **analytic stability.** A zeta/Abel holomorphy domain with a pole barrier.

Independently, the Standard Model gauge group is a three-factor product $SU(3) \times SU(2) \times U(1)$ [1]. We first record the protocol-level necessity of compensation under cross-site consistency, and then record a CAP-minimal gauge-factor closure under explicit compactness and factorization constraints that are forced by probability-preserving internal redundancy (Proposition R.3) and by channelwise independence (Lemma R.4).

Proposition 8.1 (Finite-fiber mismatch forces a compensating connection datum (interface))**.** *Fix a window length m and an addressing graph that renders a finite tick prefix as a locality structure (Section 3; e.g. the Hilbert-addressed grid at order $n = 3$). Let each site x carry a stable label $w_x \in X_m$ and let its microstate fiber be*

$$P(w_x) := \mathrm{Fold}_m^{-1}(w_x) \subset \{0, \ldots, 2^m - 1\},$$

so that multiple microscopic indices can project to the same stable readout label. If protocol-consistent comparison/transport of stable labels is required across a neighbor edge $x \sim y$, then the stable labels alone are insufficient: one must specify an additional transport rule that matches the endpoint fibers. After embedding endpoint fibers into a common slot set of size $r := \max_{w \in X_m} |P(w)|$ (by any deterministic padding convention), any such edge transport is represented by a permutation in S_r. Changing the local slot labeling at a vertex acts by conjugation on edge transports, so the transport rule is defined only up to local relabelings (a finite gauge redundancy). In a continuum modeling dictionary, such discrete connection data are represented by gauge connections on a bundle.

Proof. The point is finite and protocol-internal. When $|P(w)| > 1$, the stable label w identifies only an equivalence class of microstates, so comparing two neighboring stable labels requires a choice of how the two equivalence classes are matched. Once a uniform slot count r is fixed, such matchings are elements of the finite symmetry group S_r. Local relabelings at vertices change edge matchings by left/right multiplication and therefore conjugate loop products, which is the standard discrete gauge-transformation law on graphs [42,43]. At the minimal anchor $m = 6$ one has $r = 4$, and Section 6 gives an explicit deterministic construction of an S_4 edge connection and its plaquette holonomy diagnostics. □

Assumption bundle for gauge-factor closure (audit). [Audit]For audit clarity, Proposition 8.2 should be read as a conditional interface closure under an explicit assumption bundle:

- **(G1) Channelwise factorization.** The three commuting defect channels correspond to three independent local redundancy sectors (Lemma R.4).
- **(G2) Compact probability-preserving redundancy.** In a continuum dictionary, internal redundancy is represented by probability-preserving transformations on a finite-dimensional local Hilbert space, hence is compact at the connected level (Proposition R.3).
- **(G3) Candidate family.** The non-abelian redundancy closes to two simple compact factors G_2, G_3 (non-isomorphic) together with the $U(1)$ sector forced by local rephasing (Proposition 8.4).
- **(G4) Complexity label and tie-break.** CAP selects the lexicographically minimal factor pair under a declared discrete complexity label; the main text uses $\dim(\mathfrak{g})$, and Appendix AI audits sensitivity to alternative labels.

Proposition 8.2 (CAP-minimal three-factor gauge closure (interface))**.** *Fix a continuum modeling dictionary in which the compensation redundancy is internal and probability-preserving (hence compact at the connected level; Proposition R.3) and in which the three defect channels define three independent redundancy sectors (Lemma R.4). Equip compact gauge factors with the intrinsic complexity label* $\dim(\mathfrak{g})$ *(Lie-algebra dimension) and select the lexicographically minimal triple, under CAP (Axiom 1.5), among compact gauge groups of the form*

$$U(1) \times G_2 \times G_3,$$

where G_2 and G_3 are compact, non-abelian, simple, and non-isomorphic. Then the unique minimizer is $U(1) \times SU(2) \times SU(3)$ (up to finite group quotients).

Proof. By Proposition 8.4, local rephasing redundancy enforces an abelian $U(1)$ connection sector in any local continuum dictionary. Compact Lie algebras split as a direct sum of an abelian torus algebra and compact simple factors; requiring two additional inequivalent non-abelian simple factors and applying minimality in $\dim(\mathfrak{g})$ selects dimensions 3 and 8, hence $\mathfrak{su}(2)$ and $\mathfrak{su}(3)$ by Lemma 9.4. □

The content of Proposition 8.1 is operational: gauge redundancy arises because compensation is only defined up to local rephasing of the readout basis. The three-factor structure is not assumed as a premise, but closed as a CAP-minimal identification within the stated compactness/factorization constraints (Proposition 8.2).

Proposition 8.3 (Three commuting defect channels force a three-factor compensation structure (interface))**.** *Suppose protocol mismatch certificates decompose into three commuting defect channels and that, at the modeling level, compensation is defined only up to independent local basis changes associated with each channel (the channelwise redundancy stance of Lemma R.4). Then the minimal compensating connection splits into three independent connection components, so the effective local redundancy factorizes into a product of three gauge redundancies.*

Proof. Since the defect channels commute, a mismatch certificate can be represented as a triple of channelwise components and compared channel-by-channel. By the channelwise redundancy stance, each channel admits its own local basis redundancy, so at each site x the modeling dictionary permits independent local changes $(g_\varphi(x), g_\pi(x), g_{\mathrm{e}}(x))$. Consequently, any channelwise covariant transport rule along an edge $x \sim y$ is a triple of group elements

$$(A_\varphi, A_\pi, A_{\mathrm{e}})_{x\to y} \in G_\varphi \times G_\pi \times G_{\mathrm{e}},$$

transforming under local basis changes as

$$(A_\varphi, A_\pi, A_{\mathrm{e}})_{x\to y} \;\mapsto\; (g_\varphi(y)A_\varphi g_\varphi(x)^{-1},\; g_\pi(y)A_\pi g_\pi(x)^{-1},\; g_{\mathrm{e}}(y)A_{\mathrm{e}} g_{\mathrm{e}}(x)^{-1}).$$

Thus the minimal redundancy group is the direct product of the three independent channel redundancies. □

Uniqueness at the Lie-algebra level. Under probability-preserving internal redundancy (hence compactness at the connected level; Proposition R.3) and using Lie-algebra dimension as an intrinsic complexity label, the dimensions $(1, 3, 8)$ already pin the factor Lie algebras uniquely to $\mathfrak{u}(1) \oplus \mathfrak{su}(2) \oplus \mathfrak{su}(3)$ (up to finite group quotients), by the Cartan–Killing classification (Lemma 9.4). In this sense, once the three-channel template is fixed and one commits to dimension-as-complexity, the choice of $U(1)$, $SU(2)$, and $SU(3)$ is rigid rather than a naming convention. Appendix AI records a bounded sensitivity sweep showing that the same minimizer persists under several alternative discrete complexity labels in the tested window. Moreover, Proposition AI.1 gives a short theorem-level reason for this robustness for the most natural low-complexity labels (dimension, rank, dimension+rank, and $d_{\min}$).

Compensation as a locality cost. In the finite protocol language, a gauge field is not an extra substance but the bookkeeping of enforcing phase consistency across neighboring addresses. When the local stable sector is defined by defect suppression, neighboring sites generically disagree on which microstates project to which stable types. A compensating connection is the minimal additional datum required to compare (and transport) stable types between sites without ambiguity. In this paper, we formulate this as an implementation budget: compensation has a cost, and the effective dynamics favors minimal discrepancy subject to protocol constraints (Axiom 1.5).

Rigidity and defects. In topologically trivial regions a compensating connection can be gauged away (pure gauge), while persistent mismatch requires nontrivial holonomy supported by defects. This aligns the "matter as defect" view with the "gauge as compensation" view: matter is a stable obstruction that prevents global trivialization of the connection.

Proposition 8.4 (From local rephasing to a connection field (standard))**.** *Let $\psi(x)$ be a complex matter field and impose local $U(1)$ redundancy $\psi(x) \mapsto \mathrm{e}^{\mathrm{i}\lambda(x)}\psi(x)$. Then invariance of a local kinetic term under this redundancy requires introducing a compensating connection A_μ and replacing ∂_μ by the covariant derivative $D_\mu = \partial_\mu - \mathrm{i}A_\mu$. Assuming locality and Lorentz covariance and restricting to bulk terms quadratic in A_μ and its first derivatives, the unique gauge-invariant quadratic kinetic term is proportional to $F_{\mu\nu}F^{\mu\nu}$, where $F_{\mu\nu} = \partial_\mu A_\nu - \partial_\nu A_\mu$.*

Proof. This is standard; see, e.g., [1, 48, 50]. □

Proposition 8.5 (From local $SU(N)$ redundancy to a Yang–Mills connection (standard))**.** *Let $\psi(x)$ transform in a representation of $SU(N)$ and impose local redundancy $\psi(x) \mapsto U(x)\psi(x)$ with $U(x) \in SU(N)$. Then invariance of a local kinetic term under this redundancy requires introducing an $SU(N)$ connection $A_\mu(x)$ and replacing ∂_μ by the covariant derivative $D_\mu = \partial_\mu - \mathrm{i}g\,A_\mu$. The corresponding curvature (field strength) is*

$$F_{\mu\nu} := \frac{\mathrm{i}}{g}[D_\mu, D_\nu] = \partial_\mu A_\nu - \partial_\nu A_\mu - \mathrm{i}g\,[A_\mu, A_\nu],$$

and, restricting to local bulk terms quadratic in $F_{\mu\nu}$, the gauge-invariant kinetic term is proportional to $\mathrm{Tr}(F_{\mu\nu}F^{\mu\nu})$.

Proof. Standard; see, e.g., [1, 48, 51]. □

Remark 8.6 (Relation to the CAP gauge-field viewpoint)**.** *The standard continuum statements above are included only as a matching dictionary: they translate local basis redundancy into the familiar connection-field language. In the HPA–Ω program, the same structural conclusion—that a compensating connection is forced once local phase consistency is demanded—is developed directly from finite readout and CAP-minimal discrepancy logic; see the companion CAP manuscript [4] for an extended presentation.*

8.2 Stable types as minimal defect-carrying modes

In the protocol viewpoint adopted here, matter is modeled as persistent topological defects whose stability is constrained by an implementation budget. In the present finite-resolution setting, the stable types X_6 provide a minimal, explicitly enumerable set of defect labels.

Definition 8.7 (Particles as stable types (interface))**.** *Physical particle labels at the chosen anchor scale are identified with stable readout types in X_6 (or with protocol-invariant functionals thereof), while microstates in $\Omega_6 \setminus X_6$ are protocol-unstable and do not survive as visible outputs under projection.*

The $18\oplus3$ split of X_6 then becomes a structural interface candidate: boundary types are non-closed readout defects (endpoints), while cyclic types are closed defects (loops). This matches the qualitative distinction between colorless endpoint-like excitations and loop-carrying excitations that can support nontrivial holonomy.

Why the $18 \oplus 3$ split is a rigid interface constraint. The split is enforced by a concrete wrap-around defect predicate D_π, hence has an intrinsic "closure vs endpoint" meaning at the protocol level. Interpreting cyclic types as loop-like carriers and boundary types as endpoint-like carriers is therefore not an analogy but a direct reading of the π-constraint. The numbers also provide a rigid counting target: any SM identification must explain why exactly 18 stable types admit closure while exactly 3 do not at the anchor scale.

A rigid integer pattern tying 21 to SM data. Beyond closure semantics, the minimal stable count admits a nontrivial arithmetic decomposition that matches Standard Model integers used elsewhere in this paper:

$$|X_6| = 21 = (18 + 3) = (8 + 3) + 10.$$

Here $8 = \dim(\mathfrak{su}(3))$ and $3 = \dim(\mathfrak{su}(2))$ are the gauge-sector dimensions, while $10 = \sum_{f\in \mathrm{SM}} Y_f^2$ is the hypercharge-squared sum over the chiral fermion content in three generations under the PDG normalization $Q = T_3 + Y$. The identity $21 = (8 + 3) + 10$ is an integer constraint and does not involve any post-hoc fitting freedom; it is recorded as an auditable counting target for the closed labeling interface (Proposition 8.10). The same integers reappear in the electroweak normalization ($13 = 10 + 3$; Section AF.2) and in the CP-odd multiplicity ($d_{\mathrm{CP}} = 8 + 3$; Section AF.3), providing a cross-checked integer backbone across multiple independent interface diagnostics.

Lemma 8.8 (Hypercharge-squared sum $\sum Y^2$)**.** *Under the PDG convention $Q = T_3 + Y$ [2], the Standard Model chiral fermion content without right-handed neutrinos satisfies*

$$\sum Y^2 = \frac{10}{3} \quad \textit{per generation,} \qquad \sum_{f\in \mathrm{SM}} Y_f^2 = 10 \quad \textit{for three generations.}$$

Proof. For one generation, sum Y^2 over left-handed Weyl fields with multiplicities (color and weak components):

$$6\left(\frac{1}{6}\right)^2 + 3\left(\frac{2}{3}\right)^2 + 3\left(\frac{1}{3}\right)^2 + 2\left(\frac{1}{2}\right)^2 + 1\cdot(1)^2 = \frac{10}{3},$$

corresponding to Q_L, u_R, d_R, L_L, and e_R. Multiplying by three generations yields 10. A sterile singlet ν_R has $Y = 0$ and does not change the sum. □

8.3 Minimal mapping problem

We record the interface as an explicit mapping problem. A closed, computable field-level labeling map is provided in Section 9.

How the closed labeling is constructed (preview). The labeling closure is not an unstructured guess: it is a deterministic order-isomorphism between two finite totally ordered sets. On the protocol side, the 18 cyclic stable types are totally ordered by intrinsic invariants (Definition 9.9 and Definition 9.11). On the Standard Model side, the 18 chiral multiplets are totally ordered by the tuple $(g, \dim(SU(3)\text{-rep}), (6Y)^2, \dim(SU(2)\text{-rep}), \text{name})$ under the PDG convention $Q = T_3 + Y$ (Definition 9.12). Matching ranks yields a unique cyclic assignment, while the three boundary types are assigned to $\{U(1), SU(2), SU(3)\}$ by monotone matching of intrinsic value and gauge-sector complexity (Lemma 9.3); see Theorem 9.17 and Table 15.

Definition 8.9 (Intrinsic invariants available at window length 6)**.** *For $w \in X_6$, the finite protocol provides several intrinsic, directly computable invariants:*

- ***closure/boundary tag:*** $D_\pi(w) \in \{0, 1\}$ *(cyclic vs. boundary);*
- ***Zeckendorf value:*** $V(w) \in \{0, \ldots, 20\}$ *(Definition 4.14);*
- ***Hamming weight:*** $|w|_1 \in \{0, 1, 2, 3\}$ *(Appendix AE);*
- ***folding degeneracy:*** $g(w) := |\mathrm{Fold}_6^{-1}(w)| \in \{2, 3, 4\}$ *(Theorem 4.18).*

Proposition 8.10 (Closed Standard Model labeling at $(m, n) = (6, 3)$)**.** *The Standard Model labeling of the* 21 *stable types at the chosen anchor* $(m, n) = (6, 3)$ *is closed and unique: Theorem 9.17 constructs a unique split-compatible labeling map* $\mathcal{L}_{\mathrm{SM}} : X_6 \to \mathcal{F}_{\mathrm{SM}} \sqcup \mathcal{G}_{\mathrm{SM}}$ *by order isomorphism on the cyclic sector and the unique monotone assignment on the boundary sector. Moreover, under window uplift* $m \mapsto m'$ *the labeling admits a canonical functorial lift by prefix projection together with explicit refinement multiplicities and deterministic refinement indices (Appendix V).*

8.4 No-Go Theorem: the scalar exclusion principle (interface)

At the chosen anchor instance $(m, n) = (6, 3)$, the 21-type interface is optimized for a chiral/gauge closure: 18 cyclic labels for chiral fermion multiplets and 3 boundary labels for gauge-factor classes (Section 9). In this setting we record a no-go statement on the physical identification layer: the directed-scan geometry of the minimal stable alphabet excludes parity-even scalar degrees of freedom as distinct primitive stable types, so scalar effective modes should arise only as coarse-grained and uplift-dependent observables. At the audit level, this is already forced by the closed 21-type contract at the anchor: there is no unused stable label in X_6 available for an additional Higgs-like primitive type (Proposition R.6). The additional geometric constraint is that the minimal stable-sector closure is tied to directional protocol data (scan order and the chirality sign datum) and to compensation transport, whereas a scalar mode is, by definition, an observable whose effective appearance is insensitive to these orientation-sign choices.

The vector nature of the linear universe (interface). Under Axiom 1.1 the primitive ontology is a directed scan: the microscopic description is not a static configuration but an ordered stream. As a result, the elementary readout carriers at the minimal stable alphabet inherit directional protocol data (in particular the orientation-sign information that controls chirality in the Hilbert addressing family). A fundamental scalar (spin-0) would amount to a directionless primitive mode whose effective appearance is insensitive to the scan-direction and chirality sign datum already at the minimal window. This contradicts the directed-scan identification at the interface level. Therefore, within the minimal stable-sector closure at $m = 6$, a fundamental Higgs-like scalar cannot be a primitive stable type. Accordingly, the observed Higgs boson must be realized as a composite or statistical emergent mode supported by higher-resolution texture and coarse graining, where directional protocol data effectively averages out.

Remark 8.11 (Relation to composite/Goldstone Higgs paradigms)**.** *Treating the Higgs doublet as an EFT-level degree of freedom rather than a primitive elementary mode is compatible with mature composite/Goldstone Higgs frameworks, in which a scalar arises as an emergent low-energy excitation of a more microscopic sector; see, e.g., [52, 53]. The present protocol formulation differs in microscopic language, but it implies the same practical expectation: scalar behavior can be resolution-dependent and should admit additional diagnostic constraints beyond a minimal chiral labeling at* $m = 6$*.*

In particular, a renormalizable Standard Model EFT includes a scalar Higgs doublet whose vacuum structure controls electroweak symmetry breaking. In the present protocol language, the Higgs is therefore treated as an EFT-level completion (Appendix T) rather than as an additional minimal stable type at $m = 6$ (Remark 9.1). The resolution-uplift narrative fixes a concrete locus for scalar emergence: in the admissible-set sweep one has $|X_{10}| = 144 = 123 \oplus 21$ (Table 66), and under the minimal staircase calibration the threshold for $m = 10$ lies near the electroweak scale (Section 14.2.1, Table 19). Accordingly, in the present interface language electroweak-scalar behavior is modeled as an emergent, parity-even background supported by higher-resolution texture, not as a primitive type at the minimal window.

Proposition 8.12 (Scalar-sector closure in the protocol language)**.** *At the minimal stable alphabet* $(m, n) = (6, 3)$*, parity-even scalar modes are closed as protocol-emergent observables rather than as additional primitive stable types:*

- ***(parity-even scalar observables)*** *Coarse-grained scalar observables are obtained by spatial block-averaging intrinsic stable-type functionals on the Hilbert-addressed grid (Definition 8.13); by construction they are invariant under* P_{prot} *up to pullback (Remark 8.14).*
- ***(coupling to compensating connections)*** *In a lattice-gauge modeling dictionary, scalar site variables couple to link connections by gauge-covariant nearest-neighbor terms that reduce to* $(D_\mu H)^\dagger (D^\mu H)$ *in a continuum limit [42, 43, 54]; in protocol language this corresponds to allowing the local implementation cost of transport/holonomy to depend on a coarse-grained scalar observable (Remark 8.14 and Remark T.1).*
- ***(uplift dependence)*** *A distinct scalar "type" is therefore expected only under resolution uplift and coarse graining, not as a new label in* X_6*; the first audited locus is the* $m = 10$ *uplift where* $|X_{10}| = 144 = 123 \oplus 21$ *and the staircase calibration places* $\mu_{\mathrm{th}}(10)$ *near the electroweak scale (Table 66 and Table 19).*

Quantitative scalar-scale closure (supplement). [Audit]The bounded-denominator Higgs–Z depth-offset rigidity audit is recorded in Appendix AH (Proposition AH.1, Table 99).

Definition 8.13 (Coarse-grained protocol scalars)**.** *Fix a Hilbert order* n *and view the scan index as embedded on the grid by* H_n *(Section 5). Let* q *be any intrinsic protocol functional on stable types (for example* $q(w) \in \{V(w), |w|_1, g(w), D_\pi(w)\}$ *at* $m = 6$*). A* coarse-grained scalar observable *is any block-averaged field obtained by spatial averaging of* q *over a finite neighborhood on the Hilbert-addressed grid. Block averaging as a coarse-graining operation is standard in lattice models; see, e.g., [42, 43].*

Remark 8.14 (A minimal protocol route to scalar effective modes)**.** *By construction, coarse-grained observables of Definition 8.13 are parity-even in the protocol sense: under* P_{prot} *they transform by pullback of the spatial reflection on the grid rather than by an intrinsic sign flip. They are likewise insensitive to the traversal-direction sign datum used to define the discrete chirality index* χ*. This provides a concrete protocol interpretation for a scalar exclusion at the minimal stable alphabet: parity-even scalar modes are naturally modeled as composite or protocol-emergent observables whose appearance depends on coarse graining and resolution uplift, consistent with the Higgs-sector status recorded in Remark 9.1.*

A minimal finite check (supplement). [Audit]The parity-contrast check between the chirality sign datum and coarse-grained scalar summaries is recorded in Appendix AH (Table 100).

Remark 8.15 (Coupling scalars to connections (interface viewpoint))**.** *In lattice gauge theory, gauge fields live on links while scalar fields can be modeled as site variables transforming in a representation of the gauge group, with gauge-covariant nearest-neighbor couplings that reduce to* $(D_\mu H)^\dagger (D^\mu H)$ *in a continuum limit [42, 43, 54]. In the present protocol language, this provides a concrete modeling route for scalar-sector closure (Proposition 8.12): allow the local implementation cost of compensating transport to depend on a coarse-grained scalar observable (Definition 8.13), yielding a site-dependent modulation of transport/holonomy statistics without introducing a new minimal stable type at* $m = 6$*.*

8.5 Protocol flow under uplift and coarse graining (interface)

The program treats finite resolution as primary: both the window length m and the spatial addressing scale n are protocol parameters. Changing resolution (uplift in m and/or n) and applying coarse graining are therefore the protocol-native candidates for a discrete renormalization

step. In this paper, the protocol flow law is fixed explicitly as a discrete uplift–coarse-graining flow together with a standard RG dictionary in the resolution coordinate r [42, 43].

Definition 8.16 (Protocol flow step and flowing objects)**.** *Fix a family of protocol parameters* (m, n) *and a chosen coarse-graining map* C *on the Hilbert-addressed grid (e.g. block averaging or kernel readout). The* protocol flow step *is the deterministic update*

$$(m, n) \mapsto (m', n')$$

together with the induced map on observables obtained by: (i) recomputing the finite stable sector $X_{m'}$ *and intrinsic invariants at the new window length, (ii) pushing observables forward/backward along the canonical prefix projection(s)* $\pi_{m' \to m}$ *(Appendix V), and (iii) applying* C *to obtain coarse observables. The* flowing objects *are any protocol observables defined at finite resolution (stable-type counts, degeneracy histograms, holonomy distributions, bounded-complexity minimizers, and derived effective couplings defined as functions of these invariants).*

Proposition 8.17 (RG dictionary in the Fibonacci resolution coordinate)**.** *Let* $\mu(r) = \mu_0 \, \varphi^r$ *be the Fibonacci resolution map (Section 10.1) and let* $g(\mu)$ *be any scale-dependent effective parameter with a standard RG equation* $\mathrm{d}g/\mathrm{d}\log\mu = \beta(g)$ *away from thresholds. Then, in the resolution coordinate,*

$$\frac{\mathrm{d}g}{\mathrm{d}r} = (\log\varphi)\,\beta(g).$$

Proof. Since $\log\mu = \log\mu_0 + r\log\varphi$, one has $\mathrm{d}/\mathrm{d}r = (\log\varphi)\,\mathrm{d}/\mathrm{d}\log\mu$. □

9 Closure: field-level labeling of the 21 stable types

This section closes the Standard Model labeling interface by giving an explicit, computable assignment of field-level labels to the finite stable type set X_6. We work at the chosen anchor scale $(m, n) = (6, 3)$, where $|X_6| = 21$ and $X_6 = X_6^{\mathrm{cyc}} \sqcup X_6^{\mathrm{bdry}}$ with $|X_6^{\mathrm{cyc}}| = 18$ and $|X_6^{\mathrm{bdry}}| = 3$ (Proposition 4.9).

9.1 Field-level targets and audit discipline

We use "field-level" in the Standard Model sense of chiral multiplets per generation (rather than individual Weyl components), with the unique minimal extension forced by the closure of the 18 cyclic types under anomaly-neutrality (Proposition R.5). Concretely, for each generation $g \in \{1, 2, 3\}$, we consider the six chiral multiplets

$$Q_L^{(g)},\ u_R^{(g)},\ d_R^{(g)},\ L_L^{(g)},\ e_R^{(g)},\ \nu_R^{(g)},$$

with the usual $SU(3) \times SU(2) \times U(1)$ quantum numbers under the PDG convention $Q = T_3 + Y$ [1, 2]. Here $\nu_R^{(g)}$ denotes a neutral singlet (hypercharge $Y = 0$) that is absent in the minimal SM, but standard in minimal sterile extensions used to parametrize neutrino mass interfaces [2]. Within the explicit minimal candidate family "one additional multiplet per generation", anomaly neutrality and the global $SU(2)$ consistency condition force the choice of a sterile singlet with $Y = 0$ (Proposition R.5); in particular, adding a gauge singlet with $Y = 0$ does not change the SM anomaly-cancellation identities (Proposition 9.6). This yields 18 fermion multiplets. The remaining three stable types in the $18 \oplus 3$ split are reserved for the three gauge-factor connection classes, aligned with the three-channel template (Proposition 8.2).

Remark 9.1 (Higgs sector and what is (not) covered by the 21 stable types)**.** *The* 21 *stable types at* $(m, n) = (6, 3)$ *are used here to close a minimal* chiral labeling *interface:* 18 *cyclic labels for fermion multiplets and* 3 *boundary labels for gauge-factor classes. This does not, by itself,*

provide a stable-type label for the Higgs doublet. Accordingly, when we discuss a field-theoretic embedding (Appendix T), the Higgs is treated as an additional field required for a renormalizable SM EFT, not as a claim that it must appear as a distinct stable type at the minimal window length. At the protocol-geometry layer, Hilbert addressing enters through an oriented scan order on the grid, and parity-odd sign data such as the discrete chirality index χ in (15) *are built from signed turns along this order (Section 5). Accordingly, the minimal labeling interface closed at $(m, n) = (6, 3)$ emphasizes chiral/gauge degrees of freedom tied to the orientation-class choice (Section 7). By contrast, Lorentz-scalar sectors carry no intrinsic handedness and are treated, in the present interface language, as composite or protocol-emergent modes whose effective appearance depends on resolution uplift and on the choice of coarse graining, rather than on the minimal $m = 6$ stable alphabet. The corresponding scalar-sector closure in protocol language is recorded in Proposition 8.12.*

Non-negotiable interface constraints (audit contract). From an audit viewpoint, the labeling stage is closed under an explicit constraint set:

- **Split compatibility.** Cyclic vs. boundary types are fixed by the π-predicate D_π, so the $18 \oplus 3$ split is not negotiable (Section 4); we therefore require $\mathcal{L}_{\mathrm{SM}}(X_6^{\mathrm{cyc}}) \subset \mathcal{F}_{\mathrm{SM}}$ and $\mathcal{L}_{\mathrm{SM}}(X_6^{\mathrm{bdry}}) \subset \mathcal{G}_{\mathrm{SM}}$.
- **Standard consistency constraints.** The field-level target set obeys the standard anomaly-cancellation identities and hypercharge quantization under $Q = T_3 + Y$ [1, 2]; adding a sterile ν_R with $Y = 0$ is the minimal anomaly-neutral closure of the cyclic count (Proposition 9.6).
- **No numerical SM targets in the labeling stage.** Masses, couplings, and fit-derived continuous parameters are not used to construct $\mathcal{L}_{\mathrm{SM}}$; only discrete quantum-number invariants enter (representation dimensions and the integer invariant $(6Y)^2$).
- **Deterministic closure.** Any remaining ties are resolved by explicit deterministic rules (Definitions 9.11 and 9.12), and the sensitivity to the SM-side ordering-key choice is audited (Table 14).

Within this contract, the labeling is not a free-form assignment: once the protocol-side order and SM-side order are fixed, the cyclic-sector bijection is forced as the unique order isomorphism (Theorem 9.17). To address the concern that the result is a vacuous relabeling, we additionally report inverse diagnostics that test recoverability of several SM quantum-number patterns from intrinsic stable-type invariants by bounded-complexity rules (Table 13 and Appendix W).

Definition 9.2 (Gauge-sector complexity order)**.** *For a gauge factor $G \in \{U(1), SU(2), SU(3)\}$, define its protocol-level complexity by the Lie-algebra dimension*

$$\dim(\mathfrak{g}),$$

equivalently the number of gauge bosons in the corresponding factor.

Lemma 9.3 (Dimension order of the SM gauge factors)**.** *For the Standard Model gauge factors one has*

$$\dim(\mathfrak{u}(1)) = 1, \qquad \dim(\mathfrak{su}(2)) = 3, \qquad \dim(\mathfrak{su}(3)) = 8,$$

hence $U(1) \prec SU(2) \prec SU(3)$ in the complexity order of Definition 9.2.

Proof. This is standard: $\dim(\mathfrak{u}(1)) = 1$ and $\dim(\mathfrak{su}(N)) = N^2 - 1$; see, e.g., [1]. □

Lemma 9.4 (Uniqueness of compact simple factors at dimensions 3 and 8 (standard))**.** *Among compact simple real Lie algebras, the only isomorphism class of dimension* 3 *is* $\mathfrak{su}(2) \cong \mathfrak{so}(3)$*, and the only isomorphism class of dimension* 8 *is* $\mathfrak{su}(3)$*. Consequently, if the gauge-sector complexity in Definition 9.2 is identified with* $\dim(\mathfrak{g})$ *and one assumes compact (semi)simple gauge factors, then the dimension triple* $(1, 3, 8)$ *pins the factor Lie algebras uniquely to*

$$\mathfrak{u}(1) \oplus \mathfrak{su}(2) \oplus \mathfrak{su}(3),$$

up to finite quotients at the group level.

Proof. This follows from the Cartan–Killing classification of compact simple Lie algebras and their dimension formulas; see, e.g., [18, 55]. □

Lemma 9.5 (A standard $\mathbb{Z}_6$ quotient in the global gauge group)**.** *Let* $G := SU(3) \times SU(2) \times U(1)$ *and normalize hypercharge by* $Q = T_3 + Y$ *so that* $6Y \in \mathbb{Z}$ *(Lemma 9.13). Let the* $U(1)$ *factor act on a field of hypercharge* Y *by the integer charge* $Q_Y := 6Y$*, i.e.* $u \in U(1)$ *acts as* u^{Q_Y}*. Define the central element*

$$z := \left(\mathrm{e}^{2\pi \mathrm{i}/3}\, \mathbf{1}_3,\ -\mathbf{1}_2,\ \mathrm{e}^{\mathrm{i}\pi/3}\right) \in SU(3) \times SU(2) \times U(1).$$

Then z *acts trivially on all Standard Model fermion multiplets used in this paper (including a sterile* ν_R*), and the resulting faithful gauge group may be taken as* $G/\langle z \rangle \cong (SU(3) \times SU(2) \times U(1))/\mathbb{Z}_6$*.*

Proof. For each multiplet $(SU(3), SU(2))_Y$, the $SU(3)$ center contributes $\mathrm{e}^{2\pi \mathrm{i}/3}$ on triplets and 1 on singlets, the $SU(2)$ center contributes -1 on doublets and 1 on singlets, and the $U(1)$ factor contributes $\mathrm{e}^{\mathrm{i}\pi Q_Y/3} = \mathrm{e}^{\mathrm{i}\pi(6Y)/3}$. Using the standard hypercharges under $Q = T_3 + Y$ for $Q_L, u_R, d_R, L_L, e_R, \nu_R$ [1, 2], one checks that the product phase equals 1 in each case. □

We note two standard consistency facts for this fermion content (per generation), recorded here as audit-level requirements and referenced to the standard literature: (i) the hypercharge-squared sum (with multiplicities) equals $\sum Y^2 = 10/3$ under $Q = T_3 + Y$ (Lemma 8.8), and (ii) the gauge and mixed gravitational anomalies cancel (a neutral singlet does not affect these cancellations) [1, 2, 56].

Proposition 9.6 (Anomaly cancellation is unchanged by adding ν_R)**.** *Under the PDG convention* $Q = T_3 + Y$*, the Standard Model chiral fermion content (per generation, without* ν_R*) has vanishing gauge and mixed gravitational anomalies. Adding a sterile singlet* ν_R *with* $Y = 0$ *preserves these cancellations.*

Proof. The anomaly-cancellation identities for the Standard Model hypercharge assignments are standard [1,2,56]. A sterile singlet ν_R contributes $Y = 0$ to all anomaly sums and therefore does not change them. □

Lemma 9.7 (Explicit anomaly sums in a left-handed basis (one generation))**.** *Under the PDG convention* $Q = T_3 + Y$*, write one generation in a left-handed Weyl basis*

$$Q_L, \quad u^c, \quad d^c, \quad L_L, \quad e^c \qquad (\text{and optionally } \nu^c \text{ with } Y = 0),$$

with hypercharges $Y(Q_L) = 1/6$*,* $Y(u^c) = -2/3$*,* $Y(d^c) = 1/3$*,* $Y(L_L) = -1/2$*, and* $Y(e^c) = 1$*. Then the mixed gravitational–hypercharge anomaly and the cubic hypercharge anomaly vanish:*

$$\sum Y = 0, \qquad \sum Y^3 = 0,$$

where the sums include multiplicities from color and weak isospin components. Moreover, the mixed non-abelian anomalies vanish:

$$SU(3)^2U(1): \quad 2 \cdot \frac{1}{6} - \frac{2}{3} + \frac{1}{3} = 0, \qquad SU(2)^2U(1): \quad 3 \cdot \frac{1}{6} - \frac{1}{2} = 0,$$

equivalently $\sum Y\,T(R) = 0$ *for each non-abelian factor (with* T *the Dynkin index of the fundamental representation).*

Proof. For the gravitational sum, include multiplicities of left-handed Weyl components:

$$6\left(\frac{1}{6}\right) + 3\left(-\frac{2}{3}\right) + 3\left(\frac{1}{3}\right) + 2\left(-\frac{1}{2}\right) + 1\cdot(1) = 0.$$

For the cubic $U(1)_Y^3$ sum:

$$6\left(\frac{1}{6}\right)^3 + 3\left(-\frac{2}{3}\right)^3 + 3\left(\frac{1}{3}\right)^3 + 2\left(-\frac{1}{2}\right)^3 + 1\cdot(1)^3 = 0.$$

For $SU(3)^2U(1)$, only color triplets contribute, and all fundamental/antifundamental contributions share the same Dynkin index; factoring it out yields $2Y(Q_L) + Y(u^c) + Y(d^c) = 0$. For $SU(2)^2U(1)$, only weak doublets contribute; factoring out the $SU(2)$ fundamental Dynkin index yields $3Y(Q_L) + Y(L_L) = 0$. These are the standard anomaly-cancellation identities in a chiral left-handed basis [1, 2, 56]. □

Remark 9.8 (Why the minimal extension is chosen as a neutral singlet)**.** *The role of* ν_R *in this paper is purely interface-level and audit-driven: it closes the cyclic-cardinality count to* 18 *using the smallest additional bookkeeping burden. Adding new chiral multiplets charged under* $U(1)$ *and/or* $SU(3)$ *would introduce nontrivial local anomaly contributions unless accompanied by additional compensating matter [1, 2]. Moreover, adding* $SU(2)$ *doublets is constrained by the global* $SU(2)$ *anomaly (Witten anomaly), which depends on the parity of half-integer isospin representations [57]. Choosing* ν_R *as a sterile singlet with* $Y = 0$ *preserves both the standard local anomaly cancellations and the* $SU(2)$ *global consistency condition while matching a minimal sterile extension widely used in neutrino-mass parametrizations [2].*

The construction is auditable in the finite protocol language: we build the labeling map from intrinsic invariants of stable types (Definition 8.9), with the Hilbert order entering through the depth assignment in Definition 9.9.

9.2 Nontriviality checks: inverse diagnostics and ordering sensitivity

The closed labeling map in this section is an explicit deterministic rank-matching between two finite ordered sets (Theorem 9.17). To demonstrate that this assignment is not a vacuous relabeling, we record two audit-level nontriviality diagnostics.

Inverse interface diagnostics (recoverability of quantum-number patterns). Appendix W treats the closed labeling as supervised data on the cyclic stable types and asks, for several Standard Model targets, whether bounded-complexity rules built from intrinsic invariants can recover target patterns above fixed chance/majority baselines (and in some targets exactly). Table 13 summarizes those inverse diagnostics; full details and model families are recorded in Appendix W. These inverse diagnostics are not premises for any result in the main text: they are post-hoc audits of structure.

Ordering sensitivity. To test how much the induced cyclic assignment depends on SM-side ordering conventions in Definition 9.12, we run a bounded sensitivity sweep that varies: (i) the component order among $\{\dim(SU(3)), (6Y)^2, \dim(SU(2))\}$, (ii) whether the generation index appears first or later, and (iii) whether the final deterministic tie-break uses the SM name or a name-free integer code (e.g. $Y_{\text{num}} = 6Y$). For each variant we recompute the induced cyclic pairing by rank matching. As a summary metric we report, for each induced pairing, the Hamming distance (and fraction) between the resulting ordered multiplet-type list and the baseline ordering used in this paper. Table 14 records the resulting sensitivity sweep.

target	baseline	best accuracy	detail
$(6Y)^2$ class	1/6	0.389	Table 55
sign(Y)	1/2	0.667	Table 56
$Y_{\text{num}} = 6Y$	1/6	1.000	Table 57
$\dim(SU(3))$	1/2	0.833	Table 58
$\dim(SU(2))$	2/3	0.778	Table 58
generation g	1/3	1.000	Table 59

Table 13: Summary of inverse interface diagnostics on cyclic stable types at $m = 6$: each row compares a fixed chance/majority baseline to the best bounded-complexity accuracy achieved by a reproducible inverse diagnostic (Appendix W). Rows are reproduced by the deterministic bounded sweeps described in Appendix W (`scripts/exp_inverse_diag_summary.py`).

SM ordering key	labels changed (of 18)	fraction
$(g, \dim(SU(3)), (6Y)^2, \dim(SU(2)), \textbf{name})$	**0**	**0.000**
$(g, \dim(SU(3)), \dim(SU(2)), (6Y)^2, \text{name})$	15	0.833
$(g, (6Y)^2, \dim(SU(3)), \dim(SU(2)), \text{name})$	15	0.833
$(g, (6Y)^2, \dim(SU(2)), \dim(SU(3)), \text{name})$	15	0.833
$(g, \dim(SU(2)), \dim(SU(3)), (6Y)^2, \text{name})$	15	0.833
$(g, \dim(SU(2)), (6Y)^2, \dim(SU(3)), \text{name})$	15	0.833
$(g, \dim(SU(3)), (6Y)^2, \dim(SU(2)), Y_{\text{num}})$	0	0.000
$(\dim(SU(3)), (6Y)^2, \dim(SU(2)), g, \text{name})$	14	0.778
$(\dim(SU(3)), (6Y)^2, \dim(SU(2)), g, Y_{\text{num}})$	14	0.778

Table 14: Ordering sensitivity audit: varying SM-side ordering conventions (component order, generation placement, and name vs. name-free tie-break) and counting how many cyclic multiplet labels change relative to the baseline ordering used in Definition 9.12. The bold row is the baseline. Rows are reproduced by a deterministic finite sweep over the stated ordering-key variants (`scripts/exp_labeling_order_sensitivity.py`).

9.3 A canonical labeling map

We first define an intrinsic protocol depth from stable-type invariants.

Definition 9.9 (Effective protocol depth at $(m, n) = (6, 3)$)**.** *For $w \in X_6$, define*

$$r_*(w) := V(w) + n\,(g(w) - 2), \tag{18}$$

where $V(w) \in \{0, \dots, 20\}$ is the Zeckendorf value, $g(w) \in \{2, 3, 4\}$ is the folding degeneracy, and $n = 3$ is the Hilbert order at the chosen anchor $(m, n) = (6, 3)$.

Lemma 9.10 (Discrete range of r_* at $(m, n) = (6, 3)$)**.** *At the minimal anchor $(m, n) = (6, 3)$ one has $r_*(w) \in \{0, 1, \dots, 26\}$ for every $w \in X_6$.*

Proof. By Proposition 4.15, $V(w) \in \{0, \dots, 20\}$. By Theorem 4.18, $g(w) \in \{2, 3, 4\}$, hence $n(g(w) - 2) \in \{0, 3, 6\}$ for $n = 3$. Therefore $r_*(w) = V(w) + n(g(w) - 2) \in [0, 20] + [0, 6] = \{0, \dots, 26\}$. □

Why r_* is used in the labeling order. The quantity $r_*(w)$ is an intrinsic protocol-level scalar built only from finite-resolution invariants at $(m, n) = (6, 3)$. It is reused consistently

across the paper: it is the same unnormalized depth that enters the closed mass template (Definition 13.3) and therefore ties the labeling interface to the resolution-depth spectrum closure by a shared protocol cost coordinate. Using r_* in the cyclic ordering makes the labeling stage deterministic without importing any Standard-Model numerical targets as premises.

We now turn the labeling into a closed optimization statement.

Definition 9.11 (Ordering of cyclic stable types)**.** *On the cyclic sector X_6^{cyc}, define the total order $\prec_X$ by*

$$w_1 \prec_X w_2 \quad \Longleftrightarrow \quad (r_*(w_1), V(w_1), w_1) \text{ is lexicographically smaller than } (r_*(w_2), V(w_2), w_2).$$

Definition 9.12 (Ordering of SM fermion multiplets)**.** *Let $\mathcal{F}_{\mathrm{SM}}$ be the set of 18 chiral fermion multiplets used in Section 9.1. Define the total order $\prec_F$ on $\mathcal{F}_{\mathrm{SM}}$ by lexicographic comparison of the tuple*

$$\Big(g,\ \dim(SU(3)\text{-}rep),\ (6Y)^2,\ \dim(SU(2)\text{-}rep),\ name\Big),$$

where $g \in \{1,2,3\}$ is the generation index and Y is the hypercharge under the PDG convention $Q = T_3 + Y$ [1, 2].

Lemma 9.13 (Hypercharge quantization and the integer invariant $(6Y)^2$)**.** *Under the PDG convention $Q = T_3 + Y$, every Standard Model chiral multiplet (including a sterile singlet ν_R with $Y = 0$) has hypercharge $Y \in \frac{1}{6}\mathbb{Z}$. Consequently $6Y \in \mathbb{Z}$ and $(6Y)^2 \in \mathbb{N}$ is an intrinsic integer invariant of the field-level label.*

Proof. This is the standard hypercharge assignment for one generation: $Y(Q_L) = 1/6$, $Y(u_R) = 2/3$, $Y(d_R) = -1/3$, $Y(L_L) = -1/2$, $Y(e_R) = -1$, and $Y(\nu_R) = 0$ under $Q = T_3 + Y$ [1,2]. Each value is an integer multiple of $1/6$. □

Remark 9.14 (Why $(6Y)^2$ is used in the ordering)**.** *Using $(6Y)^2$ replaces the rational invariant Y^2 by the minimal integer normalization compatible with Lemma 9.13. This keeps the ordering rule fully discrete and bounded-complexity. For the minimal fermion multiplet set used here, the discrete gauge-quantum-number tuple already distinguishes the six multiplet types within each generation, so the final deterministic tie-break can be taken either as the SM name or as a name-free integer code (Table 14).*

Lemma 9.15 (Representation dimensions in the SM multiplet set)**.** *Within the Standard Model fermion multiplets used in this paper, the $SU(3)$ representation is either the singlet ($\dim = 1$) or the fundamental triplet ($\dim = 3$), and the $SU(2)$ representation is either the singlet ($\dim = 1$) or the fundamental doublet ($\dim = 2$).*

Proof. This is standard for the chiral matter content of the Standard Model (per generation): Q_L and (u_R, d_R) are color triplets, while leptons are color singlets; Q_L and L_L are weak doublets, while the right-handed singlets are weak singlets [1, 2]. □

Remark 9.16 (Generation labels and deterministic tie-breaks)**.** *The generation index g in Definition 9.12 is a bookkeeping label for the three copies of the same gauge-quantum-number pattern; any permutation of $\{1,2,3\}$ corresponds to a relabeling at the level of gauge interactions. We fix the conventional naming order and take $g = 1$ to be the charged-lepton reference generation used later in the mass template (Definition 13.3). The final "name" entry is used only as a deterministic tie-break when the gauge-quantum-number tuple is otherwise identical. Within the multiplet set $\mathcal{F}_{\mathrm{SM}}$ used in this paper, that name tie-break is redundant: the tuple $(\dim(SU(3)), (6Y)^2, \dim(SU(2)))$ already separates the six multiplet types per generation. Table 14 includes a name-free variant (replacing the final name tie-break by Y_{num}) and confirms that the induced cyclic labeling is unchanged.*

We define a labeling map

$$\mathcal{L}_{\mathrm{SM}} : X_6 \to \mathcal{F}_{\mathrm{SM}} \sqcup \mathcal{G}_{\mathrm{SM}},$$

where $\mathcal{G}_{\mathrm{SM}} := \{SU(3), SU(2), U(1)\}$ denotes the three gauge-factor connection classes. The map is chosen to satisfy:

- **(split compatibility)** $\mathcal{L}_{\mathrm{SM}}(X_6^{\mathrm{cyc}}) \subset \mathcal{F}_{\mathrm{SM}}$ and $\mathcal{L}_{\mathrm{SM}}(X_6^{\mathrm{bdry}}) \subset \mathcal{G}_{\mathrm{SM}}$;
- **(protocol covariance)** rotations preserve labels while reflections/traversal reversal act by the protocol-level $P_{\mathrm{prot}}/T_{\mathrm{prot}}$ rules (Section 7);
- **(minimality)** among all assignments satisfying the above, we select the unique minimal-complexity solution under a fixed lexical tie-break rule.

Theorem 9.17 (Closed labeling as the unique order-preserving assignment)**.** *There exists a unique labeling map $\mathcal{L}_{\mathrm{SM}}$ such that:*

- *it is split-compatible;*
- *on the cyclic sector it is order-preserving:*

$$w_1 \prec_X w_2 \quad \Longrightarrow \quad \mathcal{L}_{\mathrm{SM}}(w_1) \prec_F \mathcal{L}_{\mathrm{SM}}(w_2);$$

- *on the boundary sector, it assigns the three boundary types in increasing $V(w)$ order to $\{U(1), SU(2), SU(3)\}$ in increasing gauge-sector complexity order (Lemma 9.3).*

Proof. Both $(X_6^{\mathrm{cyc}}, \prec_X)$ and $(\mathcal{F}_{\mathrm{SM}}, \prec_F)$ are finite totally ordered sets with the same cardinality 18, hence admit a unique order isomorphism given by matching ranks. The boundary words in X_6^{bdry} have distinct values $V(w)$, hence a unique increasing order. Likewise, the three gauge factors have distinct complexity values $\dim(\mathfrak{g})$, hence a unique increasing order by Lemma 9.3. Matching ranks gives the unique order-preserving boundary assignment. □

Remark 9.18 (CAP minimality of the monotone boundary assignment)**.** *Among the $3! = 6$ boundary permutations, the monotone assignment is the unique one compatible with the complexity order of Definition 9.2 and therefore the unique CAP-minimal choice under any monotone mismatch cost between intrinsic boundary value and gauge-sector complexity. Any non-monotone assignment would map a larger intrinsic boundary value to a lower-complexity gauge factor, creating an avoidable ordering mismatch that must be compensated elsewhere in the interface.*

Operationally, the assignment is therefore constructed as follows (equivalently: among the $3! = 6$ boundary permutations, it is the unique one that is monotone in the intrinsic value $V(w)$ and the gauge-sector complexity).

- The three boundary types are sorted by $V(w)$ and assigned to $\{U(1), SU(2), SU(3)\}$ in increasing gauge-sector complexity order (Definition 9.2).
- The 18 cyclic types are sorted by $\prec_X$ and assigned to the 18 fermion multiplets sorted by $\prec_F$.

Remark 9.19 (Explicit boundary-value order at $m = 6$)**.** *At $m = 6$, the boundary words are* 100001*,* 101001*, and* 100101 *(Corollary 4.9). Their Zeckendorf values are $V(100001) = 14$, $V(101001) = 17$, and $V(100101) = 19$ (Definition 4.14). Thus the intrinsic increasing boundary order is*

$$100001 \ \prec \ 101001 \ \prec \ 100101,$$

which is the order used for the unique monotone assignment to $U(1) \prec SU(2) \prec SU(3)$ (Lemma 9.3).

stable type w	$V(w)$	$g(w)$	$\lvert w\rvert_1$	$r_*(w)$	$D_\pi(w)$	label $\mathcal{L}_{\mathrm{SM}}(w)$	$(SU(3), SU(2))_Y$
000000	0	4	0	6	0	$\nu_R^{(1)}$	$(1,1)_0$
100000	1	4	1	7	0	$L_L^{(1)}$	$(1,2)_{-1/2}$
010000	2	4	1	8	0	$e_R^{(1)}$	$(1,1)_{-1}$
001000	3	4	1	9	0	$Q_L^{(1)}$	$(3,2)_{1/6}$
101000	4	4	2	10	0	$d_R^{(1)}$	$(3,1)_{-1/3}$
000100	5	4	1	11	0	$u_R^{(1)}$	$(3,1)_{2/3}$
100100	6	4	2	12	0	$\nu_R^{(2)}$	$(1,1)_0$
010100	7	4	2	13	0	$e_R^{(2)}$	$(1,1)_{-1}$
000010	8	4	1	14	0	$u_R^{(2)}$	$(3,1)_{2/3}$
100010	9	3	2	12	0	$L_L^{(2)}$	$(1,2)_{-1/2}$
010010	10	3	2	13	0	$Q_L^{(2)}$	$(3,2)_{1/6}$
001010	11	3	2	14	0	$\nu_R^{(3)}$	$(1,1)_0$
101010	12	3	3	15	0	$L_L^{(3)}$	$(1,2)_{-1/2}$
000001	13	2	1	13	0	$d_R^{(2)}$	$(3,1)_{-1/3}$
100001	14	2	2	14	1	$U(1)$	–
010001	15	2	2	15	0	$e_R^{(3)}$	$(1,1)_{-1}$
001001	16	2	2	16	0	$Q_L^{(3)}$	$(3,2)_{1/6}$
101001	17	2	3	17	1	$SU(2)$	–
000101	18	2	2	18	0	$d_R^{(3)}$	$(3,1)_{-1/3}$
100101	19	2	3	19	1	$SU(3)$	–
010101	20	2	3	20	0	$u_R^{(3)}$	$(3,1)_{2/3}$

Table 15: Closed field-level labeling of the 21 stable types at $(m,n) = (6,3)$. The labeling map is the unique order-preserving assignment of Theorem 9.17. Rows are reproduced by a deterministic implementation of the same rank-matching construction (`scripts/exp_sm_labeling_solver.py`).

Remark 9.20 (Determinism vs. reproducibility)**.** *Theorem 9.17 is the logical closure: it pins a unique map $\mathcal{L}_{\mathrm{SM}}$ once the two total orders $\prec_X$ and $\prec_F$ and the boundary monotonicity convention are fixed. The script* `scripts/exp_sm_labeling_solver.py` *is only a deterministic implementation of this rank-matching construction used to* reproduce *the table rows and to avoid manual transcription errors; it is not an additional premise and it does not select among multiple solutions.*

10 Mass as latency: the Fibonacci resolution coordinate (interface)

This section records the resolution-depth coordinate and the operational mass-as-delay dictionary used at the matching layer. These definitions are used downstream by the closed mass-spectrum template and by the falsifiability statements formulated in the protocol language.

A readout viewpoint (interface). In a static-ontology reading (Remark 1.2), the underlying protocol substrate is fixed while physical episodes reflect sequential access and finite-resolution projection. On this viewpoint, increasing effective resolution does not change the substrate; it changes which structure is rendered/accessible in the readout, and how much overhead (latency) is paid to stabilize it.

10.1 Fibonacci resolution coordinate

Fix the reference scale $\mu_0 = m_e$ and define the resolution coordinate

$$r(\mu) := \frac{\log(\mu/m_e)}{\log \varphi}, \tag{19}$$

where $\varphi = (1+\sqrt{5})/2$ is the golden ratio. Equivalently, the exponential map is

$$\mu(r) = m_e\, \varphi^{\,r}. \tag{20}$$

This is the resolution-flow dictionary used throughout the paper.

Tick-first meaning. In the tick-first dictionary (Section 3), mass and energy are not primitive substances: they are calibrated names for *time-scale ratios*. Accordingly, the coordinate $r(\mu)$ is used as a single log-time coordinate: by the Compton-clock relation, it is simultaneously a log-frequency coordinate and (up to sign) a log-time coordinate (Remark 10.1 and Appendix Y). This is the precise sense in which the present framework treats "mass as depth" as "mass as a time-lag / overhead coordinate" rather than as an independent input.

10.1.1 Mass as delay: scattering time lag as inertia (interface)

In the scan-based identification dictionary used in this paper, "mass as depth" is read as "mass as protocol overhead": deeper stabilization requires additional local protocol resources. An operational proxy for such overhead is measurable scattering delay. Let $S(\omega)$ be a (nearly) unitary scattering matrix at angular frequency ω. The Wigner–Smith time-delay matrix is

$$Q(\omega) := -\mathrm{i}\, S(\omega)^{\dagger} \frac{\mathrm{d}S}{\mathrm{d}\omega}, \qquad \tau_{\mathrm{WS}}(\omega) := \mathrm{Tr} Q(\omega),$$

and in a one-channel setting $S(\omega) = \mathrm{e}^{\mathrm{i}\delta(\omega)}$ one has $\tau_{\mathrm{WS}}(\omega) = \mathrm{d}\delta/\mathrm{d}\omega$ (Section Y).

Why should depth create mass? Physically, high information density forces the one-dimensional scan to execute additional local folding and consistency operations to stabilize a persistent pattern. When probed through a scattering channel, this manifests as an excess time delay. To an external observer, a localized excitation that systematically "lags" in response behaves as an inertial degree of freedom. Throughout this paper this dictionary is used only at the matching layer: it complements the Compton-clock relation below and provides an independent falsifiability route via delay-derived lapse ratios (Section 14.3.3 and Section Y).

Remark 10.1 (Mass as a clock rate (matching dictionary))**.** *By the standard relations $E = mc^2$ and $E = \hbar\omega$ [24, 58], a mass scale μ defines a Compton angular frequency $\omega_C(\mu) = \mu c^2/\hbar$ and a Compton time scale $\tau_C(\mu) = 1/\omega_C(\mu) = \hbar/(\mu c^2)$. Therefore the resolution coordinate* (19) *is equivalently a log-frequency (or log-time) coordinate:*

$$r(\mu) = \log_\varphi\!\left(\frac{\omega_C(\mu)}{\omega_C(m_e)}\right) = -\log_\varphi\!\left(\frac{\tau_C(\mu)}{\tau_C(m_e)}\right).$$

In particular, the depth mismatch $\Delta r = r - \widehat{r}$ reported later in the mass-spectrum closure is the same multiplicative mismatch in Compton-clock period, $\tau_C/\tau_{C,\mathrm{pred}} = \varphi^{-\Delta r}$, and can be compared to operational delay proxies (Section Y) at the matching layer. The same logarithmic coordinate also linearizes Schwarzschild black-hole thermodynamics: $\log_\varphi S_{\mathrm{BH}} = 2\, r(M) + const$ and $\log_\varphi T_H = -\, r(M) + const$ (Appendix X).

Remark 10.2 (Why the base φ is canonical on the golden branch)**.** *Lemma 4.5 gives $|X_m| = F_{m+2}$ for the admissible language at window length m. By Binet's formula, F_{m+2} grows exponentially as φ^m up to a fixed prefactor [27]. Equivalently, the golden-mean shift has topological entropy $\log\varphi$ and its Artin–Mazur zeta function is $\zeta(z) = 1/(1-z-z^2)$ (Lemma 4.10) [23]. Thus using $\log\varphi$ as the denominator in* (19) *matches the intrinsic exponential growth rate of the admissible symbolic language on the golden branch.*

Quantity	closed value	reference (CODATA/PDG)	log(closed/ref)
$\alpha_{\mathrm{em}}^{-1}$ (low energy)	$4\pi^3 + \pi^2 + \pi$	137.035999084 (CODATA 2022)	$+2.22 \times 10^{-6}$
$\alpha^{-1}(\mu_Z)$	$13\pi^2$	127.955 (PDG)	$+2.73 \times 10^{-3}$
$\sin^2\theta_W(\mu_Z)$	$3/13$	0.23122 (PDG, $\overline{\mathrm{MS}}$)	-1.95×10^{-3}
J (CKM)	$1/(11\pi^7)$	3.00×10^{-5} (PDG)	$+3.31 \times 10^{-3}$

Table 16: Quantitative rigidity targets of the closed model in this paper, together with standard reference values and signed log mismatches in the audit norm. For small deviations, log(closed/ref) $\approx$ (closed $-$ ref)/ref. Domain sizes, uniqueness gaps, uncertainty-robustness checks, and counterfactual baselines for the associated bounded-complexity closures are recorded in Appendix AE (Tables 70–74) [2, 59]. Rows are reproduced by the deterministic script `scripts/exp_quant_summary.py`.

Delay / lapse matching dictionaries (supplement). [Match]The Wigner–Smith delay proxy, Compton-clock ratios, and GR/SR lapse reference formulas used at the matching layer are recorded in Appendix Y and Appendix Z.

11 Couplings and CP violation as geometric normalization

This section records two interface points: (i) coupling constants as geometric normalization costs, and (ii) CP violation as a CP-odd phase-space volume with discrete multiplicity. We treat the closed expressions as CAP-closed interface normalizations: they follow from explicitly declared finite candidate families and canonical geometric data, and their mismatch to scheme-/scale-dependent experimental conventions is recorded as a matching-layer factor.

Audit pointer (bounded-family closure). [Audit]Quantitative selections in this section are CAP closures within explicitly declared finite candidate families with deterministic tie-break rules; see Appendix H and Appendix G for the audit contract, and Appendix AE and Appendix AF for domain/gap tables and reproducibility pointers.

Detailed constructions (supplement). The explicit geometric constructions, bounded-complexity enumerations, and CKM reconstruction tables are recorded in Appendix AF.

11.1 Summary table: closed values vs. CODATA/PDG

Interpretation of mismatch. The closed expressions in Table 16 are not free fit parameters: they are rigidity targets selected by explicit bounded-complexity closure rules. The mismatch log(closed/ref) is recorded as a protocol-level matching factor between an idealized closed normalization and a scheme-/scale-dependent reference convention. This plays the same structural role as the matching-layer depth shift Δr used later for masses (Appendix AG). The corresponding finite rigidity enumerations (top candidates and gaps within the declared domains) are recorded in Appendix AE (Tables 76–79).

Supplementary sigma-normalized view. [Audit]A sigma-normalized mismatch view (for interpretive convenience only) is recorded in Appendix AE; the closed-model statement remains the log-mismatch/matching-layer interpretation used throughout.

ordering	eigenstate	reference μ [GeV]	$r(\mu)$	nearest $\widehat{r}$	Δr	μ/μ_{pred}
NO	m_1	0	–	–	–	–
NO	m_2	$8.61394e-12$	-37.195	-37	-0.195	0.910594
NO	m_3	$5.01697e-11$	-33.533	-34	0.467	1.25199
IO	m_1	$4.998e-11$	-33.541	-34	0.459	1.24726
IO	m_2	$5.07169e-11$	-33.510	-34	0.490	1.26565
IO	m_3	0	–	–	–	–

Table 17: A minimal neutrino mass-scale interface in the resolution coordinate. For each reference mass μ we compute $r(\mu) = \log(\mu/m_e)/\log\varphi$ and select the nearest integer depth $\widehat{r}$, yielding a depth mismatch $\Delta r = r - \widehat{r}$ and the implied multiplicative matching factor. Rows are reproduced by the deterministic script `scripts/exp_neutrino_mass_interface.py`.

12 Lepton mixing and a neutrino-scale interface

This section extends the bounded-complexity closure program to the lepton sector. We record a minimal, auditable closure for the PMNS mixing angles and provide a corresponding matrix reconstruction in the PDG standard parameterization. Majorana phases do not affect oscillation probabilities and are not constrained by this minimal closure, so we ignore them here [2].

Audit pointer (bounded-family closure). [Audit]The reported PMNS closures are CAP selections within explicitly declared finite candidate families with deterministic tie-break rules; see Appendix H and Appendix G for the audit contract, and Appendix AF and Appendix AE for the enumerations, gaps, and robustness tables.

12.1 PMNS angles as bounded-complexity amplitudes

The bounded-complexity candidate family, the stabilized minimizers, and the associated rigidity/robustness tables are recorded in Appendix AF.

12.2 Matrix reconstruction and a discrete CP-phase closure

The bounded-denominator Dirac-phase selection and the induced PMNS matrix/ unitarity diagnostics are recorded in Appendix AF.

12.3 A minimal neutrino mass-scale interface

At the anchor resolution $(m, n) = (6, 3)$, the mass-spectrum closure of Section 13 anchors scheme-stable charged-lepton scales and treats neutrino absolute masses as an interface input. To express neutrino scales in the same resolution language, we record a deterministic nearest-integer depth assignment for representative minimal-mass normal/inverted orderings inferred from oscillation splittings. We use representative central values for $(\Delta m^2_{21}, |\Delta m^2_{31}|)$ from standard global fits [2, 60].

Remark 12.1 (Status of the neutrino-scale assignment)**.** *The nearest-integer depth assignment in Table 17 is an interface-level bookkeeping device: it expresses commonly quoted oscillation-inferred mass scales in the same additive depth coordinate used elsewhere, without claiming a unique absolute-mass prediction at $(m, n) = (6, 3)$. Any stronger neutrino-mass prediction requires additional physical identification input (e.g. a concrete mass-generation mechanism and threshold/matching conventions) beyond the minimal closure reported in this paper.*

13 Closure: mass spectrum as resolution depth and protocol cost

This section closes the interface by connecting the field-level labeling map (Section 9) to a concrete, reproducible mass-spectrum template. We work with dimensionless ratios relative to the electron reference, and we phrase running/threshold effects in the Fibonacci resolution coordinate of the golden branch.

We use the resolution-depth coordinate and the operational delay/lapse dictionaries recorded in Section 10 and Section Y.

Audit pointer (bounded-family closure). [Audit]The depth template and its integer-coefficient rigidity are CAP closures within explicitly declared bounded families with deterministic tie-break rules; see Appendix H and Appendix G for the audit contract and Appendix AG for the bounded-domain searches, gaps, and robustness diagnostics.

Tick-only interpretation. The closure below is written in the r-coordinate precisely because r is a log-time coordinate: it linearizes multiplicative time-scale ratios. On this view, the predicted depth $\widehat{r}$ is a discrete protocol overhead (in tick-derived units), while the mismatch $\Delta r = r - \widehat{r}$ is a matching-layer time-scale factor (Compton-clock and delay dictionaries; Appendix Y).

13.1 A closed depth assignment from stable-type invariants

Let $w \in X_6$ and recall the intrinsic invariants $(V(w), g(w), D_\pi(w))$ (Definition 8.9). We use the effective protocol depth $r_*(w)$ from Definition 9.9. The folding degeneracy $g(w)$ is the fiber size of the finite projection Fold_6 and therefore measures the intrinsic multiplicity of microstates that share the same stable readout label (Section 6).

Lemma 13.1 (Uniform fiber distribution and residual uncertainty)**.** *Let N be uniformly distributed on $\{0, \dots, 63\}$ and set $W := \mathrm{Fold}_6(N) \in X_6$. Then for each $w \in X_6$ one has*

$$\mathbb{P}(W = w) = \frac{g(w)}{64}, \qquad \mathbb{P}(N = k \mid W = w) = \frac{1}{g(w)} \quad \text{for } k \in \mathrm{Fold}_6^{-1}(w),$$

and the conditional Shannon entropy of N given $W = w$ equals $\log g(w)$ (in nats) [17, 61].

Proof. Immediate from uniformity and Bayes' rule; see, e.g., [17]. □

Remark 13.2 (Protocol depth as a cost coordinate (interface))**.** *Lemma 13.1 makes explicit that $g(w)$ controls the intrinsic residual multiplicity of microstates that share the same stable readout label at $m = 6$. In a scan-based identification dictionary (Axiom 1.1), resolving or compensating such multiplicities across space requires additional protocol resources (extra scan steps, deeper matching, or additional connection data), and therefore fixes the use of $g(w)$ as a discrete cost term in r_* and in the normalized depth* (21)*. The closed quantitative content used for mass matching in this paper is the auditable template* (22) *together with the bounded-complexity rigidity certificate for its integer coefficients (Proposition AG.1). A stronger time/mass matching dictionary based on scattering delay (Wigner–Smith) and relativistic lapse/redshift templates is recorded in Section Y and provides the operational closure used at the matching layer.*

Definition 13.3 (Closed mass template)**.** *Fix the electron reference field $e := e_R^{(1)}$ and let $w_e \in X_6$ denote its stable-type label under $\mathcal{L}_{\mathrm{SM}}$. Define the normalized depth*

$$\widehat{r}(f) := \kappa\big(r_*(w_f) - r_*(w_e)\big) \;+\; \big(|w_f|_1 - |w_e|_1\big) \;+\; \big(g(w_e) - g(w_f)\big), \tag{21}$$

where $w_f \in X_6$ satisfies $\mathcal{L}_{\mathrm{SM}}(w_f) = f$, $\kappa := m/n = 2$ for the balanced coupling at the chosen anchor $(m, n) = (6, 3)$ on the 2D Hilbert screen, $|w|_1$ is Hamming weight, and $g(w)$ is folding degeneracy (Definition 8.9). Then define the closed template mass prediction by

$$\mu_{\mathrm{pred}}(f) := m_e \, \varphi^{\widehat{r}(f)}. \tag{22}$$

Remark 13.4 (Choice of charged-lepton reference)**.** *We take $e := e_R^{(1)}$ as the charged-lepton reference because the three singlet multiplets $\{e_R^{(1)}, e_R^{(2)}, e_R^{(3)}\}$ form a minimal family already present in the field-level labeling closure (Section 9). Since* (21) *uses only depth differences relative to w_e, any global normalization shift is absorbed into the matching-layer depth shift Δr (Section AG.2).*

It is useful to express $\widehat{r}$ directly as a bounded-complexity integer combination of stable-type differences.

Proposition 13.5 (Simplified depth formula)**.** *Let $\Delta V := V(w_f) - V(w_e)$, $\Delta g := g(w_f) - g(w_e)$, and $\Delta|w|_1 := |w_f|_1 - |w_e|_1$. Under Definition 13.3 at $(m, n) = (6, 3)$ one has*

$$\widehat{r}(f) = 2\,\Delta V + 5\,\Delta g + \Delta|w|_1. \tag{23}$$

Proof. By Definition 9.9, $r_*(w) = V(w) + 3(g(w) - 2)$ at $n = 3$. Hence $\kappa(r_*(w_f) - r_*(w_e)) = 2\Delta V + 6\Delta g$. The remaining two correction terms in (21) contribute $\Delta|w|_1 - (\Delta g)$, yielding $2\Delta V + 5\Delta g + \Delta|w|_1$. □

Equation (22) yields a discrete spectrum of reference scales. Threshold and scheme effects are recorded as multiplicative matching factors (equivalently, additive shifts in r) as in effective field theory [1, 2].

13.2 Predicted spectrum and PDG/CODATA comparisons

Table 18 records the closed template values. Standard reference values are listed using PDG and CODATA conventions. For quarks we use a scheme-dependent reference (e.g. $\overline{\mathrm{MS}}$ running masses) and treat scheme dependence as a matching input rather than an integer-depth anchor, consistent with the resolution-map calibration philosophy used in this paper. For neutrinos we record an order-of-magnitude reference scale inferred from oscillation data, but we do not fix a unique absolute mass prediction at this minimal resolution [2, 60]. For W, Z, and H we include the canonical electroweak anchor depths as discrete reference points in the r-coordinate. These bosonic rows are not identified with individual stable types in X_6; they serve as protocol-calibration thresholds for the electroweak interface in the same sense as the Z-scale normalization recorded in Section 11 [2].

Remark 13.6 (Bosonic anchor depths as nearest-integer reference points)**.** *The bosonic anchor depths reported for W, Z, and H are taken as the nearest-integer reference points to $r(\mu) = \log(\mu/m_e)/\log\varphi$ at the corresponding PDG masses. This keeps the bosonic thresholds fully discrete (no continuous fit) while allowing the residual mismatch to be recorded explicitly in the same additive form Δr used elsewhere. The same nearest-depth convention is used in the minimal neutrino-scale interface table (Table 17).*

Scheme dependence and matching inputs. For light quarks, PDG masses are convention-dependent and quoted as running masses in a chosen scheme; even for heavy quarks, perturbative matching and threshold conventions affect the quoted reference values [2]. Accordingly, the extended fermion rows in Table 18 are diagnostic: they record the implied depth mismatch Δr and the corresponding multiplicative matching factor μ/μ_{pred} under the stated reference convention, rather than serving as scheme-independent rigidity anchors.

field	reference μ [GeV]	$r(\mu)$	$\widehat{r}$	$\Delta r := r - \widehat{r}$	μ/μ_{pred}
Anchor scales					
e	5.10999×10^{-4}	0.000	0	0.000	1
μ	0.10565838	11.080	11	0.080	1.03901
τ	1.77686	16.945	17	-0.055	0.973741
W	80.377	24.866	25	-0.134	0.937607
Z	91.1876	25.128	25	0.128	1.06371
H	125.25	25.788	26	-0.212	0.902982
Quark refs (scheme)					
u	0.00216	2.996	6	-3.004	0.235563
d	0.00467	4.598	5	-0.402	0.82406
s	0.093	10.814	12	-1.186	0.565212
c	1.27	16.247	12	4.247	7.71848
b	4.18	18.722	23	-4.278	0.127656
t	172.76	26.456	28	-1.544	0.47574
Neutrino scale					
ν (scale)	5×10^{-11}	-33.540	–	–	–

Table 18: Mass-spectrum closure in the resolution-depth language. The predicted values use the normalized depth (21) (equivalently (23)) together with the exponential map (20). The depth mismatch Δr is additive, while $\mu/\mu_{\mathrm{pred}} = \varphi^{\Delta r}$ is the corresponding multiplicative matching factor. All rows are reproduced by the deterministic script `scripts/exp_mass_spectrum.py`.

Rigidity audits and matching-layer summaries (supplement). Bounded-coefficient rigidity searches, leave-one-out robustness diagnostics, and the quantized matching-layer tables are recorded in Appendix AG.

Audit reading and failure criteria. [Audit]The depth-coefficient closure is anchored on the scheme-stable charged-lepton set $\{\mu, \tau\}$ (Appendix AG.1); quark rows are treated as diagnostic matching inputs under a stated scheme convention rather than as scheme-independent rigidity anchors. Operationally, the closure would be falsified *within its stated hypothesis class* if (i) the bounded-integer minimizer for (a, b, c) were not unique or did not stabilize across modest bound increases, or (ii) the matching-layer residuals required substantially finer denominators than the minimal dyadic quarter-step lattice to be compactly summarized (Appendix AG.2).

Part VI
Dynamics: continuum representatives, free energy, RG, cosmology

Pointer. [Audit]This part is a reader-facing index to the closed continuum representative modules recorded in the appendices; it introduces no additional theorem-level inputs beyond tick and CAP.

- Appendix C: Wish/Motive templates and a generic Lyapunov certificate (reader-facing; not used in proofs).
- Appendix D: semigroup and exponential-kernel notes (arrow-of-time template; reader-facing; not used in proofs).

- Appendix E: Abel finite parts and a resolvent-style unit-disk holomorphy template (reader-facing; not used in proofs).
- Appendix F: holomorphy versus interior poles (pole-barrier rigidity template; reader-facing; not used in proofs).
- Appendix AA: equivalence semantics and a frequency-first dictionary.
- Appendix AB: modular geodesic flow and Gauss-map renormalization (mother-space notes; not used in proofs).
- Appendix AC: Morita equivalence and Fourier exchange (equivalence structures; not used in proofs).
- Appendix AD: Hecke operators and the prime skeleton (cross-scale symmetry template; not used in proofs).
- Appendix AD.4: CAP-closed minimal continuum action skeleton.
- Appendix AD.5: variational field equations (Einstein/Yang–Mills/χ templates).
- Appendix AD.6: thermodynamics from equivalence/coarse graining (entropy/temperature/free energy dictionary).
- Appendix AD.7: overhead/χ to lapse and weak-field gravity closures.
- Appendix AD.8: $\chi(x)$ reconstruction protocol from finite diagnostics.
- Appendix AD.10: quantum readout interfaces and Born-probability rigidity.
- Appendix AD.11: running couplings in the resolution coordinate r.
- Appendix AD.12: cosmology as resolution flow (interface, audited assumptions).
- Appendix Y: unified delay closure and matching-layer dictionaries.

Part VII
Validation and falsifiability (and open closures)

14 Falsifiability: predictions in the protocol language

The folding counts and tables are mathematical-layer facts. The statements below are physical-layer predictions: they can be tested by observational constraints, laboratory bounds, and reproducible protocol-level audits.

Time-first test strategy. In the tick-first dictionary of this paper (Section 3), the primitive input is the sequential update count and the primitive closure rule is CAP. Accordingly, the most direct experimental handles are *time dictionaries*: delay and clock-rate proxies that test the overhead interpretation of mass and scale. For a time-first reading, begin with P6 (scattering delay as a lapse proxy). Predictions P1/P2/P4/P5 are protocol-level structural or rigidity statements that do not require a numerical staircase calibration. Prediction P3 is special: its *threshold locations* depend on the bounded-complexity calibration of r_{step} and the chosen reference anchors, and should therefore be read as a conditional prediction within that calibrated hypothesis class.

14.1 Independent protocol predictions (no staircase calibration required)

14.1.1 P1: right-handed neutrinos as protocol-external / ghost modes

If weak chirality is tied to the Hilbert-protocol orientation bit and its mirror-protocol swap (Definition 7.2), then a neutral singlet ν_R can behave as a protocol-decoupled mode: it can be stable at the level of type labeling while remaining effectively unobservable through the weak compensation connection within a fixed protocol. Operationally, this manifests as an "invisible" or "ghost-like" degree of freedom with extremely suppressed couplings at the readout level [2].

Remark 14.1 (Relation to standard sterile-neutrino extensions)**.** *Gauge-singlet right-handed neutrinos are also the standard minimal extension used in neutrino-mass model building (e.g. seesaw completions of the dimension-five Weinberg operator); see, e.g., [2, 62, 63].*

A concrete interface reason at the chosen 2D anchor (m,n)=(6,3). In the closed labeling map, ν_R carries $(SU(3), SU(2))_Y = (1, 1)_0$ (Table 15), hence is neutral under all three gauge-factor connection classes. In this sense, ν_R is the forced protocol-external candidate within the closed labeling: it can exist as a stable label without participating in the weak $SU(2)$ compensation transport within a fixed protocol.

Relation to the hidden microstates. At $m = 6$, the protocol-unstable complement has size $|\Omega_6 \setminus X_6| = 64 - 21 = 43$. In addition to protocol-decoupling within X_6, a stronger possibility is protocol-instability: if certain degrees of freedom are implemented as readout patterns outside X_6, they reside in this ghost sector and are absent from stable visible outputs.

Data channel. Laboratory sterile-neutrino searches (oscillation anomalies, beta-decay spectral distortions, missing-energy signatures) and cosmological bounds on extra relativistic degrees of freedom provide direct constraints on protocol-decoupled neutral singlets.

Fail condition. Evidence for an unsuppressed weakly coupled right-handed neutrino mode within the same protocol class (i.e. a ν_R that participates in the $SU(2)$ compensation transport comparably to left-handed leptons) would contradict the protocol-external/decoupled identification used here.

14.1.2 P2: chirality-domain defects and large-scale statistical signatures

If early-universe initialization admitted domains with different Hilbert orientation classes, domain boundaries would act as protocol defects. Such defects should leave parity-sensitive statistical signatures (e.g. polarization correlations) tied to the chirality index sign. *Remark:* domain walls as macroscopic defect remnants are standard in symmetry-breaking narratives; see, e.g., [64, 65].

Test strategy. The prediction is protocol-level: one should search for statistics that are invariant under orientation-preserving layout changes but change sign under reflection-like protocol swaps, consistent with Proposition 5.4. Conversely, parity-even observables provide a control: coarse-grained scalars such as those in Definition 8.13 should be coherent across orientation domains up to pullback and should not exhibit an intrinsic sign flip.

Concrete observable channel: CMB parity-odd correlators and cosmic birefringence. A standard parity-sensitive testbed is CMB polarization: the E/B decomposition separates parity-even and parity-odd modes [66, 67]. In statistically isotropic parity-invariant models, the TB and EB cross-correlations vanish (up to foreground/systematics), while a parity-odd

polarization-rotation (cosmic birefringence) angle β mixes E and B and induces nonzero TB/EB with a sign controlled by β [68,69]. In the present protocol language, different Hilbert orientation domains flip $\mathrm{sgn}(\chi)$; therefore any fitted parity-odd estimator whose sign tracks an effective rotation/birefringence sign is expected to flip sign between domains while parity-even control statistics remain coherent up to pullback.

Data channel. CMB polarization (parity-odd TB/EB correlators), cosmic-birefringence estimators, and other large-scale parity-odd correlation searches provide concrete observational channels.

Fail condition. If improved multi-frequency data and systematics-controlled analyses exclude any domain-like sign-flip pattern in parity-odd estimators while the protocol-chirality mapping remains fixed, the chirality-domain defect scenario is disfavored.

14.2 Calibration-dependent staircase prediction (requires a calibrated r_{step})

14.2.1 P3: resolution jumps and Fibonacci-structured spectrum thresholds

At window length m, the admissible stable type count is $|X_m| = F_{m+2}$ (Lemma 4.5). Moreover, the π-channel cyclic/boundary split is itself Fibonacci-rigid: for $m \geq 4$,

$$|X_m^{\mathrm{bdry}}| = F_{m-2}, \qquad |X_m^{\mathrm{cyc}}| = F_{m+2} - F_{m-2}$$

(Proposition 4.8). If effective window length changes with energy or environment, the number of stable types should exhibit threshold behavior constrained by Fibonacci growth rather than arbitrary particle additions.

Collider as an active observer: forced zoom (interface). In this framework, a high-energy collider is not merely a kinetic machine but an information-focusing device. By concentrating energy density into a small interaction region, the experiment can force the local protocol to operate at higher effective resolution and thereby make higher-m structure accessible in readout. Operationally, this corresponds to pushing the local scale across the calibrated thresholds $\mu_{\mathrm{th}}(m)$ so that the deterministic selection $m_{\mathrm{eff}}(\mu)$ jumps (Corollary 14.2). We refer to this experimental act as *active renormalization*: one does not change the theorem-level folding core, but forces the protocol to render latent high-complexity modes that are otherwise inaccessible at the $m = 6$ ground-state readout.

Fibonacci-structured thresholds. Since F_{m+2} obeys $F_{m+2} = F_{m+1} + F_m$, any one-step resolution uplift $m \mapsto m + 1$ admits only a constrained increment of stable type count. This provides a rigid spectral-template prediction: new stable modes, if any, should enter in Fibonacci-structured batches. At the minimal anchor $m = 6$, the split is $18 \oplus 3$; the next two uplifts would yield $29 \oplus 5$ at $m = 7$ and $47 \oplus 8$ at $m = 8$.

A minimal $\mu \leftrightarrow m$ calibration. To compare these discrete uplifts to energy thresholds, we use the golden resolution coordinate already employed in the mass-spectrum closure:

$$r(\mu) = \frac{\log(\mu/m_e)}{\log \varphi}.$$

We record a minimal calibration in which a one-step window uplift $m \mapsto m + 1$ corresponds to a fixed additive depth increment

$$r_{\mathrm{step}} := 2\pi, \qquad r_{\mathrm{th}}(m) := (m - 6)\, r_{\mathrm{step}}, \qquad \mu_{\mathrm{th}}(m) = m_e\, \varphi^{\, r_{\mathrm{th}}(m)}.$$

In this calibration, the threshold for $m = 10$ lies near the electroweak scale ($\mu_{\mathrm{th}}(10) \approx 91\,\mathrm{GeV}$), providing a concrete protocol-level staircase template for where Fibonacci-structured stable-type uplifts may occur. The resulting spectrum template is summarized in Table 2.

Odd steps as bridges between even stability islands (interface). The even steps $m = 6, 8, 10$ are already singled out by the combination of the $m = 6$ coarse-lock anchor and the bounded-complexity staircase calibration: they align the minimal matter anchor (electron), a conservative hadronic-scale reference (QCD onset), and the electroweak layer, respectively. Once this scaffold is fixed, the odd steps are no longer optional: the same staircase necessarily places intermediate thresholds at $m = 7, 9, 11$ (Table 2). This yields three concrete, falsifiable targets for where additional stable-mode structure should concentrate if it arises through resolution uplifts:

- **Prediction 1 (nuclear binding scale):** $m = 7$ corresponds to $\mu_{\mathrm{th}}(7) \sim 10\,\mathrm{MeV}$, near the characteristic nuclear binding scale (few–10 MeV), suggesting an intermediate "binding" information density that can glue $m = 6$ matter-like objects into nuclei without yet requiring the full hadronic confinement structure of $m = 8$.
- **Prediction 2 (bottom onset):** $m = 9$ corresponds to $\mu_{\mathrm{th}}(9) \sim 4.4\,\mathrm{GeV}$, close to the bottom threshold ($m_b \approx 4.18\,\mathrm{GeV}$), marking the staircase onset point for heavy-flavor physics under the fixed calibration [2].
- **Prediction 3 (BSM frontier target):** $m = 11$ corresponds to $\mu_{\mathrm{th}}(11) \sim 1.9\,\mathrm{TeV}$ and provides a protocol-level BSM target at the LHC/FCC frontier: any additional stable modes entering as an effective uplift to $m = 11$ should be constrained by the finite topological capacity $|X_{11}| = 233$ and by the inherited cyclic/boundary split constraints from the π channel.

Corollary 14.2 (Resolution selection by least discrepancy (interface))**.** *Fix $r_{\mathrm{step}} > 0$ and the threshold map $\mu_{\mathrm{th}}(m)$ above. Given an effective energy (or mass) scale μ, define $r(\mu) = \log(\mu/m_e)/\log\varphi$ and select an* effective window length *by the deterministic rule*

$$m_{\mathrm{eff}}(\mu) := 6 + \left\lfloor \frac{r(\mu)}{r_{\mathrm{step}}} \right\rfloor,$$

equivalently: $m_{\mathrm{eff}}(\mu) = m$ if and only if $\mu_{\mathrm{th}}(m) \le \mu < \mu_{\mathrm{th}}(m+1)$. This is the minimal closed selection principle compatible with CAP (Axiom 1.5): window length increases only when the scale crosses a calibrated threshold, and within each band the protocol uses the smallest admissible m.

Remark 14.3 (Why the step size 2π is canonical (interface))**.** *The factor 2π is the canonical period of phase in the unitary scan language (circle normalization), and it is also the canonical normalization that relates horizon surface gravity to Hawking temperature, $T_H = \kappa_{\mathrm{sg}}/(2\pi)$, in the standard semiclassical dictionary [70, 71]. Accordingly, using an additive increment $r_{\mathrm{step}} = 2\pi$ is the minimal-description choice for a dimensionless "one-step" uplift in a protocol depth coordinate. We nevertheless keep it auditable: the bounded family $r_{\mathrm{step}} = k\pi$ is explicitly swept and selected by deterministic objectives (Tables 20–21 and Proposition 14.4).*

A bounded-complexity calibration comparison. To make the choice $r_{\mathrm{step}} = 2\pi$ explicit as a low-complexity calibration, we compare the small candidate family $r_{\mathrm{step}} = k\pi$ for $1 \le k \le 10$ against the single electroweak anchor scale m_Z (PDG), using the template threshold at $m = 10$. Table 20 reports the induced $\mu_{\mathrm{th}}(10)$ and the log mismatch $\log(\mu_{\mathrm{th}}(10)/m_Z)$ for each candidate.

m	$r_{\mathrm{th}}(m)$	$\mu_{\mathrm{th}}(m)$ [GeV]	$\lvert X_m\rvert$	$\lvert X_m^{\mathrm{cyc}}\rvert$	$\lvert X_m^{\mathrm{bdry}}\rvert$	$\Delta\lvert X_m\rvert$
6	0.000	5.10999×10^{-4}	21	18	3	0
7	6.283	0.0105082	34	29	5	13
8	12.566	0.216091	55	47	8	21
9	18.850	4.44369	89	76	13	34
10	25.133	91.3802	144	123	21	55
11	31.416	1879.15	233	199	34	89
12	37.699	3.86428×10^4	377	322	55	144
13	43.982	7.94651×10^5	610	521	89	233
14	50.265	1.63412×10^7	987	843	144	377
15	56.549	3.36041×10^8	1597	1364	233	610
16	62.832	6.91036×10^9	2584	2207	377	987

Table 19: A concrete resolution-uplift staircase template under the minimal calibration $r_{\mathrm{step}} = 2\pi$. The stable-type counts use $\lvert X_m\rvert = F_{m+2}$ and the cyclic/boundary split $\lvert X_m^{\mathrm{bdry}}\rvert = F_{m-2}$ for $m \geq 4$ (Proposition 4.8). Rows are reproduced by the deterministic script `scripts/exp_resolution_thresholds.py`.

candidate r_{step}	r_{step}	$\mu_{\mathrm{th}}(10)$ [GeV]	$\log(\mu_{\mathrm{th}}(10)/m_Z)$	$\lvert\cdot\rvert$
π	3.14159	0.216091	-6.0450	6.0450
2π	**6.28319**	91.3802	**+0.0021**	**0.0021**
3π	9.42478	3.86428×10^4	+6.0492	6.0492
4π	12.5664	1.63412×10^7	+12.0963	12.0963
5π	15.708	6.91036×10^9	+18.1434	18.1434
6π	18.8496	2.92225×10^{12}	+24.1905	24.1905
7π	21.9911	1.23576×10^{15}	+30.2375	30.2375
8π	25.1327	5.22576×10^{17}	+36.2846	36.2846
9π	28.2743	2.20986×10^{20}	+42.3317	42.3317
10π	31.4159	9.34505×10^{22}	+48.3788	48.3788

Table 20: Calibration sweep at $m = 10$ over the bounded family $r_{\mathrm{step}} = k\pi$ $(1 \leq k \leq 10)$, using $m_Z = 91.1876\,\mathrm{GeV}$ as a reference scale. Rows are reproduced by the deterministic script `scripts/exp_resolution_calibration_sweep.py`.

A two-anchor minimax calibration (diagnostic). As an additional diagnostic (still on the physical identification layer), we can calibrate r_{step} against two reference anchors simultaneously: the Z pole mass at $m = 10$ and an order-of-magnitude nonperturbative QCD reference scale $\mu_{\mathrm{QCD}} = 0.2\,\mathrm{GeV}$ at $m = 8$ (a conservative hadronic-scale anchor; see, e.g., [2]). We evaluate the same bounded family $r_{\mathrm{step}} = k\pi$ with a deterministic minimax objective across the anchors. Table 21 reports the resulting mismatches and selects the unique minimizer by lexicographic tie-break rules.

Proposition 14.4 (Bounded-complexity calibration selection of $r_{\mathrm{step}} = 2\pi$)**.** *Within the bounded candidate family $r_{\mathrm{step}} = k\pi$ for $1 \leq k \leq 10$, the calibration $r_{\mathrm{step}} = 2\pi$ is the unique minimizer against the single Z-anchor objective in Table 20. Under the two-anchor minimax objective reported in Table 21, the same choice remains the unique minimizer under the stated deterministic tie-break rules.*

Proof. Finite exhaustive enumeration over the stated candidate family; see the generated tables and the scripts cited in their captions. □

candidate r_{step}	r_{step}	$\mu_{\text{th}}(10)$ [GeV]	$\log(\mu_{\text{th}}(10)/m_Z)$	$\mu_{\text{th}}(8)$ [GeV]	$\log(\mu_{\text{th}}(8)/\mu_{\text{QCD}})$	E_∞	E_1
π	3.14159	0.216091	-6.0450	0.0105082	-2.9462	6.0450	8.9911
2π	**6.28319**	91.3802	**+0.0021**	0.216091	**+0.0774**	**0.0774**	**0.0795**
3π	9.42478	3.86428×10^4	+6.0492	4.44369	+3.1009	6.0492	9.1501
4π	12.5664	1.63412×10^7	+12.0963	91.3802	+6.1245	12.0963	18.2207
5π	15.708	6.91036×10^9	+18.1434	1879.15	+9.1480	18.1434	27.2914
6π	18.8496	2.92225×10^{12}	+24.1905	3.86428×10^4	+12.1716	24.1905	36.3620
7π	21.9911	1.23576×10^{15}	+30.2375	7.94651×10^5	+15.1951	30.2375	45.4326
8π	25.1327	5.22576×10^{17}	+36.2846	1.63412×10^7	+18.2186	36.2846	54.5033
9π	28.2743	2.20986×10^{20}	+42.3317	3.36041×10^8	+21.2422	42.3317	63.5739
10π	31.4159	9.34505×10^{22}	+48.3788	6.91036×10^9	+24.2657	48.3788	72.6445

Table 21: Two-anchor minimax calibration over the bounded family $r_{\text{step}} = k\pi$ ($1 \le k \le 10$), using $m_Z = 91.1876\,\text{GeV}$ and $\mu_{\text{QCD}} = 0.2\,\text{GeV}$ as reference anchors at $m = 10$ and $m = 8$, respectively. Rows are reproduced by the deterministic script `scripts/exp_resolution_calibration_multianchor.py`.

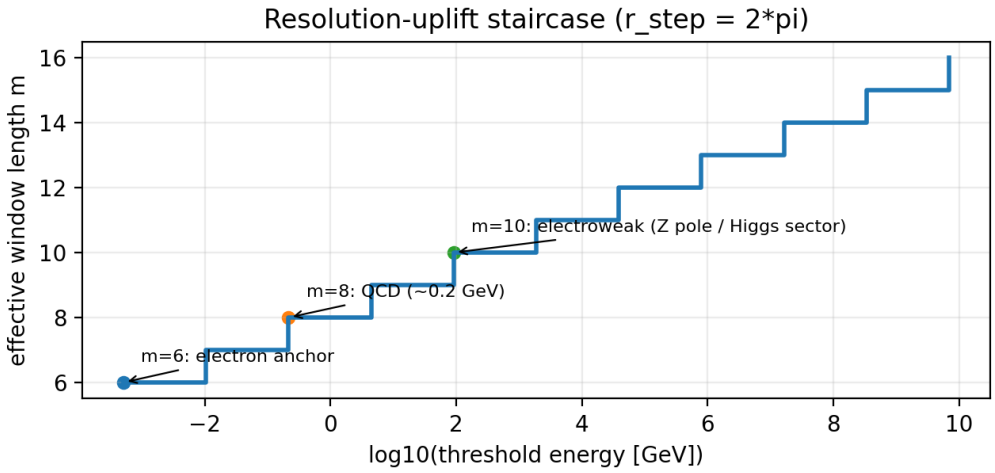

Figure 4: Optional visualization of the staircase $m(\mu)$ under the same calibration, if the figure file is generated.

Why this is not post-hoc tuning. The step size is selected from a small explicit candidate family $r_{\text{step}} = k\pi$ with deterministic objectives and tie-break rules, and the residual mismatches to the reference anchors are reported explicitly in the same log-mismatch language used throughout. Thus the staircase calibration is a discrete audited selection rather than a continuous fit.

Test strategy. The prediction is not that a specific new particle must appear at every $\mu_{\text{th}}(m)$, but that if additional stable modes do appear as effective resolution uplifts, they should enter in Fibonacci-structured batches $\Delta|X_m| = F_m$ and inherit the cyclic/boundary split constraints from the π channel.

Data channel. Collider and fixed-target threshold scans (new stable-mode onsets, heavy-flavor thresholds, and clustering of new phenomena in energy) provide the primary laboratory channels; astrophysical threshold phenomena provide complementary constraints.

Fail condition. Conditional on the stated staircase calibration, the framework is falsified if new stable modes appear in a way that is incompatible with Fibonacci-constrained batch structure across uplifts, or if statistically significant new-mode onsets systematically avoid the

calibrated threshold bands without an alternative calibrated r_{step} explanation within the stated bounded family.

14.3 Independent quantitative rigidity and time-dictionary tests

14.3.1 P4: CP violation magnitude tied to a rigid phase-space volume

If CP violation is controlled by a CP-odd phase space $\mathcal{M}_{\text{CP}}$ with fixed volume and multiplicity as in (85), then CP-odd observables should exhibit rigid low-complexity signatures and constrained drift patterns under protocol deformation.

Numerical rigidity target. Equation (85) provides a concrete normalization target for the CKM Jarlskog invariant: $J_{\text{geo}} = 1/(11\pi^7)$. Any protocol deformation model that claims to explain CP violation should either reproduce this rigidity signal or explain its systematic deviation in a controlled, testable way.

Data channel. Global CKM fits and direct CP-odd observables that determine the Jarlskog invariant under standard conventions provide the primary test channel.

Fail condition. If the experimentally inferred J converges to a value incompatible with the rigid target $1/(11\pi^7)$ under fixed CKM conventions (i.e. the mismatch cannot be represented as a stable matching-layer factor comparable to the other closed normalizations in this paper), the CP-volume normalization dictionary is falsified.

14.3.2 P5: discrete mixing predictions and quantified robustness

Beyond qualitative protocol narratives, the bounded-complexity closures used for CKM and PMNS provide concrete discrete targets: Tables 83–85 record the CKM magnitude closure, the induced PDG-parameter reconstruction, and unitarity diagnostics, while Tables 88–92 record the analogous PMNS closure together with the bounded-denominator Dirac phase selection (Table 90). These are falsifiable as measurement precision improves: the candidate families are finite, the minimizers are unique at the stated bounds, and the mismatches are reported in the same log-norm used across the paper.

Quantified robustness. Appendix AE.7 reports minimizer stability rates under explicit perturbation models for the reference targets (Table 72). This provides an audit-level quantification of how sensitive each discrete prediction is to plausible shifts in the quoted reference values (PDG/global-fit or conservative stress-test scales), and it sharpens the distinction between a rigid discrete selection and a fragile post-hoc match.

Data channel. Precision determinations of CKM/PMNS mixing parameters (magnitudes, angles, and phases) directly test whether the reported minimizers remain the unique best candidates within the stated finite families.

Fail condition. If future measurements shift the reference targets such that, within the same stated bounds, the reported minimizers cease to be unique/stable or are no longer the best candidates in the declared finite families without enlarging the complexity budget, then the low-complexity discrete closure claim fails as stated.

14.3.3 P6: scattering delay as a measurable lapse proxy (interface)

If protocol overhead admits a direct operational proxy in terms of measurable delay, then scattering experiments provide a concrete test channel. In settings where a (nearly) unitary scattering matrix $S(\omega)$ can be measured as a function of frequency, one can compute the Wigner–Smith delay $\tau_{\mathrm{WS}}(\omega) = \mathrm{Tr}(-\mathrm{i}S^{\dagger}\mathrm{d}S/\mathrm{d}\omega)$ [20, 21]. Normalizing by a calibrated tick duration τ_0 yields a dimensionless overhead proxy $\kappa_{\mathrm{WS}} = \tau_{\mathrm{WS}}/\tau_0$ and a lapse proxy $N_{\mathrm{WS}} = \kappa_0/\kappa_{\mathrm{WS}}$ (Section Y). The prediction is that, under any concrete platform identification that ties the measured scattering channel to protocol-local degrees of freedom, delay-derived lapse ratios should behave like redshift/clock-slowing ratios under the same identification, providing an independent falsifiability route for the overhead–lapse dictionary.

Data channel. Platforms with measurable near-unitary scattering matrices (microwave/optical cavities, mesoscopic quantum transport, cold-atom scattering, nuclear/particle scattering phase-shift analyses) provide channels where Wigner–Smith delay can be extracted and compared across controlled conditions.

Fail condition. If delay-derived lapse ratios fail to correlate with independently measured clock-rate/redshift proxies under the same platform identification (beyond stated experimental/systematic uncertainty), the overhead–lapse matching dictionary is disfavored.

14.3.4 P7: γ cross-observation consistency (interface/audit)

Appendix AD.13 records a deterministic, auditable multi-channel estimate of the single parameter γ that appears in the overhead-to-lapse and overhead-to-gravity dictionaries. The intended falsifiability target is not that every channel yields the same point estimate at present precision, but that the same γ is not systematically forced into incompatible values by independent operational proxies once the data protocol and counterfactual baselines are declared.

Data channel. Independent constraints from rotation-curve fits, lensing/delay proxies, and redshift/clock-rate proxies, together with explicit uncertainty and stability sweeps, provide the channel. The paper includes a small vendored audit subset and a deterministic script that generates Table 64, Table 65, and Figure 7.

Fail condition. If, under declared protocol baselines and stated uncertainties, the per-channel $\widehat{\gamma}$ estimates are mutually inconsistent beyond tolerance (e.g. a large χ^2 with negligible p-value and unstable conclusions under counterfactual baseline sweeps), then the single-parameter cross-channel closure claimed by the overhead dictionary is disfavored as stated.

15 Limitations, scope, and relation to prior work

15.1 Mathematical results vs. physical identifications

The paper is organized around an auditable separation (Section 1.4). The folding statements at $(m, n) = (6, 3)$ (e.g. $64 \to 21$ and the $18 \oplus 3$ split) are mathematical-layer results with explicit tables and reproducible scripts. By contrast, the physical identifications (gauge sectors, chirality, antimatter, and CP violation) are recorded as *interface* statements stated in protocol language (e.g. Proposition 8.1, Proposition 8.2, Definition 7.2, Definition 8.7). The finite combinatorics alone is not a Lagrangian; the Standard Model interface is fixed here by explicit closure rules that are stated at the protocol layer and are audited by finite searches. Concretely, the paper provides a rigid finite substrate (X_6 with intrinsic invariants) on which any identification must act, closed auditable interface maps at the level of discrete assignments (e.g. the labeling closure in

Section 9), and falsifiable protocol-level predictions that go beyond post-hoc parameter matching (Section 14). Within the declared protocol class, the remaining selection freedom is closed by deterministic bounded-complexity rules (Definition H.1) and by explicit refinement maps (Appendix V); uniqueness/stability is recorded via rigidity certificates and stabilization tables throughout. Appendix K records the resulting "no-new-input" dependency ledger in a compact audit form, separating theorem-level consequences, finite protocol constructions, conditional interface implications, and bounded-complexity closures.

15.2 On the CAP-selected anchor $(m, n) = (6, 3)$

For the chosen 2D Hilbert readout screen, the balanced coupling condition $m = 2n$ is used to match two independent finite cardinalities: the local readout alphabet size $|\Omega_m| = 2^m$ and the number of sites on the Hilbert-addressed grid 4^n (Section 4.1). This is a diagnostic convention used to attach spatial statistics; it is not a theorem-level necessity for the folding core (Remark 4.3). Other addressing dimensions correspond to $m = dn$ rather than $m = 2n$ (Remark 4.2), and other space-filling curves can be used as alternative readout bases (Remark 5.1). The choice $(m, n) = (6, 3)$ is then the smallest nontrivial instance of this match: $2^6 = 4^3 = 64$. This choice is an *anchor scale* for an auditable finite model, not a claim that the dynamics must select $m = 6$. On the physical identification layer, we record a CAP selection principle for this anchor: within the balanced family on the chosen 2D screen, the smallest pair for which the deterministic holonomy diagnostic becomes nontrivial is $(n, m) = (3, 6)$. Concretely, the balanced-chain sweep in Table 30 shows that $n = 1, 2$ yield only trivial (identity) plaquette holonomy while $n = 3$ is the first scale with nontrivial 3/4-cycle content. This provides a low-complexity interface constraint whose compatibility with uplift and coarse-graining behavior is audited and falsifiable. We partially control parameter sensitivity by recording m-sweeps and balanced refinement chains (Appendix AE and Section 6), which show that several structural counts (Fibonacci admissible sizes, cyclic/boundary split) persist across m. To close the energy↔m interface at the protocol layer, we fix a deterministic staircase selection rule $m_{\mathrm{eff}}(\mu)$ in Corollary 14.2, together with an auditable calibration of the step size r_{step} (Section 14.2.1). At the purely mathematical level, the persistence statements are theorem-level: $|X_m| = F_{m+2}$ and $|X_m^{\mathrm{bdry}}| = F_{m-2}$ for all m (Lemma 4.5 and Proposition 4.8), and the truncation map Fold_m is surjective onto X_m for all $m \geq 1$ (Proposition 4.20).

15.3 Rigidity targets, look-elsewhere context, and counterfactual baselines

Several quantitative statements are presented as low-complexity rigidity targets (Section 11). We do not interpret these as "agreement within experimental error bars" when the reference uncertainties are far smaller than the quoted mismatches (e.g. $\alpha_{\mathrm{em}}^{-1}$), but as matching-layer factors between an idealized closed normalization and scheme/scale-dependent reference conventions. To reduce the risk of numerology, we treat each target as a *bounded-complexity closure* with an explicit finite candidate family and a fully specified tie-break rule (Definition H.1). Appendix AE records audit context beyond point estimates: candidate-domain sizes, second-best gaps, distribution quantiles, stability under target perturbations, and deterministic counterfactual baselines (Tables 70–74). These audits provide look-elsewhere information within stated hypothesis classes; they are not a substitute for a complete statistical analysis over unrestricted expression families.

Error control from protocol outputs to continuum fields. Several falsifiability channels in this paper involve reconstructing a field $\chi(x)$ from discrete protocol statistics (Appendix AD.8) and then applying derivative operators (e.g. $\chi'(r)$ or $\Delta\chi$) to form weak-field observables such as ρ_{eff} (Appendix AD.7). Such steps are intrinsically noise-amplifying: finite differences can trade $O(h^2)$ truncation bias against $O(\epsilon/h)$ or $O(\epsilon/h^2)$ noise amplification, so any empirical use must

declare the discretization/smoothing rules and report stability under explicit counterfactual baselines. Appendix AD.9 records explicit concentration and propagation bounds in a self-contained audit form (see, e.g., standard references [72–74]).

A minimal model-selection interpretation (within stated families). If one treats a candidate family Θ as a discrete hypothesis class equipped with the uniform prior, then the empirical frequency

$$p_{\le\epsilon} := \frac{N_{\le\epsilon}}{|\Theta|}$$

in Table 70 gives the probability that a uniformly random candidate achieves minimax log-mismatch $E_\infty \le \epsilon$. When the minimizer is unique, the probability that a uniformly random candidate matches *as well or better* than the selected minimizer is $1/|\Theta|$. Multiple-comparison adjustments across several simultaneously reported closures can be bounded conservatively (e.g. Bonferroni), but we emphasize that our audit tables are intended to provide transparent within-family look-elsewhere context, not a comprehensive search over unrestricted expression grammars.

15.4 Rigidity constraints and why key interface choices are forced

Some parts of the physical identification layer are not yet derived from CAP beyond the audited finite selection rules recorded here (Section 1.4); nevertheless, at the chosen anchor scale the interface is subject to strong *rigidity constraints* that sharply limit admissible choices. This subsection records, in audit language, the sense in which several design choices are "forced" once one commits to the stated protocol primitives and to minimality.

(i) The (m,n)=(6,3) anchor is CAP-minimal for nontrivial holonomy on the chosen 2D screen (interface). The balanced rule $m = 2n$ is the theorem-level cardinality match specialized to the 2D Hilbert addressing used for the explicit finite diagnostics in this paper, namely $2^m = 4^n$ (Lemma 4.1; see also Remark 4.2 for the d-dimensional general form). On the physical identification layer, we require a closed-loop (plaquette) diagnostic with nontrivial transport, as used in the holonomy constructions of Section 6. Within the balanced chain, Table 30 shows that $n = 1, 2$ produce only identity plaquette holonomy (no 3/4-cycle content), while $n = 3$ is the first scale with nontrivial 3/4 cycles. Thus $(n, m) = (3, 6)$ is selected as the minimal balanced holonomy anchor for the non-abelian holonomy diagnostic on the chosen screen. Other addressing dimensions would select different balanced relations $m = dn$ (Remark 4.2 and Remark 5.1). This is the precise sense in which the anchor is not arbitrary within the declared protocol choices: it is the meeting point of the scan-bit budget, the chosen screen/dihedral audit structure, and the minimal closed-loop diagnostic requirement.

(ii) The $18 \oplus 3$ split forces a minimal chiral/gauge allocation at $m = 6$. The π-channel induces a canonical cyclic/boundary split $X_6^{\mathrm{cyc}} \oplus X_6^{\mathrm{bdry}}$ with sizes $18 \oplus 3$ (Proposition 4.9). If one insists that boundary types represent gauge-factor connection classes while cyclic types represent matter multiplets (Proposition 8.2 and Definition 8.7), then the minimal chiral content compatible with three generations is rigidly constrained by cardinality. Closing 18 cyclic labels with the smallest anomaly-neutral extension forces the addition of ν_R with $Y = 0$ (Proposition 9.6), because any charged extension would require further compensating matter by standard anomaly constraints.

(iii) The three boundary labels admit a unique monotone gauge-factor assignment. The boundary set has exactly three elements with distinct intrinsic values $V(w)$ (Corollary 4.9). The gauge factors $\{U(1), SU(2), SU(3)\}$ have distinct Lie-algebra dimensions $1, 3, 8$

knob / input	meaning	status in this paper	where audited
m (window length)	readout resolution / admissible alphabet	anchor $m = 6$; m-sweeps and refinement chains recorded	Appendix AE (Tables 66–68)
n (Hilbert order)	addressing resolution	anchor $n = 3$ for the chosen 2D screen (via $m = 2n$); chirality sweep recorded	Table 69
B (closure budget)	finite search radius for bounded-complexity closures	reported as a sweep; stabilization is recorded when it occurs	e.g. Tables 76, 77, 82, 87, 94
Q (phase-denominator cap)	bounded rational-angle candidate family for δ	reported as a sweep $Q = 1, \ldots, 12$	Table 90
denom $= 2^p$	dyadic phase register for holonomy diagnostics	CAP-audited bounded family (phase-lift dictionary)	Section 6 and associated scripts
reference conventions	PDG/CODATA targets and scheme conventions	explicit inputs (not fit); mismatch interpreted at matching layer	Table 16 and `scripts/common_constants.py`
quark mass scheme	$\overline{\text{MS}}$/threshold conventions for quark references	treated as matching input (diagnostic rows)	Remark 13.6 and Table 18
NO/IO choice	neutrino mass ordering used for reference targets	treated as external input; sensitivity diagnostics recorded	Table 17 and Table 89
orientation class	discrete protocol initialization (mirror) via $\text{sgn}(\chi)$	not a continuous parameter; flips under mirror protocols	Definition 7.2 and Definition 7.7

Table 22: Explicit "knobs" and inputs used in the protocol/interface layer. The purpose of this table is to make clear that the paper does not hide continuous degrees of freedom: the remaining choices are either fixed by declared primitives, treated as explicit matching inputs, or audited by finite sweeps with recorded stabilization.

(Lemma 9.3). Among the $3! = 6$ possible assignments, the monotonicity requirement "larger intrinsic boundary value $\leftrightarrow$ larger gauge-sector complexity" selects a unique assignment (Theorem 9.17). This eliminates a common source of post-hoc freedom.

(iv) The mass-depth template is rigid within the minimal invariant language. At $(m, n) = (6, 3)$, the intrinsic stable-type invariants available for all $w \in X_6$ are discrete and low-entropy: $(V(w), g(w), |w|_1, D_\pi(w))$ with $V \in \{0, \ldots, 20\}$ and $g \in \{2, 3, 4\}$ (Definition 8.9). Requiring that a depth assignment be built only from these invariants and be auditable as a bounded-integer closure leads naturally to the integer ansatz (89), whose coefficients are rigidly selected as $(2, 5, 1)$ under the stated objective and tie-break rules (Proposition AG.1). This is the precise, checkable meaning of "mass is forced by rigidity" within the declared hypothesis class.

(v) Phase registers and holonomy diagnostics are closed in CAP audit form. The dyadic phase-register family $\mathbb{Z}_{2^p}$ enters only through the finite phase-lift dictionary: the phase denominator denom $= 2^p$ and the low-complexity index-map family τ are fixed as explicit bounded candidate sets, and their influence is audited by deterministic sweeps (Section 6 and Appendix AE). Thus, although the holonomy diagnostics are physical-layer constructs, they are *not* free-form: the permitted choices are enumerated, tie-breaks are explicit, and sensitivity is reported.

15.5 Status of the channel-to-gauge identification and anomaly constraints

The strongest theorem-level statements in the paper are finite combinatorial and operator facts about admissibility and projection (Sections 2 and 4). The mapping from the three stability channels to the Standard Model gauge factors is an *interface closure* (Proposition 8.2): it is CAP-minimal within explicit compactness and factorization assumptions, but it is not used as a premise for the theorem-level folding core. What the present paper supplies at the technical level is: (i) a closed, computable labeling of the 21 stable types into 18 fermion multiplets and 3 gauge-factor classes (Section 9), (ii) explicit finite connection/holonomy diagnostics that realize a non-abelian transport structure at minimal resolution (Section 6), and (iii) audit-level consistency checks against standard constraints such as anomaly cancellation and hypercharge sum rules (Lemma 8.8 and Proposition 9.6). In this framework, anomaly cancellation is treated as a non-negotiable interface consistency requirement: any candidate identification of X_6 with chiral matter must satisfy the standard anomaly sums [1,2]. Appendix W further records inverse diagnostics that probe to what extent quantum-number patterns can be recovered from intrinsic invariants by bounded-complexity rules (not used as premises).

Scalar sectors and symmetry breaking. The present paper closes a minimal *chiral* labeling interface at $(m, n) = (6, 3)$ and does not provide a stable-type label for the Higgs doublet

(Remark 9.1). When a renormalizable EFT embedding is recorded, the Higgs is introduced as an additional field (Appendix T). The corresponding scalar-sector closure in protocol language (parity-even scalar observables by coarse graining/uplift, together with a standard EFT coupling dictionary) is recorded in Proposition 8.12.

15.6 Scheme dependence and renormalization-group flow

Several reported quantities are scheme and scale dependent (e.g. $\alpha(\mu)$ and $\sin^2\theta_W(\mu)$), and the paper therefore treats deviations as matching-layer effects rather than as direct "within-error" claims (Section 11 and Section 13). At present, the paper does not derive Standard Model β-functions from the finite combinatorics. Instead, standard one-loop running is used only as an interpretive dictionary: an additive mismatch in α^{-1} corresponds to a logarithmic scale shift (Remark AF.18). The intrinsic protocol flow law used in this paper is fixed explicitly as a discrete uplift/coarse-graining flow together with the RG dictionary in the Fibonacci resolution coordinate (Definition 8.16 and Proposition 8.17).

15.7 Open problems (audit-tagged)

The following items are *not* closed by the present paper's theorem-level folding core and are recorded as explicit open problems. Each item identifies where the gap enters, what additional input would be required to close it, and what would count as a satisfactory closure. Appendix K mirrors these as **[Open]** items.

(OP1) Gauge-group uniqueness beyond the stated candidate family. The paper closes a *conditional* gauge-factor identification by CAP within an explicit compact three-factor family (Proposition 8.2). What remains open is deriving the *candidate family itself* (compactness, factorization into three commuting redundancies, and the complexity label) from a deeper microscopic scan/readout architecture, and proving uniqueness without relying on a hand-declared bounded family. Within the stated family, the particular choice of common low-complexity labels is less fragile than it may appear: Appendix AI shows the minimizer persists under several alternative labels in a bounded sweep, and Proposition AI.1 gives a short classification-based reason for this robustness for the most natural labels. Closing this would require either: (i) a theorem-level derivation that any admissible local redundancy group must lie in the stated family under the tick-only primitives, or (ii) a universality theorem showing that alternative admissible redundancy realizations coarse-grain to the same effective gauge triple.

(OP2) Uniqueness/inevitability of the folding map family. The truncation map Fold_m used here is an explicit, deterministic bridge from dyadic indices to Zeckendorf-admissible digits (Definition (14) and Remark 4.13). Appendix Q shows that alternative deterministic dyadic$\to X_m$ bridges exist and can change fiber statistics. Within the bounded counterfactual family audited there, the additional natural fixed-point constraint $F(V(w)) = w$ for all $w \in X_6$ selects the Zeckendorf-truncation map uniquely (Proposition Q.2); this is a partial closure inside the audited family. More generally, within the natural shifted Zeckendorf-window family $\mathrm{Fold}_m^{(s)}$ (Definition 4.21), the same value-consistency condition forbids all nonzero shifts and selects the unshifted digit window (Proposition 4.23). What remains open is a principled selection theorem: either derive Fold_m as uniquely forced by tick + CAP under a stated notion of protocol locality/implementability, or prove an (ε, δ)-universality statement that makes low-resolution predictions insensitive to the choice of bridge.

(OP3) Continuum Yang–Mills/EFT emergence from the finite connection. The paper constructs a fully finite non-abelian transport/holonomy diagnostic at $(m, n) = (6, 3)$ (Section 6), but it does not derive the continuum Yang–Mills action or renormalizable EFT dynamics

from this finite skeleton. Closing this would require a controlled continuum limit/renormalization argument: showing that a family of finite protocols (increasing m with suitable coarse graining) converges to a local gauge field theory with the correct degrees of freedom, and that the observed couplings/mixing data arise as stable low-energy parameters.

(OP4) Global model-selection / look-elsewhere control across families. Within each stated bounded candidate family, the paper records full audit context (domain sizes, gaps, counterfactual baselines) (Appendix AE and Tables 70–74). What remains open is a theory-level prior/description-length principle that compares *different* candidate families fairly (e.g. different invariant sets, different expression grammars, different complexity labels), and quantifies the overall look-elsewhere effect. Closing this would require an explicit global prior (or MDL-style penalty) and a combined evidence calculation across closures.

(OP5) Scalar/Yukawa sector and RG-running closure. At the anchor, the stable-type contract closes a minimal chiral labeling and does not allocate a primitive stable label to the Higgs (Remark 9.1); scalar behavior is treated as uplift/coarse-graining dependent (Appendix AH). The paper also does not derive SM β-functions from the finite combinatorics (above). Closing the full Standard Model would require a protocol-level mechanism that generates scalar/Yukawa structures and reproduces RG flow, including scheme/threshold conventions as explicit matching-layer outputs rather than inputs.

15.8 Falsifiability beyond parameter matching

While parts of the quantitative interface are expressed as parameter targets, the paper also records nontrivial protocol-level predictions that are not reducible to retrodictive matching: chirality-domain defects and parity-odd statistical signatures (Section 14.1.2), Fibonacci-structured resolution-threshold batches (Section 14.2.1), and a finite holonomy diagnostic program that produces distributional outputs rather than a single fitted number (Section 6). Each prediction is accompanied by an explicit observable channel in standard language: mixing and CP observables are compared directly to PDG/global-fit targets (Sections 11 and 12), resolution uplifts are tied to energy thresholds by the calibrated staircase and the deterministic map $m_{\mathrm{eff}}(\mu)$ (Corollary 14.2), and delay/lapse proxies are expressed via Wigner–Smith and GR reference dictionaries (Section Y).

15.9 Role of the e-channel at minimal resolution

At $m = 6$, admissibility is already enforced by the φ-grammar and the π-split, so the e-channel is not used to further reduce X_6 (Remark 4.12). Its technical role at minimal resolution is to fix a standard analytic stability template (Artin–Mazur zeta, Abel normalization) and thereby fix the use of an Abel/pole-barrier viewpoint when defining resolution-flow coordinates and exponentially small weights. At higher resolution, weighted/pressure-like variants can make the analytic channel genuinely constraining beyond a single forbidden-word predicate.

15.10 Self-containment within the declared input set

This paper is written to be closed under its declared protocol primitives and interface inputs (Table 25 and Appendix K). For audit clarity, we emphasize that no theorem-level results are imported from companion manuscripts: every protocol primitive and every finite closure used here is defined explicitly in the main text and appendices, and all tables are reproduced by deterministic scripts (Appendix AJ).

For reader navigation, the following table indicates where the main components that may also appear in companion manuscripts are located *inside this paper*:

topic (in this paper)	where it is closed and audited here
scan orbit, window projection, Weyl-pair viewpoint	Sections 2.1 and 2.2; Appendix B
phase registers $\mathbb{Z}_{2^P}$ and $\mathbb{Z}_{128}$ label	Section 1.8; Section 6.5; Appendix B
folding core and uplift template (φ–π–e)	Sections 4 and 4.5; Appendix AE and Appendix V
CAP as bounded-complexity closure with deterministic tie-breaks	Axiom 1.5 and Definition H.1; Appendix H
connection/holonomy finite diagnostics	Section 6; Appendix AE
closed normalizations and rigidity audits (α, $\sin^2\theta_W$, J)	Section 11; Appendix AE
time/mass delay dictionaries (matching layer)	Section Y

Table 23: Internal closure map: where the main protocol ingredients and audit templates are contained within this paper.

Companion manuscripts in the same repository remain useful as extended context and alternative presentations [3–11], but they are not required to follow the finite constructions and audited closures in the present paper.

15.11 Related discrete approaches and standard constraints

Several mature lines of work share the broad goal of extracting continuum physics from discrete or finite data: classical and quantum lattice gauge theory [42,43,54], quantum cellular automata models for relativistic equations [75], and causal-set approaches to discrete spacetime structure [76]. More recently, tensor-network and holographic-code frameworks provide discrete models in which geometry, error correction, and coarse graining are structurally linked [77–79]. The present work differs in emphasis: it treats *finite readout* (window projection plus protocol audit) as the primitive, and records explicit finite invariants and closure rules at a minimal scale. On the combinatorics/number-theory side, there is also a large literature on generalized Zeckendorf decompositions, digit statistics, and structural classifications beyond the classical Fibonacci case; see, e.g., [33–35].

On the Standard Model side, the interface claims are constrained by standard consistency requirements such as anomaly cancellation and scheme/scale dependence (Sections 9 and 13). For modern high-precision discussions of scheme conventions and the extraction of Standard Model parameters in a fixed $\overline{\text{MS}}$ prescription, see, e.g., [80]. For CP-violation constraints beyond mixing observables, electric-dipole-moment bounds provide an important complementary diagnostic; see, e.g., [81]. For modern treatments of flavor invariants in extended Standard Model settings, see, e.g., [82]. For electroweak mixing, it is also useful to keep in view the standard grand-unification benchmark $\sin^2\theta_W = 3/8$ at a unification scale in minimal $SU(5)$-type models [83, 84]. Our electroweak targets are stated at the Z scale and are interpreted as matching-layer normalizations rather than unification-scale relations.

Open closures (ledger-aligned; not used in proofs)

[Audit]The authoritative compact list of open problems is recorded in Appendix K.7 (within Appendix K). For discussion and pointers, see Section 15.7 and Appendix AK.

- [Audit]Gauge-group uniqueness beyond the stated bounded family.
- [Audit]Uniqueness/inevitability of the folding map beyond bounded counterfactual families.
- [Audit]Continuum Yang–Mills/EFT emergence from finite connections.
- [Audit]Global model selection / look-elsewhere across families.

- [Audit]Scalar/Yukawa sector and RG-running closure from the finite protocol.

16 Conclusion

We proposed a tick-first reformulation of Standard Model structure within the HPA scan–projection paradigm. In this framing, the only primitives are time as tick (scan iteration count) and CAP as the bounded-complexity closure rule, while finite observability appears through window projection and stability filtering (Section 3 and Section 2). At the CAP-selected anchor on the chosen 2D screen, $(m, n) = (6, 3)$, the provable folding core at $m = 6$ compresses 64 microstates to 21 stable types with a canonical $18 \oplus 3$ cyclic/boundary split (Section 4). Locality language is then introduced as a derived display structure by an addressing basis, whose minimality at the anchor is made explicit and auditable (Table 5). On the physical identification layer, we recorded interface hypotheses: gauge fields as defect-compensating connections; chirality as protocol selection among orientation classes; antimatter as conjugate readout under scan reversal; and mass/scale as time dictionaries in a Fibonacci log-time coordinate. We provided auditable scripts and generated tables that reproduce the finite folding statistics, the addressing and chirality diagnostics, and the quantitative closures, and we stated falsifiable predictions formulated directly in the protocol language (Section 14). In addition, we closed two main interface components at $(m, n) = (6, 3)$: a unique field-level labeling of the 21 stable types, and a closed mass-spectrum depth formula with a bounded-complexity rigidity signal.

Summary.

- **Theorem-level anchor.** At $(m, n) = (6, 3)$ the folding core yields $64 \to 21$ and the canonical split $21 = 18 \oplus 3$ (Section 4).
- **Closed interfaces.** We close a unique SM labeling map $\mathcal{L}_{\mathrm{SM}}$ (Theorem 9.17) and a closed mass-depth template (Definition 13.3, Table 18).
- **Audited normalizations and mixing.** Coupling/CP targets and mixing closures are recorded as bounded-complexity CAP selections with explicit audits (Section 11 and Appendix AF).
- **Falsifiability.** Protocol-level predictions and test channels are summarized in Section 14.
- **Ledger.** A compact dependency and input ledger is recorded in Appendix K.

Closing (interface shorthand). [Interface]In the tick-first framing, time is the update count, space is a derived addressing/locality dictionary, and matter/scale are protocol-stability and overhead dictionaries anchored at $m = 6$.

Part VIII
Recursive closure: self-read/write, active renormalization, Wish update

17 Final synthesis: self-readout, active renormalization, and latency unification (interface)

[Interface]This section closes, at the protocol interface, the apparent tension between scan-first language (Axiom 1.1) and the experimental fact that high-energy structure is accessed by engineered devices such as colliders.

A tick-first recap. The only primitive input in the present framing is the tick (scan iteration count), and the only primitive closure rule is CAP. Space is a derived display graph induced by an addressing basis, and at the minimal anchor the addressing choice is made explicit and auditable (Table 5). Mass and scale are time dictionaries in a Fibonacci log-time coordinate, with operational test channels through delay and lapse proxies (Section 10 and Appendix Y).

17.1 Observer as a self-read/write head

In the present framework, an "observer" is not identified with a human subject. Operationally, an observer is any interacting subsystem that (i) couples to the readout stream and (ii) induces a stable, auditable record in a chosen locality dictionary. In this sense, observation is not an external act imposed on a passive substrate: it is a protocol event realized by interaction. This is consistent with the layered audit rule stated in Section 1.1: theorem-level folding statements are static finite facts, while "measurement language" belongs to the physical identification layer.

The slogan "self-read/write head" summarizes the consequence: once interaction is treated as readout, the universe contains its own read/write events. Local subsystems act as read heads for each other whenever they exchange constraints, because the very notion of a recorded outcome is the existence of a stabilized readout relation.

17.2 Colliders as forced zoom: active renormalization

In the same protocol language, a collider is an engineered way to concentrate energy density and thereby force a localized transition in effective resolution. The relevant object is not a literal creation of new ontic degrees of freedom, but a change in the local readout budget: as the interaction region is driven across calibrated thresholds, the deterministic selection of the effective window length jumps (Corollary 14.2). This is why high-energy physics can be phrased as an act of *active renormalization* (Section 14.2.1): the experiment forces the protocol to render latent high-complexity structure that is otherwise inaccessible at the $m = 6$ ground-state readout.

On this viewpoint, "new particles" are not imported as new axioms of the mathematical layer. They correspond to stable-mode capacity made available by a resolution uplift in the same folding framework (Section 4), together with the chosen matching dictionary that connects the protocol depth coordinate to laboratory scales.

17.3 Latency unification: micro delay and macro lapse

The same interface dictionary also unifies two operational notions of "time slowing" as a single phenomenon of overhead. At the micro level, delay can be measured directly in scattering as a Wigner–Smith time delay (Section Y). At the macro level, time dilation is encoded by a lapse factor and redshift relations in the standard GR dictionary (Appendix Z). In the protocol interpretation, both are instances of a local overhead field κ and its associated clock-rate factor $N = \kappa_0/\kappa$ (Section Y.4).

This provides a concrete closing of the "mass as latency" interface: the same obstruction/complexity that increases stabilization overhead in the readout (depth, degeneracy, matching shifts) also induces operational delays (scattering) and reduced effective clock rates (lapse/redshift) when translated into standard measurement language.

Wish update (programmatic; not used in proofs)

[Audit]The paper's closed finite invariants and audited interface closures can be read programmatically as updating the admissible target set of protocol-stable data ("Wish") and the corresponding audit objective ("Motive"). This programmatic loop is recorded as a forward-looking

interface statement and is not used as a premise in theorem-level proofs. For a compact list of open closures and next-step audits, see Appendix AK.

Interpretive unification: complex exponentials and unitary spheres (not used in proofs)

[Audit]The following remarks provide a compact unifying language for three interface themes that appear separately in the paper: (i) memoryless semigroup weights (arrow of update time), (ii) phase/frequency-first dictionaries (unitary rotations), and (iii) screen-based renderings of the tick stream. None of this material is used as a premise in theorem-level proofs.

Real versus imaginary exponents. For parameters $\lambda \in \mathbb{R}$ and $\omega \in \mathbb{R}$, the complex exponential splits as

$$\mathrm{e}^{(\lambda+\mathrm{i}\omega)t} = \mathrm{e}^{\lambda t}\,\mathrm{e}^{\mathrm{i}\omega t}.$$

[Audit]In the protocol language, the real factor $\mathrm{e}^{\lambda t}$ is the canonical continuous representative of a memoryless semigroup weight (Appendix D), while the phase factor $\mathrm{e}^{\mathrm{i}\omega t}$ is the canonical representative of a unitary rotation at frequency ω (Appendix AD.10).

Unitary spheres as a representation choice. In the standard quantum interface, states may be represented as unit vectors in a complex Hilbert space, so unitary evolution preserves the norm and acts as a trajectory on the unit sphere. [Audit]We use this only as a compact language for the readout/POVM interface; we do not promote "the universe is literally a Hilbert sphere" to an additional axiom.

Scan trajectories and additional assumptions. Visual renderings of the tick stream on a screen (e.g. Section 5 and the golden-angle phyllotaxis overlay in Part II) can suggest intuitive statements about uniform coverage or ergodicity. [Audit]Any claim of density/ergodicity requires additional dynamical assumptions and is outside the closed folding chain; such statements, if used, must be recorded explicitly as [Audit]or as [Open] in Appendix K.

A Symbols and objects (summary)

This appendix records a compact list of the primary objects used in the paper.

- **Weyl pair.** A pair of unitaries (U, V) satisfying $UV = \mathrm{e}^{2\pi\mathrm{i}\alpha}VU$ (Definition B.1), used as an algebraic encoding of scan shift and phase.
- **Rotation algebra and Morita equivalence (optional notes).** The rotation algebra A_α is the C^*-algebra generated by a Weyl pair at irrational slope $\alpha \in \mathbb{R} \setminus \mathbb{Q}$. Morita equivalence classes are acted on by $\mathrm{SL}_2(\mathbb{Z})$ via $\alpha \mapsto (a\alpha+b)/(c\alpha+d)$; a Fourier transform exchanges scan shift and phase multiplication (Appendix AC).
- **Scan orbit.** Given an irrational slope α and seed $x_0 \in \mathbb{R}/\mathbb{Z}$,

$$x_n = x_0 + n\alpha \pmod 1, \qquad z_n = \mathrm{e}^{2\pi\mathrm{i}x_n} \in \mathbb{T}.$$

- **Window readout.** For a window $W \subset \mathbb{T}$,

$$w_n = \mathbf{1}\{z_n \in W\} \in \{0, 1\}.$$

- **Finite windows.** At window length m, $\Omega_m = \{0,1\}^m$ is the microstate alphabet, and $\mathcal{H}_m = \ell^2(\Omega_m)$ its linearization.

- **Wish and Motive (reader-facing; not used in proofs).** Appendix C records a template interface object $W = (m, \mathcal{I}_m, \mathcal{C}_m, \varepsilon)$ (Wish), a finite candidate family $\mathcal{F}$, an auditable objective functional $J : \mathcal{F} \to \mathbb{R}$ (Motive), and the CAP-selected minimizer $f_\star = \arg\min_{\mathcal{F}} J$ with deterministic tie-break rules.
- **Zeckendorf admissible set.** $X_m \subset \Omega_m$ is the forbidden-word admissible set (no adjacent ones), equivalently the φ-stable sector.
- **Golden base.** $\varphi = (1 + \sqrt{5})/2$ and $\log_\varphi x := \log x / \log \varphi$.
- **Resolution coordinate and exponential map.** For a mass scale μ, $r(\mu) = \log_\varphi(\mu/m_e)$ and $\mu(r) = m_e \varphi^r$ (Section 13).
- **Stable-type invariants at $(m, n) = (6, 3)$.** For $w \in X_6$, $V(w)$ is the Zeckendorf value, $|w|_1$ is Hamming weight, $g(w) = |\mathrm{Fold}_6^{-1}(w)|$ is the folding degeneracy, and $D_\pi(w)$ is the cyclic/boundary tag (Definition 8.9).
- **Depth and matching shifts.** $r_*(w) = V(w) + n(g(w) - 2)$ at $(m, n) = (6, 3)$ (Definition 9.9); the normalized depth $\widehat{r}$ and mismatch $\Delta r = r - \widehat{r}$ are defined in Section 13.
- **Defect channels.** D_φ detects the forbidden substring "11"; D_π detects cyclic wrap-around violation $w_1 = w_m = 1$; the e-channel is expressed via the normalized zeta function $\zeta_{\mathrm{e}}(r) = \zeta(r/\varphi)$.
- **Dyadic phase registers.** Phases are modeled by $\mathbb{Z}_{2^p}$ with the embedding $k \mapsto \mathrm{e}^{2\pi \mathrm{i} k/2^p}$ (Appendix B); $\mathbb{Z}_{128}$ is the baseline choice at $p = 7$ (Section 1.8).
- **Abel path and pole barrier.** An Abel-normalized sum is $F(\rho) = \sum_{n \geq 0} a_n \rho^n$ with the Abel path $\rho \uparrow 1$ (Definition B.3); the first singularity that obstructs analytic continuation along this path is the pole barrier (Appendix B and Section 4.5).
- **Abel finite part.** If an Abel generating function admits an expansion $c_{-1}/(1-r) + c_0 + \cdots$ as $r \uparrow 1$, the Abel finite part is the constant term $\mathrm{FP}_{r\uparrow 1}(\cdot) = c_0$ (Appendix E).
- **Folding map.** Fold_m maps integers (microstate indices) to stable types by Zeckendorf digits and truncation; Fold_6 gives the $64 \to 21$ stable projection.
- **Hilbert addressing.** $H_n : \{0, \ldots, 4^n - 1\} \to \{0, \ldots, 2^n - 1\}^2$ is a locality-preserving address map with a dihedral layout family D_4.
- **Hilbert chirality index.** For the Hilbert path points $p_k = H_n(k)$, χ is the net signed turning index defined by (15).
- **Compton clock dictionary (matching layer).** $\omega_C(\mu) = \mu c^2/\hbar$ and $\tau_C(\mu) = 1/\omega_C(\mu)$ (Section Y).
- **Frequency (tick units).** $\omega = \Delta\theta/\Delta t$ denotes phase advance per tick (Definition AA.1); this is the primary ratio-level bridge to energy/mass/temperature in the frequency-first closure (Appendix AA).
- **Wigner–Smith delay (operational proxy).** $Q(\omega) = -\mathrm{i}\, S(\omega)^\dagger \mathrm{d}S/\mathrm{d}\omega$ and $\tau_{\mathrm{WS}}(\omega) = \mathrm{Tr} Q(\omega)$ (Section Y).
- **Continuum representative (CAP-closed).** S_{eff} denotes the CAP-selected continuum action skeleton (Appendix AD.4); varying it yields Einstein–Yang–Mills–χ equations (Appendix AD.5).

- **Overhead, χ, and lapse.** $\kappa(x)$ denotes a local overhead and $\chi(x) = \log(\kappa/\kappa_0)$; $N(x) = \mathrm{e}^{-\gamma\chi(x)}$ is the lapse proxy in the overhead-to-gravity closure (Appendix AD.7).
- **χ reconstruction protocol.** An executable Hilbert-binning $\to$ window-word $\to$ folding-statistics pipeline reconstructs $\chi(x)$ from data/simulations (Appendix AD.8).
- **Born probabilities (quantum readout).** Finite-resolution readout is modeled by POVMs with probabilities $P_k = \mathrm{Tr}(\rho E_k)$ and instrument updates in Kraus form (Appendix AD.10).
- **RG in the r coordinate.** Running in scale is expressed in r by $\mathrm{d}g/\mathrm{d}r = (\log\varphi)\beta(g)$ (Appendix AD.11).
- **Cosmology as resolution flow.** Stable/hidden fractions are $f_{\mathrm{stab}}(m) = F_{m+2}/2^m$ and $f_{\mathrm{hid}}(m) = 1 - f_{\mathrm{stab}}(m)$; mean degeneracy is $d_m = 2^m/F_{m+2}$ (Appendix AD.12).
- **Gauss map (optional mother-space notes).** The Gauss map is $G(\xi) = \{1/\xi\}$ on $(0, 1)$; its invariant Gauss measure and digit law provide a canonical dynamical source for continued fractions (Appendix AB).
- **Hecke operators and prime skeleton (optional notes).** Hecke operators T_n act on modular forms and satisfy multiplicative relations and prime-power recursions; primes generate the Hecke algebra and Euler products factorize into prime local factors (Appendix AD).
- **Thermodynamic closure objects.** S denotes a coarse-grained entropy (state-count/channel-count); T is the conjugate temperature scale; $\mathcal{F} = E - TS$ is a free-energy functional used in CAP closure form (Appendix AD.6).
- **Black-hole scales (external targets).** $R_s = 2GM/c^2$, $A = 4\pi R_s^2$, $\ell_P^2 = G\hbar/c^3$, and $S_{\mathrm{BH}} = k_B A/(4\ell_P^2)$; T_H denotes the Hawking temperature (Appendix X).
- **Isotropic radius and inversion (external template).** For Schwarzschild exterior geometry, $\rho > 0$ denotes the isotropic radius with throat radius $\rho_h = R_s/4$ and inversion $\mathcal{I}(\rho) = \rho_h^2/\rho$ (Proposition X.6).
- **Wormhole-like pointer jump (protocol-level).** A directed (or undirected) pointer link $a \xrightarrow{\mathrm{ptr}} b$ on the scan index set defines a wormhole-like shortcut channel in the readout protocol (Definition X.7).

B Protocol primitives and regularization conventions

This appendix records, in one place, a compact set of protocol primitives and analytic conventions that are used throughout the paper. It introduces *no new axioms or assumptions* beyond the declared input set in the main text; it only restates standard definitions and short supporting lemmas.

B.1 A Weyl pair viewpoint for scan dynamics

The scan orbit $x_n = x_0 + n\alpha \pmod 1$ can be encoded algebraically by a Weyl pair. One convenient realization is on $L^2(\mathbb{T})$ with the shift and multiplication operators.

Definition B.1 (Weyl pair)**.** *Fix $\alpha \in \mathbb{R}$. A* Weyl pair *is a pair of unitary operators (U, V) satisfying*

$$UV = \mathrm{e}^{2\pi\mathrm{i}\alpha}\, VU.$$

Remark B.2 (A canonical realization)**.** *On $L^2(\mathbb{T})$ with coordinate $x \in \mathbb{R}/\mathbb{Z}$, define*

$$(Uf)(x) := f(x+\alpha), \qquad (Vf)(x) := \mathrm{e}^{2\pi \mathrm{i} x} f(x).$$

Then U and V are unitary and satisfy the Weyl relation in Definition B.1. This algebraic encoding is used only as a bookkeeping device for "shift" and "phase" operations consistent with Axiom 1.1.

B.2 Window projection as a readout map

Given a window $W \subset \mathbb{T}$, define the indicator kernel $K_W : \mathbb{T} \to \{0,1\}$ by $K_W(z) = \mathbf{1}\{z \in W\}$. The (deterministic) binary readout induced by W is

$$w_n = K_W(z_n) = \mathbf{1}\{\mathrm{e}^{2\pi \mathrm{i} x_n} \in W\} \in \{0,1\}.$$

Finite observability at window length m is the restriction to words $w = w_1 \cdots w_m \in \Omega_m = \{0,1\}^m$.

B.3 Zeckendorf admissibility and the golden branch

On the golden branch, admissibility is enforced by the forbidden word "11":

$$X_m = \{w \in \Omega_m : w \text{ contains no adjacent ones}\}.$$

Equivalently, if $c_k \in \{0,1\}$ are Zeckendorf digits, the admissibility constraint is $c_k c_{k+1} = 0$. The Fibonacci count $|X_m| = F_{m+2}$ (Lemma 4.5) is the combinatorial backbone of the φ-channel.

B.4 Dyadic phase registers

For a phase resolution parameter $p \geq 1$, we model phases by the finite ring

$$\mathbb{Z}_{2^p} = \mathbb{Z}/2^p\mathbb{Z},$$

equipped with the embedding into $\mathbb{T}$ given by

$$k \longmapsto \mathrm{e}^{2\pi \mathrm{i} k/2^p}.$$

In the holonomy diagnostics, denominators of the form denom $= 2^p$ and the low-complexity phase-map family are treated in CAP audit form: we fix explicit bounded candidate families and report deterministic sweeps and counterfactual baselines, rather than allowing implicit continuous tuning (Section 6 and Appendix AE). The label $\mathbb{Z}_{128}$ is the baseline choice at $p = 7$ (Section 1.8).

B.5 Abel normalization and pole barriers

The e-channel uses an Abel-type viewpoint: one studies an analytic generating function on the open unit disk and takes a limit along the *Abel path* $\rho \uparrow 1$ with $\rho \in (0,1)$. This isolates the location of the first singularity (the "pole barrier") that obstructs extending the analytic object to the boundary.

Definition B.3 (Abel-normalized sum)**.** *Let $(a_n)_{n\geq 0}$ be a complex sequence and define, for $\rho \in (0,1)$,*

$$F(\rho) := \sum_{n \geq 0} a_n \rho^n,$$

whenever the series converges. If the limit exists (finite or infinite), the Abel limit *is*

$$\lim_{\rho \uparrow 1} F(\rho).$$

Lemma B.4 (Root-test pole barrier)**.** *Let (a_n) be a sequence with*

$$\lambda := \limsup_{n\to\infty} |a_n|^{1/n} \in [0, \infty].$$

Then $F(\rho) = \sum_{n\geq 0} a_n \rho^n$ converges absolutely for $0 \leq \rho < 1/\lambda$ (with the convention $1/0 = \infty$) and diverges for $\rho > 1/\lambda$. In particular, if $\lambda > 1$ then the Abel path $\rho \uparrow 1$ necessarily encounters a singularity barrier at $\rho = 1/\lambda < 1$.

Proof. This is the standard root test applied to the power series with coefficients a_n. For $\rho < 1/\lambda$, one has $\limsup_n |a_n \rho^n|^{1/n} = \rho\lambda < 1$, so the series converges absolutely. For $\rho > 1/\lambda$, the limsup exceeds 1, so the terms do not tend to zero and the series diverges. □

Remark B.5 (Connection to the e-channel language)**.** *In this paper, the phrase "Abel pole barrier" refers to the first singularity that obstructs analytic continuation along the Abel path in the relevant generating function (Section 4.5). The Artin–Mazur zeta framework supplies a canonical class of such generating functions in symbolic dynamics and provides a standard way to encode stability information through analyticity and singularity structure [30–32].*

C Wish and Motive as auditable interface objects (template)

Scope and status. [Audit]This appendix records a reader-facing template that formalizes the terms *Wish* and *Motive* as interface/audit objects used to organize the narrative. They introduce no additional axioms beyond tick and CAP, and they are not used as premises in theorem-level proofs.

C.1 Wish: protocol-stable target data

Definition C.1 (Wish (protocol-stable target data))**.** *[Interface]A* Wish *is a protocol-stable target datum/structure specified as a finite list of invariants and admissibility predicates that an observer wishes to reproduce under a fixed readout protocol. Concretely, a Wish can be represented by a tuple*

$$W := (m,\ \mathcal{I}_m,\ \mathcal{C}_m,\ \varepsilon),$$

where m is the window length, $\mathcal{I}_m$ is a finite set of computable invariants on finite observables (e.g. stable-type statistics on X_m), $\mathcal{C}_m$ is a finite set of admissibility/consistency predicates (e.g. cross-site constraints on a chosen display graph), and ε is an explicit tolerance budget for audit comparison.

Audit note. [Audit]**Status:** [Interface]. **Depends on:** the tick-first dictionary (Section 3) and the declared audit discipline (Appendix H, Appendix K). **If:** Wish is treated as a data-structure specification (invariants + predicates + tolerance) rather than as a new physical axiom.

C.2 Motive: auditable objective functional

Definition C.2 (Motive (auditable objective functional))**.** *[Interface]Given a Wish $W = (m, \mathcal{I}_m, \mathcal{C}_m, \varepsilon)$ and a finite candidate family $\mathcal{F}$ of protocol choices/closures, a* Motive *is an explicitly declared objective functional*

$$J : \mathcal{F} \to \mathbb{R}, \qquad J = J_{\text{mismatch}} + \lambda\, J_{\text{cost}} + \eta\, J_{\text{robust}},$$

where J_{mismatch} quantifies violation of the Wish tolerance (mismatch certificate), J_{cost} quantifies bounded implementation/description cost, and J_{robust} optionally quantifies stability under a bounded counterfactual family. The coefficients $\lambda, \eta \geq 0$ are declared as part of the audit specification.

Audit note. [Audit]**Status:** [Audit] + [Interface]. **Depends on:** an explicitly declared finite candidate family $\mathcal{F}$, objective decomposition, and deterministic tie-break rules (Appendix H). **If:** all reported selections are CAP-closures over explicit finite families with deterministic tie-breaks; external targets enter only at the matching layer.

C.3 CAP closure of Motive (template)

Definition C.3 (CAP closure (finite family))**.** *[Audit]Let $\mathcal{F}$ be a finite candidate family and let $J : \mathcal{F} \to \mathbb{R}$ be an auditable objective functional. The CAP-closed output is the unique minimizer*

$$f_\star := \arg\min_{f \in \mathcal{F}} J(f),$$

with deterministic tie-break rules specified when the minimum is degenerate.

Remark C.4 (Programmatic reading (not used in proofs))**.** *[Audit]One may read the paper's audited interface closures as a sequence of CAP-closed choices in explicit finite families, each of which can be interpreted as minimizing a Motive induced by a Wish. This programmatic interpretation is reader-facing only and is not used as a premise in theorem-level proofs.*

C.4 A generic teleological dynamics statement (template)

Scope. [Audit]This subsection records a generic Lyapunov-type template that is often used to connect an explicit objective functional to an arrow of update time in a parameter space. It is included for reuse and is not used as a premise in the theorem-level folding core.

Proposition C.5 (Generic Lyapunov monotonicity (template))**.** *[Math]Let $U : \mathbb{R}^d \to \mathbb{R}$ be continuously differentiable and consider the gradient flow*

$$\dot{\theta}(t) = -\nabla U(\theta(t)).$$

Then along any solution one has

$$\frac{\mathrm{d}}{\mathrm{d}t} U(\theta(t)) = -\|\nabla U(\theta(t))\|^2 \le 0,$$

so U is non-increasing and serves as a Lyapunov certificate for the induced arrow of update time.

Proof. By the chain rule,

$$\frac{\mathrm{d}}{\mathrm{d}t} U(\theta(t)) = \nabla U(\theta(t)) \cdot \dot{\theta}(t) = \nabla U(\theta(t)) \cdot (-\nabla U(\theta(t))) = -\|\nabla U(\theta(t))\|^2 \le 0.$$

□

D Semigroup and exponential kernels (arrow-of-time template)

[Audit]This appendix records a standard functional-equation template that connects a one-way additive time law on ticks to exponential weights. It is included as a reusable mathematical note; it introduces no additional axioms and is not used as a premise in theorem-level folding proofs.

D.1 Discrete semigroup weights on ticks

Proposition D.1 (Memoryless weights on $\mathbb{N}_0$ are exponential)**.** *[Math]Let $(w_t)_{t \in \mathbb{N}_0}$ be real weights with $w_0 = 1$ and*

$$w_{t+s} = w_t\, w_s \qquad \text{for all } t, s \in \mathbb{N}_0.$$

Then $w_t = r^t$ for all $t \in \mathbb{N}_0$, where $r := w_1$.

Proof. Taking $s = 1$ gives $w_{t+1} = w_t w_1 = r\, w_t$ for all $t \in \mathbb{N}_0$. By induction, $w_t = r^t w_0 = r^t$. □

D.2 Continuous representative and the Cauchy exponential equation

Proposition D.2 (Continuous semigroup weights are exponentials)**.** *[Math]Let $w : [0,\infty) \to (0,\infty)$ be continuous and satisfy*

$$w(t+s) = w(t)\,w(s) \qquad \text{for all } t,s \geq 0, \qquad w(0) = 1.$$

Then there exists $\lambda \in \mathbb{R}$ such that $w(t) = \exp(\lambda t)$ for all $t \geq 0$.

Proof. Define $a(t) := \log w(t)$, which is well-defined and continuous because $w(t) > 0$. Then $a(t+s) = a(t) + a(s)$ for all $t,s \geq 0$ and $a(0) = 0$. By the standard Cauchy functional equation result under continuity, $a(t) = \lambda t$ for some $\lambda \in \mathbb{R}$. Exponentiating gives $w(t) = \exp(\lambda t)$. □

D.3 Calibration constants and matching-layer inputs

[Interface]Exponential laws determine a *shape* but not an absolute origin: when one solves a linear update law (discrete or continuous), an initial-condition constant remains. For example, the differential equation $x'(t) = \lambda x(t)$ has solutions $x(t) = C\exp(\lambda t)$, and the constant C is equivalent to a choice of time origin or amplitude normalization. In the audit discipline of this paper, such constants are treated as matching-layer conventions (units, calibration targets, reference scales) rather than as theorem-level outputs.

D.4 Abel-first weights and the $r \uparrow 1$ path

[Math]The discrete exponential family r^t with $0 < r < 1$ is the canonical "Abel-first" convergence weight: it suppresses late-time contributions while preserving the semigroup law $r^{t+s} = r^t r^s$. The standard Abel path is the limit process $r \uparrow 1$ (Conventions). In this paper, Abel-first conventions appear as a disciplined way to discuss finite parts and controlled limits; they do not add new premises to the finite folding core.

E Abel finite parts and unit-disk analyticity (notes)

[Audit]This appendix records a standard Abel-first/finite-part template used as an analytic stability discipline: one replaces infinite-horizon expressions by holomorphic generating functions on the unit disk and defines renormalized values by a canonical constant-term extraction along the Abel path. It introduces no new axioms and is not used as a premise in theorem-level folding proofs.

E.1 Abel generating functions and holomorphy on the unit disk

Let $(a_t)_{t\geq 0}$ be a bounded complex sequence: $|a_t| \leq M$. Define its Abel generating function

$$\mathcal{A}_a(r) := \sum_{t\geq 0} a_t r^t, \qquad |r| < 1.$$

[Math]This is holomorphic for $|r| < 1$ and satisfies the estimate

$$|\mathcal{A}_a(r)| \leq \frac{M}{1-|r|}.$$

In particular, for bounded protocol traces, the only universal singular behavior compatible with absolute convergence occurs on the boundary as $r \uparrow 1$.

E.2 Finite-part extraction along the Abel path

If $\mathcal{A}_a(r)$ admits an asymptotic expansion of the form

$$\mathcal{A}_a(r) = \frac{c_{-1}}{1-r} + c_0 + c_1(1-r) + \cdots \qquad (r \uparrow 1),$$

then the Abel finite part is defined by

$$\mathrm{FP}_{r\uparrow 1}\mathcal{A}_a(r) := c_0.$$

This is the canonical constant-term prescription used whenever an Abel-first finite part is referenced. For classical Abelian summation and finite-part asymptotics, see [85, 86].

E.3 Rotation resolvent formula and a canonical pole subtraction

We record a self-contained template for irrational rotations, which clarifies why the Abel-first viewpoint is naturally stable under protocol-level changes that preserve a bounded Fourier kernel class.

Let $\alpha \in (0,1) \setminus \mathbb{Q}$ and let $x_t = x_0 + t\alpha \pmod 1$. Let $f : \mathbb{R}/\mathbb{Z} \to \mathbb{C}$ have an absolutely summable Fourier series

$$f(x) = \sum_{m\in\mathbb{Z}} \widehat{f}(m)\, \mathrm{e}^{2\pi \mathrm{i} m x}, \qquad \sum_{m\in\mathbb{Z}} \left|\widehat{f}(m)\right| < \infty.$$

Define the Abel orbit sum

$$S_f(r) := \sum_{t\geq 0} r^t f(x_t), \qquad |r| < 1.$$

Proposition E.1 (Fourier–resolvent representation and universal pole)**.** *[Math]For every $|r| < 1$,*

$$S_f(r) = \sum_{m\in\mathbb{Z}} \widehat{f}(m)\, \mathrm{e}^{2\pi \mathrm{i} m x_0}\, \frac{1}{1 - r\, \mathrm{e}^{2\pi \mathrm{i} m \alpha}}.$$

In particular, one has the decomposition

$$S_f(r) = \frac{\widehat{f}(0)}{1-r} + H_f(r),$$

where H_f is holomorphic on $|r| < 1$ and extends continuously to $r \uparrow 1$.

Proof. Absolute summability of $\widehat{f}(m)$ implies uniform convergence of the Fourier series, allowing termwise summation of the geometric series $\sum_{t\geq 0}(r\, \mathrm{e}^{2\pi \mathrm{i} m\alpha})^t = 1/(1 - r\, \mathrm{e}^{2\pi \mathrm{i} m\alpha})$ for $|r| < 1$. The $m = 0$ term equals $\widehat{f}(0)/(1-r)$. For $m \neq 0$, irrationality of α implies $\mathrm{e}^{2\pi \mathrm{i} m\alpha} \neq 1$, hence the denominators do not vanish at $r = 1$; uniform convergence then yields holomorphy on $|r| < 1$ and continuity at $r \uparrow 1$. □

Corollary E.2 (Finite part exists and is scheme-stable within the admissible class)**.** *[Math]Under the hypotheses of Proposition E.1, the Abel finite part exists and equals $H_f(1)$:*

$$\mathrm{FP}_{r\uparrow 1} S_f(r) = H_f(1).$$

Moreover, if one modifies the subtraction by a function $g(r)$ that is holomorphic in a neighborhood of $r = 1$, then

$$\lim_{r\uparrow 1}\left(S_f(r) - \frac{\widehat{f}(0)}{1-r} - g(r) \right) = H_f(1) - g(1),$$

so the only ambiguity is an explicit additive constant determined by the declared counterterm $g(1)$.

F Holomorphy versus interior poles: a pole-barrier rigidity template (notes)

[Audit]This appendix records an abstract rigidity motif used repeatedly in Abel-first analytic stability arguments: if a protocol object is defined as a holomorphic function on the unit disk, then any competing representation that would force an interior pole is incompatible. The template is included for reuse and is not used as a premise in theorem-level folding proofs.

F.1 Exponential modes force interior poles

Lemma F.1 (Interior pole from an off-stable exponential mode)**.** *[Math]Let $\lambda \in \mathbb{C}$ with $\mathrm{Re}(\lambda) > 0$ and define the mode generating function*

$$M_\lambda(r) := \sum_{t=0}^{\infty} r^t \, \mathrm{e}^{\lambda t}, \qquad |r| < \mathrm{e}^{-\mathrm{Re}(\lambda)}.$$

Then M_λ has the meromorphic closed form

$$M_\lambda(r) = \frac{1}{1 - r\,\mathrm{e}^{\lambda}},$$

with a pole at $r_\lambda = \mathrm{e}^{-\lambda}$ satisfying $|r_\lambda| = \mathrm{e}^{-\mathrm{Re}(\lambda)} < 1$. In particular, any expression that contains a nonzero multiple of M_λ cannot extend to a holomorphic function on the full unit disk $\{|r| < 1\}$.

Proof. The series is geometric with ratio $r\,\mathrm{e}^{\lambda}$ and therefore sums to $1/(1 - r\,\mathrm{e}^{\lambda})$ on its domain of absolute convergence. The pole occurs where the denominator vanishes, at $r = \mathrm{e}^{-\lambda}$. Its modulus is $\mathrm{e}^{-\mathrm{Re}(\lambda)} < 1$ when $\mathrm{Re}(\lambda) > 0$. □

F.2 Holomorphic–meromorphic incompatibility at a pole

Lemma F.2 (Holomorphic–meromorphic incompatibility)**.** *[Math]Let $U \subset \mathbb{C}$ be open and let $r_0 \in U$. If F is holomorphic on U and G is meromorphic on U with a pole at r_0, then $F \neq G$ on $U \setminus \{r_0\}$.*

Proof. Assume for contradiction that $F = G$ on $U \setminus \{r_0\}$. On a small disk centered at r_0, F has a Taylor series while G has a Laurent expansion with a nontrivial principal part. Equality on the punctured disk forces the principal part to vanish, contradicting that G has a pole. □

F.3 How the template is used in this paper

[Audit]In this paper, the Abel-first viewpoint enters in two concrete places: (i) the e-channel analytic stability template via Artin–Mazur zeta and Abel normalization (Section 4.5 and Appendix B), and (ii) canonical finite-part prescriptions for bounded traces and orbit sums (Appendix E). The lemmas above formalize the generic obstruction: any representation that would require an interior pole is incompatible with the closed-layer holomorphy requirement on the unit disk.

G Tick + CAP derivation spine: from the sole input to all interface outputs

This appendix records the full "tick + CAP" derivation spine in one place. It introduces *no additional axioms or independent physical inputs* beyond: (i) tick as the sequential update index (Axiom 1.1), and (ii) CAP as the universal closure/selection rule on explicit finite candidate families (Axiom 1.5 and Appendix H). All other ingredients used throughout the paper are

either theorem-level definitions/proofs in the finite model, or CAP-closed interface components whose candidate families and tie-break rules are explicit and audited by deterministic scripts. External reference conventions (PDG/CODATA targets, renormalization schemes, threshold choices) enter only at the matching layer as comparison inputs and are never used as premises for theorem-level folding statements.

Two-axiom spine (reader contract). Within this paper, "physics" means the executed protocol outputs of a run. The only primitive *input* to that execution is the tick stream, and the only primitive *rule* for closing otherwise underdetermined interface components is CAP. Accordingly, every nontrivial interface component below is recorded in one of two forms: a theorem-level finite construction, or a CAP-closure over an explicitly declared bounded candidate family with deterministic tie-break rules.

G.1 Reading guide and dependency convention

We use the following status tags consistently:

- [**Tick**] definitional use of the sequential tick stream and finite window records.
- [**Math**] theorem-level finite constructions (counts, maps, explicit tables).
- [**CAP**] bounded-complexity closure: explicit finite candidate family + deterministic objective/tie-break.
- [**Match**] matching-layer comparison to external conventions (PDG/CODATA, scheme/scale).

Appendix K provides a compact ledger of these dependencies; the present appendix expands each nontrivial CAP-closure step in full audit form (candidate family, objective, tie-break, and where it is reproduced).

G.2 Tick to finite observables: words

[Tick] Finite observability is windowed. Given the tick stream (Axiom 1.1), finite observation at resolution m is represented by binary words $w \in \Omega_m = \{0,1\}^m$ obtained by window projection (Section 2 and Appendix B). This fixes the basic data type used throughout: *(tick, word)*.

G.3 CAP selection of the golden branch and the Fibonacci base

[CAP] Candidate family. At the scan layer one may choose an irrational slope $\alpha \in (0,1) \setminus \mathbb{Q}$ in the Kronecker orbit. Within the audited proxy class of finite-depth continued-fraction complexity at depth m,

$$C_m(\alpha) := \sum_{k=0}^{m} a_{k+1} \qquad \text{for } \alpha = [0; a_1, a_2, \dots],$$

CAP selects the unique minimizer at every depth.

[CAP] Objective and tie-break. Minimize $C_m(\alpha)$ at each depth m; the tie-break is trivial because the minimizer is unique.

[CAP] Result (rigidity). Proposition 2.5 shows that $\alpha = \varphi^{-1} = [0; 1, 1, 1, \dots]$ is the unique minimizer at every finite depth. This rigidly closes the symbolic/arithmetic bridge to the Zeckendorf/Fibonacci digit system used downstream (Section 2).

[Math] Consequence: Fibonacci grammar and counts. On the golden branch, admissible digit strings satisfy the forbidden-word grammar (no adjacent ones), yielding the Fibonacci stable-sector sizes $|X_m| = F_{m+2}$ (Lemma 4.5) and the canonical π-channel split (Proposition 4.8).

G.4 CAP selection of a locality screen and an addressing basis

[CAP] Screen dimension. Closed-loop transport diagnostics require cycles. In a one-dimensional display graph there are no plaquettes, hence no holonomy; therefore the minimal screen dimension that supports the finite holonomy diagnostics of Section 6 is 2. Accordingly, CAP selects a 2D screen as the minimal choice that admits an auditable loop-based diagnostic.

[CAP] Addressing basis on the chosen screen. Given a 2D screen, an addressing basis is a bijection from a finite tick prefix to grid sites. We treat the choice of addressing basis as a CAP-closed selection in an explicit finite counterfactual family:

- **candidates:** Hilbert vs. row-major on the same 8×8 screen at the anchor;
- **objectives:** protocol-internal locality/overhead metrics (scan-path jump quantiles, neighbor fiber-matching overhead quantiles, phase-lift computability failure rate);
- **tie-break:** lexicographic ordering of the objective vector.

The resulting comparison and the deterministic selection are recorded in Table 5 and reproduced by `scripts/exp_addressing_selection.py`.

G.5 CAP selection of balanced coupling and of the anchor $(n, m) = (3, 6)$

[CAP] Balanced coupling as minimal overhead. On a fixed screen, attaching spatial diagnostics requires assigning microstate labels to sites. CAP selects the bijective coupling (Remark 4.3): on the 2D screen, $2^m = 4^n$ (equivalently $m = 2n$) so that each site carries exactly one m-bit microstate label and no additional mapping conventions are required.

[CAP] Anchor selection by minimal nontrivial holonomy. Within the balanced chain $m = 2n$, CAP selects the smallest n for which the deterministic finite connection yields nontrivial plaquette holonomies (3/4 cycles) and a nonzero phase-lift signal. The balanced-chain sweep in Table 30 shows that $n = 1, 2$ yield only trivial (identity) holonomy, while $n = 3$ is the first scale with nontrivial 3/4-cycle content. Therefore the anchor on the chosen screen is $(n, m) = (3, 6)$.

G.6 The folding core and stable types at the anchor

[Math] Folding is a finite theorem-level layer. Given the golden-branch grammar and the explicit Fold_m projection, the folding core is a finite combinatorial statement: at $m = 6$ one has $64 \to 21$ with the canonical split $21 = 18 \oplus 3$ (Section 4). No additional physical identification is used as a premise.

G.7 CAP derivation of bulk dimension from the anchor bit budget

[CAP] Rigid-frame coarse-lock as a finite interface criterion. At the protocol interface, "bulk dimension" enters only when one defines what it means to display a localized rigid frame and compare poses across sites. Under the minimal two-bin-per-parameter coarse-lock convention, a single m-bit window can coarse-lock a rigid frame in dimension d only if

$$m \geq \dim SE(d) = \frac{d(d+1)}{2}$$

(Definition 3.6).

[CAP] Objective. At fixed anchor $m = 6$, CAP selects the maximal bulk dimension d compatible with the coarse-lock budget.

[CAP] Result. Proposition 3.7 shows that $d = 3$ is the unique maximal admissible dimension at $m = 6$ under the minimal convention. Thus the 3D rigid-frame dictionary is not an external input: it is a CAP output of the anchor budget.

G.8 CAP tie-break for the orientation-class bit (chirality sign)

[CAP] Candidate family. On the 2D Hilbert screen, the global layout family is D_4 and splits into two orientation classes (Section 5). Reflection swaps the two classes and flips the sign of the discrete chirality index χ (Proposition 5.4).

[CAP] Tie-break. Because the two orientation classes are symmetry-related and cost-degenerate under the locality diagnostics, CAP fixes a canonical representative by deterministic tie-break: the forward-traversal layout at $n = 3$ is chosen so that $\chi < 0$ (Definition 7.2; Appendix AE). The reflected layout defines the mirror protocol.

G.9 CAP-closed phase-register and phase-map dictionary (holonomy lift)

[CAP] Baseline closure. Phases are represented by a dyadic register $\mathbb{Z}_{2^p}$ and the phase lift uses denom $= 2^p$ together with a low-complexity index map τ (Section 6.5). The baseline choices are fixed by CAP as canonical minimal-description representatives coherent with the anchor window:

- choose denom $= 2^m$ (anchor-coherent dyadic denominator);
- choose $\tau = \tau_{\mathrm{id}}$ (identity map as the minimal bit-level transform).

[CAP] Audited bounded counterfactual families. The dyadic refinement chain and the bounded phase-map family are not hidden knobs: their influence is recorded by deterministic sweeps and counterfactual baselines. In particular, the denominator sweep is reported in Table 11 and the phase-map family sweep is reported in Tables 45–46, all reproduced by scripts listed in Appendix AJ.

G.10 CAP-closed coupling/CP normalizations from phase-volume data

[CAP] Electromagnetic normalization. Section AF.1 fixes the three-stratum impedance template and closes the phase-volume dictionary by CAP within an explicit finite primitive family (Definitions AF.2–AF.4). This yields the closed geometric impedance value $\alpha^{-1}_{\mathrm{em\,geo}} = 4\pi^3 + \pi^2 + \pi$ (Theorem AF.9).

[CAP] Electroweak normalization. At the Z scale, the electroweak normalization is closed by CAP from discrete weights already fixed by the closed labeling at the anchor (Definition AF.12), yielding $\alpha^{-1}(\mu_Z) = 13\pi^2$ and $\sin^2\theta_W(\mu_Z) = 3/13$ (Theorem AF.14).

[CAP] CP normalization. The CP-odd phase space is CAP-closed within the same primitive family (Definition AF.20 and Proposition AF.24), yielding the closed normalization target $J_{\mathrm{geo}} = 1/(11\pi^7)$ (equation (85)).

[Match] External comparisons are not premises. CODATA/PDG values enter only to report mismatch sizes, stability under perturbations, and within-family look-elsewhere context (Appendix AE); they are not used as premises for the theorem-level folding core or for the CAP-closed normalization dictionaries above.

G.11 Gauge fields as compensating connections (from fiber mismatch)

[Tick, Math] Cross-site comparison forces extra transport data. At any fixed window length m, a stable label $w \in X_m$ stands for an entire microstate fiber $\mathrm{Fold}_m^{-1}(w)$. Therefore, if the protocol requires comparing or transporting stable labels across neighboring sites in a display graph, then stable labels alone are insufficient: one must choose how the endpoint fibers are matched. This necessity is finite and intrinsic to window projection and stability folding. Proposition 8.1 formalizes the point and shows that, after a deterministic padding to a uniform slot size $r = \max_{w \in X_m} |\mathrm{Fold}_m^{-1}(w)|$, each edge transport is represented by a permutation in S_r, with local relabelings acting by conjugation (a finite gauge redundancy).

[Math] Deterministic discrete holonomy at the anchor. At the CAP-minimal anchor $m = 6$ one has $r = 4$, and the paper provides a deterministic S_4 edge-connection construction together with plaquette holonomy diagnostics (Section 6). This is the finite, protocol-internal origin of the connection/holonomy language used throughout.

[CAP] Three commuting channels close a three-factor compensation structure. The folding template isolates three commuting defect channels $(\varphi, \pi, \mathrm{e})$. If compensation is defined only up to independent local basis changes associated with each channel, then the minimal redundancy factorizes into three independent components (Proposition 8.3).

[CAP] Gauge-factor closure (bounded family, objective, tie-break). To pass from the finite graph connection to a continuum dictionary, we treat gauge redundancy as internal and unitary (hence compact at the group level), and we restrict to three-factor products with one abelian phase sector and two inequivalent compact simple non-abelian factors. Within the explicit bounded family

$$U(1) \times G_2 \times G_3,$$

with G_2 and G_3 compact, simple, non-abelian and non-isomorphic, we use $\dim(\mathfrak{g})$ as the intrinsic complexity label and apply CAP as lexicographic minimization of $(\dim \mathfrak{g}_2, \dim \mathfrak{g}_3)$ (Proposition 8.2). The unique minimizer is $U(1) \times SU(2) \times SU(3)$ (up to finite quotients), by the compact Lie classification and Lemma 9.4.

G.12 Closed Standard Model labeling as a CAP-minimal rank matching

[Math] The $18 \oplus 3$ target cardinalities are fixed at the anchor. At $(m, n) = (6, 3)$ the stable sector is $X_6 = X_6^{\mathrm{cyc}} \sqcup X_6^{\mathrm{bdry}}$ with $|X_6^{\mathrm{cyc}}| = 18$ and $|X_6^{\mathrm{bdry}}| = 3$ (Section 4). Any SM identification at the anchor must respect this split.

[CAP] Minimal closure of the cyclic target set. On the SM side we require 18 chiral multiplets (field-level labels) to match the 18 cyclic stable types. Within the bounded family of minimal extensions of the SM fermion content at fixed three generations, CAP selects the anomaly-neutral minimal addition that closes the cardinality: a sterile singlet ν_R with $Y = 0$ (Proposition 9.6). This closes $\mathcal{F}_{\mathrm{SM}}$ to 18 multiplets without changing anomaly sums or introducing new charged matter.

[CAP] Candidate family and objective for the labeling map. Consider the finite family of split-compatible maps

$$\mathcal{L}_{\mathrm{SM}} : X_6 \to \mathcal{F}_{\mathrm{SM}} \sqcup \mathcal{G}_{\mathrm{SM}},$$

where $\mathcal{G}_{\mathrm{SM}} = \{U(1), SU(2), SU(3)\}$ are the three gauge-factor connection classes. CAP closes the map by minimizing ordering mismatch subject to split compatibility:

- **cyclic sector:** fix a deterministic intrinsic order $\prec_X$ on X_6^{cyc} using only stable-type invariants (Definitions 9.9 and 9.11), and fix a deterministic SM-side order $\prec_F$ on $\mathcal{F}_{\mathrm{SM}}$ using only discrete quantum-number invariants (Definition 9.12);
- **objective:** minimize the number of inversions between the induced pairing and the target orders (equivalently: enforce order preservation);
- **tie-break:** deterministic rank matching (order isomorphism) on the cyclic sector; and on the boundary sector, monotone matching of intrinsic boundary value $V(w)$ to gauge-sector complexity $\dim(\mathfrak{g})$ (Lemma 9.3 and Remark 9.18).

[Math] Result (uniqueness). Theorem 9.17 shows that the minimizer is unique: the cyclic assignment is the unique order isomorphism between two finite total orders, and the boundary assignment is the unique monotone permutation among $3! = 6$ candidates. The explicit labeling table is recorded in Table 15 and reproduced by `scripts/exp_sm_labeling_solver.py`.

G.13 Mass as latency: CAP-closed integer depth ansatz and rigidity

[Tick] Mass/energy are time-scale ratios in a log-time coordinate. The Fibonacci resolution coordinate

$$r(\mu) = \frac{\log(\mu/m_e)}{\log \varphi}$$

is used because it linearizes multiplicative time-scale ratios (Section 10). In tick-first language, a depth mismatch Δr is a multiplicative mismatch of Compton-clock period and can be compared to operational delay proxies (Remark 10.1 and Appendix Y).

[Math] Intrinsic stable-type invariants supply a discrete cost basis. At the anchor, each stable type carries intrinsic invariants $(V(w), g(w), |w|_1)$ (Definition 8.9). The degeneracy $g(w) = |\mathrm{Fold}_6^{-1}(w)|$ measures residual microstate uncertainty under window projection (Lemma 13.1) and is therefore the protocol-native discrete overhead term in a protocol-cost dictionary.

[CAP+Match] Bounded integer closure for the depth map. To make the depth assignment auditable as a low-complexity closure, we restrict to the explicit bounded family of integer-linear depth maps

$$\widehat{r}(w) = a\,\Delta V + b\,\Delta g + c\,\Delta|w|_1, \qquad a, b, c \in \mathbb{Z}, \qquad |a|, |b|, |c| \le B$$

(Appendix AG, equation (89)). The objective is evaluated on the scheme-stable charged-lepton anchors $\{\mu, \tau\}$ in the resolution coordinate $r(\mu)$, with deterministic lexicographic tie-break rules; an extended quark set is recorded as a diagnostic.

[CAP+Match] Result (rigidity). Proposition AG.1 shows that the unique minimizer stabilizes at $(a, b, c) = (2, 5, 1)$ by $B = 5$ and remains constant up to $B = 20$ (Table 94), reproduced by `scripts/exp_mass_depth_rigidity.py`. Once the coefficients are fixed, the closed template mass prediction is $\mu_{\mathrm{pred}}(f) = m_e\,\varphi^{\widehat{r}(f)}$ (Definition 13.3), and all remaining deviations are recorded explicitly as matching-layer shifts Δr (Section 13 and Appendix AG).

G.14 Resolution staircase: CAP-closed calibration and deterministic selection

[CAP+Match] Candidate family for the step size. To close the energy↔m interface at the protocol layer, we fix a deterministic staircase template $\mu_{\mathrm{th}}(m)$ whose only free discrete choice is the step size r_{step} (Section 14.2.1). We restrict to the explicit bounded family

$$r_{\mathrm{step}} = k\pi, \qquad 1 \le k \le 10,$$

audited by deterministic sweeps.

[CAP+Match] Objectives and tie-break. Two deterministic calibration objectives are recorded:

- **single-anchor**: match the electroweak anchor by minimizing $|\log(\mu_{\mathrm{th}}(10)/m_Z)|$ over the candidate family (Table 20);
- **two-anchor minimax**: minimize the maximum absolute mismatch across $(m = 10, m_Z)$ and $(m = 8, \mu_{\mathrm{QCD}})$ with deterministic tie-break rules (Table 21).

[CAP+Match] Result. Proposition 14.4 records that $r_{\mathrm{step}} = 2\pi$ is the unique minimizer under both audited objectives within the stated bounded family. With r_{step} fixed, the effective resolution map $m_{\mathrm{eff}}(\mu)$ is selected deterministically by least discrepancy (Corollary 14.2).

G.15 Frequency-first continuum representative: equivalence, action, and equations

[Iface] Equivalence semantics fixes what counts as "the same physics". Appendix AA records the semantic quotients already used throughout the paper (tick-origin shift, projection-fiber equivalence, local basis relabeling/gauge, coarse-graining preorder, and action equivalence). In particular, frequency is treated as a primary derived quantity in tick units via phase advance $\omega = \Delta\theta/\Delta t$ (Definition AA.1).

[Iface+CAP] CAP-closed action representative on a finite family. To obtain a continuum dynamical representative without introducing new primitives, we treat the choice of action as a CAP closure:

- **candidates:** a finite term-type dictionary of local covariant invariants (gravity, gauge, information/overhead sector, matter placeholder) together with a bounded rational coefficient box (Appendix AD.4);
- **objective:** lexicographic minimality in derivative order and description complexity, compatible with the equivalence semantics and coarse-graining monotonicity;
- **tie-break:** deterministic complexity key (term count, denominator height, and declared group-dimension keys where applicable).

The resulting CAP-minimal action skeleton is recorded in Proposition AD.1.

[Math] Field equations by standard variation. Once the representative action is fixed, the dynamical equations are the Euler–Lagrange equations of that action. Appendix AD.5 records the resulting Einstein equation with total stress (Theorem AD.2), Yang–Mills equations (Proposition AD.5), and the χ-sector amplitude equation (Proposition AD.6), together with the weak-field Poisson template (Section AD.5.6).

G.16 Thermodynamics as coarse-graining and CAP free-energy closure

[Iface+CAP] Entropy/temperature and entropic force. Appendix AD.6 records a thermodynamic closure compatible with the same equivalence semantics: entropy is defined by coarse-grained state counting (or boundary channel capacity), temperature is the conjugate frequency scale, and equilibrium selection is a CAP closure on a finite family (Proposition AD.8). Force is treated as a response functional (free-energy/action gradient), aligning the entropic-force dictionary with the weak-field gravitational potential dictionary.

G.17 Overhead-to-gravity closure and a data protocol for χ

[Iface] Overhead and lapse dictionaries. Appendix AD.7 records a minimal overhead-to-lapse closure: define $\chi = \log(\kappa/\kappa_0)$ and set $N = \mathrm{e}^{-\gamma\chi}$ as the lapse proxy (Definition AD.9). In a static gauge, set $g_{00} \approx -N^2$ and identify the weak-field potential by $g_{00} \approx -(1+2\Phi/c^2)$, yielding $\Phi = -\gamma c^2(\chi - \chi_0)$. This closes a weak-field Poisson source template $\rho_{\mathrm{eff}} \propto -\Delta\chi$ (equation (68)) with a single calibration parameter γ.

[Prot] $\chi(x)$ reconstruction protocol. Appendix AD.8 records an executable pipeline: Hilbert binning $\to$ window words $\to$ folding statistics $\bar{g}_m$ (or defect proxies) $\to$ $\chi(x) = \log(\bar{g}_m/\bar{g}_0)$. Given $\chi(x)$, γ can be fit by rotation curves, lensing, or delay/redshift proxies.

G.18 Quantum readout and Born-probability rigidity

[Iface] POVM readout. Appendix AD.10 records finite-resolution readout by POVMs and instruments, giving Born probabilities $P_k = \mathrm{Tr}(\rho E_k)$.

[Iface] Closure routes for Born weights. Two complementary closures are recorded: (i) a projection-induced counting template compatible with the finite fiber semantics of this paper (Theorem AD.21), and (ii) a mature uniqueness theorem (Gleason–Busch; Theorem AD.22) that forces the Born form under noncontextual additivity.

G.19 Running couplings and cosmology as resolution flow (self-contained interfaces)

[Iface] RG in the r coordinate. Appendix AD.11 records the chain-rule form $\mathrm{d}g/\mathrm{d}r = (\log\varphi)\beta(g)$ and standard one-loop templates, together with threshold matching as discrete uplifts in the protocol flow.

[Iface] Cosmology as resolution initialization and capacity growth. Appendix AD.12 records a minimal cosmology interface: big bang as resolution bootstrapping, inflation as exponential growth of stable capacity $|X_m| \sim \varphi^m$ under approximately linear $m(t)$, and a discrete energy-budget matching hypothesis on the stable fraction $f_{\mathrm{stab}}(m) = F_{m+2}/2^m$.

H CAP closures: deterministic audit template

This appendix collects a single, reusable audit template for bounded-complexity closures under the Computational Action Principle (Axiom 1.5). It introduces *no new axioms or independent inputs* beyond those declared in the main text; it only makes explicit the finite selection logic already used throughout the paper.

H.1 Selection on a finite candidate family

The core reason the audit program is well-posed is finiteness: for each bound B, the candidate family $\Theta(B)$ is a finite set by construction (Definition H.1).

Definition H.1 (Bounded-complexity closure (audit form))**.** *Fix reference targets $x_i^{\mathrm{ref}} > 0$ and a candidate family $x_i(\theta) > 0$ indexed by discrete parameters θ. For a bound $B \in \mathbb{N}$, let $\Theta(B)$ be a finite domain of admissible parameters (the "complexity box"). Define the log-mismatch vector*

$$e_i(\theta) := \log\left(\frac{x_i(\theta)}{x_i^{\mathrm{ref}}}\right),$$

and the summary objectives

$$E_\infty(\theta) := \max_i |e_i(\theta)|, \qquad E_1(\theta) := \sum_i |e_i(\theta)|.$$

A bounded-complexity closure is the selection of a unique $\theta_B \in \Theta(B)$ by lexicographic minimization: first minimize E_∞, then E_1, then any stated secondary criteria (e.g. coefficient sum), with a fully specified tie-break rule.

Remark H.2 (Why log-mismatch is used)**.** *The log mismatch is dimensionless and symmetric under inversion: $\log(x/x^{\mathrm{ref}}) = -\log(x^{\mathrm{ref}}/x)$. It also linearizes multiplicative matching factors: if $x = s\,x^{\mathrm{ref}}$, then $\log(x/x^{\mathrm{ref}}) = \log s$. For small deviations, $|\log(x/x^{\mathrm{ref}})| \approx |x - x^{\mathrm{ref}}|/x^{\mathrm{ref}}$.*

Proposition H.3 (Deterministic closure map)**.** *Fix a bound $B \in \mathbb{N}$ and a finite candidate family $\Theta(B)$. Let $(E_\infty(\theta), E_1(\theta), T(\theta))$ be a triple of real-valued diagnostics on $\Theta(B)$, where T denotes any fully specified secondary tie-break key (possibly vector-valued with a fixed lexicographic order). Then the lexicographic minimization rule*

$$\theta_B \in \operatorname*{argmin}_{\theta \in \Theta(B)} \big(E_\infty(\theta), E_1(\theta), T(\theta)\big)$$

selects a nonempty minimizer set and defines a deterministic selection function once T is chosen so that ties are fully resolved.

Proof. Because $\Theta(B)$ is finite, the set of triples $\{(E_\infty(\theta), E_1(\theta), T(\theta)) : \theta \in \Theta(B)\}$ is finite, hence admits at least one lexicographic minimum. If the tie-break key T is defined so that equality of the full triple can occur for at most one element, the selected minimizer is unique and the rule becomes deterministic. □

H.2 Audit outputs beyond point estimates

For each closure, the paper reports additional finite statistics that quantify within-family look-elsewhere context and stability under perturbations (Section 1.6 and Appendix AE). Two frequently used diagnostics are the candidate-domain size and a uniqueness gap.

Definition H.4 (Rigidity certificate)**.** *A closure is called* rigid *on a tested range $B \in \{1, \ldots, B_{\max}\}$ if the minimizer is unique at each B and stabilizes: there exists $B_* \le B_{\max}$ such that $\theta_B = \theta_{B_*}$ for all $B_* \le B \le B_{\max}$.*

Definition H.5 (Domain size and uniqueness gap)**.** *Let Θ be a finite candidate family and let $J(\theta)$ be an objective (e.g. $E_\infty(\theta)$). Define the domain size as $|\Theta|$. If the minimizer is unique, define the* uniqueness gap *as*

$$\Delta J := J(\theta^{(2)}) - J(\theta^{(1)}),$$

where $\theta^{(1)}$ is the minimizer and $\theta^{(2)}$ is the best competitor under the same tie-break ordering restricted to J.

category	status in this paper
protocol primitive	the tick (scan iteration count) and window observables (Axiom 1.1; Section 3)
derived protocol structures	admissible languages X_m, folding maps Fold_m, and intrinsic invariants (Sections 2–4)
audited discrete closures	explicit finite candidate families selected by CAP (e.g. bounded-complexity budget B, phase denominator denom $= 2^p$, bounded rationals for mixing/phases, staircase step r_{step}; Section 1.6)
external reference conventions	PDG/CODATA targets and scheme/scale choices treated as inputs at the matching layer (not fit)

Table 24: Audit contract: what is fixed, what is swept under explicit finite bounds, and what is treated as an external reference convention.

H.3 Reference implementation sketch (audit form)

The following pseudocode summarizes the selection logic implemented by the deterministic scripts in this repository. It is intended as an audit aid (not as a new modeling premise).

```
Input:
  - finite candidate set Theta(B)
  - reference targets x_ref[i] > 0
  - candidate map x(theta)[i] > 0 for theta in Theta(B)
  - objective: E_inf(theta) = max_i |log(x_i(theta)/x_ref[i])|
               E_1(theta) = sum_i |log(x_i(theta)/x_ref[i])|
  - tie-break key T(theta) (fully specified; lexicographic)

Algorithm:
  best <- None
  for theta in Theta(B):
      compute e_i(theta) = log(x_i(theta)/x_ref[i]) for all i
      compute (E_inf(theta), E_1(theta), T(theta))
      if best is None or (E_inf, E_1, T) is lexicographically smaller than
      ↪  best:
          best <- (E_inf, E_1, T, theta)
  output theta_B = best.theta

Audit outputs (in addition to theta_B):
  - |Theta(B)| (domain size)
  - best/second-best gaps for E_inf and E_1 where feasible
  - quantiles of E_inf over Theta(B) for large domains
  - robustness under explicit target perturbations
  - counterfactual baselines within stated families
```

Remark H.6 (Why this does not add hidden knobs)**.** *The only discretionary content in a closure is the explicit declaration of the finite family $\Theta(B)$, the objectives, and the tie-break key T. Once declared, the selection is a deterministic function of these finite inputs (Proposition H.3). This is the operational meaning of the paper's "no-hidden-knobs" audit contract (Table 24).*

I Rigidity-bridge certificates and mainline checklist (audit)

[Audit]This appendix records a compact checklist for "rigidity bridges": auditable certificate forms that turn a narrative step into a verifiable implication with an explicit minimal input set. It is reader-facing audit infrastructure and is not used as a premise in theorem-level folding proofs.

I.1 Certificate forms (RB-A/B/C/D)

We use four certificate templates:

- **RB-A (finite-family minimization).** A finite candidate family $\mathcal{F}$, an explicit objective functional $J : \mathcal{F} \to \mathbb{R}$, and a deterministic tie-break rule; the output is a unique (or near-unique with a gap) minimizer $f_\star = \arg\min_{\mathcal{F}} J$.
- **RB-B (incompatibility / obstruction).** A "bad" structure would force an obstruction (e.g. an interior pole) that is incompatible with an established analytic domain or stability certificate; hence the bad structure is excluded.
- **RB-C (counting/classification rigidity).** A finite classification, counting identity, or image–preimage structure forces a unique decomposition (e.g. $64 \to 21$, $18 \oplus 3$).
- **RB-D (gap-stability / robustness).** A quantitative gap or sensitivity bound shows that the conclusion persists under bounded counterfactual families or perturbations, upgrading "accidental alignment" to a robust closure.

I.2 Mainline checklist (where each bridge is realized in this paper)

mainline jump	closure output	RB form	minimal inputs	where in this paper
Tick $\to$ CAP	deterministic finite-family closure rule	RB-A	tick + bounded complexity + tie-break	Axioms 1.1, 1.5; Appendix G; Appendix H
CAP $\to$ golden branch	finite-depth least-discrepancy selection of $\alpha = \varphi^{-1}$	RB-A/RB-D	continued-fraction proxy + audited discrepancy bound	Proposition 2.5; Subsubsection 2.3.1; Appendix N
golden branch $\to$ φ-grammar	admissible set X_m with $\lvert X_m\rvert = F_{m+2}$	RB-C	Zeckendorf admissibility	Lemma 4.5; Appendix B
φ-grammar $\to$ π-closure	cyclic/boundary split and $18 \oplus 3$ at $m = 6$	RB-C	wrap-around constraint + Fibonacci counts	Proposition 4.8; Corollary 4.9
$(\varphi, \pi) \to$ e stability	zeta/Abel normalization and pole-barrier template	RB-B/RB-D	unit-disk holomorphy + Abel path conventions	Section 4.5; Appendix B; Appendix E; Appendix F
π-closure $\to$ anchor	minimal explicit screen anchor $(m, n) = (6, 3)$ and audited addressing choice	RB-A/RB-C	finite screen family + cardinality match + tie-break	Section 4; Remark 4.3; Table 5
anchor $\to$ gauge/holonomy	finite connection/holonomy invariants modulo local relabeling	RB-C/RB-D	local fiber relabeling + loop invariants + bounded families	Section 6; Appendix S
gauge $\to$ SM labeling/mass	bounded-family labeling closures at the anchor	RB-A/RB-D	explicit candidate families + gap/robustness audits	Section 9; Appendix AE; Appendix AF
overhead $\to$ gravity/dynamics	overhead-to-lapse/potential closure with error control	RB-B/RB-D	error budget + counterfactual regularization sweeps	Appendix AD.7; Appendix AD.9

I.3 A minimal workflow for upgrading intuition to audit statements

[Audit]When adding an interface intuition, we recommend the following minimal workflow:

- **Step 0 (decide the layer).** Decide whether the target sentence belongs to the theorem layer ([Math]), the operational dictionary ([Interface]), external calibration ([Match]), or audit/provenance ([Audit]).
- **Step 1 (objectify and constrain).** Replace narrative words ("stable", "unique", "memoryless") by explicit objects and constraints (functional equation, finite minimization, counting identity, or obstruction).

item	status	where defined	audit / falsifiability channel
tick-only primitive	Axiom 1.1	Section 1.1; Section 3	Fold_6 checks; Appendix AJ
CAP closure rule	Axiom 1.5, Definition H.1	Section 1.6; Appendix H	audit tables; Appendix AE
dyadic phase registers $\mathbb{Z}_{2^p}$	CAP-audited bounded closure (phase-lift dictionary)	Section 1.8 and Section 6.5; Appendix B	denom/map-family audits; Section 6
addressing basis (screen)	CAP-audited counterfactual closure	Section 5; Section 3.5	Table 5; Appendix AJ
rigid-frame display anchor	interface dictionary (derived localization criterion)	Section 1.3; Section 3	resolution staircase; Section 14
Hilbert orientation class	CAP tie-break (one-bit canonical representative)	Section 7.2; Definition 7.2	χ sign flips; Proposition 5.4; Prediction P2
three channels $\leftrightarrow$ three gauge factors	Proposition 8.2	Section 8.1	closed labeling; Theorem 9.17; holonomy diagnostics; Section 6
geometric normalization dictionaries	CAP-closed dictionaries (bounded families)	Section 11	rigidity targets and audits; Table 16; Appendix AE

Table 25: Audit-facing interface contract: tick and CAP as the primitive inputs; all other interface components are CAP-closed within explicit finite candidate families and audited by the listed channels.

- **Step 2 (choose a certificate form).** Record which RB form (A/B/C/D) certifies the step, and state the minimal inputs used.
- **Step 3 (separate matching inputs).** Move unit choices, reference scales, and external targets into [Match]and/or the inference ledger, never as premises.
- **Step 4 (audit hooks).** Record the candidate family, objective, tie-break, and reproduction script entry points when applicable.

J Audit overview: contract and inference map (supplement)

This appendix records two reader-facing audit summaries used throughout the main text: the audit-facing interface contract and the inference map.

K Inference ledger: what is implied within the declared input set

This appendix answers a compact audit question that arises repeatedly in the HPA–Ω program: if one does *not* introduce any additional axioms or free continuous inputs beyond what is explicitly declared in the main text, what physically meaningful conclusions can be inferred, and what is their dependency status? We summarize the answer as a layered ledger. The purpose is not to add new claims, but to make explicit which statements are (i) theorem-level consequences of finite combinatorics, (ii) finite protocol constructions, (iii) conditional interface implications under stated dictionaries, and (iv) bounded-complexity closures with reported mismatch factors. Appendix G provides the expanded tick + CAP derivation spine (candidate families, objectives, and tie-breaks); the present ledger is the compact status summary.

Notation for status tags. We use five audit-facing tags:

- **[Math]** theorem-level statement in the mathematical layer (finite definitions and proofs).

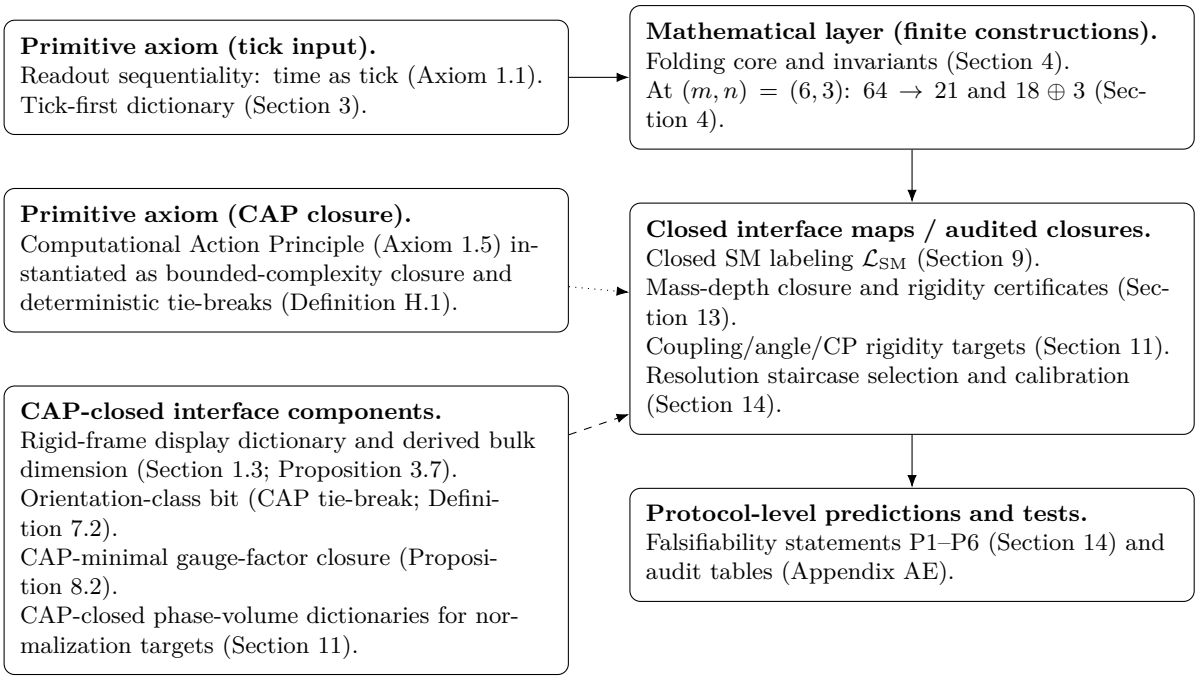

Figure 5: Inference map of the paper under the two-axiom spine (tick input and CAP closure). Solid: theorem-level; dashed: interface dictionaries in protocol language; dotted: CAP-audited selection.

- [**Prot**] finite protocol construction (explicit algorithm on a finite model; no continuum limit assumed).
- [**Iface**] physical identification statement (a dictionary/closure declaration stated in protocol language).
- [**CAP**] bounded-complexity closure (finite candidate family + deterministic tie-break rules).
- [**Open**] explicitly recorded open problem (not closed within the declared input set).

Matching-layer dictionaries (units, scheme dependence, threshold conventions) are recorded explicitly as such in the main text; they are not treated as new premises here.

K.1 Declared inputs (minimal list)

The paper's declared protocol primitives are recorded in Table 25 and Figure 5. In the strict tick-only program pursued here, the only *primitive* inputs are:

- **Tick** (scan iteration count) as the time variable (Axiom 1.1; Section 3).
- **CAP** as the universal selection/closure rule within declared finite candidate families (Axiom 1.5; Definition H.1; Appendix H).

All other items that appear throughout the paper (golden-branch slope, addressing basis, anchor selection, orientation-class tie-break, phase-register choices, and coupling/CP normalizations) are treated either as theorem-level definitions in the finite model, or as CAP-closed interface components *within explicitly declared finite candidate families with deterministic tie-break rules*; matching-layer reference conventions (PDG/CODATA, scheme/scale) are recorded explicitly and are not counted as premises.

Audit reading. Whenever the main text reports a "closed" numerical value for a physical quantity, the intended status is **[Iface]** (a dictionary/normalization choice) together with **[CAP]** (closure within a stated finite hypothesis class), and any residual deviation from PDG/CODATA conventions is interpreted as a matching-layer factor rather than as a theorem-level claim.

K.2 Mathematical-layer consequences (no physical identification needed)

Stable-sector grammar and counts.

- **[Math] Fibonacci admissible counts.** For every $m \geq 1$, the φ-admissible set $X_m \subset \Omega_m$ (forbidden substring "11") satisfies $|X_m| = F_{m+2}$ (Lemma 4.5). In particular, $|X_6| = 21$.
- **[Math] Canonical π-split.** For $m \geq 4$, the wrap-around predicate D_π induces a canonical cyclic/boundary split $X_m = X_m^{\mathrm{cyc}} \sqcup X_m^{\mathrm{bdry}}$ with $|X_m^{\mathrm{bdry}}| = F_{m-2}$ and $|X_m^{\mathrm{cyc}}| = F_{m+2} - F_{m-2}$ (Proposition 4.8). At $m = 6$ this is $21 = 18 \oplus 3$ with explicit boundary words (Corollary 4.9).
- **[Math] Fold surjectivity.** The truncation folding map $\mathrm{Fold}_m : \{0, \ldots, 2^m - 1\} \twoheadrightarrow X_m$ is surjective for every $m \geq 1$ (Proposition 4.20), and in particular $\mathrm{Fold}_6 : \{0, \ldots, 63\} \twoheadrightarrow X_6$ (Lemma 4.16).
- **[Math] Canonical integer labeling of X_6.** The Zeckendorf-value map $V : X_6 \to \{0, \ldots, 20\}$ is a bijection (Proposition 4.15).

Hilbert-path chirality sign law.

- **[Math] Parity and traversal reversal flip χ.** For the discrete Hilbert chirality index χ defined in (15), any reflection and traversal reversal flip its sign, while orientation-preserving rigid motions preserve it (Proposition 5.4).

K.3 Finite protocol constructions (computable, no continuum limit assumed)

Discrete connection/holonomy skeleton at $(m, n) = (6, 3)$.

- **[Prot] A deterministic S_4 edge connection.** At the $m = 6$ anchor, stable-type fibers satisfy $|P(w)| \in \{2, 3, 4\}$. Padding to 4 slots and minimizing Hamming-cost matchings yields a deterministic edge transport $p_{a \to b} \in S_4$ (Lemma 6.4).
- **[Prot] Gauge-invariant plaquette signatures.** Under local relabelings of fiber slots, plaquette holonomy transforms by conjugation, so its S_4 cycle type is invariant (Proposition 6.6).
- **[Prot] Dyadic phase-lift and a CP-odd invariant.** Given a bounded low-complexity phase map family τ and dyadic denominator $\mathrm{denom} = 2^p$, the phase-lifted edge transport produces a finite holonomy model with an induced Jarlskog-type invariant J (Section 6.5). The role of $\mathbb{Z}_{128}$ is explicit at $p = 7$ (Remark 6.11).

K.4 Interface-level implications (conditional on stated dictionaries)

Rigid-frame coarse-lock anchor and the vacuum sector.

- **[Iface] Localization admissibility threshold.** Under the rigid-frame display anchor (Section 1.3), window lengths $m < 6$ are sub-admissible for *single-window* coarse rigid-frame display and are treated as protocol-rejected as localized matter within this interface dictionary (Section 1.3.1; see also Remark 1.4 for scope).

- [Iface] **Ghost-sector vacuum microstructure at fixed m.** Even at fixed m, microstates outside the admissible grammar are protocol-unstable. At $m = 6$, the ghost-sector size is $|\Omega_6 \setminus X_6| = 64 - 21 = 43$ (Section P).

Gauge fields as compensating connections.

- [Iface] **Compensation is forced by finite fibers.** When stable labels have nontrivial fibers, cross-site comparison requires an additional transport rule; local relabelings imply a gauge redundancy (Proposition 8.1).
- [Iface]+[CAP] **Three-factor closure and the SM gauge triple.** If compensation decomposes into three commuting classes and gauge factors are modeled as compact unitary groups, then CAP-minimal selection within the stated factorization family yields $U(1) \times SU(2) \times SU(3)$ up to finite quotients (Proposition 8.2).

Chirality, antimatter, and CP-sign anchoring.

- [Iface] **Parity as protocol change.** Under the canonical orientation-bit convention, the only physically distinguishable discrete choice in the D_4 layout family is the orientation class detected by $\mathrm{sgn}(\chi)$ (Definition 7.2, Proposition 7.3).
- [Iface] **Conjugation-as-reversal and antimatter dual.** Phase conjugation of the scan orbit corresponds to scan reversal up to an initial-phase flip (Lemma 7.5 and Lemma 7.6), yielding a protocol antimatter dual by word reversal (Definition 7.9).
- [Iface] **Chirality-anchored CP sign.** Within a fixed protocol class and a fixed PDG parameterization, CP-odd sign conventions are anchored by $\mathrm{sgn}(\chi)$ (Definition 7.7).

Closed labeling and minimal chiral content.

- [Iface]+[CAP] **Closed 21-type labeling at the anchor.** Once one commits to the split semantics (cyclic $\leftrightarrow$ matter multiplets, boundary $\leftrightarrow$ gauge-factor classes) and to the stated deterministic ordering rules, the labeling map $\mathcal{L}_{\mathrm{SM}}$ is uniquely fixed (Theorem 9.17).
- [Iface] **Anomaly-neutral closure forces a sterile ν_R.** Closing the cyclic count to 18 with the smallest anomaly-neutral extension selects a sterile singlet ν_R with $Y = 0$; anomaly cancellation is unchanged by adding ν_R (Proposition 9.6).

K.5 Quantitative rigidity targets and closures (within stated finite families)

The following are recorded in the main text as explicit low-complexity targets or bounded-complexity selections, together with mismatch factors and audit context (Appendix AE):

- [Iface]+[CAP] **Electromagnetic impedance target.** $\alpha_{\mathrm{em\,geo}}^{-1} = 4\pi^3 + \pi^2 + \pi$ under the declared primitive phase-space family and serial aggregation dictionary (Theorem AF.9).
- [Iface]+[CAP] **Electroweak volume target.** $\alpha^{-1}(\mu_Z) = 13\pi^2$ and $\sin^2\theta_W(\mu_Z) = 3/13$ under the weighted-volume dictionary fixed by discrete invariants (Theorem AF.14).
- [Iface]+[CAP] **CP volume/multiplicity target.** $J_{\mathrm{geo}} = 1/(11\pi^7)$ under the declared CP-odd phase-space and multiplicity dictionary (equation (85) and Proposition AF.25).
- [CAP] **Discrete mixing closures.** CKM magnitudes (Proposition AF.27) and PMNS mixing sines plus bounded-denominator δ closure (Proposition AF.30 and Table 90).

- **[CAP] Mass-depth rigidity.** Within the bounded integer ansatz, the coefficients $(2, 5, 1)$ are rigidly selected (Proposition AG.1).
- **[CAP] Resolution staircase calibration.** Within the bounded family $r_{\text{step}} = k\pi$ ($1 \leq k \leq 10$), the calibration $r_{\text{step}} = 2\pi$ is uniquely selected under the stated objectives against fixed reference anchors (the Z scale, and optionally a conservative QCD-scale anchor), which enter only as matching-layer comparison inputs (Proposition 14.4).
- **[CAP] Scalar-sector uplift marker.** The Higgs–Z depth offset closure $\Delta r_{HZ} = 2/3$ is selected within the stated bounded rational family (Proposition AH.1), consistent with treating scalar behavior as uplift/coarse-graining dependent rather than as a new $m = 6$ stable type (Proposition 8.12).

K.6 Continuum representatives: action, field equations, and thermodynamics (frequency-first)

Equivalence semantics and the frequency-first dictionary.

- **[Iface] Physical objects as equivalence classes.** Appendix AA formalizes the semantic quotients already used throughout the paper (tick-origin shifts, projection-fiber equivalence, local relabelings/gauge, coarse-graining preorder, and action equivalence).
- **[Iface] Frequency as a primary derived quantity.** Frequency in tick units is defined by phase advance $\omega = \Delta\theta/\Delta t$ (Definition AA.1) and tied to mass/energy/temperature dictionaries (Appendix AA and Appendix Y).

CAP-closed continuum action skeleton.

- **[Iface]+[CAP] CAP-minimal covariant action representative.** Appendix AD.4 records a finite candidate family of local covariant term types and a bounded rational coefficient box, and states a CAP-minimal action skeleton S_{eff} (Proposition AD.1).

Field equations from variation.

- **[Math] Einstein–Yang–Mills equations (given the CAP-selected representative).** Appendix AD.5 records the Euler–Lagrange equations obtained by varying the representative action: Einstein equation with total stress (Theorem AD.2), Yang–Mills equations (Proposition AD.5), and the χ-sector amplitude equation (Proposition AD.6).

Thermodynamics and entropic force.

- **[Iface]+[CAP] Entropy as state counting and CAP as free-energy closure.** Appendix AD.6 closes entropy/temperature in coarse-graining language and records a CAP free-energy selection template on finite candidate families (Proposition AD.8), together with the entropic-force response definition.

Overhead gravity and the χ reconstruction protocol.

- **[Iface] Overhead-to-gravity closure (weak field).** Appendix AD.7 records the dictionary $\chi \mapsto N \mapsto g_{00} \mapsto \Phi$ and the resulting weak-field source template $\rho_{\text{eff}} \propto -\Delta\chi$, together with a one-parameter fit for γ.
- **[Prot] Executable $\chi(x)$ reconstruction protocol.** Appendix AD.8 records a Hilbert-binning $\to$ window-word $\to$ folding-statistics pipeline that reconstructs $\chi(x)$ from data or simulations.

Quantum readout and Born probabilities.

- [**Iface**] **POVM/instrument interface.** Appendix AD.10 records POVM readout and instrument update rules as the minimal quantum interface for finite observers.
- [**Iface**] **Born-probability rigidity.** Appendix AD.10 records two closure routes: a counting template aligned with projection-induced degeneracies and the Gleason–Busch uniqueness theorem.

Running couplings and cosmology as resolution flow.

- [**Iface**] **RG dictionary in the r coordinate (self-contained).** Appendix AD.11 records the r-flow form of RG equations and the semantics of threshold matching as discrete uplifts.
- [**Iface**] **Cosmology as resolution initialization/flow.** Appendix AD.12 records the capacity-growth (inflation-like) mechanism from $|X_m| \sim \varphi^m$ and a discrete background energy-budget matching hypothesis.

Connection to falsifiability. The falsifiability statements P1–P6 in Section 14 are phrased entirely in this protocol language: they depend on the declared interface items above and on audited finite constructions, and they do not add new theorem-level premises beyond the stated input set. In particular, the staircase-threshold locations in P3 are conditional on the stated r_{step} calibration and its reference anchors, while P1/P2/P4/P5/P6 do not require that numerical calibration to be stated.

K.7 Open problems (not closed within the declared input set)

The following gaps are explicitly acknowledged as [**Open**]. They are *not* implied by the tick-only primitives or by the finite folding core, and closing them would require additional theorem-level inputs or a stronger universality framework. For discussion and pointers, see Section 15.7.

- [**Open**] **Gauge-group uniqueness beyond the stated bounded family.** The paper closes $U(1) \times SU(2) \times SU(3)$ only conditionally under compactness/factorization and a declared finite candidate family (Proposition 8.2). Deriving the candidate family from microscopic scan/readout architecture remains open; within the stated family, the minimizer is robust under several natural label choices (Appendix AI and Proposition AI.1).
- [**Open**] **Uniqueness/inevitability of the folding map.** Alternative deterministic dyadic$\to X_m$ bridges exist and can change fiber statistics (Appendix Q). Within the bounded counterfactual family audited at $m = 6$, the natural value-consistency condition $F(V(w)) = w$ selects the Zeckendorf-truncation map uniquely (Proposition Q.2). More generally, within the natural shifted Zeckendorf-window family $\text{Fold}_m^{(s)}$ the same condition forbids all nonzero shifts (Proposition 4.23). Global uniqueness beyond such bounded families remains open. More generally, a principled uniqueness theorem for Fold_m, or an operational universality theorem making predictions bridge-insensitive at readout scale, remains open.
- [**Open**] **Continuum Yang–Mills/EFT emergence from finite connections.** The finite S_4 holonomy diagnostic is closed at the protocol layer (Section 6), but deriving continuum gauge dynamics and EFT running from the finite skeleton is not done here.
- [**Open**] **Global model selection / look-elsewhere across families.** Within-family audits are provided (Appendix AE), but a global prior/MDL principle comparing different hypothesis families and quantifying the overall look-elsewhere effect remains open.

- **[Open] Scalar/Yukawa sector and RG-running closure.** The anchor closes a minimal chiral labeling and treats scalar behavior as uplift/coarse-graining dependent (Appendix AH); deriving Yukawa structures and SM β-functions from the finite protocol is open.

L Sturmian readouts: factor complexity and entropy-rate bounds

This appendix closes a small proof gap used implicitly in Remark 2.3 of Section 2: for the canonical two-interval window partition associated with an irrational rotation, the induced binary readout is Sturmian and has linear factor complexity $p(n) = n + 1$, hence zero entropy rate. The argument is elementary and is included here to keep the paper self-contained at the theorem level.

L.1 Mechanical words as canonical interval codings

Fix an irrational slope $\alpha \in (0,1) \setminus \mathbb{Q}$ and an intercept $\rho \in \mathbb{R}$. Let $R_\alpha : \mathbb{T} \to \mathbb{T}$ be the rotation $R_\alpha(x) = x + \alpha \pmod 1$, and write $x_n := \rho + n\alpha \pmod 1$. Consider the *canonical* half-open window of length α,

$$W_\alpha := [1-\alpha, 1) \subset \mathbb{T}. \tag{24}$$

Define the binary readout by

$$w_n := \mathbf{1}\{x_n \in W_\alpha\} \in \{0,1\}. \tag{25}$$

Proposition L.1 (Window coding as a mechanical word)**.** *For every $n \in \mathbb{Z}$ one has*

$$w_n = \lfloor (n+1)\alpha + \rho \rfloor - \lfloor n\alpha + \rho \rfloor. \tag{26}$$

Proof. Write $\{t\} := t - \lfloor t \rfloor$ for the fractional part. Then $x_n = \{n\alpha + \rho\}$. One has $w_n = 1$ iff $x_n \in [1-\alpha, 1)$, i.e. iff $\{n\alpha + \rho\} \geq 1 - \alpha$, which is equivalent to $\{n\alpha + \rho\} + \alpha \geq 1$. This last condition holds iff $\lfloor n\alpha + \rho + \alpha \rfloor = \lfloor n\alpha + \rho \rfloor + 1$, which is exactly the stated difference-of-floors identity. □

Remark L.2 (Why the window length matters)**.** *The reduction of the factor complexity to $p(n) = n+1$ hinges on the canonical choice that the window length equals the rotation slope. For a general interval window W of arbitrary length, the coding $\mathbf{1}\{x_n \in W\}$ is still a rotation coding, but it need not be Sturmian. The present paper uses only the canonical two-interval partition determined by α (equivalently, a length-α window or its complement).*

L.2 Factor complexity $p(n) = n + 1$

For a bi-infinite binary sequence $w = (w_n)_{n \in \mathbb{Z}}$ and $n \geq 1$, let $\mathcal{L}_n(w)$ denote the set of length-n factors (contiguous subwords)

$$\mathcal{L}_n(w) := \{w_k w_{k+1} \cdots w_{k+n-1} : k \in \mathbb{Z}\} \subset \{0,1\}^n,$$

and define the *factor complexity* by $p(n) := |\mathcal{L}_n(w)|$.

Theorem L.3 (Canonical rotation window coding is Sturmian)**.** *Let $\alpha \in (0,1) \setminus \mathbb{Q}$ and let $w_n = \mathbf{1}\{\rho + n\alpha \in W_\alpha\}$ with $W_\alpha = [1-\alpha, 1)$ as above. Assume $\rho \not\equiv -k\alpha \pmod 1$ for all $k \in \mathbb{Z}$ (so the orbit never lands exactly on the window boundary). Then w is aperiodic and satisfies*

$$p(n) = n + 1 \qquad \text{for all } n \geq 1. \tag{27}$$

Equivalently, w is Sturmian in the standard complexity sense.

Proof. **Step 1: $p(n) \le n+1$ (a partition by n+1 breakpoints).** Fix $n \ge 1$ and define the length-n block map

$$F_n : \mathbb{T} \to \{0,1\}^n, \qquad F_n(x) := (\mathbf{1}\{x \in W_\alpha\}, \mathbf{1}\{x+\alpha \in W_\alpha\}, \dots, \mathbf{1}\{x+(n-1)\alpha \in W_\alpha\}).$$

For each $j = 0, \dots, n-1$, the indicator $\mathbf{1}\{x + j\alpha \in W_\alpha\}$ can change only when $x + j\alpha$ crosses a boundary point of W_α, namely 0 or $1-\alpha$. Thus F_n is locally constant on $\mathbb{T}$ away from the set of breakpoints

$$B_n := \bigcup_{j=0}^{n-1} \left(\{-j\alpha\} \cup \{1-\alpha-j\alpha\}\right) \subset \mathbb{T}.$$

Because $1-\alpha-j\alpha \equiv -(j+1)\alpha \pmod 1$, one has

$$B_n = \{-k\alpha : k = 0, 1, \dots, n\},$$

which has exactly $n+1$ distinct points since $\alpha \notin \mathbb{Q}$. These points partition $\mathbb{T}$ into $n+1$ half-open intervals $I_0, \dots, I_n$ on each of which F_n is constant. Therefore the image $F_n(\mathbb{T})$ contains at most $n+1$ distinct length-n words, so $p(n) \le n+1$.

Step 2: $p(n) \ge n+1$ (every interval is realized). Since α is irrational, the rotation R_α is minimal: the orbit $\{x_k\}_{k\in\mathbb{Z}}$ is dense in $\mathbb{T}$. Because the orbit avoids the finite breakpoint set B_n by assumption, it intersects the interior of each interval I_r. For any $r \in \{0, \dots, n\}$ choose k_r with $x_{k_r} \in \mathrm{int}(I_r)$. Then $F_n(x_{k_r}) \in \mathcal{L}_n(w)$ is the length-n factor starting at k_r. Moreover, if $r \ne r'$ then x_{k_r} and $x_{k_{r'}}$ lie in different intervals on which F_n is constant. At each breakpoint $b_k = -k\alpha \in B_n$, at least one coordinate of F_n changes across b_k (indeed b_k is a boundary point for the $j = k$ or $j = k-1$ coordinate, within $0 \le j \le n-1$), so adjacent intervals yield distinct words. Hence $F_n(x_{k_r}) \ne F_n(x_{k_{r'}})$. Thus at least $n+1$ distinct factors occur, so $p(n) \ge n+1$.

Combining Step 1 and Step 2 gives $p(n) = n+1$.

Step 3: aperiodicity. If w were periodic with period $q \ge 1$, then $\mathbf{1}\{x_k \in W_\alpha\} = \mathbf{1}\{x_k + q\alpha \in W_\alpha\}$ for all $k \in \mathbb{Z}$, i.e. the sets W_α and $W_\alpha - q\alpha$ have identical membership on the dense orbit $\{x_k\}$. If $W_\alpha \ne W_\alpha - q\alpha$ as subsets of $\mathbb{T}$, then their symmetric difference contains a nonempty open arc (both are half-open intervals). By density, that arc would contain some orbit point x_k, contradicting the membership equality above. Hence $W_\alpha = W_\alpha - q\alpha$. For a nontrivial interval W_α this implies $q\alpha \equiv 0 \pmod 1$, contradicting $\alpha \notin \mathbb{Q}$. Therefore w is aperiodic. □

L.3 Zero entropy rate

The linear factor bound $p(n) = n+1$ immediately implies that Sturmian readouts carry information in correlations but have vanishing entropy *rate*.

Corollary L.4 (Topological entropy)**.** *Let w be as in Theorem L.3. Then the topological entropy of its factor language is zero:*

$$h_{\mathrm{top}} := \lim_{n\to\infty} \frac{1}{n} \log p(n) = \lim_{n\to\infty} \frac{1}{n} \log(n+1) = 0.$$

Corollary L.5 (Block Shannon entropy bound)**.** *Let (X, σ) be the shift-orbit closure of w, and let μ be any shift-invariant probability measure on X. Let $P_n(u) := \mu([u])$ denote the μ-probability of the cylinder set of a word $u \in \{0,1\}^n$. Then the block entropy*

$$H_n(\mu) := -\sum_{u\in\{0,1\}^n} P_n(u) \log P_n(u)$$

satisfies

$$H_n(\mu) \le \log p(n) = \log(n+1), \qquad \textit{hence} \qquad \limsup_{n\to\infty} \frac{H_n(\mu)}{n} = 0.$$

Proof. Only words $u \in \mathcal{L}_n(w)$ can have $P_n(u) > 0$, so the sum is supported on at most $p(n)$ terms. Any probability distribution supported on at most $p(n)$ points has Shannon entropy at most $\log p(n)$, with equality only for the uniform distribution. Using $p(n) = n + 1$ from Theorem L.3 gives the claimed bound. □

M Sturmian readout language vs. golden-mean admissible language

The main text uses two closely related but *different* symbolic objects:

- the *Sturmian* word produced by a scan–projection readout (Section 2 and Appendix L), and
- the *Zeckendorf-admissible* digit language X_m (Section 4), equivalently the length-m block language of the golden-mean shift.

This appendix records the precise relationship and resolves a common point of confusion: a Sturmian readout has zero entropy rate, while the golden-mean admissible language has exponential growth with rate $\log \varphi$. There is no contradiction because the Sturmian factor language is a strict subset of the golden-mean admissible block language.

M.1 Golden-mean shift and its block language

Definition M.1 (Golden-mean shift)**.** *Let*

$$\Sigma_{\mathrm{GM}} := \{x \in \{0,1\}^{\mathbb{Z}} : \ x_i x_{i+1} = 0 \ \forall i \in \mathbb{Z}\},$$

and let $\sigma : \Sigma_{\mathrm{GM}} \to \Sigma_{\mathrm{GM}}$ be the left shift $(\sigma x)_i = x_{i+1}$.

Definition M.2 (Block language)**.** *For $n \geq 1$, define the length-n block language of Σ_{GM} by*

$$\mathcal{L}_n(\Sigma_{\mathrm{GM}}) := \{x_i x_{i+1} \cdots x_{i+n-1} : \ x \in \Sigma_{\mathrm{GM}}, \ i \in \mathbb{Z}\}.$$

Equivalently, $\mathcal{L}_n(\Sigma_{\mathrm{GM}})$ is the set of all length-n binary words containing no adjacent 1's.

Lemma M.3 (Identification with X_n and Fibonacci growth)**.** *For every $n \geq 1$ one has*

$$\mathcal{L}_n(\Sigma_{\mathrm{GM}}) = X_n, \qquad |X_n| = F_{n+2}.$$

In particular, the topological entropy of Σ_{GM} is $h_{\mathrm{top}}(\Sigma_{\mathrm{GM}}) = \log \varphi$.

Proof. The identification $\mathcal{L}_n(\Sigma_{\mathrm{GM}}) = X_n$ is immediate from the forbidden-adjacency definition. The Fibonacci count is Lemma 4.5. Finally, $h_{\mathrm{top}}(\Sigma_{\mathrm{GM}}) = \lim_{n\to\infty} \frac{1}{n} \log |\mathcal{L}_n(\Sigma_{\mathrm{GM}})| = \lim_{n\to\infty} \frac{1}{n} \log F_{n+2} = \log \varphi$ by Binet asymptotics (Remark 10.2). □

M.2 A Sturmian representative inside the golden-mean shift

Definition M.4 (Fibonacci word (substitution fixed point))**.** *Let τ be the substitution on $\{0,1\}$ given by*

$$\tau(0) = 01, \qquad \tau(1) = 0.$$

Starting from 0 and iterating τ yields a nested sequence of finite words $\tau^k(0)$. Their limit in the product topology is a one-sided infinite word $f = f_0 f_1 f_2 \cdots$, called the Fibonacci word.

Lemma M.5 (No adjacent ones; no triple zeros)**.** *The Fibonacci word f contains no adjacent ones. Moreover, it contains no factor 000.*

Proof. **No adjacent ones.** In $\tau(0) = 01$ the symbol 1 is always followed by 0, and $\tau(1) = 0$ contains no 1 at all. Therefore, in every iterate $\tau^k(0)$ any occurrence of 1 is followed by 0, so the factor 11 never appears. Passing to the limit preserves forbidden factors, hence f contains no 11.

No triple zeros. Every 0 in $\tau^k(0)$ is either the image of a 1 (namely $\tau(1) = 0$) or the first symbol of $\tau(0) = 01$. In particular, every 0 produced as the first symbol of $\tau(0)$ is immediately followed by a 1. Thus a run of zeros can only arise from a pattern where a 1-image 0 is adjacent to the initial 0 of some $\tau(0)$ block, creating at most two consecutive zeros. Since 11 never occurs, two 1-images cannot be adjacent, so runs of zeros have length at most 2 and 000 is impossible. □

Corollary M.6 (Strict language inclusion)**.** *Let $\mathcal{L}_n(f)$ denote the set of length-n factors of the Fibonacci word f. Then for every $n \geq 1$,*

$$\mathcal{L}_n(f) \subseteq X_n,$$

and the inclusion is strict for all $n \geq 3$.

Proof. By Lemma M.5, f contains no 11, hence every factor of length n contains no 11 and therefore lies in X_n. For strictness at $n \geq 3$, the word 000 is in X_3 but is not a factor of f by Lemma M.5, so $\mathcal{L}_3(f) \neq X_3$ and hence $\mathcal{L}_n(f) \neq X_n$ for all $n \geq 3$. □

M.3 Two entropies and what $\log \varphi$ means here

The Fibonacci word is Sturmian (it is the canonical characteristic word on the golden branch), so its factor complexity satisfies $|\mathcal{L}_n(f)| = n + 1$ and its entropy rate is zero (Appendix L). In contrast, the full admissible block language X_n grows as F_{n+2} and defines a positive topological entropy $\log \varphi$ (Lemma M.3).
In this paper, the base φ in the resolution coordinate is tied to the *capacity/growth rate of the admissible stable-type language* X_n (Remark 10.2), not to the Shannon entropy rate of the Sturmian time-series readout.

N Discrepancy certificates from continued fractions (Ostrowski/Denjoy–Koksma)

This appendix makes explicit the quantitative link used in Section 2.3.1: continued-fraction data of the scan slope α yield deterministic finite-N discrepancy bounds for the Kronecker orbit $x_n = x_0 + n\alpha \pmod 1$. We keep the discussion in the one-dimensional setting relevant to window counts, where the key estimate reduces to interval indicators.

N.1 Star discrepancy and a rational baseline

For a finite point set $P_N = \{x_0, \ldots, x_{N-1}\} \subset [0, 1)$, the one-dimensional star discrepancy is

$$D_N^*(P_N) := \sup_{a \in [0,1]} \left| \frac{1}{N} \#\{0 \leq n \leq N-1 : \ x_n < a\} - a \right|.$$

Lemma N.1 (Equally spaced points have discrepancy $1/N$)**.** *Let $y_n = \{y_0 + n/N\}$ for $n = 0, \ldots, N-1$. Then $D_N^*(\{y_0, \ldots, y_{N-1}\}) = 1/N$.*

Proof. The set $\{y_n\}$ is a translate of the uniform grid $\{j/N\}_{j=0}^{N-1}$, and star discrepancy is translation invariant on the circle. For the grid, for any $a \in [0, 1]$ the count $\#\{j/N < a\}$ equals either $\lfloor Na \rfloor$ or $\lceil Na \rceil - 1$, so the normalized error differs from a by at most $1/N$. Taking $a = j/N$ shows the bound is attained, hence $D_N^* = 1/N$. □

N.2 Continued fractions and convergents

Let $\alpha \in (0,1) \setminus \mathbb{Q}$ with continued fraction $\alpha = [0; a_1, a_2, \ldots]$ and convergents p_k/q_k. We use the standard recurrences

$$q_{-1} = 0,\ q_0 = 1, \qquad q_{k+1} = a_{k+1} q_k + q_{k-1} \quad (k \geq 0),$$

and similarly for p_k.

Lemma N.2 (Best-approximation error of convergents)**.** *For every $k \geq 0$,*

$$\left| \alpha - \frac{p_k}{q_k} \right| < \frac{1}{q_k q_{k+1}} \leq \frac{1}{q_k^2}.$$

Proof. This is a standard continued-fraction property; see, e.g., [27, Ch. 10] or [28]. □

N.3 A discrepancy bound at convergent lengths

Let $x_n = \{x_0 + n\alpha\}$ be the scan orbit. At convergent lengths $N = q_k$, the orbit is uniformly close to the rational orbit with step p_k/q_k. This yields a simple $O(1/N)$ discrepancy bound with an explicit constant.

Lemma N.3 (Convergent-length discrepancy bound)**.** *Fix $k \geq 0$ and set $N := q_k$. Let $P_N(\alpha) = \{x_0, \ldots, x_{N-1}\}$ with $x_n = \{x_0 + n\alpha\}$. Then*

$$D_N^*(P_N(\alpha)) \leq \frac{8}{N}.$$

Proof. Let $\beta := p_k/q_k$ and define the rational reference points $y_n := \{x_0 + n\beta\}$. Since $\gcd(p_k, q_k) = 1$, the set $\{y_n\}_{n=0}^{N-1}$ is exactly an equally spaced grid (a permutation of $\{x_0 + j/N\}$), so by Lemma N.1 one has $D_N^*(\{y_n\}) = 1/N$.

By Lemma N.2, $\delta := |\alpha - \beta| < 1/N^2$. For each $n \in \{0, \ldots, N-1\}$, the points x_n and y_n differ by the rotation $n(\alpha - \beta)$ on the circle, so their *circular distance* obeys

$$d_{\mathbb{T}}(x_n, y_n) \leq n\,\delta < \frac{1}{N}, \qquad d_{\mathbb{T}}(u, v) := \min\{|u - v|,\, 1 - |u - v|\}.$$

Fix $a \in [0,1]$ and compare the counts $C_x(a) := \#\{0 \leq n \leq N-1 :\ x_n < a\}$ and $C_y(a) := \#\{0 \leq n \leq N-1 :\ y_n < a\}$. If x_n and y_n fall on different sides of the interval boundary of $[0, a)$, then y_n must lie within circular distance $< 1/N$ of one of the two boundary points $\{0, a\}$ (otherwise a $< 1/N$ perturbation cannot change membership in the half-open interval). Since the y_n are $1/N$-spaced, there are at most 3 indices n within circular distance $< 1/N$ of each boundary point, hence $|C_x(a) - C_y(a)| \leq 6$ for every a.

Hence

$$\left| \frac{C_x(a)}{N} - a \right| \leq \left| \frac{C_y(a)}{N} - a \right| + \frac{|C_x(a) - C_y(a)|}{N} \leq \frac{1}{N} + \frac{6}{N} = \frac{7}{N},$$

uniformly over a. Taking the supremum gives $D_N^*(P_N(\alpha)) \leq 7/N$. We state the slightly looser constant $8/N$ for a clean margin. □

N.4 Ostrowski decomposition and a general finite-N bound

The convergent-length bound uplifts to arbitrary N using the Ostrowski representation, which decomposes N into a sum of convergent denominators.

Definition N.4 (Ostrowski representation (statement)). *Let $\alpha = [0; a_1, a_2, \ldots]$ be irrational with convergent denominators q_k. Every integer $N \geq 1$ admits a (unique) representation*

$$N = \sum_{k=0}^{m} b_k q_k, \qquad 0 \leq b_k \leq a_{k+1},$$

with the usual local admissibility constraint $b_k = a_{k+1} \Rightarrow b_{k-1} = 0$ for $k \geq 1$.

Proposition N.5 (Digit-sum discrepancy bound). *Let $x_n = \{x_0 + n\alpha\}$ and let $P_N(\alpha) = \{x_0, \ldots, x_{N-1}\}$. Write $N = \sum_{k=0}^{m} b_k q_k$ in Ostrowski form. Then*

$$D_N^*(P_N(\alpha)) \leq \frac{8}{N} \sum_{k=0}^{m} b_k.$$

Proof. Decompose the prefix $\{0, 1, \ldots, N-1\}$ into consecutive blocks of lengths q_k, repeated b_k times for each k (largest k to smallest). For each such block of length q_k, apply Lemma N.3 with the intercept shifted to the block start (i.e. replace x_0 by x_t for the corresponding start index t). This bounds the star discrepancy of each length-q_k block by $8/q_k$, equivalently its *count error* (unnormalized) by at most 8. Summing count errors over all blocks yields a total count error bounded by $8 \sum_k b_k$ uniformly in the threshold a. Dividing by N and taking the supremum in the definition of D_N^* gives the stated bound. □

N.5 Bounded type and why the golden branch is minimax

Corollary N.6 (Bounded-type logarithmic rate). *Assume α has bounded partial quotients: $a_k \leq A$ for all k. Then for every $N \geq 1$,*

$$D_N^*(P_N(\alpha)) \leq \frac{8A}{N}\Big(4 + \log_\varphi N\Big), \qquad E_N := N D_N^*(P_N(\alpha)) \;\leq\; 8A\,(4 + \log_\varphi N).$$

Proof. Let $N = \sum_{k=0}^{m} b_k q_k$ be the Ostrowski representation. Since $b_k \leq a_{k+1} \leq A$, one has $\sum_{k=0}^{m} b_k \leq A(m+1)$.

Next, since $a_{k+1} \geq 1$ for all k, the denominators satisfy $q_{k+1} = a_{k+1} q_k + q_{k-1} \geq q_k + q_{k-1}$. With $q_0 = 1$ and $q_1 \geq 1$, this implies $q_m \geq F_{m+1}$ for all $m \geq 1$. By Binet's formula, $F_{m+1} \geq \varphi^{m-1}/\sqrt{5}$ for $m \geq 1$, hence if $q_m \leq N$ then

$$m - 1 \leq \log_\varphi(\sqrt{5}\, N) \leq 2 + \log_\varphi N.$$

Therefore $m + 1 \leq 4 + \log_\varphi N$.

Combining with Proposition N.5 yields

$$D_N^*(P_N(\alpha)) \leq \frac{8}{N} \sum_{k=0}^{m} b_k \leq \frac{8A(m+1)}{N} \leq \frac{8A}{N}(4 + \log_\varphi N),$$

and multiplying by N gives the bound on E_N. □

Remark N.7 (Golden branch as a minimax bounded-type choice). *The constant in Corollary N.6 depends monotonically on the bound A on continued-fraction digits. The golden branch is characterized by $a_k \equiv 1$, i.e. it is the unique irrational of constant type with the minimal possible bound $A = 1$. Thus, within the bounded-type class, it is the canonical minimax choice for discrepancy certificates at finite N: it gives the smallest explicit worst-case upper bound in the audited family of certificates derived from digit sums.*

O Folding-core proofs and technical details (supplement)

This appendix collects longer proofs and technical details underlying the folding core in Section 4. It is intended to keep the main narrative short while preserving a fully explicit, auditable mathematical layer.

Scope. All proofs in this appendix refer to the folding map and admissible language as defined in Section 4 (in particular the Zeckendorf-truncation definition of Fold_6). The paper does not claim invariance of the reported fiber statistics under arbitrary alternative maps from $\{0,\dots,63\}$ to X_6; a bounded counterfactual sensitivity sweep is recorded separately in Appendix Q.

O.1 Defect operators and relaxation dynamics (optional interface semantics)

Definition O.1 (Defect operators on $\ell^2(\Omega_m)$)**.** *Given a nonnegative defect function $D:\Omega_m\to\mathbb{R}_{\geq 0}$, define the associated defect operator (still denoted D) on $\mathcal{H}_m=\ell^2(\Omega_m)$ by pointwise multiplication:*

$$(D\psi)(w) := D(w)\,\psi(w), \qquad \psi\in\ell^2(\Omega_m),\ w\in\Omega_m.$$

If D_1, D_2 are defect functions, then the corresponding operators commute.

Definition O.2 (Defect relaxation on $\ell^2(\Omega_m)$)**.** *Fix m and consider the nonnegative φ-defect operator D_φ (Definition O.1). Define the defect-relaxation semigroup by the auxiliary-time evolution*

$$\frac{\mathrm{d}}{\mathrm{d}\tau}\psi(\tau) = -D_\varphi\,\psi(\tau), \qquad \psi(0)=\psi_0\in\ell^2(\Omega_m), \tag{28}$$

where $\tau\geq 0$ indexes stabilization steps rather than scan iteration time.

Proposition O.3 (Attractor: convergence to the admissible sector)**.** *The solution of* (28) *is given pointwise by*

$$\psi(\tau)(w) = \mathrm{e}^{-\tau D_\varphi(w)}\psi_0(w).$$

Consequently $\psi(\tau)\to P_\varphi\psi_0$ in $\ell^2(\Omega_m)$ as $\tau\to\infty$, where P_φ is the orthogonal projection onto $\ell^2(X_m)$. Moreover the mismatch functional $\mathcal{M}(\tau):=\|D_\varphi\psi(\tau)\|_2^2$ obeys the explicit decay law

$$\mathcal{M}(\tau) = \mathrm{e}^{-2\tau}\,\mathcal{M}(0).$$

Proof. Since D_φ is a multiplication operator, (28) decouples on the basis $\{\delta_w\}_{w\in\Omega_m}$ and yields the stated closed form. Because $D_\varphi(w)\in\{0,1\}$, one has $\mathrm{e}^{-\tau D_\varphi(w)}\to\mathbf{1}\{D_\varphi(w)=0\}=\mathbf{1}\{w\in X_m\}$ as $\tau\to\infty$, which is exactly the action of P_φ on basis vectors and therefore gives ℓ^2 convergence. Finally, $D_\varphi\psi(\tau)=\mathrm{e}^{-\tau}D_\varphi\psi_0$, so $\mathcal{M}(\tau)=\mathrm{e}^{-2\tau}\mathcal{M}(0)$. □

Remark O.4 (Relation to least-discrepancy dynamics (context))**.** *Equation* (28) *is the minimal linear relaxation that suppresses defect support and makes the admissible sector an attractor. More general least-discrepancy dynamics can be formulated at the protocol layer as gradient flows on bounded parameter families, trading discrepancy certificates against implementation costs; see, e.g., [4–7]. In the present paper we use* (28) *only as a dynamical semantics for the static folding constraint and do not treat it as an additional premise for any theorem-level count.*

O.2 Full proofs and auxiliary tables for Fold_6

Full proof of Proposition 4.15. By Zeckendorf's theorem [25], every integer $M\in\mathbb{N}$ admits a unique expansion

$$M=\sum_{k\geq 1} c_k F_{k+1}, \qquad c_k\in\{0,1\}, \qquad c_k c_{k+1}=0.$$

For $0 \le M \le 20$, this expansion uses no Fibonacci weight beyond $F_7 = 13$, hence the digit vector $(c_1, \ldots, c_6)$ is well-defined and belongs to X_6, and satisfies $V(c_1 \cdots c_6) = M$. This proves that V is surjective onto $\{0, 1, \ldots, 20\}$.

For the range bound, if $w \in X_6$ has no adjacent ones, then the maximal value of $V(w)$ is attained by the alternating pattern $w = 010101$, giving

$$V(010101) = 2 + 5 + 13 = 20,$$

so indeed $V(X_6) \subset \{0, 1, \ldots, 20\}$. Finally, the Zeckendorf expansion is unique, so the digit vector (and therefore the word in X_6) realizing a given M is unique, hence V is injective. □

Full proof of Lemma 4.17. Let $N \in \{0, \ldots, 63\}$ and write its Zeckendorf digits as $N = \sum_{k \ge 1} c_k F_{k+1}$. Since $63 < F_{11} = 89$, one has $c_k = 0$ for all $k \ge 10$, so

$$N = \sum_{k=1}^{9} c_k F_{k+1} := \sum_{k=1}^{6} c_k F_{k+1} \; + \; 21\, c_7 \; + \; 34\, c_8 \; + \; 55\, c_9.$$

If $\mathrm{Fold}_6(N) = w$, then $c_k = w_k$ for $k = 1, \ldots, 6$, hence $\sum_{k=1}^{6} c_k F_{k+1} = V(w) = v$ and

$$N = v + 21\, c_7 + 34\, c_8 + 55\, c_9.$$

The Zeckendorf admissibility constraint is $c_k c_{k+1} = 0$. Thus if $w_6 = 1$ then $c_6 = 1$ forces $c_7 = 0$; and since $v \ge 13$ in this case, one also has $v + 55 > 63$, so $c_9 = 0$. The remaining admissible choices are $c_8 \in \{0, 1\}$, giving $N \in \{v, v + 34\}$.

If $w_6 = 0$ then $c_6 = 0$ imposes no restriction on c_7. The admissible one-hot tail choices $(c_7, c_8, c_9) \in \{(0,0,0), (1,0,0), (0,1,0), (0,0,1)\}$ produce the four candidates v, $v + 21$, $v + 34$, $v + 55$. The candidate with $c_9 = 1$ is valid if and only if $v + 55 \le 63$, i.e. $v \le 8$. If $9 \le v \le 12$, then $v + 55 > 63$, so only the first three candidates lie in $\{0, \ldots, 63\}$. All listed candidates satisfy Zeckendorf admissibility (no adjacent ones), hence their Zeckendorf digits have the same first six digits, so they map to w under Fold_6. □

Full proof of Theorem 4.18. Surjectivity follows from Lemma 4.16. The explicit fiber description in Lemma 4.17 shows that $|\mathrm{Fold}_6^{-1}(w)| \in \{2, 3, 4\}$ for every $w \in X_6$. Moreover, $|\mathrm{Fold}_6^{-1}(w)| = 2$ holds exactly when $w_6 = 1$. The number of admissible length-6 words ending with 1 is $|X_4| = F_6 = 8$ (fix the last two digits as 01 and choose any admissible 4-bit prefix), hence $|V_2| = 8$. Among the remaining 13 words with $w_6 = 0$, Lemma 4.17 gives preimage size 4 exactly when $V(w) \le 8$, i.e. for $v \in \{0, \ldots, 8\}$, yielding $|V_4| = 9$ by Proposition 4.15. The remaining 4 values $v \in \{9, 10, 11, 12\}$ yield preimage size 3, hence $|V_3| = 4$. Finally, for each boundary word w listed in Corollary 4.9 one has $w_6 = 1$ and $V(w) \in \{14, 17, 19\}$, so Lemma 4.17 gives the stated boundary-sector preimages. Appendix AE records the full table; the script `scripts/exp_fold6_stats.py` deterministically reproduces the same finite enumeration and writes the corresponding LaTeX fragments (Appendix AJ). □

Preimage size $\lvert\mathrm{Fold}_6^{-1}(w)\rvert$	number of types
2	8
3	4
4	9

Table 26: Degeneracy histogram for $\mathrm{Fold}_6 : \{0, \ldots, 63\} \twoheadrightarrow X_6$. Rows are reproduced by a deterministic enumeration over $N \in \{0, \ldots, 63\}$ implementing the definition of Fold_6 (`scripts/exp_fold6_stats.py`).

P The vacuum sector: ontology of protocol-unstable states

This section records diagnostics for the protocol-unstable complement $\Omega_m \setminus X_m$ (the *ghost sector*) across window lengths. For the protocol-level vacuum interpretation and the relation of the ghost sector to the folding core, see Section 1.3.1 and Remark 4.7.

A minimal instability witness. As a minimal instability witness on the full alphabet, define the adjacent-ones count

$$N_{11}(w) := \#\{\, i \in \{1, \dots, m-1\} \;:\; w_i = w_{i+1} = 1 \,\}.$$

Then $X_m = \{w \in \Omega_m : \; N_{11}(w) = 0\}$ and the protocol-unstable complement (ghost sector) is $\Omega_m \setminus X_m$.

Table 27 records the ghost-sector size together with the distribution mass in the first few violation bins and the mean violation count restricted to $\Omega_m \setminus X_m$. Rows are reproduced by the deterministic script `scripts/exp_ghost_sector_violation_stats.py`.

m	$\lvert X_m \rvert$	$\lvert \Omega_m \setminus X_m \rvert$	frac	$N_{11} = 1$	$N_{11} = 2$	$N_{11} = 3$	$N_{11} \geq 4$	mean N_{11} (ghost)
6	21	43	0.671875	20	13	7	3	1.8605
7	34	94	0.734375	38	29	16	11	2.0426
8	55	201	0.785156	71	60	39	31	2.2289
9	89	423	0.826172	130	122	86	85	2.4208
10	144	880	0.859375	235	241	187	217	2.6182
11	233	1815	0.886230	420	468	392	535	2.8209
12	377	3719	0.907959	744	894	806	1275	3.0288
13	610	7582	0.925537	1308	1686	1624	2964	3.2414
14	987	15397	0.939758	2285	3144	3222	6746	3.4583
15	1597	31171	0.951263	3970	5807	6304	15090	3.6793
16	2584	62952	0.960571	6865	10636	12189	33262	3.9039

Table 27: Vacuum-sector diagnostics in the adjacent-violation count N_{11} for the protocol-unstable complement $\Omega_m \setminus X_m$. The column "frac" is the fraction $|\Omega_m \setminus X_m|/|\Omega_m|$.

Distance to admissibility. As an additional diagnostic, we define a minimal repair cost $c(w)$ as the minimum number of bit flips $1 \to 0$ required to remove all adjacent-ones violations. Equivalently, if a word contains maximal runs of consecutive ones of lengths L, then $c(w) = \sum \lfloor L/2 \rfloor$. Table 28 summarizes the repair-cost distribution for the same m-sweep. Rows are reproduced by the deterministic script `scripts/exp_ghost_sector_repair_cost_stats.py`.

m	$\lvert X_m \rvert$	$\lvert \Omega_m \setminus X_m \rvert$	frac	$c = 1$	$c = 2$	$c = 3$	$c = 4$	$c \geq 5$	mean c (ghost)
6	21	43	0.671875	30	12	1	0	0	1.3256
7	34	94	0.734375	58	31	5	0	0	1.4362
8	55	201	0.785156	109	73	18	1	0	1.5572
9	89	423	0.826172	201	162	54	6	0	1.6809
10	144	880	0.859375	365	344	145	25	1	1.8102
11	233	1815	0.886230	655	707	361	85	7	1.9433
12	377	3719	0.907959	1164	1416	850	255	34	2.0804
13	610	7582	0.925537	2052	2778	1918	701	133	2.2209
14	987	15397	0.939758	3593	5358	4184	1806	456	2.3647
15	1597	31171	0.951263	6255	10188	8880	4425	1423	2.5113
16	2584	62952	0.960571	10835	19139	18422	10415	4141	2.6605

Table 28: Vacuum-sector diagnostics in the minimal repair cost $c(w)$ to reach admissibility (no consecutive ones) for the protocol-unstable complement $\Omega_m \setminus X_m$. The column "frac" is the fraction $|\Omega_m \setminus X_m|/|\Omega_m|$.

Q Folding-map counterfactuals at the $m = 6$ anchor

This appendix records a bounded counterfactual family of deterministic maps from the dyadic microstate index set $\{0, \ldots, 63\}$ to the admissible set X_6. The purpose is audit clarity: it makes explicit which finite combinatorial properties of the $64 \to 21$ folding picture are tied to the specific folding map adopted in the paper, and which properties survive under nearby low-complexity alternatives.

Q.1 A bounded counterfactual family

At the $m = 6$ anchor we identify microstates with a dyadic register $\{0, \ldots, 2^6 - 1\}$ and identify stable types with admissible words X_6 (no adjacent ones). The main text fixes the folding map Fold_6 by truncating Zeckendorf digits (Section 4). To provide look-elsewhere context at the level of the folding map itself, we compare Fold_6 to a small explicit family of counterfactual deterministic maps of comparable discrete description complexity:

- **FoldZ:** the baseline Zeckendorf-truncation map Fold_6 as defined in (12);
- **FoldZ-shift:** a one-digit shift of the Zeckendorf digit window (still a Zeckendorf substring);
- **FoldZ-rev:** reversal of the baseline output word (preserves admissibility as a word grammar);
- **Bin-repair:** a direct dyadic-word repair rule that removes each occurrence of the substring "11" by deterministically flipping the right bit in each offending pair.

Explicit definitions (self-contained). Let $N \in \{0, \ldots, 63\}$ and let $(c_k)_{k \geq 1}$ be its Zeckendorf digits.

- **FoldZ.** $\mathrm{FoldZ}(N) := (c_1, \ldots, c_6)$ (Definition (12)).
- **FoldZ-shift.** $\text{FoldZ-shift}(N) := (c_2, \ldots, c_7)$, padding by zeros if needed (i.e. set $c_k := 0$ for k beyond the Zeckendorf expansion length).
- **FoldZ-rev.** $\text{FoldZ-rev}(N) := \mathrm{rev}(\mathrm{FoldZ}(N))$ where $\mathrm{rev}(w_1 \cdots w_6) := w_6 \cdots w_1$.
- **Bin-repair.** Write the dyadic word of N as $b(N) = b_1 \cdots b_6 \in \{0,1\}^6$. Scan left-to-right and whenever a substring $b_i b_{i+1} = 11$ occurs, flip the right bit $b_{i+1} \leftarrow 0$. The resulting repaired word lies in X_6 by construction.

For each map we record: the image size (how many stable types are realized), whether the image equals X_6, and the induced preimage-size histogram over $\{0, \ldots, 63\}$. Rows are generated by `scripts/exp_fold_family_sensitivity.py`. Since the map family is defined explicitly above, the script serves only as a deterministic reproducer of the same finite sweep (audit artifact generation), not as an additional premise.

map	|Im|	surj. onto X_6	$g_{\min}$	$g_{\max}$	degeneracy histogram	status
`FoldZ`	21	yes	2	4	`2:8,3:4,4:9`	OK
`FoldZ-shift`	21	yes	1	6	`1:3,2:8,3:2,4:4,5:1,6:3`	OK
`FoldZ-rev`	21	yes	2	4	`2:8,3:4,4:9`	OK
`Bin-repair`	21	yes	1	8	`1:2,2:9,4:9,8:1`	OK

Table 29: Bounded counterfactual sweep of deterministic folding maps at $m = 6$. Here $g(w) := |\mathrm{Fold}^{-1}(w)|$ is the preimage size over $\{0, \ldots, 63\}$ for each map, and the histogram is reported as a compact list "g : #types". This table is an audit artifact: it shows which finite invariants are map-dependent within the stated small family.

Interpretation. Within this bounded family, surjectivity onto X_6 is not unique. What varies across maps is the induced fiber structure (the support and distribution of $g(w)$), which is the protocol-native input for later compensation/connection constructions. The main text fixes Fold_6 by the Zeckendorf-truncation definition and therefore fixes a specific fiber statistics package (Section 4 and Appendix O).

A partial closure: a natural fixed-point property selects FoldZ in this family. Define the Zeckendorf value map $V : X_6 \to \{0, \ldots, 20\}$ by Definition 4.14.

Definition Q.1 (Value consistency at the anchor)**.** *A deterministic map $F : \{0, \ldots, 63\} \to X_6$ is* value-consistent *if*

$$F(V(w)) = w \qquad \textit{for all } w \in X_6.$$

Proposition Q.2 (Within the bounded family, value consistency selects FoldZ)**.** *Within the four-map family* $\{\mathrm{FoldZ}, \mathrm{FoldZ\text{-}shift}, \mathrm{FoldZ\text{-}rev}, \mathrm{Bin\text{-}repair}\}$*, the unique value-consistent map (Definition Q.1) is* FoldZ*.*

Proof. Lemma 4.16 shows $\mathrm{FoldZ}(V(w)) = w$ for all $w \in X_6$, hence FoldZ is value-consistent.

To rule out the other three maps, take $w = 100000 \in X_6$. Then $V(w) = 1$ by (13). The Zeckendorf digits of 1 satisfy $c_1 = 1$ and $c_k = 0$ for $k \geq 2$. Therefore $\mathrm{FoldZ\text{-}shift}(1) = (c_2, \ldots, c_7) = 000000 \neq 100000$, so FoldZ-shift is not value-consistent. Also $\mathrm{FoldZ\text{-}rev}(1) = \mathrm{rev}(\mathrm{FoldZ}(1)) = 000001 \neq 100000$, so FoldZ-rev is not value-consistent. Finally, $b(1) = 000001$ and Bin-repair leaves it unchanged, hence $\mathrm{Bin\text{-}repair}(1) = 000001 \neq 100000$, so Bin-repair is not value-consistent. □

Scope. All theorem-level statements in Section 4 and Appendix O apply to the folding map as defined there. This appendix does not claim invariance under arbitrary map changes; it only records sensitivity within an explicit bounded counterfactual family.

R Forced interface lemmas under the tick + CAP spine

This appendix records several short interface lemmas in a form suitable for audit. It introduces *no new axioms* beyond the two declared primitives of the paper: tick as the executed input stream (Axiom 1.1) and CAP as the unique closure/selection rule on explicit finite candidate families (Axiom 1.5). The purpose is to make explicit the sense in which several "interface conventions" used in the main text are *forced* (or uniquely selected as minimal nontrivial choices) once one commits to the tick + CAP discipline.

R.1 Minimal coarse locking: one bit per independent parameter

Lemma R.1 (Minimal nontrivial coarse binning forces one bit per independent parameter)**.** *Let a protocol claim to* coarsely distinguish *k independent parameters in a single observation, in the minimal nontrivial sense that for each parameter there exist at least two disjoint bins whose membership is distinguishable in the readout. Then any single-shot readout alphabet that supports such a coarse distinction must have size at least 2^k. In particular, if the single-shot readout alphabet is binary length-m words $\Omega_m = \{0,1\}^m$, then necessarily $m \geq k$.*

Proof. For each parameter choose two distinguishable bins and label them by $\{0, 1\}$. Independence means that all 2^k bin-combinations are admissible joint coarse states. Therefore the readout alphabet must have at least 2^k distinct outcomes. If the alphabet is Ω_m, then $|\Omega_m| = 2^m \geq 2^k$, so $m \geq k$. □

Corollary R.2 (Single-window coarse rigid-frame budget)**.** *In a rigid-frame display dictionary in bulk dimension d, a pose is an element of the Euclidean group $SE(d)$ with*

$$\dim SE(d) = \frac{d(d+1)}{2}.$$

Under the minimal nontrivial coarse-binning convention of Lemma R.1, a single length-m window can support a single-shot coarse rigid-frame display only if

$$m \geq \dim SE(d) = \frac{d(d+1)}{2}.$$

Proof. Apply Lemma R.1 with $k = \dim SE(d)$. The dimension formula for $SE(d)$ is standard; see, e.g., [18]. □

Relation to the main text. Section 1.3 uses exactly this minimal nontrivial convention at the anchor $m = 6$ and then applies CAP to select the maximal admissible bulk dimension, yielding $d = 3$ (Proposition 3.7). The quantization/metric-entropy scaling used there for finer accuracy is standard [16, 17].

R.2 Unitarity forces compact internal redundancy groups

Proposition R.3 (Probability-preserving internal redundancy is compact (finite-dimensional case))**.** *Assume a continuum modeling dictionary in which local internal redundancy acts on a finite-dimensional complex Hilbert space by transformations that preserve transition probabilities between rays. Then the connected component of the internal redundancy group is (projectively) unitary and is therefore compact (up to finite quotients).*

Proof. By Wigner's theorem, any bijection of rays preserving transition probabilities is implemented by a unitary or antiunitary operator on the underlying Hilbert space, uniquely up to phase [48, 49, 87]. Antiunitary operators form a disconnected component, so any connected internal redundancy group is represented (projectively) by unitary operators. Thus the redundancy group embeds as a (closed) subgroup of the compact projective unitary group $PU(N) = U(N)/U(1)$, hence is compact. □

Relation to the main text. In the interface language of this paper, "gauge redundancy" is the freedom to relabel local readout bases without changing observable overlap/probability data. Under a standard continuum dictionary that represents this freedom by internal unitary rotations, compactness is therefore not an extra primitive but a consequence of probability preservation in finite-dimensional local descriptions. This is the compactness input used in Proposition 8.2.

R.3 Three commuting channels force a three-factor redundancy structure

Lemma R.4 (Independent local redundancy across commuting channels factorizes)**.** *Assume protocol mismatch certificates decompose into three commuting channel components and that, in the interface dictionary, each channel admits an independent local basis redundancy. Then the minimal local redundancy group factorizes as a direct product of three channelwise redundancies.*

Proof. Since channels commute, a mismatch certificate can be compared channel-by-channel. If the basis redundancy is independent in each channel, local gauge changes act independently on each component. Therefore the channelwise covariance law is a direct-product action, and the minimal redundancy group is the direct product of the three channel groups. □

Relation to the main text. This is the structural content of Proposition 8.3 in Section 8.1. Once a three-factor structure is fixed, CAP-minimal selection within the compact-factor candidate family yields the Standard Model triple up to finite quotients under the declared factor complexity label (Proposition 8.2 and Lemma 9.4); a bounded sensitivity sweep across alternative labels is recorded in Appendix AI.

R.4 Why the minimal chiral closure selects a sterile ν_R

Proposition R.5 (Minimal anomaly-neutral one-multiplet-per-generation closure forces a sterile singlet)**.** *Work under the PDG convention $Q = T_3 + Y$. Consider extending the Standard Model chiral fermion multiplet content by adding* exactly one *additional chiral multiplet per generation, with the requirement that: (i) local gauge and mixed gravitational anomalies remain canceled, and (ii) the global $SU(2)$ consistency condition is preserved. Then the added multiplet must be a gauge singlet with hypercharge $Y = 0$. Equivalently (up to charge conjugation), the unique minimal closure is a sterile right-handed neutrino ν_R per generation.*

Proof. The Standard Model anomaly-cancellation identities under $Q = T_3 + Y$ are standard [1, 2, 56]. If the added multiplet carries nontrivial $SU(3)$ charge, it contributes to $SU(3)^3$ and $SU(3)^2U(1)$ anomaly sums; with only one added multiplet per generation there is no compensator, so anomaly cancellation forces it to be an $SU(3)$ singlet.

If the added multiplet is an $SU(2)$ doublet (or any half-integer isospin representation), the parity of the number of $SU(2)$ doublets changes and can violate the global $SU(2)$ anomaly constraint [57]. With only one additional multiplet per generation and no compensator, preserving the global consistency condition forces the added multiplet to be an $SU(2)$ singlet.

Thus the only remaining possible charge is hypercharge. The mixed gravitational–hypercharge anomaly is proportional to $\sum Y$ and the cubic $U(1)_Y^3$ anomaly to $\sum Y^3$ over left-handed Weyl fields with multiplicities; the Standard Model sums vanish per generation [1, 56]. Adding a single $SU(3) \times SU(2)$ singlet multiplet contributes Y and Y^3. To preserve both anomaly cancellations without additional compensating matter, one must have $Y = 0$. □

Relation to the main text. Section 9 uses ν_R as the minimal anomaly-neutral closure of the 18 cyclic field-level targets and treats it as an interface choice audited by standard consistency constraints (Proposition 9.6). Proposition R.5 records the stronger uniqueness statement within the explicit minimal candidate family "one extra multiplet per generation".

R.5 Scalar absence at the minimal alphabet is forced by the closed 21-type contract

Proposition R.6 (No additional primitive stable type remains for a Higgs label at $m = 6$)**.** *At the anchor $(m, n) = (6, 3)$, the stable sector splits as $X_6 = X_6^{\mathrm{cyc}} \sqcup X_6^{\mathrm{bdry}}$ with $|X_6^{\mathrm{cyc}}| = 18$ and $|X_6^{\mathrm{bdry}}| = 3$. Under the closed interface contract adopted in this paper—cyclic types label the 18 field-level chiral multiplets and boundary types label the three gauge-factor connection classes—there is no remaining element of X_6 that can be assigned as an additional primitive stable-type label for a Higgs-like scalar. Accordingly, any scalar sector must enter either as (i) an EFT-level completion field in the continuum dictionary, or (ii) a protocol-emergent observable supported by resolution uplift and coarse graining.*

Proof. The split cardinalities are theorem-level facts at $m = 6$ (Section 4). The closed labeling map assigns the 18 cyclic types to the 18 chiral multiplets and assigns the 3 boundary types to the three gauge factors (Theorem 9.17). Therefore all 21 stable types are already consumed by the closed chiral/gauge interface at the anchor, leaving no unused stable label in X_6. □

n	m	plaquettes	1	2	2×2	3	4	mean $\lvert J\rvert$ (3/4)	mean J (3/4)	failures
1	2	1	1	0	0	0	0	0	+0	0
2	4	9	9	0	0	0	0	0	+0	0
3	6	49	24	19	1	3	2	0.0470847	+0.0207138	0
4	8	225	126	44	3	42	10	0.0284115	+0.0101108	0
5	10	961	619	198	24	95	25	0.0325905	+0.00800293	0
6	12	3969	2512	788	82	378	209	0.0191774	+0.00111322	0
7	14	16129	11566	2623	268	1210	462	0.0104386	+0.000145988	0
8	16	65025	50323	10731	1420	1781	770	0.00748166	+0.000270661	0

Table 30: Balanced-chain sweep for the holonomy and phase-lifted CP signal across $(n,m) \in \{(1,2),(2,4),(3,6),(4,8),(5,10),(6,12),(7,14),(8,16)\}$. Rows are generated by `scripts/exp_holonomy_balanced_chain_sweep.py`.

Relation to the main text. This is the audit-level content behind the Higgs-status remarks in Section 9 (Remark 9.1) and the scalar-sector closure statements in Section 8.4.

S Extended holonomy sweeps and robustness diagnostics (supplement)

This appendix records extended finite sweeps and robustness variants for the protocol-connection holonomy diagnostics of Section 6. The main text focuses on definitions and representative diagnostics at the minimal anchor; the material below provides additional evidence across refined balanced pairs (n,m) and across bounded-complexity variant families.

Audit note (bounded scans, not free-form fitting). All tables in this appendix are produced by deterministic *bounded scans* over explicitly specified finite families (loop sizes, phase denominators, phase-map families, and global relabelings), with deterministic tie-break rules. The accompanying scripts write the resulting LaTeX fragments for reproducibility; they do not introduce new degrees of freedom beyond the stated bounded families.

S.1 Balanced-chain sweep across $(n,m) = (1,2),(2,4),(3,6),(4,8),(5,10),(6,12),(7,14),(8,16)$

To probe how the finite connection/holonomy statistics behave under a minimal balanced refinement, we sweep the chain $m = 2n$ for $n \in \{1,2,3,4,5,6,7,8\}$. At each scale we build the same deterministic S_4-valued edge transport by truncating/padding each Fold_m fiber to rank 4 and selecting the minimum-cost bijection under Hamming distance on m-bit microstates. We then summarize plaquette holonomy cycle types and the phase-lifted CP-odd signal at the phase denominator $\mathrm{denom} = 2^m$.

Balanced-chain permutation-robust mixing fits. Using the same phase-lifted holonomy extraction at each (n,m) in the balanced chain, we can apply the same global $S_3 \times S_3$ relabeling fit to PMNS- and CKM-style target sines. Tables 31 and 32 report the resulting best fits at each scale.

Loop-scale sweep (k×k square holonomies). The unit-plaquette holonomy is the smallest closed loop. As an additional finite-resolution diagnostic, we can compute phase-lifted holonomies around $k \times k$ square loops (for small k) and repeat the same 3/4-cycle restriction and $S_3 \times S_3$ permutation-robust mixing fits. Tables 33–40 summarize the resulting cycle-type counts and PMNS/CKM fit objectives for $k \in \{1,2,3\}$ on the $n = 3$ grid.

n	m	plaquettes	best (σ_r, σ_c)	s_{12}	s_{23}	s_{13}	E_∞	E_1	mean $\lvert J\rvert$
3	6	49	`(2, 0, 1)/(1, 2, 0)`	0.7387	0.8513	0.1546	0.288	0.476	0.00480456
4	8	225	`(0, 2, 1)/(1, 0, 2)`	0.8434	0.8706	0.1895	0.420	0.835	0.0068287
5	10	961	`(1, 2, 0)/(0, 1, 2)`	0.8658	0.9017	0.1881	0.446	0.889	0.00420356
6	12	3969	`(1, 2, 0)/(0, 1, 2)`	0.8721	0.9011	0.1730	0.454	0.811	0.00289537
7	14	16129	`(1, 2, 0)/(0, 1, 2)`	0.9114	0.9485	0.1116	0.498	1.028	0.00110661
8	16	65025	`(0, 2, 1)/(1, 0, 2)`	0.9318	0.9331	0.0879	0.520	1.272	0.00031132

Table 31: Balanced-chain permutation-robust fit to PMNS target sines (finite diagnostic). Rows are generated by `scripts/exp_holonomy_balanced_chain_perm_fit.py`.

n	m	plaquettes	best (σ_r, σ_c)	s_{12}	s_{23}	s_{13}	E_∞	E_1	mean $\lvert J\rvert$
3	6	49	`(2, 1, 0)/(2, 1, 0)`	0.4036	0.2930	0.1546	3.670	6.195	0.00480456
4	8	225	`(2, 1, 0)/(2, 1, 0)`	0.2964	0.3150	0.1612	3.712	6.000	0.0068287
5	10	961	`(2, 1, 0)/(2, 1, 0)`	0.2309	0.2424	0.1774	3.807	5.584	0.00420356
6	12	3969	`(2, 1, 0)/(2, 1, 0)`	0.2205	0.2398	0.1575	3.688	5.443	0.00289537
7	14	16129	`(2, 1, 0)/(2, 1, 0)`	0.1381	0.1643	0.0859	3.082	4.926	0.00110661
8	16	65025	`(0, 1, 2)/(0, 1, 2)`	0.1283	0.1247	0.0879	3.105	4.747	0.00031132

Table 32: Balanced-chain permutation-robust fit to CKM target sines (finite diagnostic). Rows are generated by `scripts/exp_holonomy_balanced_chain_perm_fit.py`.

Single-loop best fits (bounded scan). Finally, instead of averaging over a loop family, one can select a single loop together with a bounded phase denominator and a global $S_3 \times S_3$ relabeling to best fit a target triple of sines. Table 36 reports the best single-loop fits for PMNS- and CKM-style targets over a bounded search space.

Two-loop chains (bounded composition). One can also form a bounded family of effective holonomies by composing two selected loops (allowing inverses) before extracting the sines. Table 37 reports the best two-loop chain fits over a finite search family built from 3/4-cycle square loops.

Two-loop chains with mixed cycle types. If one enlarges the admissible loop pool to include additional nontrivial holonomy cycle types (e.g. 2-cycles and 2×2 cycles), one can obtain a substantially improved CKM-style fit within a still finite, auditable search box. Table 38 reports the best two-loop chain fits under a restricted phase family and a mixed-cycle loop pool.

Angle/CP trends under phase-denominator refinement. Finally, we can sweep the phase denominator denom $= 2^p$ and record the induced mean angles (s_{12}, s_{23}, s_{13}) and mean $|J|$ on the nontrivial holonomy subset (3/4 cycles), together with the log mismatch to J_{geo}. Table 41 reports this diagnostic sweep.

A bounded-denominator PMNS fit (finite diagnostic). As an illustrative closure-style diagnostic, we can select denom $= 2^p$ to fit representative PMNS sines (s_{12}, s_{23}, s_{13}) using the same 3/4-cycle aggregated mean angles. Table 42 reports the candidate sweep and the minimax/sum objectives.

Permutation-robust fits (global relabeling search). The mapping from an effective 3×3 unitary matrix to PDG angles depends on how row/column indices are identified with flavor/mass labels. As a bounded-complexity diagnostic, we therefore allow a *global* relabeling by a pair of permutations in $S_3 \times S_3$ and select the best pair for each denominator by the same

k	loops	1	2	2×2	3	4	other
1	49	24	19	1	3	2	0
2	36	10	17	1	3	5	0
3	25	7	10	1	6	1	0
4	16	2	9	2	2	1	0
5	9	1	3	0	5	0	0
6	4	0	2	0	0	2	0
7	1	0	0	0	0	1	0

Table 33: Cycle-type counts of S_4 holonomy permutations for $k \times k$ square loops on the $n = 3$ grid. Rows are generated by `scripts/exp_holonomy_loop_scale_sweep.py`.

k	3/4 loops	mean angle [deg]	min [deg]	max [deg]
1	5	108.000	90.000	120.000
2	8	101.250	90.000	120.000
3	7	115.714	90.000	120.000
4	3	110.000	90.000	120.000
5	5	120.000	120.000	120.000
6	2	90.000	90.000	90.000
7	1	90.000	90.000	90.000

Table 34: Loop-scale sweep of rotation angles in the sign-twisted standard $SO(3) \subset SU(3)$ representation bridge, restricted to 3/4-cycle holonomies. Rows are generated by `scripts/exp_holonomy_loop_scale_su3_angle_sweep.py`.

minimax objective on (s_{12}, s_{23}, s_{13}). Tables 43 and 44 report the resulting denominator sweeps for PMNS- and CKM-style target sines.

Phase-map family sweep (low-complexity index transforms). The phase lift attaches a discrete phase to each microstate index. To bound look-elsewhere freedom, we restrict to a small explicit family of low-complexity bit transforms τ (identity, Gray map, bit reversal, and complement) and rerun the bounded-denominator fits. Tables 45 and 46 report, for each map in a fixed small family, the best $(\text{denom}, \sigma_r, \sigma_c)$ under the same objective, together with the log mismatch of the resulting mean $|J|$ (3/4 cycles) to J_{geo}.

S.2 A soft transport variant (temperature-like smoothing)

The strict minimum-cost matching rule produces a discrete S_4 transport on edges. As an optional robustness diagnostic, one can form a *soft* transport matrix from the full 4×4 cost matrix between padded fibers, weighted by a temperature-like parameter β via $\exp(-\beta\,\text{cost})$, and then deterministically orthonormalize columns to obtain a unitary edge transport. Sweeping β interpolates between a highly mixed transport ($\beta \to 0$) and a sharp near-minimum transport (large β). Tables 47 and 48 report permutation-robust fits to PMNS- and CKM-style target sines under this soft transport, together with the mean $|J|$ on the resulting effective holonomies.

T Protocol EFT embedding (supplement)

This appendix collects a concrete local field-theoretic embedding whose purpose is consistency and translation to standard continuum language. The finite folding and labeling results of the paper remain theorem-level statements in finite readout language; the present section is an interface/matching supplement.

k	3/4 loops	mean W	min W	max W	mean $1-W$
1	5	0.318352	0.168535	0.428145	0.681648
2	8	0.182942	-0.00151624	0.428145	0.817058
3	7	0.186643	0	0.377409	0.813357
4	3	0.117196	-0.0883019	0.441406	0.882804
5	5	0.399583	0	0.642398	0.600417
6	2	0.102449	-0.0017954	0.206693	0.897551
7	1	-0.00151624	-0.00151624	-0.00151624	1.00152

Table 35: Loop-scale Wilson-loop style diagnostics $W = \Re(\mathrm{tr}(Q))/3$ from phase-lifted effective holonomies, restricted to 3/4-cycle loops [42, 43]. Rows are generated by `scripts/exp_holonomy_wilson_loop_sweep.py`.

target	map	denom	k	(x,y)	cycle	best (σ_r,σ_c)	s_{12}	s_{23}	s_{13}	$\lvert J\rvert$	E_∞	E_1	$E_\infty^{(2)}$	Δ
PMNS	gray	64	4	(1,0)	2	(0, 1, 2)/(2, 0, 1)	0.6159	0.8334	0.164866	1.12757e-17	0.121	0.337	0.121	0.000
CKM	gray	512	3	(3,0)	2	(1, 0, 2)/(1, 0, 2)	0.1137	0.0804	0.00457281	1.79584e-19	0.679	1.473	0.706	0.027

Table 36: Best single-loop fits to PMNS/CKM target sines under a bounded scan over $k \times k$ loops ($k \le 7$), phase denominators denom $= 2^p$ ($6 \le p \le 18$), and global relabelings in $S_3 \times S_3$. Rows are generated by `scripts/exp_holonomy_single_loop_bestfit.py`.

T.1 A minimal effective field theory embedding (protocol EFT)

This subsection records a concrete field-theoretic embedding whose purpose is *consistency*, not a full derivation from the folding layer. It answers a minimal technical question: given the three-channel stable-sector template and the closed labeling of Section 9, what is a well-defined local action whose gauge structure is $SU(3) \times SU(2) \times U(1)$, whose matter content matches the 18 cyclic labels, and for which anomaly cancellation holds in the standard sense?

Fields. Let $\{\psi_f\}_{f \in \mathcal{F}_{\mathrm{SM}}}$ denote the 18 left-handed Weyl fermion multiplets in one-to-one correspondence with the cyclic labels of Theorem 9.17, with quantum numbers $(SU(3), SU(2))_Y$ as recorded in Table 15. Let $G_\mu = G_\mu^A T^A$ be an $SU(3)$ gauge field, $W_\mu = W_\mu^a \tau^a$ an $SU(2)$ gauge field, and B_μ a $U(1)$ gauge field. Optionally (to form the usual renormalizable SM EFT), include a complex scalar Higgs doublet H with $(SU(3), SU(2))_Y = (1,2)_{1/2}$. In the present paper, this Higgs field is included only at the level of a standard EFT completion (Remark 9.1); it is not asserted to correspond to a distinct stable type at the minimal window length. The corresponding protocol-level scalar-sector closure (scalar observables by coarse graining/uplift and an EFT coupling dictionary) is recorded in Proposition 8.12.

Gauge-invariant action. With standard normalizations [1,2,48], define the local Lagrangian density

$$\begin{aligned}\mathcal{L}_{\text{prot-EFT}} = &-\frac{1}{4} G^A_{\mu\nu} G^{A\,\mu\nu} - \frac{1}{4} W^a_{\mu\nu} W^{a\,\mu\nu} - \frac{1}{4} B_{\mu\nu} B^{\mu\nu} \\ &+ \sum_{f \in \mathcal{F}_{\mathrm{SM}}} \psi_f^\dagger \, \mathrm{i} \bar{\sigma}^\mu D_\mu \psi_f \\ &+ (D_\mu H)^\dagger (D^\mu H) - V(H) \; + \; \mathcal{L}_{\mathrm{Yuk}}(H, \psi)\,, \end{aligned} \tag{29}$$

where the covariant derivative is

$$D_\mu = \partial_\mu - \mathrm{i} g_3 \, G^A_\mu T^A - \mathrm{i} g_2 \, W^a_\mu \tau^a - \mathrm{i} g_1 \, Y \, B_\mu, \tag{30}$$

target	$\lvert\Theta\rvert$	map	denom	loop 1	loop 2	best (σ_r,σ_c)	s_{12}	s_{23}	s_{13}	$\lvert J\rvert$	E_∞	E_1	$E_\infty^{(2)}$	Δ
PMNS	7195968	gray	256	(7,0,0,4,-)	(2,5,4,4,+)	(2,1,0)/(2,1,0)	0.5512	0.7422	0.149208	0.0262604	0.011	0.021	0.011	0.000
CKM	7195968	id	512	(6,0,1,4,-)	(4,2,3,3,+)	(1,2,0)/(2,1,0)	0.3490	0.0353	0.00287544	3.21877e-05	0.442	0.934	0.442	0.000

Table 37: Best two-loop chain fits to PMNS/CKM target sines under a bounded scan over a finite family: (i) choose two square loops whose underlying S_4 holonomy is a 3/4-cycle, allowing inverses; (ii) choose a phase map (`id/gray/bitrev/not`) and denominator denom $= 2^p$ $(6 \le p \le 18)$; (iii) choose a global relabeling in $S_3 \times S_3$. Rows are generated by `scripts/exp_holonomy_two_loop_chain_bestfit.py`.

target	$\lvert\Theta\rvert$	map	denom	loop 1	loop 2	best (σ_r,σ_c)	s_{12}	s_{23}	s_{13}	$\lvert J\rvert$	E_∞	E_1	$E_\infty^{(2)}$	Δ
PMNS	7962624	gray	256	(7,0,0,4,-)	(2,5,4,4,+)	(2,1,0)/(2,1,0)	0.5512	0.7422	0.149208	0.0262604	0.011	0.021	0.011	0.000
CKM	7962624	gray	512	(1,3,4,2,+)	(2,3,5,3,+)	(2,1,0)/(1,2,0)	0.2776	0.0374	0.00445891	3.40912e-05	0.213	0.459	0.213	0.000

Table 38: Best two-loop chain fits to PMNS/CKM target sines under a bounded scan over mixed-cycle square loops (cycle types in `{2,2x2,3,4}`), with a restricted phase family (map `{id,gray}`, denom $\in \{256, 512, 1024\}$) and a global relabeling in $S_3 \times S_3$. Rows are generated by `scripts/exp_holonomy_two_loop_chain_mixed_cycles_bestfit.py`.

with T^A and τ^a the generators in the representation appropriate to the field and Y its hypercharge. The Yukawa sector $\mathcal{L}_{\rm Yuk}$ is included only if one wishes to match the renormalizable Standard Model EFT; its detailed structure is not needed for the finite folding claims of this paper.

Equations of motion (standard). Varying (29) yields the standard gauge and matter field equations [1, 2, 48]. For the non-abelian sectors one obtains the Yang–Mills equations with currents determined by the chiral matter and (optionally) the Higgs field,

$$(D^\mu G_{\mu\nu})^A = g_3\, J^A_\nu, \qquad (D^\mu W_{\mu\nu})^a = g_2\, J^a_\nu, \tag{31}$$

while the abelian hypercharge sector satisfies

$$\partial^\mu B_{\mu\nu} = g_1\, J^Y_\nu. \tag{32}$$

The fermions obey the chiral Dirac equations $\mathrm{i}\bar\sigma^\mu D_\mu \psi_f = \partial\mathcal{L}_{\rm Yuk}/\partial\psi_f^\dagger$, and, when included, the Higgs satisfies a covariant Klein–Gordon equation $D^\mu D_\mu H + \partial V/\partial H^\dagger = -\partial\mathcal{L}_{\rm Yuk}/\partial H^\dagger$. Thus the protocol EFT provides an explicit dynamical embedding in standard field-theory language; the folding layer enters only through the finite stable-sector selection and labeling that determine which degrees of freedom are retained at the anchor.

Electroweak symmetry breaking and the Higgs mode (standard). If one chooses the usual Mexican-hat potential $V(H) = -\mu^2 H^\dagger H + \lambda (H^\dagger H)^2$ with $\mu^2 > 0$ and $\lambda > 0$, then the vacuum selects $\langle H\rangle \neq 0$ and breaks $SU(2) \times U(1)$ to $U(1)_{\rm em}$. In unitary gauge one may write

$$H(x) = \frac{1}{\sqrt{2}} \begin{pmatrix} 0 \\ v + h(x) \end{pmatrix},$$

so that three would-be Goldstone modes are absorbed as the longitudinal polarizations of $W^\pm$ and Z, while h is the physical spin-0 Higgs excitation. This standard mechanism supplies gauge-boson masses through $(D_\mu H)^\dagger (D^\mu H)$ and fermion masses through $\mathcal{L}_{\rm Yuk}$, but it is not used as a premise for any of the finite-resolution folding or labeling statements in this paper.

k	loops	3/4 loops	best (σ_r, σ_c)	s_{12}	s_{23}	s_{13}	E_∞	E_1	mean $\lvert J\rvert$
1	49	5	`(1, 2, 0)/(2, 0, 1)`	0.5890	0.7457	0.3389	0.831	0.902	0.0470847
2	36	8	`(1, 2, 0)/(2, 0, 1)`	0.5673	0.7137	0.3252	0.790	0.847	0.0350064
3	25	7	`(1, 0, 2)/(2, 0, 1)`	0.4841	0.7469	0.3028	0.718	0.865	0.0304645
4	16	3	`(2, 1, 0)/(1, 2, 0)`	0.6599	0.7382	0.2988	0.705	0.880	0.0172157
5	9	5	`(2, 1, 0)/(2, 1, 0)`	0.5003	0.7064	0.4070	1.014	1.160	0.0154748
6	4	2	`(0, 1, 2)/(1, 0, 2)`	0.5569	0.9274	0.1825	0.228	0.445	0.0281961
7	1	1	`(2, 1, 0)/(1, 2, 0)`	0.3556	0.8503	0.1623	0.443	0.679	0.0200472

Table 39: Permutation-robust fit to PMNS target sines for $k \times k$ square holonomies (finite diagnostic), restricted to 3/4-cycle loops. Rows are generated by `scripts/exp_holonomy_loop_scale_sweep.py`.

k	loops	3/4 loops	best (σ_r, σ_c)	s_{12}	s_{23}	s_{13}	E_∞	E_1	mean $\lvert J\rvert$
1	49	5	`(1, 0, 2)/(2, 0, 1)`	0.5890	0.6378	0.3389	4.455	8.136	0.0470847
2	36	8	`(1, 0, 2)/(2, 0, 1)`	0.5673	0.6476	0.3252	4.413	8.072	0.0350064
3	25	7	`(1, 2, 0)/(2, 0, 1)`	0.4841	0.6172	0.3028	4.342	7.794	0.0304645
4	16	3	`(2, 0, 1)/(1, 2, 0)`	0.6599	0.6368	0.2988	4.329	8.122	0.0172157
5	9	5	`(2, 0, 1)/(2, 1, 0)`	0.5003	0.6676	0.4070	4.638	8.201	0.0154748
6	4	2	`(0, 2, 1)/(1, 0, 2)`	0.5569	0.3740	0.1825	3.836	6.927	0.0281961
7	1	1	`(2, 0, 1)/(1, 2, 0)`	0.3556	0.5264	0.1623	3.718	6.703	0.0200472

Table 40: Permutation-robust fit to CKM target sines for $k \times k$ square holonomies (finite diagnostic), restricted to 3/4-cycle loops. Rows are generated by `scripts/exp_holonomy_loop_scale_sweep.py`.

Where the φ–π–e channels enter. The folding layer provides three commuting defect predicates/operators at finite window length (Section 4). In this EFT embedding, the three channels enter as *protocol constraints* that restrict which local readout modes are treated as light degrees of freedom:

- the φ-channel selects admissible words (no adjacent ones), yielding a stable subspace of dimension $|X_m| = F_{m+2}$ at window length m (Lemma 4.5);
- the π-channel further splits the stable space into cyclic/boundary sectors, with $|X_m^{\mathrm{cyc}}| \oplus |X_m^{\mathrm{bdry}}|$ given by Proposition 4.8;
- the e-channel records the standard analytic normalization of the golden-mean shift via its Artin–Mazur zeta function (Lemma 4.10 and Lemma 4.11).

Operationally, one may view (29) as the low-energy EFT *after* this selection: the fields ψ_f represent the cyclic stable labels, and the three boundary labels select the three gauge-factor classes (Section 9). This does *not* yet constitute a derivation of the SM gauge group from the finite combinatorics; it is an explicit consistent embedding compatible with the interface axioms.

Anomaly cancellation. Because the gauge sector is chiral, the EFT is consistent only if gauge and mixed anomalies cancel. For the Standard Model hypercharge assignments under $Q = T_3 + Y$, the anomaly sums vanish per generation [1, 2, 56]. In our labeling closure, adding ν_R with $Y = 0$ does not affect these sums (Proposition 9.6), so (29) is anomaly-free with the stated matter content.

Remark T.1 (Status)**.** *The purpose of the protocol EFT is to make the "compensating connections" claim mathematically precise at the level of a local gauge-invariant action with the correct*

denom	p	mean s_{12} (3/4)	mean s_{23} (3/4)	mean s_{13} (3/4)	mean $\lvert J\rvert$ (3/4)	$\log(\text{mean}/J_{\text{geo}})$	$\lvert\cdot\rvert$
64	6	0.6836	0.8197	0.4799	0.0470847	+7.355	7.355
128	7	0.6934	0.7867	0.4642	0.034465	+7.043	7.043
256	8	0.7156	0.8792	0.4045	0.0221376	+6.601	6.601
512	9	0.7186	0.8895	0.3655	0.010419	+5.847	5.847
1024	10	0.7194	0.8916	0.3463	0.00511243	+5.135	5.135
2048	11	0.7196	0.8921	0.3366	0.00254376	+4.437	4.437
4096	12	0.7196	0.8922	0.3316	0.00127032	+3.743	3.743
8192	13	0.7196	0.8923	0.3291	0.000634963	+3.049	3.049
16384	14	0.7196	0.8923	0.3279	0.000317457	+2.356	2.356
32768	15	0.7196	0.8923	0.3272	0.000158725	+1.663	1.663
65536	16	0.7196	0.8923	0.3269	7.93623e-05	+0.970	0.970
131072	17	0.7196	0.8923	0.3268	3.96811e-05	**+0.276**	**0.276**
262144	18	0.7196	0.8923	0.3267	1.98406e-05	-0.417	0.417

Table 41: Phase-denominator sweep for mean extracted angles and mean $|J|$ on 3/4-cycle plaquettes at $n = 3$ (finite diagnostic), together with the log mismatch to J_{geo}. Rows are generated by `scripts/exp_holonomy_phase_lift_angles_denom_sweep.py`.

denom	p	s_{12} (3/4)	s_{23} (3/4)	s_{13} (3/4)	E_∞	E_1
64	6	0.6836	0.8197	0.4799	1.179	1.493
128	7	0.6934	0.7867	0.4642	1.146	1.433
256	8	0.7156	0.8792	0.4045	1.008	1.438
512	9	0.7186	0.8895	0.3655	0.906	1.353
1024	10	0.7194	0.8916	0.3463	0.853	1.302
2048	11	0.7196	0.8921	0.3366	0.824	1.275
4096	12	0.7196	0.8922	0.3316	0.809	1.260
8192	13	0.7196	0.8923	0.3291	0.802	1.253
16384	14	0.7196	0.8923	0.3279	0.798	1.249
32768	15	0.7196	0.8923	0.3272	0.796	1.247
65536	16	0.7196	0.8923	0.3269	0.795	1.246
131072	17	0.7196	0.8923	0.3268	0.794	1.245
262144	18	0.7196	0.8923	0.3267	**0.794**	**1.245**
`best/second`	$p = 18/17$	–	–	–	0.794/0.794	$\Delta = 0.000$

Table 42: Bounded-denominator fit to representative PMNS mixing sines using the phase-lifted holonomy angle extraction (finite diagnostic). Rows are generated by `scripts/exp_holonomy_phase_lift_pmns_denom_fit.py`.

group structure and anomaly constraints. Within the stated interface rules (three compensation classes, dimension-as-complexity for gauge factors, and the auditable ordering closure), the gauge-factor assignment and the chiral representation content are uniquely fixed at the minimal anchor: the Lie-algebra factor dimensions $(1, 3, 8)$ *pin the compact factors to* $\mathfrak{u}(1) \oplus \mathfrak{su}(2) \oplus \mathfrak{su}(3)$ *(Lemma 9.4), and the matter multiplet assignment is the unique closed labeling map (Theorem 9.17). Accordingly,* (29) *is recorded here as a closed EFT embedding consistent with those uniquely fixed interface identifications and with standard anomaly constraints.*

U Interface isomorphisms: stable sectors, mismatch certificates, and active correction

This appendix records a shared protocol-level template in the HPA–Ω program: finite-resolution scan–projection readout induces symbolic words and coarse observables; stability/consistency constraints select a compressed visible sector; and sustained low-entropy structure requires either passive compensation (connections enforcing consistency) or active correction (feedback control

denom	p	best (σ_r, σ_c)	s_{12}	s_{23}	s_{13}	E_∞	E_1
64	6	`(1, 2, 0)/(2, 0, 1)`	0.5890	0.7457	0.3389	0.831	0.902
128	7	`(1, 0, 2)/(2, 1, 0)`	0.5263	0.7071	0.4583	1.133	1.227
256	8	`(1, 2, 0)/(2, 0, 1)`	0.5279	0.6661	0.2715	0.609	0.760
512	9	`(1, 2, 0)/(2, 0, 1)`	0.5273	0.6690	0.1979	0.293	0.441
1024	10	`(1, 2, 0)/(2, 0, 1)`	0.5271	0.6693	0.1752	0.171	0.319
2048	11	`(1, 2, 0)/(2, 0, 1)`	0.5270	0.6693	0.1688	0.134	0.282
4096	12	`(1, 2, 0)/(2, 0, 1)`	0.5270	0.6693	0.1672	0.124	0.273
8192	13	`(1, 2, 0)/(2, 0, 1)`	0.5270	0.6693	0.1668	0.122	0.270
16384	14	`(1, 2, 0)/(2, 0, 1)`	0.5270	0.6693	0.1667	0.121	0.269
32768	15	`(1, 2, 0)/(2, 0, 1)`	0.5270	0.6693	0.1667	0.121	0.269
65536	16	`(1, 2, 0)/(2, 0, 1)`	0.5270	0.6693	0.1667	0.121	0.269
131072	17	`(1, 2, 0)/(2, 0, 1)`	0.5270	0.6693	0.1667	0.121	0.269
262144	18	`(1, 2, 0)/(2, 0, 1)`	0.5270	0.6693	0.1667	**0.121**	**0.269**
`best/second`	–		–	–	–	0.121/0.121	$\Delta = 0.000$

Table 43: Permutation-robust bounded-denominator fit to PMNS target sines using a global $S_3 \times S_3$ relabeling. Rows are generated by `scripts/exp_holonomy_phase_lift_perm_fit.py`.

denom	p	best (σ_r, σ_c)	s_{12}	s_{23}	s_{13}	E_∞	E_1
64	6	`(1, 0, 2)/(2, 0, 1)`	0.5890	0.6378	0.3389	4.455	8.136
128	7	`(1, 2, 0)/(2, 1, 0)`	0.5263	0.6556	0.4583	4.756	8.352
256	8	`(1, 0, 2)/(2, 0, 1)`	0.5279	0.6576	0.2715	4.233	7.835
512	9	`(1, 0, 2)/(2, 0, 1)`	0.5273	0.6469	0.1979	3.916	7.501
1024	10	`(1, 0, 2)/(2, 0, 1)`	0.5271	0.6448	0.1752	3.795	7.375
2048	11	`(1, 0, 2)/(2, 0, 1)`	0.5270	0.6443	0.1688	3.758	7.338
4096	12	`(1, 0, 2)/(2, 0, 1)`	0.5270	0.6441	0.1672	3.748	7.328
8192	13	`(1, 0, 2)/(2, 0, 1)`	0.5270	0.6441	0.1668	3.746	7.325
16384	14	`(1, 0, 2)/(2, 0, 1)`	0.5270	0.6441	0.1667	3.745	7.325
32768	15	`(1, 0, 2)/(2, 0, 1)`	0.5270	0.6441	0.1667	3.745	7.324
65536	16	`(1, 0, 2)/(2, 0, 1)`	0.5270	0.6441	0.1667	3.745	7.324
131072	17	`(1, 0, 2)/(2, 0, 1)`	0.5270	0.6441	0.1667	3.745	7.324
262144	18	`(1, 0, 2)/(2, 0, 1)`	0.5270	0.6441	0.1667	**3.745**	**7.324**
`best/second`	–		–	–	–	3.745/3.745	$\Delta = 0.000$

Table 44: Permutation-robust bounded-denominator fit to CKM target sines using a global $S_3 \times S_3$ relabeling. Rows are generated by `scripts/exp_holonomy_phase_lift_perm_fit.py`.

reducing mismatch).

U.1 A shared interface template

We use the same auditable layering rule adopted in the main text: a mathematical layer (finite-resolution definitions and computable statements) and a physical identification layer (interfaces and falsifiable mapping hypotheses). Within the operational layer, a broad class of problems can be organized by the following interface objects:

- **Readout alphabet.** A finite word alphabet $\Omega_m = \{0,1\}^m$ (or a finite outcome set for a POVM-like instrument) obtained by window projection [24].
- **Stability/mismatch mechanism.** Either (i) explicit stability predicates/defect functions that select a stable subset $X_m \subset \Omega_m$, or (ii) computable mismatch certificates comparing finite readout statistics to an ideal reference (e.g. discrepancy-based certificates).
- **Coarse-graining and degeneracy.** Many-to-one maps from microstates to stable types (or from microscopic configurations to discrete outputs) generate degeneracy distributions that trade resolution for robustness.

map	denom	p	best (σ_r, σ_c)	s_{12}	s_{23}	s_{13}	E_∞	E_1	log(mean$\|J\|/J_{\text{geo}}$)
`id`	262144	18	`(1, 2, 0)/(2, 0, 1)`	0.5270	0.6693	0.1667	0.121	0.269	-0.417
`gray`	262144	18	`(1, 2, 0)/(2, 0, 1)`	0.5270	0.6693	0.1667	0.121	0.269	+0.013
`bitrev`	262144	18	`(1, 2, 0)/(2, 0, 1)`	0.5270	0.6693	0.1667	0.121	0.269	-0.245
`not`	262144	18	`(1, 2, 0)/(2, 0, 1)`	0.5270	0.6693	0.1667	0.121	0.269	-0.417

Table 45: Phase-map family sweep for the PMNS target sines. Rows are generated by `scripts/exp_holonomy_phase_lift_map_family_sweep.py`.

map	denom	p	best (σ_r, σ_c)	s_{12}	s_{23}	s_{13}	E_∞	E_1	log(mean$\|J\|/J_{\text{geo}}$)
`id`	262144	18	`(1, 0, 2)/(2, 0, 1)`	0.5270	0.6441	0.1667	3.745	7.324	-0.417
`gray`	262144	18	`(1, 0, 2)/(2, 0, 1)`	0.5270	0.6441	0.1667	3.745	7.324	+0.013
`bitrev`	262144	18	`(1, 0, 2)/(2, 0, 1)`	0.5270	0.6441	0.1667	3.745	7.324	-0.245
`not`	262144	18	`(1, 0, 2)/(2, 0, 1)`	0.5270	0.6441	0.1667	3.745	7.324	-0.417

Table 46: Phase-map family sweep for the CKM target sines. Rows are generated by `scripts/exp_holonomy_phase_lift_map_family_sweep.py`.

- **Correction/compensation.** Consistency can be enforced passively by compensating connections (a protocol-geometric bookkeeping of local rephasing/transport) or actively by feedback that reduces mismatch relative to a passive baseline.
- **Audit closure under bounded complexity.** Quantitative claims are framed as deterministic selections from finite candidate families under explicit complexity bounds, together with rigidity/stabilization diagnostics (cf. Definitions H.1–H.4).

The measurement-theoretic notion of coarse readout as a finite-outcome instrument is standard in quantum information [24]. The feedback-control viewpoint on active mismatch reduction is standard in control theory, and the physical cost of logically irreversible operations has a canonical lower bound in the Landauer principle [14, 15].

U.2 Isomorphism dictionary (stable sectors $\leftrightarrow$ AEC)

Table 49 summarizes a protocol-level correspondence between (a) stable-sector constructions in finite-resolution readout models and (b) predictive AEC mechanisms that suppress readout-induced mismatch.

U.3 Transferable falsifiable problems

The interface dictionary yields cross-domain falsifiability questions that do not rely on post-hoc freedom:

- **Degeneracy–robustness link.** Do observed many-to-one code degeneracies correlate with reduced mismatch certificates under matched protocols, at the expected energetic cost?
- **Anti-locking selection.** Under an operational tolerance δ, do inferred coupling ratios exhibit an upward shift in Q_δ relative to baselines that preserve sampling/noise structure?
- **Thresholded sector growth.** If effective window length changes with environment or scale, do stable-type counts and splits change in constrained batches dictated by the underlying grammar/stability channel?

β	plaquettes	best (σ_r, σ_c)	s_{12}	s_{23}	s_{13}	E_∞	E_1	mean $\lvert J\rvert$	failures
0	25	`(0, 1, 2)/(0, 2, 1)`	0.5151	0.7661	0.4074	1.015	1.125	0.0246486	64
0.25	25	`(2, 0, 1)/(1, 2, 0)`	0.6468	0.8308	0.4101	1.022	1.294	0.0351224	64
0.5	25	`(2, 0, 1)/(2, 1, 0)`	0.6458	0.8254	0.3966	**0.988**	**1.253**	0.0271959	64
1	25	`(2, 0, 1)/(2, 1, 0)`	0.6283	0.7472	0.4718	1.162	1.299	0.0372322	64
2	25	`(0, 2, 1)/(0, 1, 2)`	0.6554	0.6738	0.4933	1.206	1.466	0.0296337	64
4	15	`(0, 1, 2)/(1, 0, 2)`	0.6508	0.7486	0.4525	1.120	1.295	0.0267211	93

Table 47: Soft-transport β sweep with permutation-robust fit to PMNS target sines (robustness diagnostic). Rows are generated by `scripts/exp_holonomy_soft_transport_beta_sweep.py`.

β	plaquettes	best (σ_r, σ_c)	s_{12}	s_{23}	s_{13}	E_∞	E_1	mean $\lvert J\rvert$	failures
0	25	`(0, 2, 1)/(0, 2, 1)`	0.5151	0.5440	0.4074	4.639	8.026	0.0246486	64
0.25	25	`(2, 1, 0)/(1, 2, 0)`	0.6468	0.5017	0.4101	4.645	8.180	0.0351224	64
0.5	25	`(2, 1, 0)/(2, 1, 0)`	0.6458	0.4799	0.3966	**4.612**	**8.100**	0.0271959	64
1	25	`(2, 1, 0)/(2, 1, 0)`	0.6283	0.5826	0.4718	4.785	8.440	0.0372322	64
2	25	`(0, 1, 2)/(0, 1, 2)`	0.6554	0.6457	0.4933	4.830	8.630	0.0296337	64
4	15	`(0, 2, 1)/(1, 0, 2)`	0.6508	0.5703	0.4525	4.744	8.412	0.0267211	93

Table 48: Soft-transport β sweep with permutation-robust fit to CKM target sines (robustness diagnostic). Rows are generated by `scripts/exp_holonomy_soft_transport_beta_sweep.py`.

- **Cost slopes.** Does maintenance power admit a lower-envelope slope consistent with a computational temperature scale when regressed against a protocol-matched mismatch-rate estimator?

V Functorial refinement under window uplift

This appendix records a minimal, auditable notion of functorial refinement of the field-level labeling map under window uplift $m \mapsto m'$.

Audit note (tables as deterministic checks). All tabulated refinement multiplicities and refinement-index catalogs below are theorem-level consequences of the prefix-projection definition together with Zeckendorf admissibility. Scripts referenced in captions reproduce these deterministic counts and write LaTeX fragments; they do not introduce additional free choices beyond the stated definitions.

V.1 Prefix projection and a functorial lift

For $m \geq 6$, define the truncation (prefix) projection

$$\pi_{m\to 6} : X_m \to X_6, \qquad \pi_{m\to 6}(w_1 \cdots w_m) := w_1 \cdots w_6.$$

Lemma V.1 (Well-definedness and surjectivity of $\pi_{m\to 6}$)**.** *For every $m \geq 6$, the map $\pi_{m\to 6}$ is well-defined and surjective.*

Proof. If $w \in X_m$ has no adjacent ones, then any prefix has no adjacent ones, hence $\pi_{m\to 6}(w) \in X_6$ and the map is well-defined. For surjectivity, given any $u \in X_6$, the word $u0\cdots 0 \in X_m$ (padding with $m-6$ zeros) satisfies $\pi_{m\to 6}(u0\cdots 0) = u$. □

Given the closed labeling map $\mathcal{L}_{\mathrm{SM}} : X_6 \to \mathcal{F}_{\mathrm{SM}} \sqcup \mathcal{G}_{\mathrm{SM}}$ (Section 9), we define its functorial lift to window length m by composition:

$$\mathcal{L}_m := \mathcal{L}_{\mathrm{SM}} \circ \pi_{m\to 6} : X_m \to \mathcal{F}_{\mathrm{SM}} \sqcup \mathcal{G}_{\mathrm{SM}}.$$

Interface object	Stable-sector language	AEC/biological language
finite readout alphabet	window words $w \in \Omega_m = \{0,1\}^m$	discretized outcomes from finite-resolution sensors/thresholds
stability selection	admissible/stable subset $X_m \subset \Omega_m$ defined by protocol constraints	viable operating region of the agent under implementation and readout constraints
mismatch/defect quantifier	defect predicates $D(\cdot)$ certifying protocol inconsistency	discrepancy/mismatch certificates D_N^*, E_N certifying readout bias accumulation
coarse graining	many-to-one folding $\Omega_m \twoheadrightarrow X_m$ with degeneracy	many-to-one coding (e.g. genetic degeneracy) increasing robustness under readout noise
consistency enforcement	compensating connections (protocol-local bookkeeping of transport/rephasing)	feedback control and repair redirecting dissipation into waste channels
resource accounting	implementation cost as an audit constraint (bounded-complexity closure)	Landauer-scale and architecture-dependent costs bounding sustainable correction
observable signatures	rigid finite counts/histograms and thresholded spectrum changes	statistical biases/scaling laws in Q_δ, E_N, Σ under matched protocols

Table 49: A protocol-level isomorphism dictionary: stable-sector constructions and predictive AEC can be viewed as two realizations of the same interface template (finite readout, mismatch/stability, correction, and bounded-complexity audit).

This definition makes the refinement under successive truncations explicit: for $m \geq k \geq 6$, one has $\pi_{m\to 6} = \pi_{k\to 6} \circ \pi_{m\to k}$, hence $\mathcal{L}_m = \mathcal{L}_k \circ \pi_{m\to k}$.

V.2 Deterministic refinement multiplicities

Although $\mathcal{L}_m$ uses only the first six digits to assign an SM label, each base type in X_6 admits multiple higher-window extensions in X_m. This yields a computable refinement multiplicity per base label.

Proposition V.2 (Extension counts depend only on the last bit)**.** *Fix $m \geq 6$ and $u = u_1 \cdots u_6 \in X_6$. Let*

$$\mathrm{Ext}_m(u) := \{w \in X_m : \ \pi_{m\to 6}(w) = u\}.$$

Then $|\mathrm{Ext}_m(u)|$ depends only on u_6:

$$|\mathrm{Ext}_m(u)| = \begin{cases} F_{m-4}, & u_6 = 0, \\ F_{m-5}, & u_6 = 1, \end{cases}$$

where (F_k) are Fibonacci numbers with $F_1 = F_2 = 1$.

Proof. Let $L := m - 6$ be the extension length. If $u_6 = 1$, the next bit must be 0, and the remaining $L - 1$ bits form an admissible word in X_{L-1}, so $|\mathrm{Ext}_m(u)| = |X_{L-1}| = F_{(L-1)+2} = F_{m-5}$ by Lemma 4.5. If $u_6 = 0$, there is no forced initial 0 and the L extension bits form an admissible word in X_L, so $|\mathrm{Ext}_m(u)| = |X_L| = F_{L+2} = F_{m-4}$. □

base type $u \in X_6$	label $\mathcal{L}_{\mathrm{SM}}(u)$	u_6	$\lvert\mathrm{Ext}_8(u)\rvert$	$\lvert\mathrm{Ext}_{10}(u)\rvert$	$\lvert\mathrm{Ext}_{12}(u)\rvert$	$\lvert\mathrm{Ext}_{14}(u)\rvert$	$\lvert\mathrm{Ext}_{16}(u)\rvert$
000000	$\nu_R^{(1)}$	0	3	8	21	55	144
100000	$L_L^{(1)}$	0	3	8	21	55	144
010000	$e_R^{(1)}$	0	3	8	21	55	144
001000	$Q_L^{(1)}$	0	3	8	21	55	144
101000	$d_R^{(1)}$	0	3	8	21	55	144
000100	$u_R^{(1)}$	0	3	8	21	55	144
100100	$\nu_R^{(2)}$	0	3	8	21	55	144
010100	$e_R^{(2)}$	0	3	8	21	55	144
000010	$u_R^{(2)}$	0	3	8	21	55	144
100010	$L_L^{(2)}$	0	3	8	21	55	144
010010	$Q_L^{(2)}$	0	3	8	21	55	144
001010	$\nu_R^{(3)}$	0	3	8	21	55	144
101010	$L_L^{(3)}$	0	3	8	21	55	144
000001	$d_R^{(2)}$	1	2	5	13	34	89
100001	$U(1)$	1	2	5	13	34	89
010001	$e_R^{(3)}$	1	2	5	13	34	89
001001	$Q_L^{(3)}$	1	2	5	13	34	89
101001	$SU(2)$	1	2	5	13	34	89
000101	$d_R^{(3)}$	1	2	5	13	34	89
100101	$SU(3)$	1	2	5	13	34	89
010101	$u_R^{(3)}$	1	2	5	13	34	89

Table 50: Functorial refinement multiplicities under the prefix lift $\mathcal{L}_m = \mathcal{L}_{\mathrm{SM}} \circ \pi_{m\to 6}$. Proposition V.2 predicts that each base type has 2 or 3 lifts at $m = 8$, 5 or 8 lifts at $m = 10$, 13 or 21 lifts at $m = 12$, 34 or 55 lifts at $m = 14$, and 89 or 144 lifts at $m = 16$, depending only on the last bit u_6. Rows are generated by `scripts/exp_labeling_lift_consistency.py`.

V.3 A canonical suffix index for lift refinement

The lift multiplicities in Table 50 depend only on the adjacency constraint between the prefix last bit u_6 and the first extension bit. To obtain a concrete refinement of the coarse lift $\mathcal{L}_m$ (beyond counting multiplicities), it is useful to attach a deterministic index to each lift in $\mathrm{Ext}_m(u)$.

Definition V.3 (Free suffix index)**.** *Fix $m \geq 6$ and a base type $u \in X_6$. Write any lift $w \in \mathrm{Ext}_m(u)$ as $w = u\,s$, where s is the length-$(m-6)$ suffix. If $u_6 = 0$, define the free suffix to be $t := s$. If $u_6 = 1$, admissibility forces s to begin with 0, and we define the free suffix to be $t := s_2 \cdots s_{m-6}$ (drop the forced leading 0). Define the free suffix index*

$$\rho(w) := V_Z(t),$$

where V_Z is the Zeckendorf/Fibonacci value computed from the binary word t using the standard Fibonacci weights (starting at $F_2 = 1$).

At fixed (m, u_6), the possible free suffixes form an admissible set and the index ρ enumerates them deterministically. Table 51 records the explicit suffix catalog for the balanced-coupling uplifts $m = 8$ and $m = 10$.

m	u_6	full suffix s	free suffix t	ρ	last bit s_{m-6}
8	0	00	00	0	0
8	0	10	10	1	0
8	0	01	01	2	1
8	1	00	0	0	0
8	1	01	1	1	1
10	0	0000	0000	0	0
10	0	1000	1000	1	0
10	0	0100	0100	2	0
10	0	0010	0010	3	0
10	0	1010	1010	4	0
10	0	0001	0001	5	1
10	0	1001	1001	6	1
10	0	0101	0101	7	1
10	1	0000	000	0	0
10	1	0100	100	1	0
10	1	0010	010	2	0
10	1	0001	001	3	1
10	1	0101	101	4	1

Table 51: Canonical suffix catalog for the free suffix index ρ in Definition V.3 at $m \in \{8, 10\}$. Rows are generated by `scripts/exp_labeling_lift_refinement_indices.py`.

V.4 Boundary subsets under the π-channel wrap-around defect

The π-channel boundary predicate on X_m is $w_1 = w_m = 1$. Since $w_1 = u_1$ is fixed by the base type, the boundary subset within $\mathrm{Ext}_m(u)$ is determined by whether the last suffix bit equals 1. Table 52 records the boundary-lift subsets in the ρ index language for $m = 8$ and $m = 10$.

base type u	label $\mathcal{L}_{\mathrm{SM}}(u)$	u_1	u_6	boundary ρ at $m = 8$	boundary ρ at $m = 10$
000000	$\nu_R^{(1)}$	0	0	$\varnothing$	$\varnothing$
100000	$L_L^{(1)}$	1	0	$\{2\}$	$\{5, 6, 7\}$
010000	$e_R^{(1)}$	0	0	$\varnothing$	$\varnothing$
001000	$Q_L^{(1)}$	0	0	$\varnothing$	$\varnothing$
101000	$d_R^{(1)}$	1	0	$\{2\}$	$\{5, 6, 7\}$
000100	$u_R^{(1)}$	0	0	$\varnothing$	$\varnothing$
100100	$\nu_R^{(2)}$	1	0	$\{2\}$	$\{5, 6, 7\}$
010100	$e_R^{(2)}$	0	0	$\varnothing$	$\varnothing$
000010	$u_R^{(2)}$	0	0	$\varnothing$	$\varnothing$
100010	$L_L^{(2)}$	1	0	$\{2\}$	$\{5, 6, 7\}$
010010	$Q_L^{(2)}$	0	0	$\varnothing$	$\varnothing$
001010	$\nu_R^{(3)}$	0	0	$\varnothing$	$\varnothing$
101010	$L_L^{(3)}$	1	0	$\{2\}$	$\{5, 6, 7\}$
000001	$d_R^{(2)}$	0	1	$\varnothing$	$\varnothing$
100001	$U(1)$	1	1	$\{1\}$	$\{3, 4\}$
010001	$e_R^{(3)}$	0	1	$\varnothing$	$\varnothing$
001001	$Q_L^{(3)}$	0	1	$\varnothing$	$\varnothing$
101001	$SU(2)$	1	1	$\{1\}$	$\{3, 4\}$
000101	$d_R^{(3)}$	0	1	$\varnothing$	$\varnothing$
100101	$SU(3)$	1	1	$\{1\}$	$\{3, 4\}$
010101	$u_R^{(3)}$	0	1	$\varnothing$	$\varnothing$

Table 52: Boundary-lift subsets expressed in the free suffix index ρ (Definition V.3) under the π-channel wrap-around defect predicate $w_1 = w_m = 1$. Rows are generated by `scripts/exp_labeling_lift_refinement_indices.py`.

V.5 Audit: contiguity and Fibonacci boundary blocks

For completeness, Table 53 records a compact audit of the free suffix index. The audit is performed at $m \in \{8, 10, 12, 14, 16\}$. The index enumerates the admissible free suffixes contiguously and the "ends in 1" subset occupies the top Fibonacci block of indices.

m	u_6	free length ℓ	$\lvert\Theta\rvert$	ρ range	boundary ρ block	status
8	0	2	3	$0 \ldots 2$	$\{2\}$	PASS
8	1	1	2	$0 \ldots 1$	$\{1\}$	PASS
10	0	4	8	$0 \ldots 7$	$\{5, \ldots, 7\}$	PASS
10	1	3	5	$0 \ldots 4$	$\{3, \ldots, 4\}$	PASS
12	0	6	21	$0 \ldots 20$	$\{13, \ldots, 20\}$	PASS
12	1	5	13	$0 \ldots 12$	$\{8, \ldots, 12\}$	PASS
14	0	8	55	$0 \ldots 54$	$\{34, \ldots, 54\}$	PASS
14	1	7	34	$0 \ldots 33$	$\{21, \ldots, 33\}$	PASS
16	0	10	144	$0 \ldots 143$	$\{89, \ldots, 143\}$	PASS
16	1	9	89	$0 \ldots 88$	$\{55, \ldots, 88\}$	PASS

Table 53: Audit checks for the free suffix index ρ (Definition V.3) at $m \in \{8, 10, 12, 14, 16\}$ and both cases $u_6 \in \{0, 1\}$. Rows are generated by `scripts/exp_audit_label_lift_refinement.py`.

V.6 High-m invariants inside lift fibers

Beyond the purely combinatorial lift multiplicities and the suffix index ρ, the window length m provides additional intrinsic invariants on X_m. As a minimal refinement diagnostic, Table 54 summarizes two such invariants inside each prefix fiber $\mathrm{Ext}_m(u)$: (i) the Fold_m degeneracy $g_m(w) = |\mathrm{Fold}_m^{-1}(w)|$ over $N \in \{0, \ldots, 2^m - 1\}$, and (ii) the π-channel cyclic/boundary split on X_m.

Table 54: Intrinsic invariant summaries inside lift fibers at $m \in \{8, 10, 12, 14, 16\}$. The g histogram reports the Fold_m degeneracy counts within $\mathrm{Ext}_m(u)$, while the V_m range reports the minimum and maximum Zeckendorf values among the lifts. Rows are generated by `scripts/exp_labeling_lift_highm_invariants.py`.

m	base type u	label	$\lvert\mathrm{Ext}_m(u)\rvert$	cyc	bdry	$g_{\min}$	$g_{\max}$	g histogram	V_m range
8	000000	$\nu_R^{(1)}$	3	3	0	3	6	3:1, 6:2	0..34
8	100000	$L_L^{(1)}$	3	2	1	3	6	3:1, 6:2	1..35
8	010000	$e_R^{(1)}$	3	3	0	3	6	3:1, 5:1, 6:1	2..36
8	001000	$Q_L^{(1)}$	3	3	0	3	6	3:1, 5:1, 6:1	3..37
8	101000	$d_R^{(1)}$	3	2	1	3	6	3:1, 5:1, 6:1	4..38
8	000100	$u_R^{(1)}$	3	3	0	3	6	3:1, 5:1, 6:1	5..39
8	100100	$\nu_R^{(2)}$	3	2	1	3	6	3:1, 5:1, 6:1	6..40
8	010100	$e_R^{(2)}$	3	3	0	3	6	3:1, 5:1, 6:1	7..41
8	000010	$u_R^{(2)}$	3	3	0	3	6	3:1, 5:1, 6:1	8..42
8	100010	$L_L^{(2)}$	3	2	1	3	6	3:1, 5:1, 6:1	9..43
8	010010	$Q_L^{(2)}$	3	3	0	3	6	3:1, 5:1, 6:1	10..44
8	001010	$\nu_R^{(3)}$	3	3	0	3	6	3:1, 5:1, 6:1	11..45
8	101010	$L_L^{(3)}$	3	2	1	3	6	3:1, 5:1, 6:1	12..46
8	000001	$d_R^{(2)}$	2	2	0	3	6	3:1, 6:1	13..47
8	100001	$U(1)$	2	1	1	3	6	3:1, 6:1	14..48
8	010001	$e_R^{(3)}$	2	2	0	3	6	3:1, 6:1	15..49
8	001001	$Q_L^{(3)}$	2	2	0	3	6	3:1, 6:1	16..50
8	101001	$SU(2)$	2	1	1	3	6	3:1, 6:1	17..51
8	000101	$d_R^{(3)}$	2	2	0	3	6	3:1, 6:1	18..52

m	base type u	label	$\lvert\mathrm{Ext}_m(u)\rvert$	cyc	bdry	$g_{\min}$	$g_{\max}$	g histogram	V_m range
8	100101	$SU(3)$	2	1	1	3	6	3:1, 6:1	19..53
8	010101	$u_R^{(3)}$	2	2	0	3	6	3:1, 6:1	20..54
10	000000	$\nu_R^{(1)}$	8	8	0	5	9	5:3, 8:2, 9:3	0..123
10	100000	$L_L^{(1)}$	8	5	3	5	9	5:3, 8:2, 9:3	1..124
10	010000	$e_R^{(1)}$	8	8	0	5	9	5:3, 8:2, 9:3	2..125
10	001000	$Q_L^{(1)}$	8	8	0	5	9	5:3, 8:3, 9:2	3..126
10	101000	$d_R^{(1)}$	8	5	3	5	9	5:3, 8:3, 9:2	4..127
10	000100	$u_R^{(1)}$	8	8	0	5	9	5:3, 8:3, 9:2	5..128
10	100100	$\nu_R^{(2)}$	8	5	3	5	9	5:3, 8:3, 9:2	6..129
10	010100	$e_R^{(2)}$	8	8	0	5	9	5:3, 8:3, 9:2	7..130
10	000010	$u_R^{(2)}$	8	8	0	5	9	5:3, 8:3, 9:2	8..131
10	100010	$L_L^{(2)}$	8	5	3	5	9	5:3, 8:3, 9:2	9..132
10	010010	$Q_L^{(2)}$	8	8	0	5	9	5:3, 8:3, 9:2	10..133
10	001010	$\nu_R^{(3)}$	8	8	0	5	9	5:3, 8:3, 9:2	11..134
10	101010	$L_L^{(3)}$	8	5	3	5	9	5:3, 8:3, 9:2	12..135
10	000001	$d_R^{(2)}$	5	5	0	5	9	5:2, 8:2, 9:1	13..136
10	100001	$U(1)$	5	3	2	5	9	5:2, 8:2, 9:1	14..137
10	010001	$e_R^{(3)}$	5	5	0	5	9	5:2, 8:2, 9:1	15..138
10	001001	$Q_L^{(3)}$	5	5	0	5	9	5:2, 8:2, 9:1	16..139
10	101001	$SU(2)$	5	3	2	5	9	5:2, 8:2, 9:1	17..140
10	000101	$d_R^{(3)}$	5	5	0	5	9	5:2, 8:2, 9:1	18..141
10	100101	$SU(3)$	5	3	2	5	9	5:2, 8:2, 9:1	19..142
10	010101	$u_R^{(3)}$	5	5	0	5	9	5:2, 8:2, 9:1	20..143
12	000000	$\nu_R^{(1)}$	21	21	0	8	13	8:8, 12:4, 13:9	0..356
12	100000	$L_L^{(1)}$	21	13	8	8	13	8:8, 12:4, 13:9	1..357
12	010000	$e_R^{(1)}$	21	21	0	8	13	8:8, 12:4, 13:9	2..358
12	001000	$Q_L^{(1)}$	21	21	0	8	13	8:8, 12:4, 13:9	3..359
12	101000	$d_R^{(1)}$	21	13	8	8	13	8:8, 12:5, 13:8	4..360
12	000100	$u_R^{(1)}$	21	21	0	8	13	8:8, 12:5, 13:8	5..361
12	100100	$\nu_R^{(2)}$	21	13	8	8	13	8:8, 12:5, 13:8	6..362
12	010100	$e_R^{(2)}$	21	21	0	8	13	8:8, 12:5, 13:8	7..363
12	000010	$u_R^{(2)}$	21	21	0	8	13	8:8, 12:5, 13:8	8..364
12	100010	$L_L^{(2)}$	21	13	8	8	13	8:8, 12:5, 13:8	9..365
12	010010	$Q_L^{(2)}$	21	21	0	8	13	8:8, 12:5, 13:8	10..366
12	001010	$\nu_R^{(3)}$	21	21	0	8	13	8:8, 12:5, 13:8	11..367
12	101010	$L_L^{(3)}$	21	13	8	8	13	8:8, 12:5, 13:8	12..368
12	000001	$d_R^{(2)}$	13	13	0	8	13	8:5, 12:3, 13:5	13..369
12	100001	$U(1)$	13	8	5	8	13	8:5, 12:3, 13:5	14..370
12	010001	$e_R^{(3)}$	13	13	0	8	13	8:5, 12:3, 13:5	15..371
12	001001	$Q_L^{(3)}$	13	13	0	8	13	8:5, 12:3, 13:5	16..372
12	101001	$SU(2)$	13	8	5	8	13	8:5, 12:3, 13:5	17..373
12	000101	$d_R^{(3)}$	13	13	0	8	13	8:5, 12:3, 13:5	18..374
12	100101	$SU(3)$	13	8	5	8	13	8:5, 12:3, 13:5	19..375
12	010101	$u_R^{(3)}$	13	13	0	8	13	8:5, 12:3, 13:5	20..376
14	000000	$\nu_R^{(1)}$	55	55	0	12	20	12:21, 19:18, 20:16	0..966
14	100000	$L_L^{(1)}$	55	34	21	12	20	12:21, 19:18, 20:16	1..967
14	010000	$e_R^{(1)}$	55	55	0	12	20	12:21, 19:18, 20:16	2..968
14	001000	$Q_L^{(1)}$	55	55	0	12	20	12:21, 19:19, 20:15	3..969
14	101000	$d_R^{(1)}$	55	34	21	12	20	12:21, 19:19, 20:15	4..970
14	000100	$u_R^{(1)}$	55	55	0	12	20	12:21, 19:19, 20:15	5..971
14	100100	$\nu_R^{(2)}$	55	34	21	12	20	12:21, 19:19, 20:15	6..972
14	010100	$e_R^{(2)}$	55	55	0	12	20	12:21, 19:19, 20:15	7..973
14	000010	$u_R^{(2)}$	55	55	0	12	20	12:21, 19:19, 20:15	8..974
14	100010	$L_L^{(2)}$	55	34	21	12	20	12:21, 19:19, 20:15	9..975
14	010010	$Q_L^{(2)}$	55	55	0	12	20	12:21, 19:19, 20:15	10..976
14	001010	$\nu_R^{(3)}$	55	55	0	12	20	12:21, 19:19, 20:15	11..977
14	101010	$L_L^{(3)}$	55	34	21	12	20	12:21, 19:19, 20:15	12..978

m	base type u	label	$\lvert\mathrm{Ext}_m(u)\rvert$	cyc	bdry	$g_{\min}$	$g_{\max}$	g histogram	V_m range
14	000001	$d_R^{(2)}$	34	34	0	12	20	12:13, 19:12, 20:9	13..979
14	100001	$U(1)$	34	21	13	12	20	12:13, 19:12, 20:9	14..980
14	010001	$e_R^{(3)}$	34	34	0	12	20	12:13, 19:12, 20:9	15..981
14	001001	$Q_L^{(3)}$	34	34	0	12	20	12:13, 19:12, 20:9	16..982
14	101001	$SU(2)$	34	21	13	12	20	12:13, 19:12, 20:9	17..983
14	000101	$d_R^{(3)}$	34	34	0	12	20	12:13, 19:12, 20:9	18..984
14	100101	$SU(3)$	34	21	13	12	20	12:13, 19:12, 20:9	19..985
14	010101	$u_R^{(3)}$	34	34	0	12	20	12:13, 19:12, 20:9	20..986
16	000000	$\nu_R^{(1)}$	144	144	0	18	30	18:55, 29:7, 30:82	0..2563
16	100000	$L_L^{(1)}$	144	89	55	18	30	18:55, 29:7, 30:82	1..2564
16	010000	$e_R^{(1)}$	144	144	0	18	30	18:55, 29:7, 30:82	2..2565
16	001000	$Q_L^{(1)}$	144	144	0	18	30	18:55, 29:7, 30:82	3..2566
16	101000	$d_R^{(1)}$	144	89	55	18	30	18:55, 29:8, 30:81	4..2567
16	000100	$u_R^{(1)}$	144	144	0	18	30	18:55, 29:8, 30:81	5..2568
16	100100	$\nu_R^{(2)}$	144	89	55	18	30	18:55, 29:8, 30:81	6..2569
16	010100	$e_R^{(2)}$	144	144	0	18	30	18:55, 29:8, 30:81	7..2570
16	000010	$u_R^{(2)}$	144	144	0	18	30	18:55, 29:8, 30:81	8..2571
16	100010	$L_L^{(2)}$	144	89	55	18	30	18:55, 29:8, 30:81	9..2572
16	010010	$Q_L^{(2)}$	144	144	0	18	30	18:55, 29:8, 30:81	10..2573
16	001010	$\nu_R^{(3)}$	144	144	0	18	30	18:55, 29:8, 30:81	11..2574
16	101010	$L_L^{(3)}$	144	89	55	18	30	18:55, 29:8, 30:81	12..2575
16	000001	$d_R^{(2)}$	89	89	0	18	30	18:34, 29:5, 30:50	13..2576
16	100001	$U(1)$	89	55	34	18	30	18:34, 29:5, 30:50	14..2577
16	010001	$e_R^{(3)}$	89	89	0	18	30	18:34, 29:5, 30:50	15..2578
16	001001	$Q_L^{(3)}$	89	89	0	18	30	18:34, 29:5, 30:50	16..2579
16	101001	$SU(2)$	89	55	34	18	30	18:34, 29:5, 30:50	17..2580
16	000101	$d_R^{(3)}$	89	89	0	18	30	18:34, 29:5, 30:50	18..2581
16	100101	$SU(3)$	89	55	34	18	30	18:34, 29:5, 30:50	19..2582
16	010101	$u_R^{(3)}$	89	89	0	18	30	18:34, 29:5, 30:50	20..2583

W Inverse interface diagnostics: recovering quantum number patterns from invariants

This appendix records inverse identification diagnostics on the physical identification layer: given the closed labeling map and the intrinsic invariants available at window length 6, to what extent can Standard Model quantum-number patterns be recovered by bounded-complexity rules built from those invariants? These diagnostics are not premises for any result in the main text. Because the cyclic sector consists of exactly the 18 fermion multiplets (three generations of six chiral multiplets), the induced target class frequencies are fixed *a priori*. In particular, chance/majority baselines are 1/6 for the six-class targets $(6Y)^2$ and $Y_{\mathrm{num}} = 6Y$, 1/2 for $\mathrm{sign}(Y)$ and $\dim(SU(3))$, 2/3 for $\dim(SU(2))$, and 1/3 for the generation index.

Audit note (diagnostics vs. premises). All classifier searches reported below are deterministic bounded sweeps over explicit integer boxes (as stated in each subsection), and all reported "best/second-best" rows are computed with deterministic tie-break rules. Scripts referenced in table captions reproduce these bounded sweeps and write LaTeX fragments; the inverse diagnostics are *post-hoc audits* and are not used as premises anywhere in the main argument.

W.1 A bounded-complexity classifier for $(6Y)^2$

Under the PDG convention $Q = T_3 + Y$, the chiral fermion multiplets in one generation take hypercharges with $(6Y)^2 \in \{0, 1, 4, 9, 16, 36\}$. Using the closed labeling $\mathcal{L}_{\mathrm{SM}}$ (Section 9), we can treat $(6Y)^2$ as a supervised target on the cyclic stable types and ask whether a low-complexity rule built from intrinsic invariants can recover it.

We test the simplest linear-score family on cyclic stable types:

$$S(w) = a\,V(w) + b\,g(w) + c\,|w|_1 + d, \qquad a, b, c, d \in \mathbb{Z},$$

and predict $(6Y)^2$ by snapping $S(w)$ to the nearest allowed value in $\{0, 1, 4, 9, 16, 36\}$ with a deterministic tie-break rule. Table 55 reports the best and second-best solutions under a bounded search box together with the accuracy gap.

search box	best (a, b, c, d)	accuracy	second	gap	complexity $\sum \lvert a_i \rvert$	notes
$\lvert a \rvert, \lvert b \rvert, \lvert c \rvert, \lvert d \rvert \le 8$	$(0, -1, 5, 0)$	0.389	$(0, -2, 4, 5)$	0.000	6	$\{0, 1, 4, 9, 16, 36\}$

Table 55: Bounded-complexity inverse diagnostic for the hypercharge-squared class $(6Y)^2$ from intrinsic invariants on cyclic stable types at $m = 6$. Rows are generated by `scripts/exp_inverse_hypercharge_fit.py`.

W.2 Recovering the sign of hypercharge

The previous classifier targets $(6Y)^2$ and therefore ignores the sign of Y. As a complementary diagnostic, one can attempt to recover $\mathrm{sign}(Y) \in \{-1, 0, +1\}$ from intrinsic invariants using a bounded linear score and a two-threshold rule. Table 56 reports the best result in a fixed bounded search box.

search box	target	best parameters	errors	accuracy
$\lvert a \rvert, \lvert b \rvert, \lvert c \rvert \le 4$	$\mathrm{sign}(Y)$	$(a, b, c, t_1, t_2, \pi) = (1, 3, -4, 11, 12, (-1, 0, 1))$	6	0.667

Table 56: Bounded-complexity inverse diagnostic for $\mathrm{sign}(Y)$ from intrinsic invariants on cyclic stable types at $m = 6$. Rows are generated by `scripts/exp_inverse_hypercharge_sign_fit.py`.

W.3 Recovering the full hypercharge numerator

As a stricter test, one can attempt to recover the full hypercharge numerator $Y_{\mathrm{num}} = 6Y \in \{-6, -3, -2, 0, 1, 4\}$ from intrinsic invariants by searching for bounded score families and projecting to the nearest allowed value. Table 57 compares multiple bounded families, including affine scores in (V, g, wt), affine scores on a fixed subset of word bits, a shallow bit-decision tree with leaf labels chosen by deterministic majority vote, and an optimal bounded-depth bit-decision tree computed by dynamic programming.

search box	target	best parameters	errors	accuracy
$\lvert a\rvert,\lvert b\rvert,\lvert c\rvert,\lvert d\rvert \le 6$	Y_{num} (V,g,wt)	$(a,b,c,d) = (2,0,-5,0)$	11	0.389
$\lvert c_i\rvert \le 3$	Y_{num} (bits 1..5)	$(c_1,\dots,c_5,d) = (-3,2,1,3,-1,0)$	6	0.667
depth $= 3$	Y_{num} (bit tree)	`bits` $= (2,1,0,0,4,4,4)$, `leaf` $= (-2,-3,-6,1,1,0,-2,-3)$	5	0.722
DP, depth ≤ 6	Y_{num} (bit tree)	`depth` $= 6$, `nodes` $= 27$, `bits` $= (0,1,2,3,4,5)$	0	1.000

Table 57: Bounded-complexity inverse diagnostic for the full hypercharge numerator $Y_{\mathrm{num}} = 6Y$ from intrinsic invariants on cyclic stable types at $m = 6$. Rows are generated by `scripts/exp_inverse_hypercharge_full_fit.py`.

W.4 Recovering representation dimensions

As a simpler inverse diagnostic, one can ask whether the representation dimensions $\dim(SU(3)) \in \{1,3\}$ and $\dim(SU(2)) \in \{1,2\}$ can be recovered from the same intrinsic invariants by a low-complexity rule. Table 58 reports a bounded linear-threshold fit for each target.

search box	target	best parameters	errors	accuracy
$\lvert a\rvert,\lvert b\rvert,\lvert c\rvert,\lvert d\rvert \le 6$	$\dim(SU(3))$	$(a,b,c,d,T) = (1,4,-3,-6,11)$	3	0.833
$\lvert a\rvert,\lvert b\rvert,\lvert c\rvert,\lvert d\rvert \le 6$	$\dim(SU(2))$	$(a,b,c,d,T) = (-1,-4,4,0,-14)$	4	0.778

Table 58: Bounded-complexity inverse diagnostics for gauge-representation dimensions from intrinsic invariants on cyclic stable types at $m = 6$. Rows are generated by `scripts/exp_inverse_rep_dim_fit.py`.

W.5 Recovering the generation index

The closed fermion ordering in Definition 9.12 is organized by a generation index g. As emphasized in Remark 9.16, this index is a bookkeeping convention for the three copies of the same gauge-quantum-number pattern (fixed here by the downstream mass-template anchor). Accordingly, the following inverse diagnostic is conditional on that convention: it asks whether the assigned $g \in \{1,2,3\}$ can be recovered from a simple intrinsic scalar score on $w \in X_6$ using a two-threshold rule. Table 59 reports best thresholds for a small set of candidate scores.

score $S(w)$	best thresholds	errors	accuracy
$V(w)$	$(t_1,t_2) = (5,10)$	1	0.944
$r_*(w) = V(w) + 3(g(w)-2)$	$(t_1,t_2) = (11,13)$	1	0.944
$S(w) = aV(w) + b\,\deg(w) + c\,\mathrm{wt}(w)$ (best)	$(a,b,c,t_1,t_2) = (1,0,3,10,16)$	0	1.000

Table 59: Bounded-complexity inverse diagnostic for the generation index from intrinsic scores on cyclic stable types at $m = 6$ using a two-threshold classifier. Rows are generated by `scripts/exp_inverse_generation_fit.py`.

W.6 High-m inverse diagnostic from lift-fiber invariants

The inverse diagnostics above use only intrinsic invariants at window length $m = 6$. To probe whether additional structure becomes available under window uplift, we can build supervised targets on the cyclic base types $u \in X_6^{\mathrm{cyc}}$ and attach to each u a small set of intrinsic invariants

computed inside its lift fiber

$$\mathrm{Ext}_m(u) := \{w \in X_m : \ \pi_{m\to 6}(w) = u\}.$$

As a minimal example, we test an affine score on a small lift-fiber feature set (fiber size, boundary count, Fold_m degeneracy extrema, and the Zeckendorf range width) and attempt to recover the hypercharge-squared class $(6Y)^2$ by the same nearest-class projection rule. Table 60 reports the best and second-best solutions at several uplift values.

m	features	search box	best coeffs	accuracy	second	gap	complexity
8	`ext,bdry,gmin,gmax,Vwidth`	$\lvert a_i\rvert \le 4$	$(0,-1,0,2,0,1)$	0.333	$(0,-2,0,2,0,1)$	0.000	4
8	`ext,bdry,gmin,gmax,Vmin,Vmax`	$\lvert a_i\rvert \le 3$	$(0,0,0,0,1,0,-1)$	0.333	$(0,1,0,0,1,0,-1)$	0.000	2
8	`ext,bdry,Vmin,Vmax`	$\lvert a_i\rvert \le 4$	$(0,0,1,0,-1)$	0.333	$(0,1,1,0,-1)$	0.000	2
10	`ext,bdry,gmin,gmax,Vwidth`	$\lvert a_i\rvert \le 4$	$(-1,2,0,1,0,0)$	0.389	$(-1,2,0,1,0,1)$	0.000	4
10	`ext,bdry,gmin,gmax,Vmin,Vmax`	$\lvert a_i\rvert \le 3$	$(-1,2,0,1,0,0,0)$	0.389	$(-1,2,0,1,0,0,1)$	0.000	4
10	`ext,bdry,Vmin,Vmax`	$\lvert a_i\rvert \le 4$	$(-2,4,1,0,3)$	0.389	$(4,-3,-1,0,-2)$	0.000	10
12	`ext,bdry,gmin,gmax,Vwidth`	$\lvert a_i\rvert \le 4$	$(-1,2,2,0,0,0)$	0.389	$(-1,2,2,0,0,1)$	0.000	5
12	`ext,bdry,gmin,gmax,Vmin,Vmax`	$\lvert a_i\rvert \le 3$	$(-1,2,2,0,0,0,0)$	0.389	$(-1,2,2,0,0,0,1)$	0.000	5
12	`ext,bdry,Vmin,Vmax`	$\lvert a_i\rvert \le 4$	$(0,0,1,0,-1)$	0.333	$(0,1,0,0,1)$	0.000	2
14	`ext,bdry,gmin,gmax,Vwidth`	$\lvert a_i\rvert \le 4$	$(0,-1,1,1,0,0)$	0.333	$(0,-1,-1,2,0,0)$	0.000	3
14	`ext,bdry,gmin,gmax,Vmin,Vmax`	$\lvert a_i\rvert \le 3$	$(0,-1,1,1,-2,0,0)$	0.389	$(0,-1,1,1,-2,0,1)$	0.000	5
14	`ext,bdry,Vmin,Vmax`	$\lvert a_i\rvert \le 4$	$(0,0,1,0,-1)$	0.333	$(1,-2,0,0,-1)$	0.000	2
16	`ext,bdry,gmin,gmax,Vwidth`	$\lvert a_i\rvert \le 4$	$(0,-1,2,1,0,0)$	0.333	$(0,-1,0,2,0,2)$	0.000	4
16	`ext,bdry,gmin,gmax,Vmin,Vmax`	$\lvert a_i\rvert \le 3$	$(0,-1,2,1,-2,0,0)$	0.389	$(1,-2,-3,1,-2,0,1)$	0.000	6
16	`ext,bdry,Vmin,Vmax`	$\lvert a_i\rvert \le 4$	$(0,0,1,0,-1)$	0.333	$(0,0,1,0,0)$	0.056	2

Table 60: High-m inverse diagnostic for the hypercharge-squared class $(6Y)^2$ from lift-fiber invariants inside $\mathrm{Ext}_m(u)$ for cyclic base types $u \in X_6^{\mathrm{cyc}}$. Rows are generated by `scripts/exp_inverse_highm_hypercharge_fit.py`.

W.7 High-m inverse diagnostic for $\mathrm{sign}(Y)$

Using the same lift-fiber invariants, we can attempt to recover the sign class $\mathrm{sign}(Y) \in \{-1, 0, +1\}$ by a bounded linear score and a two-threshold rule, analogous to Table 56 at $m = 6$. Table 61 reports the selected best models at several uplifts.

m	features	search box	best parameters	errors	accuracy
8	`ext,bdry,gmin,gmax,Vwidth`	$\lvert a_i\rvert \le 2$	$(a,\dots,t_1,t_2,\pi) = (-1,1,1,0,0,0,0,1,(1,-1,0))$	7	0.611
8	`ext,bdry,Vmin,Vmax`	$\lvert a_i\rvert \le 2$	$(a,\dots,t_1,t_2,\pi) = (-1,1,0,0,2,-1,0,(1,-1,0))$	7	0.611
10	`ext,bdry,gmin,gmax,Vwidth`	$\lvert a_i\rvert \le 2$	$(a,\dots,t_1,t_2,\pi) = (-1,1,1,0,0,0,-3,0,(1,-1,0))$	7	0.611
10	`ext,bdry,Vmin,Vmax`	$\lvert a_i\rvert \le 2$	$(a,\dots,t_1,t_2,\pi) = (-1,2,1,0,-2,0,2,(1,0,-1))$	7	0.611
12	`ext,bdry,gmin,gmax,Vwidth`	$\lvert a_i\rvert \le 2$	$(a,\dots,t_1,t_2,\pi) = (-1,1,0,1,0,0,-8,0,(1,-1,0))$	7	0.611
12	`ext,bdry,Vmin,Vmax`	$\lvert a_i\rvert \le 2$	$(a,\dots,t_1,t_2,\pi) = (2,-2,1,0,-2,42,50,(-1,1,0))$	4	0.778
14	`ext,bdry,gmin,gmax,Vwidth`	$\lvert a_i\rvert \le 2$	$(a,\dots,t_1,t_2,\pi) = (-1,1,0,2,0,0,-15,6,(1,-1,0))$	7	0.611
14	`ext,bdry,Vmin,Vmax`	$\lvert a_i\rvert \le 2$	$(a,\dots,t_1,t_2,\pi) = (1,-1,1,0,-2,47,63,(-1,1,0))$	5	0.722
16	`ext,bdry,gmin,gmax,Vwidth`	$\lvert a_i\rvert \le 2$	$(a,\dots,t_1,t_2,\pi) = (-1,1,2,2,0,0,-48,7,(1,-1,0))$	7	0.611
16	`ext,bdry,Vmin,Vmax`	$\lvert a_i\rvert \le 2$	$(a,\dots,t_1,t_2,\pi) = (1,-1,2,2,-2,5276,5308,(-1,1,0))$	4	0.778

Table 61: High-m inverse diagnostic for $\mathrm{sign}(Y)$ from lift-fiber invariants inside $\mathrm{Ext}_m(u)$ for cyclic base types $u \in X_6^{\mathrm{cyc}}$. Rows are generated by `scripts/exp_inverse_highm_hypercharge_sign_fit.py`.

W.8 High-m inverse diagnostic for the full hypercharge numerator

Finally, we can attempt to recover the full hypercharge numerator $Y_{\mathrm{num}} = 6Y$ using bounded-complexity affine scores on lift-fiber invariants and the same nearest-allowed projection rule as in Table 57. Here $Y_{\mathrm{num}} \in \{-6, -3, -2, 0, 1, 4\}$. Table 62 records the resulting best and second-best solutions together with an accuracy gap.

m	features	search box	best coeffs	errors	accuracy	second	gap	complexity
8	`ext,bdry,gmin,gmax,Vwidth`	$\lvert a_i\rvert \le 3$	$(1,-2,-1,0,0,-1)$	11	0.389	$(-3,1,1,0,0,1)$	0.000	5
8	`ext,bdry,Vmin,Vmax`	$\lvert a_i\rvert \le 3$	$(0,-3,1,0,-1)$	12	0.333	$(-2,3,0,0,-1)$	0.000	5
10	`ext,bdry,gmin,gmax,Vwidth`	$\lvert a_i\rvert \le 3$	$(0,1,-1,0,0,-1)$	12	0.333	$(0,2,0,-1,0,0)$	0.000	3
10	`ext,bdry,Vmin,Vmax`	$\lvert a_i\rvert \le 3$	$(1,-2,-1,0,3)$	11	0.389	$(0,-2,1,0,0)$	0.056	7
12	`ext,bdry,gmin,gmax,Vwidth`	$\lvert a_i\rvert \le 3$	$(0,-2,0,1,0,0)$	12	0.333	$(0,-1,-1,1,0,0)$	0.000	3
12	`ext,bdry,Vmin,Vmax`	$\lvert a_i\rvert \le 3$	$(1,0,-2,0,0)$	12	0.333	$(-1,2,0,0,1)$	0.000	3
14	`ext,bdry,gmin,gmax,Vwidth`	$\lvert a_i\rvert \le 3$	$(0,1,-2,0,0,0)$	12	0.333	$(0,-1,0,1,0,-2)$	0.000	3
14	`ext,bdry,Vmin,Vmax`	$\lvert a_i\rvert \le 3$	$(0,0,1,0,-1)$	13	0.278	$(0,-1,1,0,-1)$	0.000	2
16	`ext,bdry,gmin,gmax,Vwidth`	$\lvert a_i\rvert \le 3$	$(-1,2,0,1,0,0)$	12	0.333	$(0,1,0,-2,0,1)$	0.000	4
16	`ext,bdry,Vmin,Vmax`	$\lvert a_i\rvert \le 3$	$(0,0,1,0,-1)$	13	0.278	$(0,-1,1,0,-1)$	0.000	2

Table 62: High-m inverse diagnostic for the full hypercharge numerator $Y_{\mathrm{num}} = 6Y$ from lift-fiber invariants inside $\mathrm{Ext}_m(u)$ for cyclic base types $u \in X_6^{\mathrm{cyc}}$. Rows are generated by `scripts/exp_inverse_highm_hypercharge_full_fit.py`.

X Black holes and wormhole-like channels: rigidity beyond the Standard Model (interface pointer)

This paper focuses on the minimal stable sector and the Standard Model interface at $(m, n) = (6, 3)$. However, the same HPA–Ω rigidity philosophy extends naturally to gravitational and strong-field questions once one adopts the overhead/lapse dictionary (Section Y) and treats boundaries as readout screens. To keep the present manuscript self-contained, we also record (i) a minimal overhead-to-gravity closure and (ii) an executable $\chi(x)$ reconstruction protocol in Appendices AD.7 and AD.8. For an extended treatment of a dynamical gravity interface in the same programmatic language (routing overhead and deterministic closure), see the companion CAP-II manuscript [5]. We record here, as a pointer, two established rigidity targets.

X.1 Black-hole area law as boundary channel counting (external input, rigid interface)

Black-hole thermodynamics provides a well-established link between boundary geometry and entropy: semiclassically,

$$S_{\mathrm{BH}} = \frac{k_B A}{4\ell_P^2},$$

where A is horizon area and $\ell_P^2 = G\hbar/c^3$ [41, 70, 88–90]. This is consistent with the holographic principle viewpoint that gravitational degrees of freedom admit an effective boundary description [39–41]. In the HPA interface language, a boundary screen is a finite-resolution readout cut with a maximal outcome count $\mathcal{N}_\partial(A, r)$, and the channel-count entropy is $S = k_B \log \mathcal{N}_\partial$ [17, 61]. Under the covariant entropy bound and saturation, the area law is the saturation of boundary channel capacity [41]. This viewpoint is consistent with the present paper's emphasis on finite alphabets and stable-sector compression: horizons are extreme instances of "boundary-stable" readout where channel counting dominates.

X.2 Einstein–Rosen throat and inversion continuation (wormhole-like channel)

In isotropic coordinates, the Schwarzschild exterior admits an inversion symmetry and a minimal-surface throat on the time-symmetric slice, giving the classical Einstein–Rosen bridge template [71, 91, 92]. For a minimal explicit formula package (coordinate map, metric form, and inversion), see Proposition X.6. Conceptually, throat/bridge geometries are aligned with modern organizing principles that relate entanglement, horizons, and wormhole geometries (e.g. ER=EPR in appropriate settings) [93].

X.3 Why these extensions are "forced" once rigidity is assumed (interface logic)

The purpose of this appendix is not to import a full gravitational derivation into the present paper, but to record the sense in which certain gravitational structures become the standard rigid templates (and, in limited senses, unavoidable) once one adopts the same rigidity discipline used throughout this manuscript:

- **Boundary entropy is channel capacity.** If horizons are treated as readout screens and entropy is treated as log of a finite channel count (channel-count entropy), then the covariant entropy bound supplies a canonical capacity bound, and saturation yields the area law coefficient 1/4 as the rigid leading term (cf. [41]).
- **Exterior geometry is unique under standard symmetry assumptions.** In spherically symmetric vacuum regions, the Schwarzschild exterior is the standard unique template up to diffeomorphism (Birkhoff-type uniqueness; see, e.g., [71]), so any rigid "black-hole sector" that aims to reproduce classical tests has essentially no freedom in the exterior once the mass parameter is fixed.
- **Endpoint avoidance naturally uses the Einstein–Rosen/Kruskal throat template.** The maximal analytic extension of Schwarzschild contains an Einstein–Rosen bridge on a time-symmetric slice [71, 91, 92]. If one seeks a minimal continuation that removes coordinate endpoint pathology while preserving the exterior, then using the throat/inversion structure as a gluing/continuation template is the most economical geometric move.
- **Wormhole-like channels are topological shortcuts in readout geometry.** In a protocol where boundary transport can be impedance-limited (delay) while bulk access can provide chord-like shortcuts, "wormhole-like" behavior can be interpreted as a controlled bulk-to-boundary interaction channel rather than as a violation of locality. This viewpoint is compatible with standard wormhole terminology in GR [94, 95].

X.4 Interface closure statements (audit form)

For completeness, we record the preceding logic in a compact "input ⇒ output" form, separating standard external inputs from interface identifications. In addition to entropy bounds, we also use standard kinematic delay/lapse templates as external targets at the matching layer: Section Y records the operational Wigner–Smith proxy and the GR reference formulas (47) and (49). Within this paper, the protocol-level overhead-to-gravity bridge that interprets these templates is recorded explicitly in Appendix AD.7, and an executable data protocol to reconstruct $\chi(x)$ is recorded in Appendix AD.8.

Proposition X.1 (Area law as boundary channel saturation (standard input))**.** *Assume (i) boundary entropy is channel-count entropy $S = k_B \log \mathcal{N}_\partial$ for a screen of area A, (ii) the covariant entropy bound $S \le k_B A/(4\ell_P^2)$ holds, and (iii) horizons saturate this bound at leading order. Then the Bekenstein–Hawking area law holds at leading order,*

$$S_{\mathrm{BH}} = \frac{k_B A}{4\ell_P^2}, \qquad \mathcal{N}_\partial(A) = \exp\!\left(\frac{A}{4\ell_P^2}\right).$$

Proof. This is the covariant entropy bound together with the channel-count definition of entropy; see, e.g., [41]. □

Remark X.2 (Bekenstein bound route to the coefficient 1/4 (standard))**.** *The Bekenstein bound states $S \le 2\pi k_B E R/(\hbar c)$ for a system of energy E contained in radius R [96]. For*

a Schwarzschild black hole, take $E = Mc^2$ and $R = R_s = 2GM/c^2$, and recall $A = 4\pi R_s^2$ [71]. Then

$$S \le 2\pi k_B \frac{(Mc^2)(2GM/c^2)}{\hbar c} = \frac{4\pi k_B G M^2}{\hbar c} = k_B \frac{A}{4\ell_P^2},$$

where $\ell_P^2 = G\hbar/c^3$. Equality is attained (at leading order) for black holes.

Proposition X.3 (Bekenstein bound in the r-coordinate (matching form))**.** *Let μ be a mass scale and define the resolution coordinate $r(\mu) = \log_\varphi(\mu/m_e)$ as in* (19) *(equivalently* (43)*). Let $\lambda_{C,e} := \hbar/(m_e c)$ be the electron Compton wavelength. Then the Bekenstein bound can be written as*

$$S \;\le\; 2\pi k_B \, \frac{R}{\lambda_{C,e}} \, \varphi^{\,r(\mu)}.$$

For a Schwarzschild black hole with $\mu = M$ and $R = R_s = 2GM/c^2$, this reproduces the leading area-law scaling $S \propto \varphi^{2r(M)}$ and is equivalent to the $k_B A/(4\ell_P^2)$ form.

Proof. By the Bekenstein bound [96], $S \le 2\pi k_B E R/(\hbar c)$. With $E = \mu c^2$, this is $S \le 2\pi k_B(\mu c R/\hbar) = 2\pi k_B(R/\lambda_C(\mu))$, where $\lambda_C(\mu) = \hbar/(\mu c)$. Using $\mu = m_e \varphi^{r(\mu)}$ and $\lambda_C(\mu) = \lambda_{C,e}\,(m_e/\mu)$, one obtains

$$\frac{R}{\lambda_C(\mu)} = \frac{R}{\lambda_{C,e}} \frac{\mu}{m_e} = \frac{R}{\lambda_{C,e}} \, \varphi^{r(\mu)}.$$

For $\mu = M$ and $R = 2GM/c^2$, the bound becomes $S \le 4\pi k_B G M^2/(\hbar c) = k_B A/(4\ell_P^2)$ as in the preceding remark. □

Remark X.4 (Schwarzschild thermodynamic scaling in the r-coordinate (external))**.** *For a Schwarzschild black hole, $S_{\mathrm{BH}} \propto M^2$ while the Hawking temperature scales as $T_H \propto 1/M$ [70, 71]. Therefore, in the r-coordinate one has the linear log-laws*

$$\log_\varphi S_{\mathrm{BH}} = 2\, r(M) + \mathit{const}, \qquad \log_\varphi T_H = -\, r(M) + \mathit{const}.$$

This highlights why a logarithmic mass coordinate is a canonical matching language across microphysical scales and gravitational thermodynamics.

Proposition X.5 (Schwarzschild exterior as the rigid spherically symmetric vacuum template (standard))**.** *In a spherically symmetric vacuum region, the Lorentzian metric is locally isometric to the Schwarzschild exterior (Birkhoff-type uniqueness), hence classical weak-field tests in such a region have no additional functional freedom beyond the mass parameter.*

Proof. Standard; see, e.g., [71]. □

Proposition X.6 (Einstein–Rosen throat and inversion symmetry in isotropic radius (standard))**.** *Let $R_s := 2GM/c^2$ denote the Schwarzschild radius of a mass M. Here r denotes the Schwarzschild* areal radius *coordinate (not the resolution coordinate $r(\mu) = \log_\varphi(\mu/m_e)$ used elsewhere in this paper). Introduce the isotropic radius $\rho > 0$ by the standard change of variables*

$$r = \rho \left(1 + \frac{R_s}{4\rho}\right)^2. \tag{33}$$

Then the Schwarzschild exterior metric can be written in isotropic form as

$$\mathrm{d}s^2 = -\left(\frac{1 - \frac{R_s}{4\rho}}{1 + \frac{R_s}{4\rho}}\right)^2 c^2\,\mathrm{d}t^2 + \left(1 + \frac{R_s}{4\rho}\right)^4 \left(\mathrm{d}\rho^2 + \rho^2\,\mathrm{d}\Omega^2\right), \tag{34}$$

where $\mathrm{d}\Omega^2 := \mathrm{d}\theta^2 + \sin^2\theta\,\mathrm{d}\phi^2$. Define $\rho_h := R_s/4$ and the inversion map

$$\mathcal{I} : \rho \mapsto \frac{\rho_h^2}{\rho}. \tag{35}$$

Then $r(\rho) = r(\mathcal{I}(\rho))$, and the isotropic form (34) is invariant under $\rho \mapsto \mathcal{I}(\rho)$. The horizon $r = R_s$ corresponds to $\rho = \rho_h$, and the isotropic chart covers the exterior region $r \geq R_s$. In particular, the time-symmetric spatial slice admits a two-ended completion with asymptotically flat ends ($\rho \to \infty$ and $\rho \to 0$) glued at the minimal surface $\rho = \rho_h$ (the Einstein–Rosen throat), rather than a coordinate chart of the Lorentzian black-hole interior.

Proof. The coordinate transform (33) and the isotropic form (34) are standard; see, e.g., [71]. The inversion identity $r(\rho) = r(\rho_h^2/\rho)$ follows by direct substitution into (33). Under $\rho = \rho_h^2/\tilde{\rho}$, one has $\mathrm{d}\rho^2 + \rho^2 \mathrm{d}\Omega^2 = (\rho_h^4/\tilde{\rho}^4)(\mathrm{d}\tilde{\rho}^2 + \tilde{\rho}^2 \mathrm{d}\Omega^2)$ and $(1 + R_s/(4\rho))^4 = (\tilde{\rho} + \rho_h)^4/\rho_h^4$, so the spatial conformal factor in (34) is invariant. The throat statement is the classical Einstein–Rosen bridge template on the time-symmetric slice; see [71, 91, 92]. □

Definition X.7 (Wormhole-like channel as a pointer jump (protocol-level))**.** *Fix a Hilbert order n and a locality-preserving address map $H_n : \{0, \ldots, 4^n - 1\} \to \{0, \ldots, 2^n - 1\}^2$ (Section 5). A* wormhole link *is a directed (or undirected) pointer*

$$a \xrightarrow{\text{ptr}} b, \qquad a, b \in \{0, \ldots, 4^n - 1\},$$

interpreted as an additional readout-level shortcut channel that bypasses the nearest-neighbor scan traversal between indices a and b induced by the Hilbert path. Equivalently, it explicitly relaxes the scan adjacency constraint by augmenting the protocol with a nonlocal pointer edge in index space.

Remark X.8 (Traversability is not assumed in the present paper)**.** *Classical traversable wormholes in Lorentzian GR require additional conditions and are typically associated with violations of standard energy conditions; see, e.g., [94, 95]. Accordingly, the "wormhole-like channel" language used here is protocol-level and refers to a controlled bulk–boundary interaction/shortcut template in readout geometry, not to a claim of a traversable Lorentzian wormhole in vacuum GR. In particular, the only concrete object fixed in this paper is the protocol-level pointer-jump model of Definition X.7, together with the delay/overhead dictionaries used for matching (Section Y).*

Remark X.9 (Topological censorship constraint (standard))**.** *Under standard global assumptions and energy conditions (e.g. the null energy condition), topological censorship theorems constrain macroscopic traversable wormholes connecting asymptotically flat regions in classical GR; see, e.g., [97, 98]. This provides an additional reason to keep the present paper's "wormhole-like" language explicitly at the protocol/interface level.*

For the present paper, the role of this pointer is conservative: it indicates that the same rigidity discipline used here (finite alphabets, auditable closures, explicit mismatch/overhead proxies) can be extended beyond the Standard Model interface to strong-field geometry, while keeping the theorem-level folding layer clean of continuum assumptions.

Y Time and mass as delay: scattering and relativistic lapse dictionaries (interface)

This section records the matching-layer dictionaries underlying the mass-as-delay discussion in Section 10.1.1. It connects protocol-level cost/overhead coordinates to standard measurable proxies (scattering delay, redshift/lapse) and to standard kinematic relations (special and general relativity), while keeping these statements at the interface layer rather than as theorem-level consequences of the folding core.

Y.1 Unified phase–delay dictionary (phase advance, frequency, and group delay)

Two complementary derivatives. [Interface]Frequency is the canonical "phase per tick" quantity in the frequency-first spine: Definition AA.1 fixes $\omega = \Delta\theta/\Delta t$ in tick units. Time delay is the complementary "phase per frequency" quantity: in any setting where a complex response has a measurable phase $\delta(\omega)$ as a function of angular frequency ω, the group-delay observable is the phase derivative

$$\tau(\omega) := \frac{\mathrm{d}\delta}{\mathrm{d}\omega}.$$

These are inverse-facing dictionaries built from the same primitive object (phase as a readout).

Scattering as a phase-response interface. [Interface]In scattering platforms one measures complex S-parameters as functions of frequency. When scattering is (nearly) unitary over a stated band, the phase response is the most stable observable and the delay $\tau(\omega)$ provides a direct operational bridge from phase to time. The Wigner–Smith construction below is precisely the multi-channel, basis-invariant generalization of this group-delay dictionary.

Y.2 Scattering delay as an operational proxy: Wigner–Smith

In platforms where a scattering description is available, delays are directly measurable from complex S-parameters as functions of frequency. Let $S(\omega)$ be a unitary scattering matrix (lossless elastic scattering) at angular frequency ω. The Wigner–Smith time-delay matrix is defined by [20, 21]

$$Q(\omega) := -\mathrm{i}\, S(\omega)^\dagger \frac{\mathrm{d}S}{\mathrm{d}\omega}, \tag{36}$$

and a common scalar summary is the total delay

$$\tau_{\mathrm{WS}}(\omega) := \mathrm{Tr}Q(\omega). \tag{37}$$

In a one-channel setting $S(\omega) = \mathrm{e}^{\mathrm{i}\delta(\omega)}$, (36) reduces to the group/phase derivative

$$\tau_{\mathrm{WS}}(\omega) = \frac{\mathrm{d}\delta}{\mathrm{d}\omega}. \tag{38}$$

Trace/logdet identity and basis invariance (unitary case). [Interface]For unitary $S(\omega)$ one has $S^{-1} = S^\dagger$, hence

$$\mathrm{Tr}Q(\omega) = -\mathrm{i}\,\frac{\mathrm{d}}{\mathrm{d}\omega}\log\det S(\omega).$$

Writing $\det S(\omega) = \mathrm{e}^{\mathrm{i}\Theta(\omega)}$ yields $\tau_{\mathrm{WS}}(\omega) = \mathrm{d}\Theta/\mathrm{d}\omega$, so the WS trace is the derivative of a *total scattering phase*. Moreover, under any energy-independent channel basis change $S'(\omega) = U\,S(\omega)\,U^\dagger$ with U unitary, one has $Q'(\omega) = U\,Q(\omega)\,U^\dagger$; therefore $\mathrm{Tr}Q$ and the eigenvalues of Q are basis-invariant scalar observables in multi-channel settings.

Non-unitarity, losses, and calibration. [Interface]In realistic settings absorption and imperfect calibration can make S non-unitary; one should then either restrict to frequency bands where unitarity holds to a stated tolerance or adopt an explicit loss model and treat τ_{WS} as an effective delay proxy. A minimal auditable measurement pipeline is recorded in Remark Z.1 and Appendix Z.1.

Y.3 Phase shifts and cross sections (interface note)

[Interface]Phase information is simultaneously an interface for cross sections and for time delays. For example, in standard elastic partial-wave conventions one writes $S_\ell(E) = \mathrm{e}^{2\mathrm{i}\delta_\ell(E)}$; then the same phase shifts δ_ℓ determine both the elastic cross sections (via $\sin^2\delta_\ell$) and the corresponding one-channel delays (via energy/frequency derivatives of the phase). The WS one-channel formula (38) applies once the phase convention is fixed: if the measured phase is $\arg S_\ell(E) = 2\delta_\ell(E)$, then the delay is $\tau_\ell(E) = \mathrm{d}(\arg S_\ell)/\mathrm{d}\omega = 2\,\mathrm{d}\delta_\ell/\mathrm{d}\omega$ (equivalently $\tau_\ell(E) = 2\hbar\,\mathrm{d}\delta_\ell/\mathrm{d}E$ under $E = \hbar\omega$). Thus, phase-shift datasets provide a unified operational channel where "scattering cross section" and "scattering time delay" are two facets of the same measured phase response.

Y.4 From delay to overhead and lapse (clock-rate dictionary)

Fix a reference tick duration $\tau_0 > 0$ that defines one unit of baseline protocol time in physical units (seconds). We compress delay into a dimensionless overhead proxy

$$\kappa_{\mathrm{WS}}(\omega) := \frac{\tau_{\mathrm{WS}}(\omega)}{\tau_0}, \tag{39}$$

and define an associated lapse proxy by

$$N_{\mathrm{WS}}(\omega) := \frac{\kappa_0}{\kappa_{\mathrm{WS}}(\omega)}, \tag{40}$$

where κ_0 is a chosen reference overhead (a normalization convention). Operationally, larger delay corresponds to larger overhead and hence to a smaller lapse proxy.

This matches the general "computational lapse" dictionary used elsewhere in the HPA–Ω series: a local overhead field κ induces a clock-rate factor $N = \kappa_0/\kappa$ so that local proper time satisfies

$$\mathrm{d}\tau_{\mathrm{loc}}(x) = N(x)\,\mathrm{d}t. \tag{41}$$

In this paper, we use the dictionary only as a matching layer: it is not used as a premise for any folding or labeling theorem.

Relation to the χ-based gravity dictionary (the γ map). [Interface]Appendix AD.7 defines $s = \kappa/\kappa_0$, $\chi = \log s$ and a one-parameter lapse family $N = \mathrm{e}^{-\gamma\chi} = (\kappa_0/\kappa)^\gamma$. Therefore, given a delay-derived overhead proxy $\kappa_{\mathrm{WS}}(\omega)$ one can form

$$\chi_{\mathrm{WS}}(\omega) := \log\!\left(\frac{\kappa_{\mathrm{WS}}(\omega)}{\kappa_0}\right), \qquad N(\omega) = \mathrm{e}^{-\gamma\chi_{\mathrm{WS}}(\omega)} = N_{\mathrm{WS}}(\omega)^\gamma,$$

so (40) corresponds to the special case $\gamma = 1$ (the base overhead ratio). This makes clear how scattering-delay lapse ratios can be compared to redshift/time-delay data under the same calibrated γ used in the weak-field gravity dictionary.

Y.5 Mass as a time scale: Compton clocks and the depth coordinate

Independently of any specific dynamics, a mass scale defines a frequency scale by combining the standard relations $E = mc^2$ and $E = \hbar\omega$ [24, 58]. Define the Compton angular frequency and time scale

$$\omega_C(\mu) := \frac{\mu c^2}{\hbar}, \qquad \tau_C(\mu) := \frac{1}{\omega_C(\mu)} = \frac{\hbar}{\mu c^2}. \tag{42}$$

Because the present paper works primarily with ratios relative to m_e, the constants c and $\hbar$ cancel:

$$\frac{\omega_C(\mu)}{\omega_C(m_e)} = \frac{\mu}{m_e}, \qquad \frac{\tau_C(\mu)}{\tau_C(m_e)} = \frac{m_e}{\mu}.$$

Consequently the resolution coordinate used in the mass-spectrum closure (Section 13) can be read equally as a log-frequency or log-time coordinate:

$$r(\mu) = \log_\varphi\left(\frac{\mu}{m_e}\right) := \log_\varphi\left(\frac{\omega_C(\mu)}{\omega_C(m_e)}\right) = -\log_\varphi\left(\frac{\tau_C(\mu)}{\tau_C(m_e)}\right). \tag{43}$$

This gives a strong interface meaning to "mass as depth": it is also "mass as a clock-rate coordinate" in the standard Compton sense.

Relativistic reference formulas (supplement). General-relativity lapse/redshift and Shapiro-delay formulas, as well as special-relativity time dilation/dispersion reference relations, are recorded in Appendix Z.

Z Relativistic delay and lapse reference formulas (supplement)

This appendix records standard SR/GR reference relations and optional scattering-delay benchmarks used as external matching-layer targets in the interface dictionaries of Section Y.

Z.1 Wigner–Smith delay: calibration and a one-channel resonance benchmark

Remark Z.1 (Calibration and losses)**.** *The definition* (36) *is standard for unitary S. In realistic settings, absorption and imperfect calibration can make S non-unitary; one should then either restrict to frequency bands where unitarity holds to a stated tolerance or adopt an explicit loss model and treat τ_{WS} as an effective delay proxy [20, 21]. An auditable measurement pipeline can be implemented by phase unwrapping, finite differencing, and explicit stability checks under smoothing and step-size variation.*

One-channel resonance check (Breit–Wigner). As a minimal analytic benchmark, consider a one-channel exactly unitary resonance model

$$S(\omega) = \frac{\omega - \omega_0 - \mathrm{i}\Gamma/2}{\omega - \omega_0 + \mathrm{i}\Gamma/2}, \tag{44}$$

whose phase rises by π across the resonance. Writing $S(\omega) = \mathrm{e}^{\mathrm{i}\delta(\omega)}$, one obtains the Lorentzian delay profile

$$\tau_{\mathrm{WS}}(\omega) = \frac{\mathrm{d}\delta}{\mathrm{d}\omega} := \frac{\Gamma}{(\omega-\omega_0)^2 + (\Gamma/2)^2}, \tag{45}$$

and, at resonance,

$$\tau_{\mathrm{WS}}(\omega_0) = \frac{4}{\Gamma}. \tag{46}$$

Thus the dimensionless overhead proxy (39) is proportional to the inverse linewidth, $\kappa_{\mathrm{WS}}(\omega_0) = 4/(\Gamma\,\tau_0)$. This is the simplest concrete instance of the interface slogan "stable obstruction $\Rightarrow$ additional delay" and provides an experimentally extractable handle (linewidth from phase-jump width) [20, 21].

Z.2 General relativity reference: lapse and Shapiro delay (external target)

In a 3+1 decomposition, the relativistic lapse $N(x)$ relates coordinate time to proper time of static observers by $\mathrm{d}\tau = N\,\mathrm{d}t$ [71]. Thus, identifying $N(x) = \kappa_0/\kappa(x)$ is a direct interface map between overhead and GR clock rates.

Proposition Z.2 (Static redshift law in lapse form (standard))**.** *In a static spacetime with lapse $N(x)$, the frequency ratio of the same signal measured by two static observers at x_{emit} and x_{obs} satisfies*

$$\frac{\omega_{\mathrm{obs}}}{\omega_{\mathrm{emit}}} = \frac{N(x_{\mathrm{emit}})}{N(x_{\mathrm{obs}})}.$$

Equivalently, under the interface identification $N = \kappa_0/\kappa$, one has $\omega_{\mathrm{obs}}/\omega_{\mathrm{emit}} = \kappa(x_{\mathrm{obs}})/\kappa(x_{\mathrm{emit}})$.

Proof. This is the standard gravitational redshift law for static observers in a static metric with $g_{tt} = -N^2c^2$; see, e.g., [71, 99]. □

Schwarzschild lapse. In Schwarzschild coordinates, a static clock at radius r satisfies

$$\mathrm{d}\tau = \sqrt{1 - \frac{2GM}{rc^2}}\,\mathrm{d}t, \tag{47}$$

so $N(r) = \sqrt{1 - 2GM/(rc^2)}$ [71]. Under the interface identification $\kappa(r)/\kappa_0 = 1/N(r)$, one obtains

$$\frac{\kappa(r)}{\kappa_0} = \left(1 - \frac{2GM}{rc^2}\right)^{-1/2} := 1 + \frac{GM}{rc^2} + O\left(\frac{G^2M^2}{r^2c^4}\right). \tag{48}$$

Shapiro delay. For light propagation past a gravitating body, the Shapiro time delay for a radar signal is, at leading post-Newtonian order,

$$\Delta t_{\mathrm{Shapiro}} \;\approx\; \frac{2GM}{c^3}\log\left(\frac{4r_1r_2}{b^2}\right), \tag{49}$$

for endpoints at radii r_1, r_2 and impact parameter b [99, 100]. These standard formulas provide external operational targets for any scan-based identification of additional protocol overhead with effective delay/clock slowing.

Z.3 Special relativity reference: kinematic time dilation and dispersion

In special relativity, proper time and coordinate time relate by the Lorentz factor

$$\mathrm{d}\tau = \frac{\mathrm{d}t}{\gamma}, \qquad \gamma = \frac{1}{\sqrt{1 - v^2/c^2}}, \tag{50}$$

and a relativistic particle satisfies the dispersion relation

$$E^2 = p^2c^2 + m^2c^4, \tag{51}$$

with group velocity $v = \mathrm{d}E/\mathrm{d}p = pc^2/E$ [58, 101]. In a scan/protocol interpretation, (50) is treated as a matching dictionary: once a locality basis and a baseline signal speed c are fixed (Remark 2.1), any additional protocol overhead that reduces the available local update budget can be encoded as an effective γ-factor or lapse factor. This provides a clean place to connect the discrete cost coordinates used in the present paper (depth, fiber multiplicity, connection/holonomy overhead) to standard relativistic observables *without* importing relativistic axioms into the folding layer.

AA Equivalence semantics and the frequency-first dictionary (protocol ⇔ physics)

This appendix upgrades a recurring narrative claim in the HPA–Ω program into an audit-facing contract: physical-language statements are to be read as statements about explicit mathematical objects, *modulo declared equivalence relations*, and all additional closure choices are to be performed by CAP on explicit finite candidate families. It introduces *no new axioms* beyond the two declared primitives: tick as the executed input stream (Axiom 1.1) and CAP as the unique deterministic closure/selection rule (Axiom 1.5).

Why an "equivalence appendix" is needed. The main text already uses several invariance doctrines (tick-origin shift, local fiber relabelings, holonomy cycle-type invariance, log-mismatch invariance under unit changes), but they are distributed across sections. Here we collect them as a single semantic layer so that later continuous dynamical closures (Appendices AD.4–AD.6) can be stated as *mathematical closures on equivalence classes* rather than as informal matching dictionaries.

AA.1 Physical objects as equivalence classes

Protocol objects. [Math]At fixed window length m, protocol microstates are m-bit words in $\Omega_m = \{0,1\}^m$ and stable readout labels are stable types $w \in X_m$ (Sections 2–4). At fixed Hilbert order n on the chosen screen, locality is represented by the display graph G_n (Definition 3.2).

Semantic contract. [Interface]A *physical object* in this paper is an equivalence class of protocol objects under declared equivalence relations that capture representational freedom (e.g. choice of origins, basis relabelings, coarse-graining maps). A *physical observable* is an invariant functional on these equivalence classes, or (when coarse graining is included) a functional that is monotone under the declared coarse-graining preorder.

AA.2 Minimal equivalence relations used implicitly in the main text

We record the minimal equivalence relations that are already used (often implicitly) throughout the paper. Each item below is a *semantic quotient*: it does not add new dynamical assumptions; it fixes what is meant by "the same physics".

(E1) Tick-origin shift. [Interface]Since protocol observables depend on tick differences, $t \sim t + t_0$ is a coordinate convention (Section 3.2).

(E2) Projection-fiber equivalence (finite observability). [Math]At fixed m, microstates $k, k' \in \{0, \dots, 2^m - 1\}$ are observationally equivalent if they project to the same stable type: $k \sim_m k'$ iff $\mathrm{Fold}_m(k) = \mathrm{Fold}_m(k')$. This is the formal core of finite observability and is the origin of degeneracy/fiber data.

(E3) Local fiber-slot relabelings (finite gauge redundancy). [Math]In the padded-fiber connection model (Section 6), relabeling local fiber slots at a vertex is $g_x \in S_r$ and acts by conjugation on loop products (Definition 6.5). Therefore, loop holonomy is physical only through conjugacy invariants (e.g. cycle type; Proposition 6.6).

(E4) Coarse graining (stochastic/Markov morphisms). [Interface]Any finite observer induces a coarse-graining preorder: one readout description is less informative if it is obtained from another by a stochastic map (a Markov morphism). This is the semantic input behind monotonicity requirements used when selecting canonical statistical quadratic forms (cf. Cěncov uniqueness in the CAP action closure; Appendix AD.4).

(E5) Action equivalence (boundary terms and field redefinitions). [Interface]When we speak of "an action" at the continuum closure level, the physical content is the induced equations of motion. Accordingly, actions related by adding a boundary term, or by invertible local field redefinitions, are treated as physically equivalent. CAP selection is applied to equivalence classes (by choosing canonical representatives under a stated tie-break) rather than to raw coordinate expressions.

AA.3 Frequency as a primary derived quantity (frequency-first spine)

Motivation. [Interface]In a tick-first ontology, the most primitive quantitative notion is *counting*. The next forced notion is a *rate of change per tick*. Frequency is the canonical rate: it is dimensionless in tick units and becomes the universal bridge to energy, mass, temperature, redshift, and delay once matching dictionaries are chosen.

Definition AA.1 (Frequency from phase advance (tick units))**.** *Let $\theta(t)$ be a phase variable taking values in a circle $\mathbb{R}/2\pi\mathbb{Z}$ (or in a dyadic phase register $\mathbb{Z}_{2^p}$ embedded into $\mathbb{T}$). For $t_1 \neq t_2$, define the (average) angular frequency in tick units by*

$$\omega(t_1, t_2) := \frac{\Delta\theta}{\Delta t} \quad \textit{with} \quad \Delta t := t_2 - t_1,$$

where $\Delta\theta$ denotes the phase increment in a chosen unwrapping convention (or in the discrete register).

Remark AA.2 (Operator-spectrum and DFT viewpoints (equivalent dictionaries))**.** *Frequency can also be defined as a spectral parameter: time translation by one tick is represented by a shift operator whose eigenphases define frequencies (Weyl-pair viewpoint; Appendix B). Operationally, for any tick-indexed observable $q(t)$ on a finite horizon, a discrete Fourier transform yields a finite spectrum; dominant peaks define effective frequencies. In the present paper we treat these as equivalent interface dictionaries once a specific readout/phase convention is fixed.*

AA.4 Concept index: physical quantities as invariants/closures

Table 63 records an audit-facing concept map. Each physical-language quantity is assigned (i) an invariant mathematical object, and (ii) the section(s) where it is defined/closed within the tick + CAP discipline.

Table 63: Concept index (frequency-first): physical quantities as invariants or CAP-closed outputs.

concept	mathematical object (invariant / closure output)	where fixed/closed	operational proxy (matching layer)
time	tick $t \in \mathbb{Z}$ (differences only)	Axiom 1.1; Section 3	laboratory clock ticks after calibration

concept	mathematical object (invariant / closure output)	where fixed/closed	operational proxy (matching layer)
phase	dyadic register $\mathbb{Z}_{2^p}$ and embedding $e^{i\theta}$	Appendix B; Section 1.8	phase readout / interferometry / complex S-parameters
frequency	$\omega = \Delta\theta/\Delta t$ in tick units (Definition AA.1)	Appendix AA	spectral peaks; clock ratios; redshift
space (display)	addressing map A_n and graph G_n	Section 5; Definition 3.2	locality graph used for audits
distance	d_n (graph metric)	Definition 3.3	hop count / minimal transport steps
velocity	$v = \Delta d/\Delta t$ (tick units)	Definition 3.4	propagation rate; c after calibration
gauge connection	edge transports modulo local relabeling	Section 6	Wilson/plaquette statistics
curvature (finite)	holonomy conjugacy invariant (cycle type)	Proposition 6.6	loop/plaquette statistics
metric (continuum)	Lorentzian metric representative $g_{\mu\nu}$ (CAP-closed family)	Appendix AD.4	redshift/lensing/clock-rate templates
curvature (continuum)	$R_{\mu\nu\rho\sigma}$, $G_{\mu\nu}$ from $g_{\mu\nu}$	Appendix AD.5	weak-field/PPN limits; classical tests
gauge curvature	$F_{\mu\nu}$ (field strength / curvature of connection)	Appendix AD.5	scattering/transport; effective couplings
mass/energy scale	frequency/clock ratio; $r(\mu) = \log_\varphi(\mu/m_e)$	Section 10.1; Appendix Y	Compton clock; scattering delay
lapse / redshift	$N = \kappa_0/\kappa$ from overhead κ	Appendix Y	redshift; Shapiro delay templates
action (continuum)	CAP-selected action class $[S]$ on a finite candidate family	Appendix AD.4	effective-field fit / coarse-grained cost
equations of motion	Euler–Lagrange / Einstein–Yang–Mills equations from S	Appendix AD.5	dynamical response; weak-field tests
stress-energy	$T_{\mu\nu}$ (including information/overhead sector)	Appendix AD.5	energy density, pressure, fluxes
entropy	channel-count / coarse-grained state-count functional	Appendix AD.6	log counts; thermodynamic entropy
temperature	conjugate to entropy via free-energy closure	Appendix AD.6	$k_B T$ scale; noise/thermal spectra
force	response functional (e.g. $-\nabla$ of effective free energy/action)	Appendix AD.6; Appendix AD.5	acceleration; pressure/gradient forces
overhead proxy	$\chi = \log(\kappa/\kappa_0)$ and lapse $N = e^{-\gamma\chi}$	Appendix AD.7	redshift/time delay/clock slowdown
effective potential (weak field)	$\Phi = -\gamma c^2(\chi - \chi_0)$	Appendix AD.7	Newtonian potential proxies
effective density (weak field)	$\rho_{\text{eff}} \propto -\Delta\chi$	Appendix AD.7	lensing/dynamical mass comparisons

concept	mathematical object (invariant / closure output)	where fixed/closed	operational proxy (matching layer)
χ reconstruction protocol	Hilbert binning $\to$ window words $\to$ folding stats $\to$ $\chi(x)$	Appendix AD.8	surveys / simulations / lab arrays
Born probabilities	$P_k = \mathrm{Tr}(\rho E_k)$ (POVM)	Appendix AD.10	empirical outcome frequencies
RG / running in r	$\mathrm{d}g/\mathrm{d}r = (\log\varphi)\beta(g)$	Appendix AD.11	running couplings / threshold matching
cosmology as resolution flow	$f_{\mathrm{stab}}(m) = F_{m+2}/2^m$, $d_m = 2^m/F_{m+2}$	Appendix AD.12	energy-budget fits; capacity growth

Remark on scope. [Audit]The table focuses on the quantities required for the frequency-first dynamical closure. Standard external unit conventions $(\hbar, c, k_B)$ are treated as matching-layer calibration inputs, not as additional primitives of the tick + CAP spine.

AA.5 Curvature as loop invariants (finite and continuum)

Finite curvature from holonomy. [Math]In the finite protocol language, curvature is defined operationally by loop transport: the plaquette holonomy $p_\square$ is a loop product of edge transports, and its conjugacy invariants (cycle type) are gauge invariant under local relabelings (Proposition 6.6). This is the minimal, fully finite analogue of "curvature is holonomy".

Continuum curvature as an interface limit. [Interface]In a continuum dictionary where a (gauge or Levi–Civita) connection one-form A is available, holonomy around an infinitesimal loop is controlled by the curvature two-form $F = \mathrm{d}A + A \wedge A$. In that dictionary, the finite-loop invariant above is interpreted as a coarse-grained proxy for curvature flux through the loop. Appendix AD.5 records the resulting continuum field equations after CAP closes a minimal action family.

AA.6 Force as response: gradients of action and free energy

Response definition (action). [Interface]Once a continuum representative action S is fixed (as a CAP-closed output; Appendix AD.4), "force" is defined as the response of S (or an effective reduced action S_{eff}) to a displacement/boundary perturbation, e.g.

$$F_i := -\frac{\partial S_{\mathrm{eff}}}{\partial x^i},$$

in any setting where a coordinate x^i is part of the chosen continuum representative. This is an equivalence-class notion: adding a boundary term changes S but not its Euler–Lagrange equations, so "force" is to be read as an invariant of the equations-of-motion class rather than of a raw action expression.

Response definition (free energy / entropic force). [Interface]In a thermodynamic closure, an effective free energy functional $\mathcal{F}$ is defined on coarse-grained state variables, and force is likewise a response

$$F_i = -\frac{\partial \mathcal{F}}{\partial x^i}.$$

When $\mathcal{F} = E - TS$ is used, this yields the standard decomposition into energetic and entropic components. Appendix AD.6 records the corresponding CAP closure and the frequency-first thermodynamic dictionary.

AA.7 Entropy as state counting under equivalence and coarse graining

Counting viewpoint. [Interface]Under finite observability, an observed stable label $w \in X_m$ represents a whole microstate fiber $P(w) = \mathrm{Fold}_m^{-1}(w)$. The simplest protocol-level entropy associated with this residual uncertainty is therefore a counting entropy

$$S_{\mathrm{fib}}(w) := \log |P(w)|,$$

optionally scaled by k_B in physical units. More generally, any coarse-graining map induces macrostates as equivalence classes; entropy is the logarithm of the macrostate multiplicity, or of an effective channel capacity in boundary settings (Appendix X).

Second-law semantics. [Interface]A key reason "irreversibility" can be discussed without adding a new axiom is that the map from microscopic histories to observable records is many-to-one (Section 3.2): coarse graining and stability folding discard information, so entropy in the counting sense is naturally nondecreasing along protocol time when described only at the coarse level. Appendix AD.6 makes this monotonicity precise in the CAP closure language used throughout the paper.

AB Modular geodesic flow and Gauss-map renormalization (notes)

[Audit]This appendix records standard "mother space" facts connecting continued fractions to modular dynamics. It provides a canonical source for the continued-fraction/Ostrowski structures that appear throughout the golden-branch layer (Section 2.3 and Appendix N). These results are not used as premises in theorem-level folding proofs; they serve as an audit-facing justification for why the continued-fraction module is not an ad hoc digitization.

AB.1 Modular surface and the Gauss map

Let $\mathbb{H} = \{\tau \in \mathbb{C} : \mathrm{Im}(\tau) > 0\}$ be the upper half-plane. The modular group is generated by

$$T : \tau \mapsto \tau + 1, \qquad S : \tau \mapsto -\frac{1}{\tau},$$

and the modular surface is the quotient orbifold

$$M := \mathrm{PSL}_2(\mathbb{Z})\backslash\mathbb{H}.$$

The geodesic flow on M admits a classical symbolic coding whose base map is the Gauss map

$$G(\xi) = \left\{\frac{1}{\xi}\right\}, \qquad \xi \in (0,1),$$

and whose symbols are the continued-fraction digits of $\xi = [0; a_1, a_2, \ldots]$.

Theorem AB.1 (Series suspension model (classical))**.** *[Math]There exists a Poincaré cross-section for the geodesic flow on M whose first-return map is conjugate to the Gauss map G on $(0,1)$. Moreover, the geodesic flow is measurably isomorphic to the suspension flow over G with roof function*

$$r(\xi) = -2\log\xi.$$

In particular, the continued-fraction digits of ξ arise as the symbolic itinerary of successive returns.

Remark AB.2. *See [102, 103] for standard constructions and proofs.*

AB.2 Invariant Gauss measure and digit law

Theorem AB.3 (Gauss invariant measure and digit distribution (classical))**.** *[Math]The Gauss map $G(\xi) = \{1/\xi\}$ preserves the probability measure*

$$\mathrm{d}\mu(\xi) = \frac{1}{\log 2}\,\frac{\mathrm{d}\xi}{1+\xi}, \qquad \xi \in (0,1),$$

and is ergodic with respect to μ. Writing $\xi = [0; a_1, a_2, \ldots]$, the first digit satisfies

$$\mu(a_1 = k) = \log_2\!\left(1 + \frac{1}{k(k+2)}\right) \qquad (k \geq 1).$$

Remark AB.4. *See [104] for proofs and further quantitative results.*

AB.3 Gauss–Kuzmin convergence (finite-time relaxation)

Theorem AB.5 (Gauss–Kuzmin exponential convergence (classical))**.** *[Math]Let ν be a probability measure on $(0,1)$ that is absolutely continuous with respect to Lebesgue measure with a density of bounded variation. Then there exist constants $C > 0$ and $0 < \rho < 1$ such that for all $n \geq 0$,*

$$\sup_{x \in (0,1)} |\nu(G^n(\xi) \leq x) - \mu((0,x])| \leq C\,\rho^n,$$

where μ is the Gauss invariant measure from Theorem AB.3. The optimal ρ is known as the Gauss–Kuzmin–Wirsing constant (numerically $\rho \approx 0.30366$).

Remark AB.6. *See [104] for proofs and numerical constants.*

AB.4 Relation to Ostrowski numeration used in the paper

[Audit]The modular-geodesic origin above provides a canonical meaning to the continued-fraction digits of a boundary irrational parameter. In the present paper, the scan slope α is such a boundary irrational (Section 2.1), and the Ostrowski/Zeckendorf module used for discrepancy certificates (Appendix N) is the corresponding canonical integer coordinate system built from the continued fraction of α. This appendix does not identify the scan orbit with geodesic flow; it records that, once the modular stage is adopted, the digit module is not an arbitrary choice.

AC Modular scale exchange, Morita equivalence, and Fourier exchange (notes)

[Audit]This appendix records standard symmetry/equivalence structures that strengthen the "equivalence semantics" viewpoint (Appendix AA). It introduces no new axioms beyond tick and CAP and is not used as a premise in theorem-level folding proofs.

AC.1 Modular inversion as a scale-exchange template

Consider the upper half-plane $\mathbb{H} = \{\tau = x + \mathrm{i}y : \ y > 0\}$ and the modular generators

$$T : \tau \mapsto \tau + 1, \qquad S : \tau \mapsto -\frac{1}{\tau}.$$

Writing $\tau = x + \mathrm{i}y$, one has

$$S(\tau) = -\frac{x - \mathrm{i}y}{x^2 + y^2}, \qquad \mathrm{Im}(S(\tau)) = \frac{y}{x^2 + y^2}.$$

[Interface]Thus, away from large $|x|$, the transformation S exchanges large and small imaginary parts (height) at the level of scale magnitude. On the modular curve $X(1)$, the cusp orbit is unique, so 0 and ∞ represent the same cusp in the quotient; the involution S provides a canonical endpoint exchange on the quotient.

AC.2 Morita equivalence of rotation algebras and the $\mathrm{SL}_2(\mathbb{Z})$ action

Let A_α be the (irrational) rotation algebra generated by unitaries U, V with

$$UV = \mathrm{e}^{2\pi\mathrm{i}\alpha} VU, \qquad \alpha \in \mathbb{R} \setminus \mathbb{Q}.$$

There is a canonical $\mathrm{SL}_2(\mathbb{Z})$ action on the slope parameter

$$\alpha' = \frac{a\alpha + b}{c\alpha + d}, \qquad \gamma = \begin{pmatrix} a & b \\ c & d \end{pmatrix} \in \mathrm{SL}_2(\mathbb{Z}).$$

Theorem AC.1 (Morita equivalence classification for noncommutative tori (standard))**.** *[Math]For irrational parameters $\alpha, \beta \in \mathbb{R} \setminus \mathbb{Q}$, the rotation algebras A_α and A_β are (strongly) Morita equivalent if and only if there exists $\gamma = \begin{pmatrix} a & b \\ c & d \end{pmatrix} \in \mathrm{SL}_2(\mathbb{Z})$ such that*

$$\beta = \frac{a\alpha + b}{c\alpha + d}.$$

Remark AC.2. *See [105–107] for proofs and further structure (projective modules and K-theory invariants).*

[Audit]In the scan algebra language of this paper, the parameter α controls the commutation phase between shift and multiplication (Definition B.1). Morita equivalence provides a hard mathematical mechanism for treating different α as "the same geometry" once the equivalence class is declared.

AC.3 Fourier exchange: swapping scan shift and phase multiplication

We record a concrete scan–readout exchange for the canonical Weyl-pair model.

Proposition AC.3 (Fourier exchange for the covariant Weyl pair)**.** *[Math]Let $\mathcal{H} = L^2(\mathbb{R}/\mathbb{Z})$ and define, for fixed $\alpha \in \mathbb{R}$,*

$$(U\psi)(x) = \psi(x + \alpha), \qquad (V\psi)(x) = \mathrm{e}^{2\pi\mathrm{i}x}\psi(x).$$

Let $\mathcal{F} : \mathcal{H} \to \ell^2(\mathbb{Z})$ be the Fourier transform

$$(\mathcal{F}\psi)(k) = \int_0^1 \psi(x)\, \mathrm{e}^{-2\pi\mathrm{i}kx}\, \mathrm{d}x.$$

Then on $\ell^2(\mathbb{Z})$ one has

$$\mathcal{F}U\mathcal{F}^{-1} : \widehat{\psi}(k) \mapsto \mathrm{e}^{2\pi\mathrm{i}k\alpha}\widehat{\psi}(k), \qquad \mathcal{F}V\mathcal{F}^{-1} : \widehat{\psi}(k) \mapsto \widehat{\psi}(k-1).$$

In particular, translation (scan shift) becomes phase multiplication in Fourier space, while phase multiplication becomes an index shift, realizing a concrete scan–readout exchange.

Proof. For the first identity,

$$(\mathcal{F}U\psi)(k) = \int_0^1 \psi(x+\alpha)\mathrm{e}^{-2\pi\mathrm{i}kx}\,\mathrm{d}x = \mathrm{e}^{2\pi\mathrm{i}k\alpha}\int_0^1 \psi(u)\mathrm{e}^{-2\pi\mathrm{i}ku}\,\mathrm{d}u = \mathrm{e}^{2\pi\mathrm{i}k\alpha}(\mathcal{F}\psi)(k),$$

using the substitution $u = x + \alpha$ and periodicity on $\mathbb{R}/\mathbb{Z}$. For the second identity,

$$(\mathcal{F}V\psi)(k) = \int_0^1 \mathrm{e}^{2\pi\mathrm{i}x}\psi(x)\mathrm{e}^{-2\pi\mathrm{i}kx}\,\mathrm{d}x = \int_0^1 \psi(x)\mathrm{e}^{-2\pi\mathrm{i}(k-1)x}\,\mathrm{d}x = (\mathcal{F}\psi)(k-1).$$

□

AD Hecke operators and the prime skeleton (notes)

[Audit]This appendix records a standard arithmetic "prime skeleton" template: a commuting family of symmetry-preserving operators generated by primes and constrained by rigid multiplicative relations. It is included as an optional mathematical backbone for cross-scale consistency discussions; it introduces no new axioms and is not used as a premise in theorem-level folding proofs.

AD.1 Hecke operators on q-expansions

Let M_k denote a space of modular forms of weight k (for $\mathrm{PSL}_2(\mathbb{Z})$ or a congruence subgroup). If

$$f(\tau) = \sum_{m \geq 0} a_m q^m, \qquad q = \mathrm{e}^{2\pi \mathrm{i} \tau},$$

then the Hecke operator T_n is defined on q-expansions by

$$(T_n f)(\tau) := \sum_{m \geq 0} \left(\sum_{d \mid (m,n)} d^{k-1} \, a_{mn/d^2} \right) q^m. \tag{52}$$

Hecke operators preserve modular symmetry and, on standard cusp-form subspaces with Petersson inner product, form a commuting family that can be simultaneously diagonalized; see [108, 109].

AD.2 Prime generation and multiplicative relations

The "prime skeleton" is not a restriction to primes; it is the statement that primes generate the full Hecke algebra. Two standard relations are:

$$T_m T_n = \sum_{d \mid (m,n)} d^{k-1} \, T_{mn/d^2}, \tag{53}$$

and, for prime powers,

$$T_{p^{r+1}} = T_p T_{p^r} - p^{k-1} T_{p^{r-1}}. \tag{54}$$

Thus the full family $\{T_n\}_{n \geq 1}$ is determined by the prime-indexed generators $\{T_p\}$ together with these relations [108, 109].

AD.3 Eigenforms and Euler products

If f is a normalized simultaneous eigenform, then for all $n \geq 1$,

$$T_n f = \lambda_n f,$$

and in standard normalizations one has $\lambda_n = a_n$. The associated Dirichlet series

$$L(f, s) = \sum_{n \geq 1} \frac{a_n}{n^s}$$

admits an Euler product whose local factors are determined by primes. For level 1 one has the standard shape

$$L(f, s) = \prod_{p} \left(1 - a_p p^{-s} + p^{k-1-2s} \right)^{-1}, \tag{55}$$

see [108, 109].

[Audit]In protocol language, this provides a canonical model of "cross-scale stability under symmetry-preserving coarse operations": commuting generators indexed by primes propagate rigid constraints to all composite scales via the multiplicative relations above.

AD.4 CAP closure of a continuum action: from equivalence semantics to dynamical field equations

This appendix records a single purpose: to make explicit how the familiar continuum "least-action" machinery can be treated as a *CAP-closed representative* of the tick + CAP spine, rather than as an extra ontic postulate. The output is an *action skeleton* whose terms are fixed by declared equivalence semantics (Appendix AA) together with CAP minimality on an explicit *finite* candidate family, in the audit form of Appendix H.

Status. [Interface]The continuum closure is an interface representative: it does not alter the finite folding core. It is introduced so that frequency/lapse/holonomy diagnostics can be translated into standard continuum field equations in a way that is auditable (no hidden knobs) and compatible with the paper's layering doctrine.

AD.4.1 Closure problem statement

Input data (from the tick+CAP spine). [Interface]The protocol provides: (i) a tick-indexed readout stream, (ii) finite stable-sector types with fibers under projection, (iii) a locality display dictionary via addressing, and (iv) measurable overhead/delay proxies that act as clock-rate dictionaries (Appendix Y). Appendix AA formalizes the semantic quotients (tick-origin, local relabelings, coarse graining, action equivalence).

Desired output (continuum representative). [Interface]We seek a local covariant effective description in which:

- frequency/clock-rate variation is represented by a lapse-like field (or equivalently by an overhead field κ),
- compensating transport is represented by gauge connections with curvature,
- dynamics is specified by stationarity of a CAP-selected action within a bounded candidate family.

AD.4.2 Candidate family: local covariant invariants under the equivalence semantics

Finite candidate family requirement. [Audit]To keep CAP well-posed, we restrict to finite families by construction (Appendix H). Concretely, we (i) restrict the list of admissible term *types*, and (ii) discretize coefficient choices into a bounded rational box.

Term dictionary (types). [Interface]We restrict to local scalars built from fields and at most two derivatives, consistent with minimal description complexity and with the operational meaning of locality on the addressing graph. The candidate term types are:

- **gravity sector:** $\sqrt{-g}$, $\sqrt{-g}\,R$ (cosmological constant and Einstein–Hilbert);
- **gauge sector:** $\sqrt{-g}\,\mathrm{Tr}(F_{\mu\nu}F^{\mu\nu})$ for each compact gauge factor;
- **information/overhead sector:** a scalar amplitude $\chi \geq 0$ with a quadratic gradient penalty $\sqrt{-g}\,g^{\mu\nu}(\nabla_\mu\chi)(\nabla_\nu\chi)$ and a local potential $\sqrt{-g}\,V(\chi^2)$;
- **matter sector:** a placeholder $\sqrt{-g}\,\mathcal{L}_m$ for additional effective degrees of freedom already closed at the protocol interface (e.g. the SM labeling sector).

Why these terms are "forced" (uniqueness inputs). We record three standard uniqueness inputs, each aligned with an equivalence semantic already present in this paper.

- **Diffeomorphism covariance as representation independence.** [Interface]A continuum representative should not depend on coordinate reparametrizations of the representative manifold; this is the continuum analogue of the "no privileged addressing coordinate" stance (Appendix AA). Under the additional restriction to at most second derivatives, the lowest-complexity gravitational scalar is R (Lovelock-type uniqueness in 4D; [110]).
- **Probability preservation ⇒ compact internal redundancy.** [Interface]Treating internal redundancy as probability preserving forces (projective) unitarity (Wigner; [87]), hence compactness of the connected gauge redundancy (Proposition R.3). Given a compact gauge group, the unique gauge-invariant local quadratic kinetic term is $\mathrm{Tr}(F_{\mu\nu}F^{\mu\nu})$ (Propositions 8.4 and 8.5).
- **Coarse-graining monotonicity ⇒ Fisher-type quadratic form.** [Interface]Coarse graining is modeled by stochastic maps (Appendix AA). On finite probability simplices, Cěncov's theorem implies that (up to overall scale) the Fisher information metric is the unique Riemannian metric monotone under Markov morphisms [111]. Therefore the minimal covariant quadratic penalty that measures spatial variation in statistical distinguishability is Fisher-like; we encode it by a scalar "Fisher amplitude" χ and a gradient term $g^{\mu\nu}(\nabla_\mu\chi)(\nabla_\nu\chi)$.

AD.4.3 Coefficient discretization and CAP selection (audit form)

Finite coefficient box. [Audit]Fix a bound $B \in \mathbb{N}$. Let coefficients be chosen from a bounded rational set, e.g.

$$\mathcal{C}(B) := \left\{ \frac{p}{q} : \ p, q \in \mathbb{Z},\ 1 \le |p| \le B,\ 1 \le q \le B \right\} \cup \{0\}.$$

This makes the candidate action family finite once the term-type dictionary is finite.

Complexity key (tie-break). [Audit]We use a deterministic lexicographic complexity key that prefers: (i) fewer derivatives, (ii) fewer distinct term types, (iii) smaller denominator/height in $\mathcal{C}(B)$, (iv) smaller gauge-algebra dimensions when gauge-factor choice is still open. This mirrors the "no hidden knobs" contract: every refinement is an explicit enlargement of a finite box.

AD.4.4 CAP-minimal action skeleton (closure output)

Proposition AD.1 (CAP-minimal covariant action skeleton (interface closure))**.** *Adopt the equivalence semantics of Appendix AA (tick-origin shift, local redundancy/gauge, coarse-graining preorder, action equivalence). Restrict to local covariant term types with at most two derivatives as in Section AD.4.2, and discretize coefficients into a finite box as in Section AD.4.3. Then CAP selects a minimal representative action of the form*

$$S_{\mathrm{eff}} = \int \mathrm{d}^4x\,\sqrt{-g}\left[\frac{R-2\Lambda}{16\pi G} - \lambda_F\, g^{\mu\nu}(\nabla_\mu\chi)(\nabla_\nu\chi) - V(\chi^2) \ - \ \sum_a \frac{1}{4g_a^2}\mathrm{Tr}(F^{(a)}_{\mu\nu}F^{(a)\mu\nu}) \ + \ \mathcal{L}_m\right], \tag{56}$$

where $g_{\mu\nu}$ is a Lorentzian metric representative, $F^{(a)}_{\mu\nu}$ are curvature tensors for each compact gauge factor, and χ is a nonnegative scalar amplitude encoding coarse-grained distinguishability/overhead.

Proof sketch (audit viewpoint). The term-type dictionary is constructed precisely to list the lowest-complexity local covariant invariants compatible with the equivalence semantics: the gravitational sector contributes $\sqrt{-g}$ and $\sqrt{-g}R$ at the minimal derivative order; the gauge sector contributes $\mathrm{Tr}(F^2)$ as the unique local quadratic gauge-invariant kinetic term; the coarse-graining semantics forces a Fisher-type quadratic penalty for distinguishability variation, represented by χ. Discretizing coefficients makes the family finite; CAP then selects a canonical representative under the stated lexicographic tie-break. Numerical values of $(G, \Lambda, \lambda_F, g_a)$ are treated as matching/calibration data unless further protocol-level closures are imposed. □

Frequency-first interpretation. [Interface]The field χ can be read as an information-density amplitude and therefore as a proxy for local clock/frequency structure once a cost-to-clock dictionary is fixed: overhead κ defines a lapse $N = \kappa_0/\kappa$ (Appendix Y), and frequency ratios are primary observables (Appendix AA). Appendix AD.5 records the resulting field equations obtained by varying (56).

AD.5 Field equations from variation (Einstein–Yang–Mills + information sector)

This appendix records the standard variational consequences of the CAP-closed continuum action skeleton in Appendix AD.4. The role here is not novelty in calculus, but audit alignment: the dynamical equations used in later interface interpretations are explicitly the Euler–Lagrange equations of the declared action class.

AD.5.1 Reference action

We take as reference representative (Appendix AD.4)

$$S_{\mathrm{eff}} = \int \mathrm{d}^4x\,\sqrt{-g}\,\left[\frac{R-2\Lambda}{16\pi G} - \lambda_F\, g^{\mu\nu}(\nabla_\mu\chi)(\nabla_\nu\chi) - V(\chi^2)\;-\;\sum_a \frac{1}{4g_a^2}\mathrm{Tr}(F^{(a)}_{\mu\nu}F^{(a)\mu\nu})\;+\;\mathcal{L}_m\right]. \tag{57}$$

AD.5.2 Metric variation: Einstein equation with gauge and information stress

Theorem AD.2 (Einstein equation with total stress tensor)**.** *Varying* (57) *with respect to the metric yields*

$$G_{\mu\nu} + \Lambda g_{\mu\nu} = 8\pi G\left(T^{(m)}_{\mu\nu} + T^{(\chi)}_{\mu\nu} + T^{(\mathrm{YM})}_{\mu\nu}\right), \tag{58}$$

where $T^{(m)}_{\mu\nu}$ is the matter stress tensor, $T^{(\chi)}_{\mu\nu}$ is the information/amplitude stress tensor, and $T^{(\mathrm{YM})}_{\mu\nu}$ is the gauge-field stress tensor.

Proof sketch. This is the standard metric variation of a diffeomorphism-invariant local action. The Einstein–Hilbert term yields $G_{\mu\nu}$; the constant term yields $\Lambda g_{\mu\nu}$. The remaining contributions are, by definition, the stress tensors obtained from varying the corresponding Lagrangian densities with respect to $g^{\mu\nu}$. □

Proposition AD.3 (Information/amplitude stress tensor)**.** *The contribution of the χ-sector in* (57) *is*

$$T^{(\chi)}_{\mu\nu} = 2\lambda_F\left(\nabla_\mu\chi\,\nabla_\nu\chi - \frac{1}{2}g_{\mu\nu}(\nabla\chi)^2\right) - g_{\mu\nu}V(\chi^2), \qquad (\nabla\chi)^2 := g^{\alpha\beta}\nabla_\alpha\chi\,\nabla_\beta\chi. \tag{59}$$

Proposition AD.4 (Yang–Mills stress tensor (per factor))**.** *For each gauge factor a, the curvature term contributes*

$$T^{(\mathrm{YM},a)}_{\mu\nu} = \frac{1}{g_a^2}\mathrm{Tr}\left(F^{(a)}_{\mu\alpha}F^{(a)\,\alpha}_{\nu} - \frac{1}{4}g_{\mu\nu}F^{(a)}_{\alpha\beta}F^{(a)\alpha\beta}\right), \tag{60}$$

and $T^{(\mathrm{YM})}_{\mu\nu} = \sum_a T^{(\mathrm{YM},a)}_{\mu\nu}$.

AD.5.3 Gauge variation: Yang–Mills equations

Proposition AD.5 (Yang–Mills equation (schematic))**.** *Varying* (57) *with respect to the gauge connection of factor a yields*

$$\nabla_\mu \left(\frac{1}{g_a^2} F^{(a)\mu\nu} \right) = J^{(a)\nu}, \tag{61}$$

where $J^{(a)\nu}$ *is the matter current induced by* $\mathcal{L}_m$ *(and any explicit* χ *couplings, if present).*

Remark. [Interface]Equation (61) is the continuum dictionary corresponding to the finite connection/holonomy skeleton (Section 6), where "curvature" is read as loop holonomy and sources correspond to persistent mismatch/defect sectors.

AD.5.4 Amplitude variation: the χ equation

Proposition AD.6 (Amplitude equation)**.** *Varying* (57) *with respect to* χ *yields*

$$2\lambda_F \,\Box\chi - \frac{\mathrm{d}V}{\mathrm{d}\chi} = 0, \qquad \Box := \nabla^\mu \nabla_\mu. \tag{62}$$

AD.5.5 Conservation and frequency-redshift semantics

Covariant conservation. [Math]By diffeomorphism invariance one has $\nabla^\mu G_{\mu\nu} = 0$ (Bianchi identity), hence (58) implies covariant conservation of the total stress:

$$\nabla^\mu \left(T^{(m)}_{\mu\nu} + T^{(\chi)}_{\mu\nu} + T^{(\mathrm{YM})}_{\mu\nu} \right) = 0, \tag{63}$$

with exchange terms between sectors determined by explicit couplings in $\mathcal{L}_m$.

Frequency-first interpretation (lapse/redshift). [Interface]In a static or adiabatic regime, the lapse N (Appendix Y) can be identified with $\sqrt{-g_{00}}$ in a suitable gauge. Then a primary observable is the *frequency ratio* between two locations:

$$\frac{\omega_{\mathrm{obs}}(x)}{\omega_{\mathrm{obs}}(y)} = \frac{N(y)}{N(x)},$$

which is the continuum encoding of the tick-first idea that mass/energy and redshift are frequency dictionaries.

AD.5.6 Weak-field limit: Poisson equation and a $1/r$ potential

Newtonian template. [Interface]In the weak-field, slow-motion regime one writes $g_{00} \approx -(1 + 2\phi)$ with Newtonian potential ϕ. Keeping only leading order and taking the 00 component of (58) yields a Poisson-type equation

$$\Delta\phi = 4\pi G \, \rho_{\mathrm{eff}},$$

where ρ_{eff} is the effective energy density extracted from the total stress tensor. In vacuum outside localized sources, $\Delta\phi = 0$ and the spherically symmetric exterior solution is $\phi(r) = -GM/r$.

Relation to delay/lapse dictionaries. [Match]The standard GR lapse and Shapiro-delay formulas used elsewhere in this paper as matching templates are recorded in Appendix Z. In the frequency-first reading, these are equivalently statements about how clock rates and signal frequencies vary in the weak-field potential.

AD.6 Thermodynamics from equivalence: entropy, temperature, and entropic force (frequency-first)

This appendix closes a thermodynamic dictionary compatible with the tick + CAP spine and the equivalence semantics of Appendix AA. The goal is not to import thermodynamics as an independent axiom set, but to record how the standard thermodynamic notions can be treated as *derived* from: (i) finite observability (many-to-one coarse graining) and (ii) CAP selection of minimal-cost macroscopic representatives.

AD.6.1 Entropy as coarse-grained state counting

Macrostate as an equivalence class. [Interface]Fix a coarse-graining map C from microscopic protocol data to macroscopic descriptors. Two microdescriptions are macroscopically equivalent if they map to the same coarse descriptor. This is the semantic content of the coarse-graining equivalence in Section AA.2.

Counting entropy (finite). [Interface]For a macrostate M with microstate set $\Gamma(M)$, define the counting entropy

$$S(M) := \log |\Gamma(M)|, \tag{64}$$

optionally scaled to physical units by k_B. At fixed window length m, the simplest instance is the fiber-count entropy $S_{\mathrm{fib}}(w) = \log |P(w)|$ for a stable type $w \in X_m$ (Appendix AA.7).

Boundary/channel entropy. [Interface]In boundary-screen settings (black-hole or holographic cuts), the same idea is channel capacity: if $\mathcal{N}_\partial$ is the maximum number of distinguishable boundary outcomes at a given resolution, then $S = k_B \log \mathcal{N}_\partial$ (Appendix X).

AD.6.2 Energy and temperature as frequency dictionaries

Energy as frequency (ratio-first). [Interface]In the tick-first stance, a primary dimensionless quantity is a frequency ratio. Mass/energy scales are therefore organized by the log-frequency coordinate $r(\mu) = \log_\varphi(\mu/m_e)$ (Section 10.1 and Appendix Y). In matching form one may use $E = \hbar\omega$ and $E = mc^2$ (Appendix Y), but the present program prefers ratios where constants cancel.

Temperature as a frequency scale. [Interface]Temperature is the natural "frequency scale" of coarse excitations: in thermal field theory one has Matsubara frequencies $\omega_n = 2\pi n k_B T/\hbar$, and in classical statistical mechanics $k_B T$ sets typical energy increments. Accordingly, in the frequency-first dictionary we treat T as the scale conjugate to entropy, with the k_B and $\hbar$ conversion treated as matching-layer calibration.

Definition AD.7 (Thermodynamic temperature (conjugate definition))**.** *Let $E(M)$ be an effective energy functional of macrostates and $S(M)$ an entropy functional. In regimes where E can be treated as a function of S along a one-parameter family, define temperature by*

$$\frac{1}{T} := \frac{\partial S}{\partial E}.$$

AD.6.3 CAP as a free-energy principle

Free energy as CAP objective. [Interface]A standard thermodynamic closure defines a free energy functional

$$\mathcal{F}(M) := E(M) - T\,S(M),$$

and asserts that equilibria minimize $\mathcal{F}$ subject to constraints. In the present program, this is read as a CAP closure: among all coarse representatives compatible with the protocol constraints, the realized representative minimizes a total cost that includes (i) mismatch/overhead and (ii) residual uncertainty.

Proposition AD.8 (CAP free-energy closure (audit form))**.** *Fix a finite coarse-graining family* $\{\mathsf{C}_\theta : \theta \in \Theta(B)\}$ *and a finite parameter family of macroscopic representatives* $M(\theta)$*. Define an objective of the form*

$$J(\theta) = \kappa\, E(M(\theta)) + \kappa_S\, (-S(M(\theta))) + \kappa_c\, \mathrm{Comp}(\theta),$$

with a deterministic tie-break key as in Appendix H. Then CAP selects a unique minimizer θ_B *and therefore a unique macroscopic representative* $M(\theta_B)$ *within the declared finite family.*

Interpretation. [Interface]The minus sign in $-S$ reflects the conventional role of entropy as a stabilizing/typicality factor in equilibrium selection. Whether one writes the objective as $E - TS$ or as a weighted sum depends on which quantities are treated as fixed constraints and which as adjustable parameters; the audit requirement is only that the candidate family is finite and the tie-break is explicit.

AD.6.4 The three laws (protocol reading)

First law (bookkeeping identity). [Interface]Once an energy functional E is fixed at the coarse level, the first law is a bookkeeping identity for how E changes under (i) changes of macrostate multiplicity (heat) and (ii) changes of external constraints (work). In a frequency-first description, the "internal energy" is a frequency/clock-rate functional, and work corresponds to controlled changes in constraints that shift that functional.

Second law (monotonicity under coarse graining). [Interface]Irreversibility does not require a new axiom here: it follows from many-to-one projection and coarse graining. When only macrovariables are tracked, information about microhistories is discarded (Section 3.2), and the counting entropy (64) is naturally nondecreasing under refinement-forgetting operations. CAP additionally selects representatives of minimal cost, giving a Lyapunov-style monotonicity for a total objective (Proposition AD.8).

Third law (stability floor and unattainability). [Interface]In protocol terms, the third law is a statement about the existence of a minimal stable background (a reference macrostate) and about the cost of reaching lower-entropy configurations: as $T \to 0$ (frequency scale of fluctuations collapses), the reachable macrostates shrink toward a stable sector whose residual entropy is determined by the remaining coarse-grained degeneracy (e.g. fiber multiplicities at the anchor). In the CAP language, reaching strictly zero entropy would require eliminating all residual equivalence-class multiplicity, which generally requires unbounded resources/resolution.

AD.6.5 Entropic force and the gravity/delay dictionary

Entropic force as response. [Interface]Given a free energy (or any CAP objective) depending on a position-like parameter x, force is defined as the response

$$F(x) = -\nabla_x \mathcal{F}(x).$$

If E is approximately constant while S varies with x, this yields the entropic-force form

$$F(x) \approx T\, \nabla_x S(x).$$

Relation to lapse and delay. [Interface]The delay/lapse dictionary (Appendix Y) identifies overhead with clock-rate slowdown, so spatial variation of overhead induces spatial variation of local clock frequency. In the weak-field limit of Section AD.5.6, the same variation is encoded by $g_{00} \approx -(1+2\phi)$ and therefore by a potential ϕ. Thus, in a frequency-first language, "gravitational force" is equivalently the response of frequency/clock-rate structure to spatial displacement, consistent with the response definition above.

AD.7 Overhead-to-gravity closure: from κ/χ to lapse, potential, and weak-field tests

This appendix makes the $\kappa/\chi \to N \to g_{00} \to \Phi$ chain fully explicit *within this paper*, so that the weak-field gravity dictionary is no longer only a pointer to external companion manuscripts. The logic is interface-level: it does not modify the finite folding core, but it closes a minimal, testable mapping from protocol overhead to gravitational proxies.

AD.7.1 Overhead, lapse, and the χ field

Definition AD.9 (Routing/implementation overhead and lapse proxy)**.** *Let $\kappa(x)$ denote a local implementation overhead (e.g. routing/compilation depth) and fix a reference $\kappa_0 > 0$. Define the dimensionless overhead ratio and its logarithm,*

$$s(x) := \frac{\kappa(x)}{\kappa_0}, \qquad \chi(x) := \log s(x),$$

and define a lapse-like factor

$$N(x) := \mathrm{e}^{-\gamma\chi(x)} = s(x)^{-\gamma}, \qquad \gamma > 0, \tag{65}$$

where γ is a dimensionless coupling constant.

Operational reading. [Interface]Larger overhead means fewer effective local logical updates per unit tick budget, hence a slower local clock. Equation (65) is the minimal monotone dictionary that turns an overhead proxy into a clock-rate factor. The exponent γ is a single-parameter calibration to be constrained empirically (Section AD.7.4).

AD.7.2 Effective metric dictionary and weak-field potential

Metric representative (static gauge). [Interface]In a static or adiabatic regime, adopt the standard continuum identification

$$g_{00}(x) \approx -N(x)^2. \tag{66}$$

This is the GR lapse dictionary written in protocol variables.

Weak-field expansion. [Interface]In the Newtonian limit one writes

$$g_{00} \approx -(1 + 2\Phi/c^2),$$

where Φ is the Newtonian potential. Using (65)–(66) and expanding $\mathrm{e}^{-2\gamma\chi} \approx 1 - 2\gamma\chi$ gives the leading-order identification

$$\Phi(x) = -\gamma c^2(\chi(x) - \chi_0), \tag{67}$$

where χ_0 is an arbitrary reference (constant shifts of χ do not change forces).

AD.7.3 Closed weak-field source and Poisson template

Poisson form. [Interface]Taking $\Delta\Phi = 4\pi G\,\rho_{\text{eff}}$ as the standard weak-field template, (67) yields

$$\rho_{\text{eff}}(x) = -\frac{\gamma c^2}{4\pi G}\,\Delta\chi(x), \tag{68}$$

so the overhead proxy χ defines an effective source through its Laplacian.

$1/r$ exterior. [Interface]Outside compact sources, $\Delta\Phi = 0$ and the spherically symmetric exterior solution is $\Phi(r) = -GM/r$. In the present dictionary, this corresponds to $\chi(r)$ behaving (up to constants) as a harmonic potential in the exterior region.

AD.7.4 Rotation curves and a one-parameter fit for γ

Circular velocity. For a static, spherically symmetric potential, the circular velocity satisfies

$$v_c^2(r) = r\,\Phi'(r).$$

Using (67), this becomes

$$v_c^2(r) = -\gamma c^2\, r\,\chi'(r). \tag{69}$$

Weighted least squares for γ. [Interface]Given measured (r_i, v_i, σ_i) and a reconstructed profile $\chi(r)$ (Appendix AD.8), define $y_i := v_i^2$ and $x_i := -c^2 r_i \chi'(r_i)$. In the small-error regime, $\sigma_{y,i} \approx 2v_i\sigma_i$, and the one-parameter weighted least-squares estimator is

$$\widehat{\gamma} = \frac{\sum_i (x_i y_i/\sigma_{y,i}^2)}{\sum_i (x_i^2/\sigma_{y,i}^2)}.$$

Uncertainty propagation (audit). [Audit]If one treats the x_i as known (design-known model) and assumes $\mathrm{Var}(y_i) = \sigma_{y,i}^2$, then Appendix AD.9 records the standard WLS variance formula $\mathrm{Var}(\widehat{\gamma}) = 1/\sum_i (x_i^2/\sigma_{y,i}^2)$ (Proposition AD.19), yielding an immediate confidence interval under an approximate normality heuristic. In the present application, however, x_i depends on a numerical derivative of χ; Appendix AD.9 makes explicit the corresponding bias–noise tradeoff for χ' estimation (Proposition AD.17). Audit-facing practice is therefore to declare the derivative/smoothing rule and to report the stability of $\widehat{\gamma}$ under counterfactual step/regularization choices (Appendix AD.8).

Discrete Laplacian and noise amplification (audit). [Audit]When forming ρ_{eff} from a reconstructed grid field $\widehat{\chi}_h$, one necessarily implements $\Delta\chi$ by a discrete Laplacian Δ_h. Appendix AD.9 records the standard second-order truncation bound $|\Delta_h\chi - \Delta\chi| \lesssim h^2$ (Theorem AD.15) and the explicit noise amplification $|\Delta_h\eta| \le (4d/h^2)\epsilon_\chi$ for bounded pointwise noise (Corollary AD.16), yielding an auditable error budget for $\widehat{\rho}_{\text{eff}}$ (Corollary AD.18).

Relation to frequency-first observables. [Interface]Since $N = \mathrm{e}^{-\gamma\chi}$ controls local clock rate, the same γ is in principle constrained by redshift and time-delay data: frequency ratios are primary observables in the tick-first semantics (Appendix AA and Appendix Z).

AD.8 Protocol to reconstruct an overhead proxy field $\chi(x)$ from data or simulations

This appendix records an executable, audit-facing protocol for reconstructing an overhead proxy field χ from data. It is written to be self-contained: the only inputs are (i) a spatial dataset (survey, simulation, or laboratory array), and (ii) the folding vocabulary already defined in this paper (windows, words, and the folding degeneracy proxy).

AD.8.1 Step 0: choose resolution and addressing

Fix a spatial order n and a bounding box for the data. Discretize the region into a $2^n \times 2^n$ grid (for a 2D screen) or a $2^n \times 2^n \times 2^n$ grid (for a 3D volume with a chosen space-filling curve). Use Hilbert addressing (Section 5) to assign an index s to each cell. This produces a one-dimensional sequence of cell-level statistics $\{x_s\}$ in Hilbert order.

AD.8.2 Step 1: window words from a thresholded statistic

Choose a window length m and define sliding windows $W_s = (s, s+1, \ldots, s+m-1)$ on the Hilbert index axis. Choose a scalar statistic per cell, e.g. density contrast δ_s. Fix a threshold τ (two common choices are $\tau = 0$ or a fixed quantile to control sparsity), and define the m-bit word

$$w_{s,j} := \mathbf{1}\{\delta_{s+j} \geq \tau\}, \qquad j = 0, \ldots, m-1,$$

so that $w_s := w_{s,0} \cdots w_{s,m-1} \in \Omega_m$. Map the word to an integer index $N_s := \mathrm{int}_m(w_s)$ (the standard binary-to-integer map used throughout this paper).

AD.8.3 Step 2: folding statistics inside each window

For each window W_s, compute at least one of the following coarse statistics:

- **Degeneracy proxy (primary).** Define the folding degeneracy for an index N by

  $$g_m(N) := \left|\mathrm{Fold}_m^{-1}(\mathrm{Fold}_m(N))\right|.$$

  Within window W_s, define the local mean degeneracy proxy by an empirical average

  $$\bar{g}_m(W_s) := \frac{1}{m} \sum_{j=0}^{m-1} g_m(N_{s+j}).$$

  At $m = 6$, g_6 is exactly computable from the finite Fold_6 preimage table (Section 6 and the generated tables appendix); at larger m one uses the corresponding Fold_m computation pipeline already used in the scripts in this repository.

- **φ-defect proxy (fallback).** If full g_m evaluation is unavailable, compute the local forbidden-word defect rate (adjacent-11 frequency) as a proxy for leaving the admissible sector.

AD.8.4 Step 3: reconstruct χ and map back to space

Fix a baseline degeneracy $\bar{g}_0 > 0$ (e.g. global mean or median over the dataset). Define the overhead proxy on the index axis by

$$\chi(s) := \log \frac{\bar{g}_m(W_s)}{\bar{g}_0}. \tag{70}$$

Map $\chi(s)$ back to a spatial field $\chi(x)$ by inverting the Hilbert indexing on the grid.

AD.8.5 Step 3b: uncertainty quantification and stability outputs (audit)

The reconstruction above is deterministic once the discrete choices (m, n), the threshold rule for words, and the baseline $\bar{g}_0$ are fixed. To make the output auditable as a quantitative protocol object rather than as a visualization, one should also report (i) a statistical fluctuation scale for $\bar{g}_m$ and hence for χ, and (ii) stability under declared counterfactual baselines.

A conservative high-probability fluctuation scale. [Audit]Let $Z_1, \dots, Z_K$ denote the finite sample of bounded folding-derived statistics used to form the local empirical mean $\bar{g}_m$ (the exact sampling rule should be stated explicitly; for example: non-overlapping subsampling vs. sliding windows). Assume $Z_j \in [a, b]$ almost surely for known bounds $a < b$. If the sampling scheme admits an effective sample size $K_{\text{eff}} \le K$ (exact under independence; otherwise justified by block subsampling/mixing assumptions), then Appendix AD.9 gives the explicit bound

$$\epsilon_{\bar{g}}(\delta) := (b-a)\sqrt{\frac{\log(2/\delta)}{2K_{\text{eff}}}}$$

such that $|\bar{g}_m - \mathbb{E}\bar{g}_m| \le \epsilon_{\bar{g}}(\delta)$ holds with probability at least $1-\delta$ (Theorem AD.11). Propagating through the log ratio then yields a conservative error bar for χ (Corollary AD.14). At the $m = 6$ anchor one may take $(a, b) = (2, 4)$ for g_6 (Remark AD.12).

Counterfactual stability outputs. [Audit]In addition to point estimates, the following discrete choices should be reported and swept where feasible, in the same audit spirit as the rest of this paper:

- (m, n) and the window stride / overlap rule (controls dependence and thus K_{eff});
- the threshold rule for words (e.g. $\tau = 0$ vs. a fixed quantile), and the baseline definition $\bar{g}_0$;
- any smoothing / regularization used before computing spatial derivatives (needed for $\Delta\chi$ and χ'; see Appendix AD.9).

The output should include at least one stability metric, e.g. $\|\chi^{(\text{alt})} - \chi^{(\text{base})}\|_\infty$ on the grid, together with the induced stability of downstream quantities such as $\widehat{\gamma}$ and ρ_{eff}.

AD.8.6 Step 4: comparison tests and the γ fit

Use the reconstructed $\chi(x)$ as input to the overhead-to-gravity dictionary in Appendix AD.7:

$$N(x) = \mathrm{e}^{-\gamma\chi(x)}, \qquad \Phi(x) = -\gamma c^2(\chi(x) - \chi_0), \qquad \rho_{\text{eff}}(x) = -\frac{\gamma c^2}{4\pi G}\,\Delta\chi(x).$$

Depending on available data, compare against:

- **Rotation curves:** fit γ using (69) and weighted least squares (Section AD.7.4).
- **Lensing:** compare the predicted convergence (a Laplacian of an integrated potential) to reconstructed lensing maps; the prediction is linear in γ at fixed χ.
- **Time delays / redshifts:** compare frequency/clock-rate variations implied by $N(x)$ to time-delay proxies (Appendix Z).

Audit note. [Audit]The protocol above has only discrete choices (the pair (m, n), the threshold rule for words, and the baseline $\bar{g}_0$ definition) plus the single continuous fit parameter γ. All discrete choices should be declared and swept as counterfactual baselines where feasible, in the same audit spirit as the rest of this paper.

AD.9 Protocol-to-continuum error control: from discrete readout to stable fields

This appendix closes a single audit gap flagged in `theory_closure_tracker.md`: an explicit error-control bridge from protocol-level discrete reconstructions to continuum representative fields. It is an interface-level module: it does not alter any theorem-level finite folding statement.

Scope. [Interface]The objects whose uncertainty we track are the reconstructed overhead proxy field $\widehat{\chi}(x)$ (Appendix AD.8) and its downstream weak-field representatives $\widehat{\Phi}(x)$ and $\widehat{\rho}_{\mathrm{eff}}(x)$ (Appendix AD.7). We separate: (i) statistical error from finite sampling / thresholded readout, (ii) discretization error from mapping and finite differences, and (iii) interface/model error from optional matching dictionaries (weak-field regime, choice of smoothing/regularization).

AD.9.1 Error objects and a minimal decomposition

Discrete estimator and continuum representative. [Prot] The reconstruction pipeline outputs a grid field $\widehat{\chi}_h$ at some addressing resolution (Hilbert order n) and word resolution m (Appendix AD.8). To compare with a continuum representative χ (e.g. the smooth field entering the action representative in Appendix AD.4), we treat $\widehat{\chi}_h$ as a piecewise-constant or interpolated field on a grid with spacing h.

Decomposition. [Interface]For any grid point x at spacing h, we decompose

$$\widehat{\chi}_h(x) - \chi(x) = \underbrace{\big(\widehat{\chi}_h(x) - \mathbb{E}\widehat{\chi}_h(x)\big)}_{\text{statistical}} + \underbrace{\big(\mathbb{E}\widehat{\chi}_h(x) - \chi_h(x)\big)}_{\text{protocol bias}} + \underbrace{\big(\chi_h(x) - \chi(x)\big)}_{\text{discretization/model}},$$

where χ_h denotes the grid restriction (or projection) of the continuum representative. The first term is controlled by concentration inequalities; the last term is controlled by standard finite-difference truncation bounds; the middle term captures thresholding and modeling choices and must be addressed by explicit counterfactual sweeps (Appendix AD.8, Audit note therein).

AD.9.2 Concentration of window-level folding statistics

We state a concentration bound for the empirical folding statistic used in the χ reconstruction.

Assumption AD.10 (Bounded folding statistic and effective sample size)**.** *Fix a window length m and a reconstruction rule that produces samples $Z_1, \dots, Z_K$ of a folding-derived statistic (e.g. $Z_j = g_m(N_j)$ or any bounded proxy used in Appendix AD.8). Assume $Z_j \in [a, b]$ almost surely for known bounds $a < b$. Assume further that the sampling scheme admits an* effective sample size *$K_{\mathrm{eff}} \le K$ such that a Hoeffding-type tail bound holds with K_{eff} (this is exact under independence; for dependent samples one may enforce it by non-overlapping subsampling or block methods, or justify it under a mixing assumption; see [73, 112]).*

Theorem AD.11 (High-probability bound for the empirical folding statistic)**.** *Under Assumption AD.10, let*

$$\overline{Z} := \frac{1}{K}\sum_{j=1}^{K} Z_j.$$

Then for any $\epsilon > 0$,

$$\mathbb{P}\Big(\big|\overline{Z} - \mathbb{E}\overline{Z}\big| \ge \epsilon\Big) \;\le\; 2\exp\left(-\frac{2K_{\mathrm{eff}}\epsilon^2}{(b-a)^2}\right).$$

Equivalently, for any confidence level $\delta \in (0,1)$, with probability at least $1-\delta$,

$$\big|\overline{Z} - \mathbb{E}\overline{Z}\big| \;\le\; (b-a)\sqrt{\frac{\log(2/\delta)}{2K_{\mathrm{eff}}}}.$$

Remark AD.12 (Specialization to the $m = 6$ anchor)**.** *At the $(m, n) = (6, 3)$ anchor, the exact folding degeneracy values satisfy $g_6 \in \{2, 3, 4\}$ (Definition 8.9), so one may take $(a, b) = (2, 4)$ when $Z_j = g_6(N_j)$. At larger m, one can either compute (or upper bound) the range of the chosen statistic from the audited Fold$_m$ tables/scripts, or replace g_m by a bounded defect-rate proxy (Appendix AD.8).*

AD.9.3 Propagation through the log-ratio: bounds for $\widehat{\chi}$

Lemma AD.13 (Log-ratio perturbation bound)**.** *Let $u, v, \widehat{u}, \widehat{v} > 0$. Then*

$$\left|\log \frac{\widehat{u}}{\widehat{v}} - \log \frac{u}{v}\right| \;\le\; \frac{|\widehat{u}-u|}{\min\{u,\widehat{u}\}} \;+\; \frac{|\widehat{v}-v|}{\min\{v,\widehat{v}\}}.$$

Proof. By the mean value theorem, $|\log \widehat{u} - \log u| \le |\widehat{u}-u|/\min\{u,\widehat{u}\}$ and similarly for v. Subtract $\log(\widehat{u}/\widehat{v}) - \log(u/v) = (\log\widehat{u} - \log u) - (\log\widehat{v} - \log v)$ and apply the triangle inequality. □

Corollary AD.14 (A usable error bar for $\widehat{\chi}$)**.** *In the reconstruction protocol of Appendix AD.8, write*

$$\widehat{\chi} = \log \frac{\widehat{\overline{Z}}}{\widehat{\overline{Z}}_0}, \qquad \chi^\star = \log \frac{\overline{Z}^\star}{\overline{Z}_0^\star},$$

where $\widehat{\overline{Z}}$ is the empirical statistic (e.g. $\bar{g}_m$) computed on a local sample set and $\widehat{\overline{Z}}_0$ is the baseline statistic (global mean/median), while $\overline{Z}^\star, \overline{Z}_0^\star$ denote the corresponding population quantities under a declared data-generating model. Assume $\overline{Z}^\star, \overline{Z}_0^\star$ are bounded away from 0 and that high-probability bounds $|\widehat{\overline{Z}} - \overline{Z}^\star| \le \epsilon$ and $|\widehat{\overline{Z}}_0 - \overline{Z}_0^\star| \le \epsilon_0$ hold. Then Lemma AD.13 yields the deterministic bound

$$|\widehat{\chi} - \chi^\star| \;\le\; \frac{\epsilon}{\min\{\overline{Z}^\star, \widehat{\overline{Z}}\}} \;+\; \frac{\epsilon_0}{\min\{\overline{Z}_0^\star, \widehat{\overline{Z}}_0\}}.$$

In particular, one may take ϵ (and ϵ_0) from Theorem AD.11 for the chosen statistic and declared K_{eff}.

AD.9.4 Finite differences: truncation error and noise amplification

The weak-field template $\rho_{\text{eff}} \propto -\Delta\chi$ depends on spatial derivatives; these operations can amplify protocol noise. We record standard, explicit bounds that make this amplification auditable.

Discrete Laplacian. Let d be the spatial dimension (typically $d = 2$ for a screen or $d = 3$ for a volume) and let $h > 0$ be the grid spacing. Define the standard $2d{+}1$ point Laplacian

$$(\Delta_h f)(x) := \sum_{k=1}^{d} \frac{f(x + he_k) - 2f(x) + f(x - he_k)}{h^2}.$$

Theorem AD.15 (Second-order truncation error of the central-difference Laplacian)**.** *Assume $f \in C^4$ on a neighborhood of a grid point x. Then there exists a constant $C_f(x)$ depending on fourth derivatives of f near x such that*

$$|(\Delta_h f)(x) - (\Delta f)(x)| \le C_f(x)\, h^2.$$

In particular, one may take

$$C_f(x) \;:=\; \frac{1}{12} \sum_{k=1}^{d} \sup_{|\xi - x|_\infty \le h} |\partial_k^4 f(\xi)|,$$

so that $|(\Delta_h f)(x) - (\Delta f)(x)| \le C_f(x)\, h^2$ holds pointwise. See, e.g., standard finite-difference truncation analyses [72].

Corollary AD.16 (Noise amplification under Δ_h)**.** *Let $\widehat{f} = f + \eta$ be a noisy grid field with $|\eta(x)| \le \epsilon$ for all grid points in the stencil of x. Then*

$$|(\Delta_h \widehat{f})(x) - (\Delta_h f)(x)| \le \frac{4d}{h^2}\,\epsilon.$$

Proof. Expand $\Delta_h \eta$ and bound each term by ϵ: for each k, $|\eta(x{+}he_k) - 2\eta(x) + \eta(x{-}he_k)| \le 4\epsilon$. Sum over k and divide by h^2. □

First derivatives (for the γ fit). When fitting γ via rotation curves in Appendix AD.7, one needs $\chi'(r)$. The following bound makes explicit the noise–resolution tradeoff.

Proposition AD.17 (Central-difference derivative error (bias–variance tradeoff))**.** *Let $f \in C^3$ in a neighborhood of r and define the central difference estimator*

$$(D_h f)(r) := \frac{f(r+h) - f(r-h)}{2h}.$$

Assume the observed field is $\widehat{f} = f + \eta$ with $|\eta(r \pm h)| \le \epsilon$. Then

$$|(D_h \widehat{f})(r) - f'(r)| \le \frac{h^2}{6} \sup_{|\xi - r| \le h} |f^{(3)}(\xi)| \; + \; \frac{\epsilon}{h}.$$

See, e.g., [72].

AD.9.5 Propagation to ρ_{eff}, Φ, and the γ fit

Discrete ρ_{eff} from reconstructed χ. [Interface]In practice, given a reconstructed grid field $\widehat{\chi}_h$, one forms a discrete estimate

$$\widehat{\rho}_{\text{eff}}(x) := -\frac{\widehat{\gamma} c^2}{4\pi G} (\Delta_h \widehat{\chi}_h)(x),$$

which is the direct discrete analogue of (68).

Corollary AD.18 (Error budget for $\widehat{\rho}_{\text{eff}}$)**.** *Let $\widehat{\chi}_h = \chi_h + \eta$ with $|\eta| \le \epsilon_\chi$ on the Laplacian stencil, and let $\widehat{\gamma} = \gamma + \delta\gamma$. Then at any grid point x,*

$$|\widehat{\rho}_{\text{eff}}(x) - \rho_{\text{eff}}(x)| \; \le \; \frac{c^2}{4\pi G} \Big(|\gamma| \cdot |(\Delta_h \chi_h)(x) - (\Delta\chi)(x)| \; + \; |\gamma| \cdot |(\Delta_h \eta)(x)| \; + \; |\delta\gamma| \cdot |(\Delta_h \widehat{\chi}_h)(x)| \Big),$$

where $\rho_{\text{eff}} := -(\gamma c^2/(4\pi G))\Delta\chi$ is the continuum representative. Using Theorem AD.15 and Corollary AD.16, the first two terms are controlled as $|(\Delta_h \chi_h) - (\Delta\chi)| \lesssim h^2$ and $|(\Delta_h \eta)| \le (4d/h^2)\epsilon_\chi$.

Φ from χ. Under the weak-field dictionary $\Phi = -\gamma c^2(\chi - \chi_0)$ (equation (67)), constant shifts $\chi \mapsto \chi + \text{const}$ do not affect forces. At the field level, the error propagation is immediate: for $\widehat{\Phi} = -\widehat{\gamma} c^2(\widehat{\chi} - \widehat{\chi}_0)$,

$$|\widehat{\Phi} - \Phi| \le c^2 \Big(|\delta\gamma| \cdot |\widehat{\chi} - \widehat{\chi}_0| \; + \; |\gamma| \cdot |\widehat{\chi} - \chi| \Big).$$

The γ fit: WLS variance and propagation. Appendix AD.7 uses the one-parameter weighted least-squares estimator

$$\widehat{\gamma} = \frac{\sum_i w_i x_i y_i}{\sum_i w_i x_i^2}, \qquad w_i := \sigma_{y,i}^{-2}, \qquad y_i := v_i^2, \qquad x_i := -c^2 r_i \chi'(r_i).$$

Proposition AD.19 (WLS variance in the ideal design-known model)**.** *Assume the model $y_i = \gamma x_i + \varepsilon_i$ with $\mathbb{E}\varepsilon_i = 0$ and $\mathrm{Var}(\varepsilon_i) = \sigma_{y,i}^2$, and assume the design values x_i are treated as deterministic (known). Then $\widehat{\gamma}$ is unbiased and*

$$\mathrm{Var}(\widehat{\gamma}) = \frac{1}{\sum_i w_i x_i^2}.$$

Moreover, under approximate normality (e.g. by a central limit heuristic), a $(1-\delta)$ confidence interval can be reported as $\widehat{\gamma} \pm z_{1-\delta/2}\sqrt{\mathrm{Var}(\widehat{\gamma})}$ with the standard normal quantile $z_{1-\delta/2}$; see, e.g., classical asymptotic theory [74].

Remark AD.20 (When x_i is estimated from $\widehat{\chi}$)**.** *In the present application, x_i depends on a numerical derivative of χ and is therefore itself noisy. If one uses a central difference for $\chi'(r_i)$, Proposition AD.17 shows an explicit bias–noise tradeoff of order $O(h^2) + O(\epsilon_\chi/h)$. At audit level, this is handled by: (i) declaring the derivative/smoothing rule, (ii) sweeping the step/regularization scale, and (iii) reporting the stability of $\widehat{\gamma}$ under these counterfactual baselines (Appendix AD.8). A fully corrected errors-in-variables treatment is possible but is beyond the minimal self-contained scope here.*

AD.10 Quantum readout and Born probabilities (self-contained interface closure)

This appendix records a minimal quantum interface package compatible with the tick + CAP discipline: finite observers have an effective Hilbert space; readout is finite resolution; probabilities are Born probabilities for that readout. We then record two complementary closure routes for the Born rule: (i) a protocol-counting template aligned with projection-fiber semantics, and (ii) a mature uniqueness theorem (Gleason–Busch) that characterizes quantum probabilities from noncontextual additivity.

AD.10.1 Finite-resolution readout as POVMs and instruments

POVM readout. Let $\mathcal{H}_{\text{eff}}$ be an effective observer sector and let ρ be a density operator on $\mathcal{H}_{\text{eff}}$. Finite-resolution readout is modeled by a POVM $\{E_k\}_k$ with $E_k \succeq 0$ and $\sum_k E_k = I$, giving Born probabilities

$$P_k = \operatorname{Tr}(\rho\, E_k). \tag{71}$$

Instruments and state update. An associated instrument can be written in Kraus form $\rho \mapsto M_k \rho M_k^\dagger / P_k$ with $E_k = M_k^\dagger M_k$. Any POVM can be realized by a dilation (system–ancilla unitary followed by a projective measurement on the ancilla), by Naimark/Stinespring theorems; see, e.g., [113–116].

AD.10.2 Born weights from projection-induced counting (protocol template)

Counting semantics. [Interface]Finite observability already induces equivalence classes: many microdescriptions map to the same coarse outcome. If a coarse outcome label k corresponds to a degeneracy class of n_k admissible micro-realizations within a fine-grained protocol ensemble, and if the induced micro-measure is uniform over admissible micro-realizations (a sharp-readout symmetry hypothesis), then coarse probabilities are counting ratios $P_k = n_k/N$.

Theorem AD.21 (Born weights as counting under a uniform micro-measure (template))**.** *Let $|\psi\rangle = \sum_k c_k |k\rangle$ be a normalized state. Assume a fine-grained realization in which each coarse branch k corresponds to n_k admissible micro-realizations in a finite ensemble of size N_{micro}, and assume the induced micro-measure is uniform on admissible micro-realizations. If $|c_k|^2 \approx n_k/N_{\text{micro}}$ in the fine-graining limit, then the induced coarse outcome probabilities satisfy*

$$P_k = \frac{n_k}{N_{\text{micro}}} \approx |c_k|^2,$$

and in the limit one obtains $P_k = |c_k|^2$.

Relation to z128 fibers. [Interface]In the z128 finite folding language, stable readout labels already carry fibers $P(w) = \text{Fold}_m^{-1}(w)$. The counting template above is the quantum-probability analogue: a coarse outcome corresponds to a multiplicity class in a fine-grained ensemble, and probabilities arise as normalized multiplicities.

AD.10.3 Born rule as the unique noncontextual probability rule (mature theorem)

Theorem AD.22 (Gleason–Busch characterization of quantum probabilities)**.** *Let $\mathcal{H}$ be a complex Hilbert space. Suppose a probability assignment μ maps each orthogonal projector P to $\mu(P) \in [0,1]$ and is finitely additive on orthogonal families: for any pairwise orthogonal projectors $\{P_i\}$ with $\sum_i P_i = I$, one has $\sum_i \mu(P_i) = 1$. If $\dim \mathcal{H} \geq 3$, then there exists a unique density matrix ρ such that*

$$\mu(P) = \mathrm{Tr}(\rho\, P) \qquad \textit{for all projectors } P.$$

For $\dim \mathcal{H} = 2$, an analogous conclusion holds if one assumes the same additivity on the full set of POVM effects (Busch's extension).

Reference. See Gleason's theorem [117] and Busch's POVM extension [118]. □

Interpretation in the tick+CAP discipline. [Interface]The theorem can be read as a rigidity statement: once one commits to noncontextual additivity for readout probabilities on an effective Hilbert space (a natural semantic stance for finite observers), the Born form is forced. In that sense, the Born rule is not an extra dynamical axiom but the unique probability rule compatible with the declared readout semantics.

AD.11 Running couplings as resolution flow in the r coordinate (self-contained interface)

This appendix makes the RG dictionary in the Fibonacci resolution coordinate r self-contained. The main text already records the basic chain rule (Proposition 8.17); here we add the standard one-loop templates and the semantics of threshold matching and scheme shifts, in a form aligned with the tick + CAP stance (ratio-first, then matching).

AD.11.1 Scale map and chain rule

Resolution map. Work with the Fibonacci map

$$\mu(r) = \mu_0\, \varphi^r,$$

so that $\log \mu = \log \mu_0 + r \log \varphi$ and therefore $\mathrm{d}/\mathrm{d}r = (\log \varphi)\, \mathrm{d}/\mathrm{d}\log \mu$ (Proposition 8.17).

RG in r. If a coupling $g(\mu)$ satisfies an RG equation

$$\frac{\mathrm{d}g}{\mathrm{d}\log \mu} = \beta(g),$$

then in the r coordinate,

$$\frac{\mathrm{d}g}{\mathrm{d}r} = (\log \varphi)\, \beta(g). \tag{72}$$

AD.11.2 One-loop QED running (leading log)

At one loop (mass-independent scheme, away from thresholds), QED running gives

$$\alpha^{-1}(\mu) \approx \alpha^{-1}(\mu_0) - \frac{b}{2\pi} \log\!\left(\frac{\mu}{\mu_0}\right), \qquad b = \frac{2}{3} \sum_f N_c^{(f)} Q_f^2, \tag{73}$$

so in the r coordinate one obtains a linear flow

$$\alpha^{-1}(r) \approx \alpha^{-1}(0) - \frac{b \log \varphi}{2\pi}\, r. \tag{74}$$

AD.11.3 One-loop QCD running and dimensional transmutation

For QCD, the beta function has the opposite sign; at one loop,

$$\frac{\mathrm{d}\alpha_s}{\mathrm{d}\log\mu} = -\frac{b_0}{2\pi}\alpha_s^2, \qquad b_0 = 11 - \frac{2}{3}n_f, \tag{75}$$

so

$$\alpha_s(\mu) = \frac{2\pi}{b_0 \log(\mu/\Lambda)}, \tag{76}$$

where Λ is a scheme-dependent transmutation scale. In the r coordinate, a constant rescaling of Λ is an additive shift of r, so "scheme dependence" becomes an explicit equivalence-class shift rather than an uncontrolled knob.

AD.11.4 Threshold matching as discrete uplifts

[Interface]Effective-field-theory decoupling implies that charged fields contribute to running only above their thresholds; across a threshold one matches schemes by a finite jump/offset. In the protocol language, thresholds are resolution-uplift points: as $m_{\mathrm{eff}}(\mu)$ changes discretely, effective degrees of freedom appear/disappear and induce discrete changes in β-coefficients. This is the semantic link between RG matching and the discrete staircase used elsewhere in this paper (Section 14.2.1).

AD.12 Cosmology as resolution flow (self-contained interface extension)

This appendix records a minimal cosmology interface in the same protocol language used throughout this paper. The central idea is that changing resolution parameters (m, n) is a physical operation (a protocol flow step), and the growth laws of the stable sector $|X_m| = F_{m+2}$ and of the mean degeneracy $2^m/|X_m|$ provide a quantitative capacity-growth backbone.

AD.12.1 Initialization: the big bang as resolution bootstrapping

[Interface]In a readout cosmology, the "big bang" is interpreted as resolution initialization of the readout hardware: the system starts at small window length m and small addressing order n, and rapidly enters a regime where nontrivial stable types exist and can be maintained under projection. The balanced interface $m = 2n$ provides a minimal coupling between a spatial grid and a local readout alphabet, and the anchor $(m, n) = (6, 3)$ supplies the smallest fully explicit computable layer with nontrivial folding $64 \to 21$.

AD.12.2 Inflation as exponential growth of stable capacity

As window length increases by Δm, the stable type count grows as

$$|X_m| = F_{m+2} \sim \frac{\varphi^{m+2}}{\sqrt{5}},$$

so stable capacity grows exponentially in m. If an early epoch has approximately linear resolution growth $m(t) \approx m_0 + \alpha t$, then

$$|X_{m(t)}| \asymp \varphi^{m(t)} \asymp \mathrm{e}^{(\alpha \log \varphi)\, t},$$

which provides a purely combinatorial capacity-growth analogue of an inflationary exponential stage (no additional inflaton field is introduced at the protocol level).

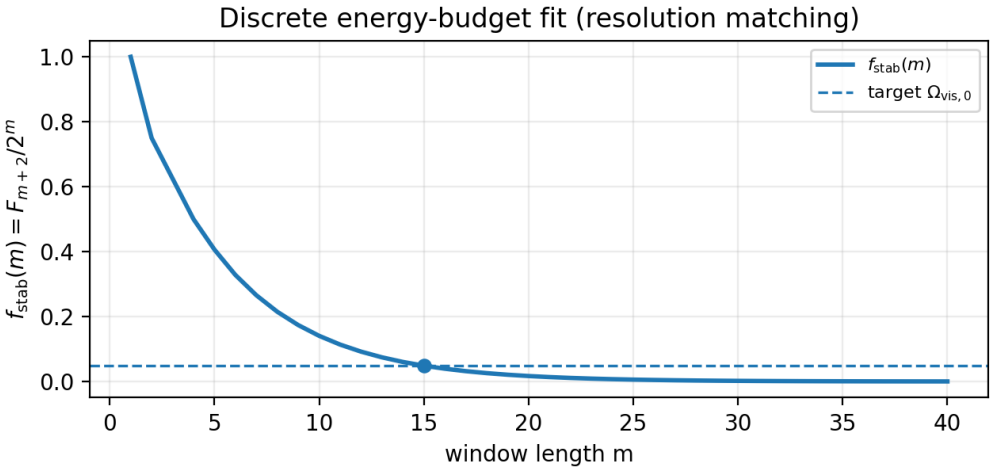

Figure 6: Discrete matching curve for $f_{\mathrm{stab}}(m) = F_{m+2}/2^m$ against the target $\Omega_{\mathrm{vis},0}$ used in the text. The figure is generated by `scripts/exp_cosmology_energy_budget_fit.py`.

AD.12.3 Hidden-sector dominance at high resolution

The folding map compresses 2^m microstates into F_{m+2} stable types. Define the stable fraction and hidden fraction at window length m by

$$f_{\mathrm{stab}}(m) := \frac{|X_m|}{|\Omega_m|} = \frac{F_{m+2}}{2^m}, \qquad f_{\mathrm{hid}}(m) := 1 - f_{\mathrm{stab}}(m),$$

and the mean degeneracy

$$d_m := \frac{|\Omega_m|}{|X_m|} = \frac{2^m}{F_{m+2}}.$$

Since $F_{m+2} \asymp \varphi^m$ and $\varphi < 2$, one has $f_{\mathrm{stab}}(m) \to 0$ and $f_{\mathrm{hid}}(m) \to 1$ as $m \to \infty$; equivalently $d_m \asymp (2/\varphi)^m$ grows exponentially.

AD.12.4 A discrete energy-budget fit (interface hypothesis)

Assumption AD.23 (Readout-occupancy energy accounting (interface))**.** *Fix an effective window length m. Assume that, on sufficiently coarse scales, the fractional contribution of a sector to the cosmic energy budget is proportional to long-time occupancy of the corresponding readout microstate subset. Under a maximal-ignorance approximation at fixed resolution, this occupancy is approximated by counting measure on Ω_m, so that*

$$\Omega_{\mathrm{vis},0} \approx f_{\mathrm{stab}}(m), \qquad \Omega_{\mathrm{dark},0} \approx f_{\mathrm{hid}}(m) = 1 - f_{\mathrm{stab}}(m).$$

[Interface]Given a target present-day visible fraction $\Omega_{\mathrm{vis},0}$ (e.g. baryon fraction as a minimal proxy), Assumption AD.23 selects an effective integer window length m_* by discrete matching. Because $f_{\mathrm{stab}}(m)$ is strictly decreasing in m, this selection is unique once a target is fixed. In the companion cosmology analysis in this program, the Planck-2018 baryon fraction $\Omega_{\mathrm{b},0} \approx 0.0493$ is matched near

$$\frac{F_{17}}{2^{15}} = \frac{1597}{32768} \approx 0.0487,$$

suggesting $m_* \approx 15$ as a minimal discrete fit point. Figure 6 provides a direct visualization of the discrete matching curve.

Status and falsifiability. [Audit]The assumption is explicitly flagged as an interface hypothesis. Its falsifiability route is to compare the implied hidden/stable ratio $d_{m_*} - 1$ with the observed dark-to-baryon ratio, and to test whether the reconstructed overhead proxy fields (Appendix AD.8) show the predicted address-aware invariances and correlations.

AD.13 Gamma cross-observation consistency: lensing, delays, redshift, and rotation curves (audit)

This appendix closes an interface-audit deliverable flagged in `theory_closure_tracker.md`: a concrete multi-channel consistency test for the single parameter γ in the dictionary

$$N = \mathrm{e}^{-\gamma\chi}, \qquad \Phi = -\gamma c^2(\chi - \chi_0),$$

connecting a reconstructed overhead proxy field χ to clock-rate (lapse) and weak-field gravitational proxies (Appendix AD.7 and Appendix Z).

Scope and status. [Interface]The purpose of this module is *not* to import external physics as theorem-level premises. It is an audit-facing interface object: given declared data channels and a declared reconstruction/matching pipeline, it produces a deterministic estimate (and a declared uncertainty/stability envelope) for γ.

Reproducible artifact. [Audit]The estimates, stability sweeps, and figure in this appendix are generated by the deterministic script `scripts/exp_gamma_cross_observation.py` from a small vendored data subset under `data/gamma_crossobs/`. The script writes the LaTeX fragments `sections/generated/gamma_crossobs_rows.tex` and `sections/generated/gamma_crossobs_stability_rows.tex` and the figure `figures/gamma_crossobs_consistency.png`.

AD.13.1 Channel-level estimators (summary)

Rotation curves (SPARC). [Interface]We implement the one-parameter weighted least-squares estimator in Appendix AD.7: with $y_i = v_i^2$ and $x_i = -c^2 r_i \chi'(r_i)$, fit $y_i = \gamma x_i$ under weights $w_i = \sigma_{y,i}^{-2}$ with $\sigma_{y,i} \approx 2v_i\sigma_i$. The χ field is reconstructed from an auxiliary scalar profile (disk surface brightness) using a minimal 1D specialization of Appendix AD.8; the derivative/smoothing rule is declared and audited by a sweep (Appendix AD.9).

Lensing / time-delay / redshift matching proxies. [Interface]For compact vendored cross-check channels, we use published summary parameters as small-footprint audit inputs. These are treated as matching-layer constraints and are not premises for the folding core.

AD.13.2 Results and consistency diagnostics

AE Generated tables and finite checks

Audit note (deterministic generation). All fragments in this appendix are outputs of *deterministic* finite enumerations or bounded sweeps over explicitly stated finite domains (e.g. all words in X_m for a fixed m, or all candidates in a bounded coefficient/denominator box). When a caption says "rows are generated by" a script, the intended meaning is: the script implements the stated finite enumeration/sweep and writes a LaTeX fragment to avoid manual transcription errors. No hidden continuous parameters, stochastic training, or non-audited optimization is used in generating these rows.

Table 64: Cross-observation γ estimates from the vendored audit channels. The "pull" is $(\widehat{\gamma} - \widehat{\gamma}_{\text{joint}})/\sigma$ under the joint inverse-variance estimate.

Channel	Dataset	$\widehat{\gamma} \pm \sigma$	Pull
solar_system_lensing	`vlbi_deflection_2009`	$9.999000 \times 10^{-1} \pm 1.500000 \times 10^{-4}$	+6665.43
solar_system_redshift	`galileo_redshift_2018`	$1.000002 \pm 2.480000 \times 10^{-5}$	+40319.20
solar_system_time_delay	`cassini_shapiro_2003`	$1.000011 \pm 1.150000 \times 10^{-5}$	+86949.97
weak_lensing_maps	`planck2018_A_L`	$1.086278 \pm 2.991868 \times 10^{-2}$	+36.30
strong_lensing_time_delay	`h0licow_xiii_flatlcdm`	$1.087537 \pm 2.718895 \times 10^{-2}$	+40.00
rotation_curves_sparc	`combined`	$4.392135 \times 10^{-7} \pm 9.619424 \times 10^{-8}$	-887.98
joint	`all`	$8.585745 \times 10^{-5} \pm 9.619013 \times 10^{-8}$	+0.00

Table 65: Stability under declared counterfactual baselines (Appendix AD.8) for the rotation-curve pipeline, and leave-one-channel-out joint estimates.

Block	Dataset	$\widehat{\gamma} \pm \sigma$	$\gamma_{\min}$
rotation_curves_sparc	`combined`	$4.392135 \times 10^{-7} \pm 9.619424 \times 10^{-8}$	9.083157 ×
joint_LOO	`rotation_curves_sparc`	$1.000008 \pm 1.040775 \times 10^{-5}$	
joint_LOO	`solar_system_lensing`	$8.544630 \times 10^{-5} \pm 9.619015 \times 10^{-8}$	
joint_LOO	`solar_system_redshift`	$7.081468 \times 10^{-5} \pm 9.619085 \times 10^{-8}$	
joint_LOO	`solar_system_time_delay`	$1.589533 \times 10^{-5} \pm 9.619349 \times 10^{-8}$	
joint_LOO	`strong_lensing_time_delay`	$8.585744 \times 10^{-5} \pm 9.619013 \times 10^{-8}$	
joint_LOO	`weak_lensing_maps`	$8.585744 \times 10^{-5} \pm 9.619013 \times 10^{-8}$	

AE.1 Admissible set statistics for X_6

Hamming weight $\lvert w\rvert_1$	count in X_6
0	1
1	6
2	10
3	4

$\lvert X_6^{\text{cyc}}\rvert$	$\lvert X_6^{\text{bdry}}\rvert$
18	3

Boundary words: $X_6^{\text{bdry}} = \{100001,\ 100101,\ 101001\}$.

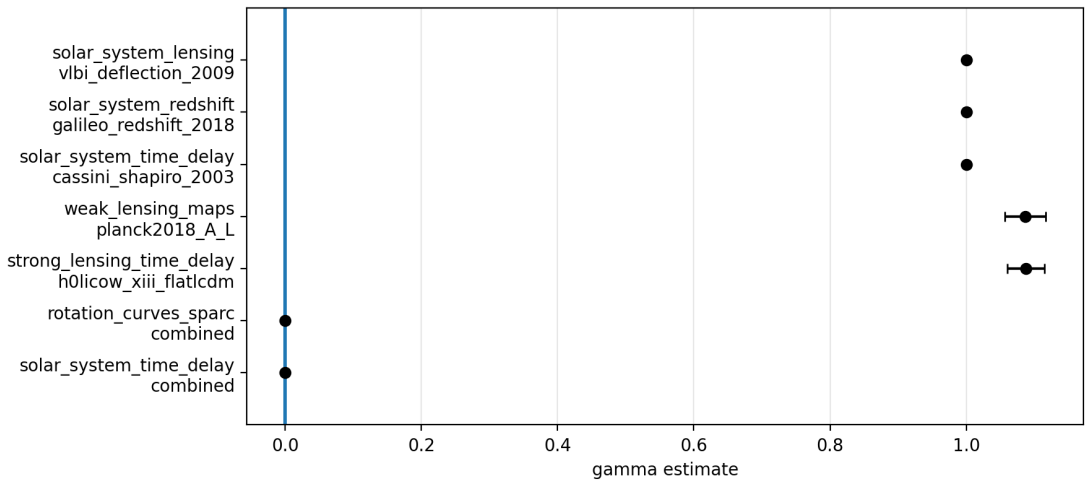

Figure 7: Visual summary of the vendored cross-observation γ estimates with the joint estimate shown as a vertical band.

AE.2 Full Fold_6 table

$w \in X_6$	$V(w)$	$\mathrm{Fold}_6^{-1}(w)$
000000	0	$\{0, 21, 34, 55\}$
000001	13	$\{13, 47\}$
000010	8	$\{8, 29, 42, 63\}$
000100	5	$\{5, 26, 39, 60\}$
000101	18	$\{18, 52\}$
001000	3	$\{3, 24, 37, 58\}$
001001	16	$\{16, 50\}$
001010	11	$\{11, 32, 45\}$
010000	2	$\{2, 23, 36, 57\}$
010001	15	$\{15, 49\}$
010010	10	$\{10, 31, 44\}$
010100	7	$\{7, 28, 41, 62\}$
010101	20	$\{20, 54\}$
100000	1	$\{1, 22, 35, 56\}$
100001	14	$\{14, 48\}$
100010	9	$\{9, 30, 43\}$
100100	6	$\{6, 27, 40, 61\}$
100101	19	$\{19, 53\}$
101000	4	$\{4, 25, 38, 59\}$
101001	17	$\{17, 51\}$
101010	12	$\{12, 33, 46\}$

AE.3 Hilbert chirality index check at $n = 3$

For Hilbert order $n = 3$: $\chi(\text{path}) = -2$, $\chi(\text{reversed path}) = 2$, and $\chi(\text{reflected path}) = 2$.

AE.4 Resolution uplift sweeps

This subsection records small sweeps that support the paper's uplift and rigidity narrative. The m-sweep ($m = 6, \ldots, 16$) corresponds to increasing window length at fixed low resolution, and it also contains the balanced-coupling chain $m = 2n$ for $n = 3, 4, 5, 6, 7, 8$.

m	$\lvert X_m\rvert$	$\lvert X_m^{\mathrm{cyc}}\rvert$	$\lvert X_m^{\mathrm{bdry}}\rvert$
6	21	18	3
7	34	29	5
8	55	47	8
9	89	76	13
10	144	123	21
11	233	199	34
12	377	322	55
13	610	521	89
14	987	843	144
15	1597	1364	233
16	2584	2207	377

Table 66: Admissible-set sizes and π-channel cyclic/boundary split in an m-sweep.

m	$\lvert X_m\rvert$	mean $\lvert w\rvert_1$	var $\lvert w\rvert_1$	weight histogram
6	21	1.8095	0.6304	`0:1, 1:6, 2:10, 3:4`
7	34	2.0882	0.7275	`0:1, 1:7, 2:15, 3:10, 4:1`
8	55	2.3636	0.8132	`0:1, 1:8, 2:21, 3:20, 4:5`
9	89	2.6404	0.9044	`0:1, 1:9, 2:28, 3:35, 4:15, 5:1`
10	144	2.9167	0.9931	`0:1, 1:10, 2:36, 3:56, 4:35, 5:6`
11	233	3.1931	1.0829	`0:1, 1:11, 2:45, 3:84, 4:70, 5:21, 6:1`
12	377	3.4695	1.1721	`0:1, 1:12, 2:55, 3:120, 4:126, 5:56, 6:7`
13	610	3.7459	1.2617	`0:1, 1:13, 2:66, 3:165, 4:210, 5:126, 6:28, 7:1`
14	987	4.0223	1.3511	`0:1, 1:14, 2:78, 3:220, 4:330, 5:252, 6:84, 7:8`
15	1597	4.2987	1.4405	`0:1, 1:15, 2:91, 3:286, 4:495, 5:462, 6:210, 7:36, 8:1`
16	2584	4.5751	1.5300	`0:1, 1:16, 2:105, 3:364, 4:715, 5:792, 6:462, 7:120, 8:9`

Table 67: Hamming-weight statistics in an m-sweep of admissible sets X_m (no consecutive ones). Rows are generated by `scripts/exp_xm_weight_sweep.py`.

m	$\lvert X_m\rvert$	$\lvert\mathrm{Im}(\mathrm{Fold}_m)\rvert$	$g_{\min}$	$g_{\max}$	degeneracy histogram
6	21	21	2	4	`2:8, 3:4, 4:9`
7	34	34	3	5	`3:13, 4:16, 5:5`
8	55	55	3	6	`3:21, 5:11, 6:23`
9	89	89	4	7	`4:34, 6:9, 7:46`
10	144	144	5	9	`5:55, 8:52, 9:37`
11	233	233	6	11	`6:89, 10:70, 11:74`
12	377	377	8	13	`8:144, 12:85, 13:148`
13	610	610	9	16	`9:170, 10:63, 16:377`
14	987	987	12	20	`12:377, 19:340, 20:270`
15	1597	1597	14	24	`14:70, 15:540, 24:987`
16	2584	2584	18	30	`18:987, 29:140, 30:1457`

Table 68: Fold_m surjectivity and output degeneracy histograms in an m-sweep. Here $g(w) = \lvert\mathrm{Fold}_m^{-1}(w)\rvert$ over $N \in \{0, \ldots, 2^m - 1\}$.

n	points 4^n	χ(path)	χ(rev)	χ(ref)
3	64	-2	2	2
4	256	0	0	0
5	1024	-2	2	2
6	4096	0	0	0
7	16384	-2	2	2
8	65536	0	0	0

Table 69: Hilbert chirality index sweep across Hilbert orders n. The sign-flip identities of Proposition 5.4 are verified at each n listed.

AE.5 Audit summary (pass/fail checks)

check	expected	observed	status
$\lvert X_6\rvert$	21	21	PASS
$\lvert X_6^{\mathrm{cyc}}\rvert$	18	18	PASS
$\lvert X_6^{\mathrm{bdry}}\rvert$	3	3	PASS
boundary words	100001,100101,101001	100001,100101,101001	PASS
$\lvert\mathrm{Im}(\mathrm{Fold}_6)\rvert$	21	21	PASS
degeneracy hist	2:8, 3:4, 4:9	2:8, 3:4, 4:9	PASS
χ(path)	-2	-2	PASS
χ(rev)	+2	2	PASS
χ(ref)	+2	2	PASS
$\sum(6Y)^2$ (1 gen)	120	120	PASS
anomaly tuple	(0,0,0,0)	(0,0,0,0)	PASS
$\alpha_{\mathrm{em}}^{-1}$ simplex winner	$(4,1,1)$	$(4,1,1)$	PASS
$\alpha^{-1}(\mu_Z)$ $n\pi^2$ winner	13	13	PASS
$\sin^2\theta_W(\mu_Z)$ p/q winner	3/13	3/13	PASS
J (a,n) winner	$(11,7)$	$(11,7)$	PASS
rigidity winner at $B=20$	$(2,5,1)$	$(2,5,1)$	PASS
r_{step} winner (1 anchor)	2π	2π	PASS
r_{step} winner (2 anchors)	2π	2π	PASS
plaquette holonomy cycle hist	1:24,2:19,2x2:1,3:3,4:2	1:24,2:19,2x2:1,3:3,4:2	PASS
phase-lift CP signal	nonzero on 3/4 cycles	|J| mean (1,2,3,4)=(1.25e-50,1.06e-17,0.0634,0.0226)	PASS
PMNS perm-fit E_∞	≤ 0.2	0.121	PASS
loop-scale PMNS E_∞ finite	finite	0.228	PASS
loop-scale $SO(3)$ angle range	$[0,180]$	count=31, range=[90.0,120.0]	PASS
Wilson W range	$[-1,1]$	[-0.088,0.642]	PASS
single-loop PMNS E_∞	≤ 0.25	0.121	PASS
single-loop CKM E_∞	≤ 1.0	0.679	PASS
two-loop PMNS E_∞	≤ 0.05	0.011	PASS
two-loop CKM E_∞	≤ 0.5	0.442	PASS
two-loop (mixed) PMNS E_∞	≤ 0.05	0.011	PASS
two-loop (mixed) CKM E_∞	≤ 0.3	0.213	PASS
inverse generation acc	1.000	1.000	PASS
inverse sign(Y) acc	≥ 0.6	0.667	PASS
inverse Y_{num} acc	≥ 0.6	1.000	PASS

AE.6 Audit metrics for bounded-complexity closures

For a positive reference target x^{ref} and a candidate prediction $x(\theta)$, we use the (dimensionless) log-mismatch

$$e(\theta) := \left|\log\left(\frac{x(\theta)}{x^{\mathrm{ref}}}\right)\right|.$$

For multi-target closures we report the minimax objective

$$E_\infty(\theta) := \max_i e_i(\theta).$$

Tables 70 and 71 record candidate-domain sizes, uniqueness gaps, and (for large candidate domains) distribution quantiles. For a fixed candidate family Θ equipped with the uniform prior, the empirical frequency $N_{\le\epsilon}/|\Theta|$ can be read as the probability that a uniformly random candidate achieves $E_\infty \le \epsilon$. When the minimizer is unique, the probability that a uniformly random candidate matches as well or better than the reported minimizer is $1/|\Theta|$. These within-family probabilities provide explicit look-elsewhere context for the stated hypothesis classes; they do not claim a global significance over unrestricted expression grammars.

closure	candidate family	$\lvert\Theta\rvert$	minimizer	best E_∞	second	gap	$N_{\le 0.01}$	$N_{\le 0.05}$
$\alpha_{\mathrm{em}}^{-1}$	$a\pi^3 + b\pi^2 + c\pi,\ a{+}b{+}c \le 10$	285	$(4, 1, 1)$	2.22344e-06	0.0032491	0.00325	2	19
$\alpha^{-1}(\mu_Z)$	$n\pi^2,\ 1 \le n \le 50$	50	$n = 13$	0.00273049	0.0768385	0.0741	1	1
$\sin^2\theta_W(\mu_Z)$	$p/q,\ 1 \le q \le 50$	773	$3/13$	0.00195143	0.00577062	0.00382	4	19
J (CKM)	$1/(a\pi^n),\ a \le 50,\ n \le 20$	1000	$(11, 7)$	0.0033087	0.0094142	0.00611	2	5
CKM magnitudes	$\lvert V_{us}\rvert{=}1/\sqrt{d},\ \lvert V_{cb}\rvert{=}\varphi^{-k_{23}/2},\ \lvert V_{ub}\rvert{=}\varphi^{-k_{13}/2}$	32000	$(d, k_{23}, k_{13}) = (20, 13, 23)$	0.0374582	0.0374582	0	0	3
PMNS sines	$s_{12}{=}\sqrt{p_{12}/q_{12}},\ s_{23}{=}\sqrt{p_{23}/q_{23}},\ s_{13}{=}\varphi^{-k_{13}/2}$	655360	$(p_{12}/q_{12}, p_{23}/q_{23}, k_{13}) = (4/13, 6/11, 8)$	0.0119246	0.0119246	0	0	98
PMNS δ	$\delta = k\pi/q,\ 1 \le q \le 12$	91	$\delta = 13\pi/12$	0.010856	0.0739731	0.0631	0	1
mass depth (leptons)	$\widehat{r} = a\,\Delta V + b\,\Delta g + c\,\Delta\lvert w\rvert_1,\ \lvert a\rvert, \lvert b\rvert, \lvert c\rvert \le 20$	34460	$(2, 5, 1)$	0.0382687	0.0382687	0	0	5

Table 70: Audit metrics for bounded-complexity closures. E_∞ is a minimax log-mismatch across the targets of each closure; for scalar targets it reduces to the single absolute log mismatch.

closure	$\lvert\Theta\rvert$	min	median	p90	p99	max
CKM magnitudes ($B = 20$)	32000	0.0374582	3.57163	5.49648	6.4589	6.4589
PMNS sines ($B = 20$)	655360	0.0119246	3.1398	6.74889	7.71131	7.71131
mass depth ($B = 20$)	34460	0.0382687	55.8472	108.299	131.397	145.834

Table 71: Quantiles of the minimax log-mismatch E_∞ over large candidate domains at $B = 20$ (for the CKM-magnitude, PMNS-sine, and mass-depth closures).

AE.7 Uncertainty robustness (minimizer stability under target perturbations)

To stress-test how stable the selected minimizers are under perturbations of the reference targets, we sample reference values within explicit uncertainty models and recompute the minimizer under the same tie-break rules. The sampling is deterministic (fixed RNG seed) and is intended as an audit-oriented robustness check. We use simple truncated-normal models designed to keep targets in their admissible domains: for positive scalar targets $x^{\mathrm{ref}} > 0$, we sample $x' \sim \mathcal{N}(x^{\mathrm{ref}}, \sigma)$ truncated to remain positive; for mixing-angle targets quoted as $\sin^2\theta$, we sample $\sin^2\theta' \sim \mathcal{N}(\sin^2\theta, \sigma)$ truncated to $(0, 1)$ and then use $s = \sqrt{\sin^2\theta'}$; and for a phase reference δ we sample $\delta' \sim \mathcal{N}(\delta, \sigma_\delta)$ truncated to $[0, 360]$ degrees. When a standard reference uncertainty is explicitly quoted (e.g. PDG for J), we use it directly; otherwise (e.g. scheme-dependent electroweak quantities and matching-layer anchors) the adopted σ values are recorded as conservative audit stress-test scales rather than as a statistical claim.

closure	reference	uncertainty model	samples	baseline minimizer	stability
$\alpha_{\mathrm{em}}^{-1}$	137.035999084000	$\sigma = 2.1 \times 10^{-8}$	200	$(4, 1, 1)$	1.000
$\alpha^{-1}(\mu_Z)$	127.955	$\sigma = 10^{-2}$	200	$n = 13$	1.000
$\sin^2\theta_W(\mu_Z)$	0.23122	$\sigma = 3 \times 10^{-5}$	200	$3/13$	1.000
J (CKM)	3.00×10^{-5}	$\sigma = 1.5 \times 10^{-6}$	200	$(11, 7)$	0.120
CKM magnitudes	$(\lvert V_{us}\rvert, \lvert V_{cb}\rvert, \lvert V_{ub}\rvert) = (0.2243, 0.0422, 0.00394)$	$\sigma = (5, 8, 36) \times 10^{-4}$	200	$(d, k_{23}, k_{13}) = (20, 13, 23)$	0.760
PMNS sines	$(\sin^2\theta_{12}, \sin^2\theta_{23}, \sin^2\theta_{13}) = (0.307, 0.545, 0.0218)$	$\sigma(\sin^2\theta) = (0.013, 0.021, 0.0007)$	200	$(p_{12}/q_{12}, p_{23}/q_{23}, k_{13}) = (4/13, 6/11, 8)$	0.025
PMNS δ (bounded denom.)	$\delta = 195^\circ$	$\sigma_\delta = 30^\circ$	200	$\delta = 195^\circ$	0.335
mass depth (leptons)	$(m_\mu, m_\tau) = (0.10565838, 1.77686)\,\mathrm{GeV}$	$\sigma/\mu = 5 \times 10^{-4}$	200	$(2, 5, 1)$	1.000

Table 72: Minimizer stability rates under sampled target perturbations for selected closures, as generated by `scripts/exp_audit_uncertainty_robustness.py`.

AE.8 Resolution calibration robustness

We also stress-test the robustness of the resolution-step calibration minimizer (Section 14.2.1) under explicit perturbations of the reference anchors.

calibration model	uncertainty model	samples	baseline minimizer	stability
single anchor ($m = 10 \to m_Z$)	$\sigma_Z = 0.1$ GeV	500	$k = 2$	1.000
two anchors ($m = 10 \to m_Z$, $m = 8 \to \mu_{\mathrm{QCD}}$)	$(\sigma_Z, \sigma_Q) = (0.1, 0.05)$ GeV	500	$k = 2$	1.000

Table 73: Minimizer stability rates for the resolution-step calibration under sampled anchor perturbations. Rows are generated by `scripts/exp_audit_resolution_calibration_robustness.py`.

AE.9 Counterfactual baseline comparisons

To provide look-elsewhere context, we compare the best achievable mismatch under the structured candidate families used in the paper to simple counterfactual families of comparable discrete complexity.

closure	candidate family	$\lvert\Theta\rvert$	minimizer	best E_∞
$\alpha_{\mathrm{em}}^{-1}$	$a\pi^3 + b\pi^2 + c\pi$	285	$(4, 1, 1)$	2.22344e-06
$\alpha_{\mathrm{em}}^{-1}$	$ae^3 + be^2 + ce$	285	$(5, 5, 0)$	0.00245594
CKM magnitudes	φ-family	32000	$(d, k_{23}, k_{13}) = (20, 13, 23)$	0.0374582
CKM magnitudes	e-family	32000	$(d, k_{23}, k_{13}) = (20, 6, 11)$	0.165335
CKM magnitudes	2-family	32000	$(d, k_{23}, k_{13}) = (20, 9, 16)$	0.0461727
PMNS sines	φ-family	16000	$(3, 2, 8)$	0.0430888
PMNS sines	e-family	16000	$(3, 2, 4)$	0.0870773
PMNS sines	2-family	16000	$(3, 2, 6)$	0.166519
Holonomy PMNS perm-fit	Hilbert addressing	468	$(262144, (1, 2, 0), (2, 0, 1))$	0.121164
Holonomy PMNS perm-fit	row-major addressing	468	$(262144, (0, 2, 1), (1, 0, 2))$	0.611674
Holonomy single-loop PMNS	Hilbert addressing	262080	`(gray,64,4,(1,0),2,(0,1,2),(2,0,1))`	0.12128
Holonomy single-loop CKM	Hilbert addressing	262080	`(gray,512,3,(3,0),2,(1,0,2),(1,0,2))`	0.679211
Holonomy single-loop PMNS	row-major addressing	262080	`(gray,64,2,(0,2),3,(0,2,1),(2,0,1))`	0.110299
Holonomy single-loop CKM	row-major addressing	262080	`(gray,1024,1,(1,6),2,(1,0,2),(1,0,2))`	0.675787

Table 74: Counterfactual baseline comparisons for selected closures. Rows are generated by `scripts/exp_audit_counterfactual_baselines.py`.

AE.10 A broader null baseline for α^{-1} from bounded π-polynomials

As an additional look-elsewhere diagnostic beyond the narrow candidate families used in the main text, we also sweep a larger explicit grammar: integer polynomials in π of degree ≤ 3 with bounded coefficients. This produces a finite hypothesis class that contains the specific closed target $\alpha_{\mathrm{geo}}^{-1} = 4\pi^3 + \pi^2 + \pi$ as one point, while allowing many nearby expressions of comparable syntactic form. Table 75 reports the best achievable log mismatch over the full domain together with the counts of candidates below fixed mismatch thresholds.

target	family	$\lvert\Theta\rvert$	minimizer	best e	ties	$N_{\leq 0.01}$	$N_{\leq 0.05}$
$\alpha_{\mathrm{em}}^{-1}$ (CODATA)	$\sum_{j=0}^{3} a_j \pi^j,\ a_j \in [-10, 10]$	194481	$4\pi^3 + \pi^2 + \pi$	2.22344e-06	1	820	4087

Table 75: Null baseline over bounded integer π-polynomials (degree ≤ 3 with coefficients in a fixed box). Here $e = |\log(x/x^{\mathrm{ref}})|$ is the absolute log mismatch to the reference target. Rows are generated by `scripts/exp_audit_pi_polynomial_null.py`.

AE.11 Rigidity enumerations for closed constant targets

Remark AE.1 (Why the coefficient-sum bound is not vacuous (order-of-magnitude check))**.** *In the simplex search domain $a, b, c \in \mathbb{Z}_{\geq 0}$ with $a + b + c \leq S$, one always has*

$$a\pi^3 + b\pi^2 + c\pi \leq (a + b + c)\pi^3 \leq S\,\pi^3.$$

Using the classical bound $\pi < 22/7$ gives $\pi^3 < (22/7)^3 \approx 31.1$ and therefore $S \leq 4 \Rightarrow a\pi^3 + b\pi^2 + c\pi < 125$. Since the reference electromagnetic inverse coupling satisfies $\alpha_{\mathrm{em}}^{-1} \approx 137 > 125$ (CODATA/PDG; Table 16), any nontrivial match requires $a + b + c \geq 5$. Thus the bounded search $a + b + c \leq 10$ is small but already above the minimal order-of-magnitude threshold.

rank	(a, b, c)	candidate	value	$\lvert x - x^{\mathrm{ref}}\rvert$	rel. error	$\lvert\log(x/x^{\mathrm{ref}})\rvert$
1	$(4, 1, 1)$	$4\pi^3 + \pi^2 + \pi$	137.0363037759	3.047e-04	2.223e-06	2.223e-06
2	$(4, 0, 4)$	$4\pi^3 + 4\pi$	136.5914773356	4.445e-01	3.244e-03	3.249e-03
3	$(3, 4, 1)$	$3\pi^3 + 4\pi^2 + \pi$	135.6388402988	1.397e+00	1.020e-02	1.025e-02
4	$(3, 4, 2)$	$3\pi^3 + 4\pi^2 + 2\pi$	138.7804329524	1.744e+00	1.273e-02	1.265e-02
5	$(3, 3, 4)$	$3\pi^3 + 3\pi^2 + 4\pi$	135.1940138585	1.842e+00	1.344e-02	1.353e-02
6	$(4, 0, 5)$	$4\pi^3 + 5\pi$	139.7330699891	2.697e+00	1.968e-02	1.949e-02
7	$(2, 7, 1)$	$2\pi^3 + 7\pi^2 + \pi$	134.2413768218	2.795e+00	2.039e-02	2.060e-02
8	$(4, 1, 2)$	$4\pi^3 + \pi^2 + 2\pi$	140.1778964295	3.142e+00	2.293e-02	2.267e-02
9	$(4, 1, 0)$	$4\pi^3 + \pi^2$	133.8947111223	3.141e+00	2.292e-02	2.319e-02
10	$(4, 0, 3)$	$4\pi^3 + 3\pi$	133.4498846820	3.586e+00	2.617e-02	2.652e-02

domain $|\Theta| = 285$; best/second gap $\Delta e = 3.247e-03$

Table 76: Finite simplex search for $\alpha_{\mathrm{em}}^{-1}$ over $a\pi^3 + b\pi^2 + c\pi$ with $a, b, c \in \mathbb{Z}_{\geq 0}$ and $a + b + c \leq 10$, ranked by the audit-norm log mismatch $e = |\log(x/x^{\mathrm{ref}})|$ with deterministic tie-break rules. Rows are generated by `scripts/exp_alpha_coeff_rigidity.py`.

Remark AE.2 (Why the integer-π^2 sweep is effectively local (order-of-magnitude check))**.** *Let $x^{\mathrm{ref}} = \alpha_{\mathrm{PDG}}^{-1}(\mu_Z)$ be the reference value (Table 16). Any integer n for which $n\pi^2$ can compete must satisfy $n \approx x^{\mathrm{ref}}/\pi^2$. Using $9 < \pi^2 < 10$ gives the crude localization*

$$\frac{x^{\mathrm{ref}}}{10} < n < \frac{x^{\mathrm{ref}}}{9}.$$

Since $x^{\mathrm{ref}} \approx 128$, only n in a narrow band around 13 can be relevant; the sweep $1 \leq n \leq 50$ is a small explicit overbound that contains this band.

rank	n	$n\pi^2$	$\lvert x - x^{\mathrm{ref}}\rvert$	rel. error	$\lvert\log(x/x^{\mathrm{ref}})\rvert$
1	13	128.3048572142	3.499e-01	2.734e-03	2.730e-03
2	14	138.1744616153	1.022e+01	7.987e-02	7.684e-02
3	12	118.4352528131	9.520e+00	7.440e-02	7.731e-02
4	15	148.0440660163	2.009e+01	1.570e-01	1.458e-01
5	11	108.5656484120	1.939e+01	1.515e-01	1.643e-01
6	16	157.9136704174	2.996e+01	2.341e-01	2.104e-01
7	10	98.6960440109	2.926e+01	2.287e-01	2.596e-01
8	17	167.7832748185	3.983e+01	3.113e-01	2.710e-01
9	18	177.6528792196	4.970e+01	3.884e-01	3.282e-01
10	9	88.8264396098	3.913e+01	3.058e-01	3.650e-01

domain $|\Theta| = 50$; best/second gap $\Delta e = 7.411e-02$

Table 77: Finite search for an integer-π^2 approximation to $\alpha^{-1}(\mu_Z)$ over $n\pi^2$ with $1 \leq n \leq 50$, ranked by the audit-norm log mismatch $e = |\log(x/x^{\mathrm{ref}})|$ to the PDG reference value $\alpha_{\mathrm{PDG}}^{-1}(\mu_Z)$ with deterministic tie-break rules. Rows are generated by `scripts/exp_ew_rigidity.py`.

Remark AE.3 (Why the bounded-denominator rational sweep is nonvacuous)**.** *For any real x and any $Q \geq 1$, Dirichlet's approximation theorem implies the existence of a reduced rational p/q with $1 \leq q \leq Q$ and*

$$\left| x - \frac{p}{q} \right| < \frac{1}{qQ} \leq \frac{1}{Q^2}.$$

Thus the choice $Q = 50$ guarantees (a priori) the existence of candidates within absolute error $\leq 4 \times 10^{-4}$ while keeping the hypothesis class finite and auditable.

rank	p/q	value	$\lvert x - x^{\mathrm{ref}} \rvert$	$\lvert \log(x/x^{\mathrm{ref}}) \rvert$
1	3/13	0.2307692308	4.508e-04	1.951e-03
2	10/43	0.2325581395	1.338e-03	5.771e-03
3	11/48	0.2291666667	2.053e-03	8.920e-03
4	7/30	0.2333333333	2.113e-03	9.098e-03
5	8/35	0.2285714286	2.649e-03	1.152e-02
6	11/47	0.2340425532	2.823e-03	1.213e-02
7	5/22	0.2272727273	3.947e-03	1.722e-02
8	4/17	0.2352941176	4.074e-03	1.747e-02
9	7/31	0.2258064516	5.414e-03	2.369e-02
10	9/38	0.2368421053	5.622e-03	2.402e-02

domain $|\Theta| = 773$; best/second gap $\Delta e = 3.819e-03$

Table 78: Finite search for a reduced rational approximation to $\sin^2\theta_W(\mu_Z)$ over p/q with $1 \leq q \leq 50$, ranked by the audit-norm log mismatch $e = |\log(x/x^{\mathrm{ref}})|$ to the PDG reference value $\sin^2\theta_{W,\mathrm{PDG}}(\mu_Z)$ with deterministic tie-break rules. Rows are generated by `scripts/exp_ew_rigidity.py`.

Remark AE.4 (A nonvacuous magnitude window for the Jarlskog (a, n) box)**.** *Let $J_{\mathrm{ref}} \approx 3 \times 10^{-5}$ be the PDG-scale target used in the paper [2]. Within the bounded box $1 \leq a \leq 50$, if $n \leq 5$ then*

$$\frac{1}{a\pi^n} \geq \frac{1}{50\pi^5} > \frac{1}{50(22/7)^5} \approx 6.5 \times 10^{-5},$$

so the entire $n \leq 5$ slab is too large to match J_{ref} even at maximal a. Thus any nontrivial rigidity search with $a \leq 50$ must include $n \geq 6$; the chosen domain $1 \leq a \leq 50$, $1 \leq n \leq 20$ contains this minimal magnitude-viable window.

rank	(a, n)	value	$\lvert x - x^{\mathrm{ref}} \rvert$	rel. error	$\lvert x - x^{\mathrm{ref}} \rvert/\sigma$	$\lvert \log(x/x^{\mathrm{ref}}) \rvert$
1	(11, 7)	3.0099425471e-05	9.943e-08	3.314e-03	6.628e-02	3.309e-03
2	(35, 6)	2.9718899237e-05	2.811e-07	9.370e-03	1.874e-01	9.414e-03
3	(34, 6)	3.0592984509e-05	5.930e-07	1.977e-02	3.953e-01	1.957e-02
4	(36, 6)	2.8893374258e-05	1.107e-06	3.689e-02	7.378e-01	3.759e-02
5	(33, 6)	3.1520044645e-05	1.520e-06	5.067e-02	1.013e+00	4.943e-02
6	(37, 6)	2.8112472251e-05	1.888e-06	6.292e-02	1.258e+00	6.498e-02
7	(32, 6)	3.2505046040e-05	2.505e-06	8.350e-02	1.670e+00	8.020e-02
8	(12, 7)	2.7591140015e-05	2.409e-06	8.030e-02	1.606e+00	8.370e-02
9	(38, 6)	2.7372670350e-05	2.627e-06	8.758e-02	1.752e+00	9.165e-02
10	(10, 7)	3.3109368018e-05	3.109e-06	1.036e-01	2.073e+00	9.862e-02

domain $|\Theta| = 1000$; best/second gap $\Delta e = 6.105e-03$

Table 79: Finite rigidity search for the Jarlskog invariant over the ansatz $J = 1/(a\pi^n)$ with $1 \leq a \leq 50$ and $1 \leq n \leq 20$, ranked by the audit-norm log mismatch $e = |\log(x/x^{\mathrm{ref}})|$ to the PDG central value with deterministic tie-break rules. Rows are generated by `scripts/exp_jarlskog_pi_rigidity.py`.

AF Closure audit details: couplings, mixing, and CP (supplement)

This appendix collects the detailed finite constructions, bounded-complexity searches, and reconstruction tables underlying the coupling/CP normalizations and the CKM/PMNS closures reported in Part IV.

This section records two interface points: (i) coupling constants as geometric normalization costs, and (ii) CP violation as a CP-odd phase-space volume with discrete multiplicity. We treat the closed expressions below as CAP-closed interface normalizations: they follow from explicitly declared finite candidate families and canonical geometric data, and their mismatch to scheme-/scale-dependent experimental conventions is recorded as a matching-layer factor. The same normalization philosophy is pursued, in a broader constant-geometry context, in the companion manuscript [8].

AF.1 Three-channel impedance and the fine-structure constant

The inverse fine-structure constant admits a closed three-stratum geometric impedance expression:

$$\alpha_{\mathrm{em}\,\mathrm{geo}}^{-1} = 4\pi^3 + \pi^2 + \pi \approx 137.0363037759. \tag{77}$$

We make the interface closure declarations explicit.

Tick-first bridge: from periodic phase to geometric normalization cost. In the tick-first dictionary (Section 3), the only primitive input is the sequential update count and the only primitive closure rule is CAP. Any internal phase variable is therefore a *periodic* datum attached to tick evolution, with the canonical low-complexity period 2π (circle normalization). When independent protocol constraints must be satisfied in series, their combined effect is multiplicative at the level of weights and additive after the logarithmic readout map (Proposition AF.1). The role of compact phase spaces and their canonical volumes in the definitions below is to supply protocol-invariant, finite-description normalization costs for such periodic data, compatible with ray-space $\mathbb{Z}_2$ identifications intrinsic to finite readout.

Proposition AF.1 (Serial composition and logarithmic impedance (interface))**.** *If a readout protocol must satisfy independent constraints in a fixed hierarchy ("strata") in series, assign each stratum j a multiplicative weight $w_j \in (0,1]$ and define its log-cost $V_j := -\log w_j$ [17, 61]. If the total weight is $w_{\mathrm{tot}} = \prod_j w_j$, then the corresponding impedance is the additive cost*

$$\alpha_{\mathrm{geo}}^{-1} := -\log w_{\mathrm{tot}} = \sum_j V_j.$$

Proof. This is the identity $-\log\left(\prod_j w_j\right) = \sum_j (-\log w_j)$. □

Definition AF.2 (Geometric cost as canonical phase volume (CAP closure form))**.** *For each stratum j, let $\mathcal{M}_j$ be a compact phase space drawn from a declared finite candidate family. Define the cost as the canonical volume*

$$V_j := \mathrm{Vol}(\mathcal{M}_j),$$

where Vol *is computed using the standard bi-invariant metric on compact Lie groups together with induced quotient metrics for projective $\mathbb{Z}_2$ identifications (Lemma AF.6). The choice of $\mathcal{M}_j$ is treated as a bounded-complexity CAP closure within the stated family (Axiom 1.5 and Definition H.1).*

Remark AF.3 (Metric normalization and matching-layer rescaling)**.** *Throughout this section we use the standard unit-radius normalizations for compact groups (Lemma AF.6), so that* $SU(2) \cong S^3$ *has* $\mathrm{Vol}(SU(2)) = 2\pi^2$*. Any alternative overall metric rescaling on a stratum rescales* $\mathrm{Vol}(\mathcal{M}_j)$ *by a fixed factor and therefore shifts the corresponding impedance contribution* V_j *by a matching-layer normalization change rather than introducing additional internal degrees of freedom.*

Definition AF.4 (Electromagnetic three-stratum phase spaces (CAP closure form))**.** *For the electromagnetic normalization channel, select the three strata within an explicit finite candidate family built from the primitive set*

$$\mathfrak{P} := \{U(1), SU(2), SO(3), \mathbb{R}P^1\},$$

equipped with canonical volumes (Lemma AF.6) and with projective quotients encoding the ray-space $\mathbb{Z}_2$ *identification intrinsic to readout. At the* $m = 6$ *anchor, the CAP-minimal choice yields*

$$\mathcal{M}_{\mathrm{bulk}} \cong U(1) \times SU(2), \qquad \mathcal{M}_{\mathrm{boundary}} \cong SO(3), \qquad \mathcal{M}_{\mathrm{line}} \cong \mathbb{R}P^1$$

(Proposition AF.7).

Remark AF.5 (Geometric meaning of the three electromagnetic strata)**.** *The three strata in Definition AF.4 are chosen to align with three protocol-level geometric objects that are present once one insists on finite-resolution readout and transport. The factor* $U(1)$ *models phase,* $SU(2)$ *captures the spinorial double cover of rotations,* $SO(3)$ *encodes the orientation of a local rigid frame, and* $\mathbb{R}P^1 \cong U(1)/\{\pm 1\}$ *models the projective ray identification of a one-dimensional phase degree of freedom [18,47]. The purpose of the definition is not to claim an ontic manifold, but to fix a minimal closed normalization dictionary in which ray-space* $\mathbb{Z}_2$ *quotients are treated explicitly rather than absorbed into conventions.*

Lemma AF.6 (Canonical volumes of $U(1)$, $SU(2)$, $SO(3)$, and $\mathbb{R}P^1$)**.** *With the standard unit-radius normalizations,*

$$\mathrm{Vol}(U(1)) = 2\pi, \qquad \mathrm{Vol}(SU(2)) = \mathrm{Vol}(S^3) = 2\pi^2.$$

Moreover, the $\mathbb{Z}_2$ *quotients satisfy*

$$\mathrm{Vol}(SO(3)) = \mathrm{Vol}(SU(2)/\{\pm\mathbf{1}\}) = \pi^2, \qquad \mathrm{Vol}(\mathbb{R}P^1) = \mathrm{Vol}(U(1)/\{\pm 1\}) = \pi.$$

Consequently, $\mathrm{Vol}(U(1) \times SU(2)) = 4\pi^3$*.*

Proof. The first identity is the circumference of the unit circle. For $SU(2) \cong S^3$, integrating the standard volume form on the unit 3-sphere gives $\mathrm{Vol}(S^3) = 2\pi^2$ [18,47]. The quotient maps $SU(2) \to SO(3) = SU(2)/\{\pm\mathbf{1}\}$ and $U(1) \to \mathbb{R}P^1 = U(1)/\{\pm 1\}$ are two-sheeted Riemannian coverings under the induced quotient metrics, so the quotient volumes are halved. The product identity follows by multiplicativity of product volumes. □

Proposition AF.7 (Primitive factorization rigidity for the electromagnetic strata)**.** *Fix the primitive candidate set*

$$\mathfrak{P} := \{U(1), SU(2), SO(3), \mathbb{R}P^1\},$$

equipped with the canonical volumes of Lemma AF.6. Restrict the bulk stratum to be a product of two primitives and restrict the boundary and line strata to be single primitives. Impose the target scalings

$$\mathrm{Vol}(\mathcal{M}_{\mathrm{bulk}}) = 4\pi^3, \qquad \mathrm{Vol}(\mathcal{M}_{\mathrm{boundary}}) = \pi^2, \qquad \mathrm{Vol}(\mathcal{M}_{\mathrm{line}}) = \pi.$$

Then, up to ordering, the strata are forced as

$$\mathcal{M}_{\mathrm{bulk}} \cong U(1) \times SU(2), \qquad \mathcal{M}_{\mathrm{boundary}} \cong SO(3), \qquad \mathcal{M}_{\mathrm{line}} \cong \mathbb{R}P^1.$$

aggregation rule	value	$\log(\text{value}/\alpha_{\text{CODATA}}^{-1})$
serial sum	**137.0363037759**	$+2.22 \times 10^{-6}$
Euclidean	124.4568430929	-9.63×10^{-2}
max	124.0251067212	-9.98×10^{-2}
parallel	2.3381204994	-4.07
arithmetic mean	45.6787679253	-1.10
geometric mean	15.6670204088	-2.17

Table 80: Aggregation baselines for the three-stratum α_{em}^{-1} impedance dictionary. The baseline serial rule corresponds to Proposition AF.1; alternative rows are counterfactual aggregation semantics and are included only as look-elsewhere context. Rows are reproduced by the deterministic script `scripts/exp_aggregation_baselines.py`.

Proof. By Lemma AF.6, the one-factor values in $\mathfrak{P}$ are 2π, $2\pi^2$, π^2, and π. Any two-factor product has the form $2^m\pi^k$ with $m \in \{0,1,2\}$ and $k \in \{2,3,4\}$. The constraint $\text{Vol}(\mathcal{M}_{\text{bulk}}) = 4\pi^3$ forces exponent pattern $(1,2)$ and coefficient 4, hence the factors must be $U(1)$ and $SU(2)$. For one-factor realizations, π^2 occurs only for $SO(3)$ and π occurs only for $\mathbb{R}P^1$ in $\mathfrak{P}$, forcing the boundary and line strata. □

Remark AF.8 (Serial aggregation is not interchangeable)**.** *Under the serial semantics of Proposition AF.1, the impedance is additive after the logarithmic readout map. For context, Table 80 records a small systematic baseline sweep over several standard alternative aggregation rules acting on the three stratum costs $V_{\text{bulk}} = 4\pi^3$, $V_{\text{boundary}} = \pi^2$, and $V_{\text{line}} = \pi$, together with their log mismatches to the CODATA reference.*

Theorem AF.9 (Three-stratum geometric impedance for α_{em})**.** *Under Proposition AF.1 and the CAP-closed phase-volume dictionary in Definitions AF.2–AF.4, one has*

$$\alpha_{\text{em}\,\text{geo}}^{-1} = \text{Vol}(U(1) \times SU(2)) + \text{Vol}(SO(3)) + \text{Vol}(\mathbb{R}P^1) = 4\pi^3 + \pi^2 + \pi,$$

hence (77)*.*

Proof. By Proposition AF.1 and Definition AF.2, the impedance equals the serial sum of the three stratum volumes. By Definition AF.4 and Lemma AF.6, $\text{Vol}(U(1) \times SU(2)) = 4\pi^3$, $\text{Vol}(SO(3)) = \pi^2$, and $\text{Vol}(\mathbb{R}P^1) = \pi$. Summing gives (77). □

This matches the philosophy of the present paper: coupling strength is not an arbitrary input, but a normalization cost induced by finite-resolution readout and compensation.

Interface reading. If each defect channel induces a compensation "impedance" (a normalization cost for maintaining protocol-consistent phase transport), then the electromagnetic coupling is the effective cost seen after channel composition. In this sense, (77) is a numerical instance of the same template as Proposition 8.1, specialized to a dimensionless normalization observable.

CODATA comparison and explicit mismatch size. Let $\alpha_{\text{CODATA}}^{-1}$ denote the CODATA recommended inverse fine-structure constant [59]. The mismatch in inverse impedance is:

$$\Delta\alpha^{-1} := \alpha_{\text{em}\,\text{geo}}^{-1} - \alpha_{\text{CODATA}}^{-1} \approx 3.046 \times 10^{-4}, \qquad \frac{\Delta\alpha^{-1}}{\alpha_{\text{CODATA}}^{-1}} \approx 2.22 \times 10^{-6}. \tag{78}$$

Since the CODATA uncertainty on α^{-1} is at the 10^{-8} level [59], the ppm-scale deviation in (78) should be read as a protocol-level matching factor between a closed normalization target

and a renormalized experimental convention, not as an "agreement within error bars" claim. Equivalently, in the multiplicative weight variable $w = \exp(-\alpha^{-1})$, the interface mismatch is a single factor $s_\alpha = \exp(\Delta\alpha^{-1}) \approx 1.0003046$. Using the one-loop dictionary in Remark AF.18, the additive mismatch $\Delta\alpha^{-1}$ can be equivalently represented as a matching-layer scale ratio $\mu_*/\mu_0 = \exp(-(2\pi/b)\Delta\alpha^{-1})$ at fixed one-loop coefficient b.

Rigidity at bounded coefficient complexity. At bounded coefficient complexity (small nonnegative integers in the ansatz $a\pi^3 + b\pi^2 + c\pi$), the triple $(a, b, c) = (4, 1, 1)$ is rigidly singled out as the unique best fit in a finite search domain in the audit log-mismatch norm.

Proposition AF.10 (Bounded-coefficient rigidity for $\alpha_{\mathrm{em}}^{-1}$)**.** *Within the finite domain $a, b, c \in \mathbb{Z}_{\geq 0}$ with $a + b + c \leq 10$, the unique minimizer of the absolute log mismatch*

$$e(a, b, c) := \left| \log\left(\frac{a\pi^3 + b\pi^2 + c\pi}{\alpha_{\mathrm{CODATA}}^{-1}} \right) \right|$$

under deterministic tie-break rules (coefficient sum, then lexicographic (a, b, c)) is $(a, b, c) = (4, 1, 1)$.

Proof. This is a finite exhaustive enumeration over 286 triples in the simplex $a+b+c \leq 10$ with deterministic tie-break rules. The top candidates and runner-up gap are recorded in Table 76 and are reproducible by `scripts/exp_alpha_coeff_rigidity.py`. □

Remark AF.11 (A broader π-polynomial null baseline)**.** *To provide look-elsewhere context beyond the nonnegative-coefficient simplex used in Proposition AF.10, Appendix AE.10 reports a larger sweep over the explicit grammar $\sum_{j=0}^{3} a_j \pi^j$ with $a_j \in [-10, 10]$ (a domain of size* 194,481*). Within this broader class, the unique best candidate is still $4\pi^3+\pi^2+\pi$ with absolute log mismatch $e \approx 2.22 \times 10^{-6}$ (Table 75).*

AF.2 Electroweak normalization and the Weinberg angle

At the Z scale, we record a closed-theory electroweak matching normalization:

$$\sin^2 \theta_W(\mu_Z) = \frac{3}{13}, \tag{79}$$

and the gauge-sector normalizations can be written as

$$\alpha_w^{-1}(\mu_Z) = 3\pi^2, \qquad \alpha_Y^{-1}(\mu_Z) = 10\pi^2, \qquad \alpha^{-1}(\mu_Z) = 13\pi^2, \tag{80}$$

under a canonical volume assignment consistent with the Standard Model relation between gauge couplings and the electromagnetic coupling [1, 2, 119–121].

Definition AF.12 (Electroweak inverse couplings as weighted volumes (CAP closure form))**.** *At the matching scale $\mu = \mu_Z$, define the inverse couplings by weighted canonical volumes*

$$\alpha_w^{-1}(\mu_Z) = \dim(\mathfrak{su}(2)) \operatorname{Vol}(SO(3)), \qquad \alpha_Y^{-1}(\mu_Z) = \Big(\sum_{f \in \mathrm{SM}} Y_f^2 \Big) \operatorname{Vol}(SO(3)),$$

with hypercharge normalized by $Q = T_3 + Y$. The normalization is treated as a CAP-closed interface dictionary: the weights are discrete invariants already fixed by the closed labeling at the anchor (Lemma 9.3 and Lemma 8.8), and the remaining numerical comparison to Z-scale $\overline{\mathrm{MS}}$ conventions is recorded as a matching-layer mismatch (Table 77 and Table 78).

Remark AF.13 (Why the weight $\sum Y^2$ is canonical at the interface)**.** *In standard gauge theory, the normalization of an abelian coupling is tied to the choice of charge generator, and the leading vacuum-polarization/running coefficients depend on sums of squared charges (with multiplicities) [1, 2]. Thus the appearance of* $\sum Y^2$ *as a discrete weight in Definition AF.12 is compatible with the conventional role of hypercharge-squared sums in* $U(1)$ *normalization and renormalization, even though this paper treats the relation only as a matching-layer dictionary rather than as a derived* β*-function statement [80].*

Theorem AF.14 (Electroweak normalization and the Weinberg angle)**.** *Under Definition AF.12, one has* (80) *and, consequently,* (79)*.*

Proof. One has $\dim(\mathfrak{su}(2)) = 3$ (Lemma 9.3) and $\sum_{f\in \mathrm{SM}} Y_f^2 = 10$ for three generations (Lemma 8.8). With the canonical quotient metric, $\mathrm{Vol}(SO(3)) = \pi^2$ [47]. Thus $\alpha_w^{-1}(\mu_Z) = 3\pi^2$ and $\alpha_Y^{-1}(\mu_Z) = 10\pi^2$, giving $\alpha^{-1}(\mu_Z) = \alpha_w^{-1} + \alpha_Y^{-1} = 13\pi^2$. Finally, using the standard electroweak identity $\sin^2\theta_W = \alpha/\alpha_w = \alpha_w^{-1}/\alpha^{-1}$ [1, 2] yields $\sin^2\theta_W(\mu_Z) = 3/13$. □

Remark AF.15. *We use* α_w *as the* $SU(2)$ *coupling (often denoted* α_2 *in standard notation), and* α_Y *as the hypercharge coupling.*

Interface reading. The integer decomposition $13 = 3 + 10$ in (80) aligns with the $SU(2)$ gauge-sector dimension 3 (Lemma 9.3) and the three-generation hypercharge-squared sum 10 (Lemma 8.8), providing a shared integer backbone across the labeling interface and the electroweak normalization interface. Here it is recorded as a consistency check that the three-channel template can support the SM electroweak mixing pattern.

PDG comparison (explicit deviations). The closed model gives

$$\alpha^{-1}(\mu_Z) = 13\pi^2 \approx 128.3048572142, \qquad \sin^2\theta_W(\mu_Z) = \frac{3}{13} \approx 0.2307692308. \tag{81}$$

PDG quotes $\alpha_{\mathrm{PDG}}^{-1}(\mu_Z) \approx 127.955$ and $\sin^2\theta_{W,\mathrm{PDG}}(\mu_Z) \approx 0.23122$ in the $\overline{\mathrm{MS}}$ convention [2]. Thus,

$$13\pi^2 - 127.955 \approx 3.50 \times 10^{-1} \qquad (2.73 \times 10^{-3} \text{ relative}), \tag{82}$$

and

$$\frac{3}{13} - 0.23122 \approx -4.51 \times 10^{-4} \qquad (-1.95 \times 10^{-3} \text{ relative}). \tag{83}$$

Remark AF.16 (Unification-scale benchmarks vs. Z-scale conventions)**.** *The electroweak mixing angle is scale dependent. In minimal* $SU(5)$*-type grand-unified models, one has the familiar tree-level unification-scale relation* $\sin^2\theta_W = 3/8$ *[83, 84]. Running and threshold corrections then relate unification-scale parameters to* Z*-scale* $\overline{\mathrm{MS}}$ *conventions [1, 2]. Accordingly, our* Z*-scale targets in* (81) *are recorded as matching-layer normalizations at* μ_Z*, not as unification-scale relations.*

Bounded-complexity rigidity. Within the finite search domain $1 \le n \le 50$ in the ansatz $\alpha^{-1}(\mu_Z) = n\pi^2$, the coefficient $n = 13$ is the unique minimizer of the audit mismatch $e(n) := |\log((n\pi^2)/\alpha_{\mathrm{PDG}}^{-1}(\mu_Z))|$ (Table 77). Within the rational search domain $1 \le q \le 50$ for reduced rationals p/q, the fraction $3/13$ is the unique minimizer of $e(p/q) := |\log((p/q)/\sin^2\theta_{W,\mathrm{PDG}}(\mu_Z))|$ under the deterministic tie-break (q, p) (Table 78). Combining the two fixes yields $\alpha_w^{-1} = 3\pi^2$ and $\alpha_Y^{-1} = 10\pi^2$ by (80).

Proposition AF.17 (Integer and rational rigidity at the electroweak scale)**.** *Let* $\alpha_{\mathrm{PDG}}^{-1}(\mu_Z) \approx 127.955$ *and* $\sin^2\theta_{W,\mathrm{PDG}}(\mu_Z) \approx 0.23122$ *be the PDG reference values [2]. Within the finite*

domains $1 \le n \le 50$ *in the ansatz* $\alpha^{-1}(\mu_Z) = n\pi^2$ *and* $1 \le q \le 50$ *in reduced rationals* p/q *for* $\sin^2\theta_W(\mu_Z)$*, the unique choices are*

$$\alpha^{-1}(\mu_Z) = 13\pi^2, \qquad \sin^2\theta_W(\mu_Z) = \frac{3}{13},$$

and consequently $\alpha_w^{-1}(\mu_Z) = 3\pi^2$ *and* $\alpha_Y^{-1}(\mu_Z) = 10\pi^2$*.*

Proof. Finite exhaustive enumeration with deterministic tie-break rules; reproduced by `scripts/exp_ew_rigidity.py` and recorded in Tables 77 and 78. □

Remark AF.18 (One-loop scale shifts and additive mismatch)**.** *At one loop, gauge couplings run logarithmically: in a standard normalization one has an affine dependence*

$$\alpha^{-1}(\mu) = \alpha^{-1}(\mu_0) - \frac{b}{2\pi}\log\!\left(\frac{\mu}{\mu_0}\right) + \cdots,$$

where the coefficient b *is fixed by the charged field content and convention [1, 48]. Therefore an additive mismatch* $\Delta\alpha^{-1}$ *can be equivalently represented as a multiplicative scale ratio*

$$\frac{\mu_*}{\mu_0} = \exp\!\left(-\frac{2\pi}{b}\,\Delta\alpha^{-1}\right)$$

at fixed one-loop coefficient. This is the sense in which we interpret ppm- to per-mille-level deviations as matching-layer scale shifts rather than as "agreement within error bars" statements.

Remark AF.19 (RG flow expressed in the resolution coordinate)**.** *The paper uses the resolution coordinate* $r(\mu) = \log(\mu/m_e)/\log\varphi$*. Since* $\log\mu = \log m_e + r\log\varphi$*, derivatives convert as*

$$\frac{\mathrm{d}}{\mathrm{d}r} = (\log\varphi)\,\frac{\mathrm{d}}{\mathrm{d}\log\mu}.$$

Thus any standard renormalization-group equation $\mathrm{d}g/\mathrm{d}\log\mu = \beta(g)$ *becomes*

$$\frac{\mathrm{d}g}{\mathrm{d}r} = (\log\varphi)\,\beta(g).$$

In particular, the one-loop affine running of α^{-1} *in Remark AF.18 corresponds to a constant slope* $\mathrm{d}\alpha^{-1}/\mathrm{d}r = -(b\log\varphi)/(2\pi)$*. We use this only as a translation dictionary between standard scheme-dependent running and the protocol resolution language; the paper does not derive* β*-functions from the folding layer.*

A Fibonacci-scale interface remark. Using the one-loop scale-shift dictionary in Remark AF.18, the mismatch $13\pi^2 - \alpha_{\mathrm{PDG}}^{-1}(\mu_Z)$ can be phrased as a logarithmic scale ratio μ_*/μ_Z.

AF.3 A CP-odd phase space and the Jarlskog invariant

For quark mixing, a basis-independent measure of CP violation is the Jarlskog invariant J [45]. We record the resulting canonical closed value as a CAP-closed normalization dictionary.

Definition AF.20 (CP-odd phase space (CAP closure form))**.** *Within the primitive candidate set* $\mathfrak{P} = \{U(1), SU(2), SO(3), \mathbb{R}P^1\}$ *with canonical volumes (Lemma AF.6), define the CP-odd readout sector by*

$$\mathcal{M}_{\mathrm{CP}} \cong SO(3) \times SO(3) \times SO(3) \times \mathbb{R}P^1. \tag{84}$$

This choice is CAP-closed within the stated family by the volume-factorization rigidity in Proposition AF.24.

multiplicity rule	d_{CP}	$J = 1/(d_{\mathrm{CP}}\pi^7)$	$\log(J/J_{\mathrm{PDG}})$
$\dim(\mathfrak{su}(3)) + \dim(\mathfrak{su}(2))$	**11**	$3.009942547 \times 10^{-5}$	$+3.31 \times 10^{-3}$
$\dim(\mathfrak{su}(3)) + \dim(\mathfrak{su}(2)) + \dim(\mathfrak{u}(1))$	12	$2.759114001 \times 10^{-5}$	-8.37×10^{-2}
$\dim(\mathfrak{su}(3))$	8	$4.138671002 \times 10^{-5}$	$+3.22 \times 10^{-1}$
$\dim(\mathfrak{su}(2))$	3	$1.103645601 \times 10^{-4}$	$+1.30$
$\dim(\mathfrak{su}(3)) + \dim(\mathfrak{u}(1))$	9	$3.678818669 \times 10^{-5}$	$+2.04 \times 10^{-1}$
$\dim(\mathfrak{su}(2)) + \dim(\mathfrak{u}(1))$	4	$8.277342004 \times 10^{-5}$	$+1.01$

Table 81: Multiplicity baselines for the CP-odd normalization $J = 1/(d_{\mathrm{CP}}\pi^7)$ within the fixed primitive phase-space choice $\mathrm{Vol}(\mathcal{M}_{\mathrm{CP}}) = \pi^7$ (Lemma AF.22). The bold row is the paper's default $d_{\mathrm{CP}} = 8 + 3$; alternative rows are counterfactual multiplicity dictionaries. Rows are reproduced by the deterministic script `scripts/exp_aggregation_baselines.py`.

Remark AF.21 (Structure of $SO(3)^3 \times \mathbb{R}P^1$)**.** *In the PDG parameterization of a three-generation mixing matrix, the real mixing degrees of freedom can be organized as three independent rotations, while the physically relevant complex phase is defined only modulo rephasings and discrete identifications. The factor $SO(3)^3$ models the three rotation degrees of freedom, and the $\mathbb{R}P^1$ factor models a projective phase degree of freedom after the $\mathbb{Z}_2$ ray identification, consistent with expressing CP violation through rephasing-invariant quantities such as the Jarlskog invariant J [2, 45, 47].*

Lemma AF.22 (Canonical volume of $\mathcal{M}_{\mathrm{CP}}$)**.** *Under the canonical quotient metrics,* $\mathrm{Vol}(\mathcal{M}_{\mathrm{CP}}) = \pi^7$.

Proof. By Lemma AF.6, $\mathrm{Vol}(SO(3)) = \pi^2$ and $\mathrm{Vol}(\mathbb{R}P^1) = \pi$. Therefore $\mathrm{Vol}(\mathcal{M}_{\mathrm{CP}}) = (\pi^2)^3 \cdot \pi = \pi^7$. □

$$d_{\mathrm{CP}} := \dim(\mathfrak{su}(3)) + \dim(\mathfrak{su}(2)) = 8 + 3 = 11, \qquad J_{\mathrm{geo}} := \frac{1}{d_{\mathrm{CP}}\,\mathrm{Vol}(\mathcal{M}_{\mathrm{CP}})} = \frac{1}{11\pi^7}. \tag{85}$$

Remark AF.23 (Why the multiplicity excludes the abelian factor)**.** *The nontrivial CP-odd rephasing-invariant residue encoded by J is tied to genuinely non-abelian mixing structure in a three-generation setting [2, 45]. Accordingly, in the low-complexity multiplicity count we weight only the non-abelian gauge-sector dimensions 8 and 3; the abelian $U(1)$ factor is treated as part of the phase normalization already accounted for in the ray/projective quotient structure. Table 81 records a small baseline sweep over alternative multiplicity counts within the same π^7 phase-space normalization.*

Proposition AF.24 (Primitive factorization rigidity for the CP-odd phase space)**.** *Fix the primitive candidate set $\mathfrak{P} = \{U(1), SU(2), SO(3), \mathbb{R}P^1\}$ with canonical volumes as in Lemma AF.6. Among products of primitives with $\mathrm{Vol}(\mathcal{M}) = \pi^7$, the factorization is unique (up to ordering):*

$$\mathcal{M} \cong SO(3) \times SO(3) \times SO(3) \times \mathbb{R}P^1.$$

Proof. From Lemma AF.6, each primitive volume is one of 2π, $2\pi^2$, π^2, π. Any product therefore has the form $2^m\pi^k$ with $m \in \mathbb{Z}_{\geq 0}$. The constraint $\mathrm{Vol}(\mathcal{M}) = \pi^7$ forces $m = 0$, hence no factor can be $U(1)$ or $SU(2)$, and all factors must be chosen from $\{SO(3), \mathbb{R}P^1\}$. To achieve exponent 7 with $SO(3)$ contributing π^2 and $\mathbb{R}P^1$ contributing π, the only possibility is three $SO(3)$ factors and one $\mathbb{R}P^1$ factor. □

The interpretation compatible with the present protocol picture is that attempting to "pull back" CP (conjugation plus reflection) into a fixed readout protocol leaves an unavoidable residual geometric phase (holonomy), whose magnitude is controlled by a CP-odd phase-space volume and a discrete gauge-sector multiplicity.

Connection viewpoint. In the Standard Model, the CKM matrix is the unitary mixing matrix for quarks, with CP violation originating from an irreducible complex phase (three generations) [2, 122, 123]. The protocol picture naturally expresses such phases as holonomy data of a connection on a protocol parameter manifold. The CP-odd invariant is then a rephasing-invariant residue of holonomy, consistent with the volume/multiplicity expression (85).

PDG comparison and rigidity signal. PDG quotes $J_{\mathrm{PDG}} = (3.00 \pm 0.15) \times 10^{-5}$ [2]. The closed reference value (85) gives

$$J_{\mathrm{geo}} = \frac{1}{11\pi^7} \approx 3.009942547 \times 10^{-5}, \tag{86}$$

with relative deviation $\approx 3.31 \times 10^{-3}$ at the PDG central value. Numerically, $J_{\mathrm{geo}} - J_{\mathrm{PDG,central}} \approx 9.94 \times 10^{-8}$, corresponding to $\approx 6.6 \times 10^{-2}\sigma$ under the quoted PDG uncertainty. Moreover, within the bounded search domain $1 \le a \le 50$ and $1 \le n \le 20$ in the ansatz $J = 1/(a\pi^n)$, the pair $(a, n) = (11, 7)$ is uniquely selected by finite rigidity enumeration (Table 79).

Proposition AF.25 (Bounded-complexity rigidity for CKM CP violation)**.** *Let $J_{\mathrm{PDG}} = 3.00 \times 10^{-5}$ be the PDG central value [2]. Within the finite domain $1 \le a \le 50$ and $1 \le n \le 20$ in the ansatz $J = 1/(a\pi^n)$, the unique minimizer of the audit mismatch*

$$e(a, n) := \left| \log\left(\frac{1/(a\pi^n)}{J_{\mathrm{PDG}}} \right) \right|$$

under deterministic tie-break rules (minimize $a + n$, then lexicographic (a, n)) is $(a, n) = (11, 7)$, yielding $J_{\mathrm{geo}} = 1/(11\pi^7)$.

Proof. Finite exhaustive enumeration with deterministic tie-break rules; reproduced by `scripts/exp_jarlskog_pi_rigidity.py` and recorded in Table 79. □

AF.4 CKM mixing magnitudes as bounded-complexity depths

The protocol interface naturally expresses small dimensionless amplitudes in the golden resolution coordinate

$$r_{\mathrm{mix}}(x) := -\frac{\log x}{\log \varphi} \qquad (x > 0), \tag{87}$$

analogous to the mass-resolution coordinate used in Section 13. We test a minimal bounded-complexity closure for the three small CKM magnitudes $|V_{us}|$, $|V_{cb}|$, and $|V_{ub}|$ (PDG conventions) [2].

Candidate-family status (audit). [Audit]All "rigidity" and "uniqueness" statements in the mixing closures of this paper are conditional: they hold *within* the explicitly declared finite candidate family and complexity bound, with deterministic tie-break rules (Definition H.1). The candidate families used below are chosen to be protocol-native (normalization/equipartition and golden depth) and to remain discrete and auditable; alternative families are not excluded in principle and are treated, when needed, as counterfactual baselines in the audit tables (Appendix AE).

Forcing rationale (normalization and depth). In the protocol viewpoint, mixing magnitudes are overlap amplitudes between normalized readout modes. We restrict to a bounded candidate family fixed by two protocol-native mechanisms: (i) normalization/equipartition in an effective d-dimensional mixing subspace. For a Haar-uniform unitary matrix $U \in U(d)$ one has $\mathbb{E}|U_{ij}|^2 = 1/d$, so the minimal-description overlap scale is $|U_{ij}| \sim 1/\sqrt{d}$ [124, 125]. (ii) golden-branch depth costs produce exponentially small weights with base φ; taking square roots at the amplitude level yields half-depth factors $\varphi^{-k/2}$ (cf. the zeta/Abel pole-barrier scaling in Section 4.5). Accordingly, we treat CKM hierarchies as a bounded-complexity closure problem in discrete depth/normalization variables rather than as free continuous parameters.

Candidate family. Let $V_{\max} := \max_{w \in X_6} V(w) = 20$ at $(m, n) = (6, 3)$. We consider the bounded family

$$|V_{us}| = \frac{1}{\sqrt{d}}, \quad 1 \le d \le V_{\max}, \qquad |V_{cb}| = \varphi^{-k_{23}/2}, \quad |V_{ub}| = \varphi^{-k_{13}/2}, \qquad k_{23}, k_{13} \in \mathbb{N}, \tag{88}$$

and select coefficients by a bounded-complexity minimax search. Here d is a normalization-dimension parameter (unrelated to the fixed window length $m = 6$ used elsewhere in the paper).

Remark AF.26 (Why $d \le V_{\max}$ and why $k \le 2B$)**.** *The bound $d \le V_{\max}$ ties the normalization parameter to the intrinsic finite invariant range at $(m, n) = (6, 3)$: by Proposition 4.15, $V(w)$ takes exactly the values $\{0, \dots, V_{\max}\}$, so $V_{\max} = 20$ is a protocol-intrinsic integer cutoff available without importing external scales. For the depth exponents, the amplitudes are written in half-depth form $\varphi^{-k/2}$ (cf. (87)); therefore restricting k to a box of size $O(B)$ makes the exponent complexity comparable to the integer search radius B used for other closures. The choice $k \le 2B$ is a minimal symmetry between integer and half-integer depth budgets: it allows exponents up to depth B in the amplitude-squared scale, while keeping the candidate domain finite and auditable.*

Proposition AF.27 (Bounded-complexity rigidity for CKM magnitudes)**.** *Fix PDG reference magnitudes $|V_{us}|, |V_{cb}|, |V_{ub}|$ [2]. For each bound $B \in \{1, \dots, 20\}$, minimize the objective*

$$\max\Big\{ \big|\log(|V_{us}|_{\text{pred}}/|V_{us}|_{\text{PDG}})\big|,\ \big|\log(|V_{cb}|_{\text{pred}}/|V_{cb}|_{\text{PDG}})\big|,\ \big|\log(|V_{ub}|_{\text{pred}}/|V_{ub}|_{\text{PDG}})\big| \Big\},$$

over the finite domain $1 \le d \le \min(B, V_{\max})$ and $1 \le k_{23}, k_{13} \le 2B$, using lexicographic tie-break rules (sum error, then coefficient sum, then (d, k_{23}, k_{13})). At $B = 20$ the unique minimizer is

$$(d, k_{23}, k_{13}) = (20, 13, 23),$$

and, within the tested range $B = 1, \dots, 20$, the pair (k_{23}, k_{13}) stabilizes at $B = 12$ and remains constant for all B with $12 \le B \le 20$ (Table 82).

Proof. Finite exhaustive enumeration with deterministic tie-break rules; reproduced by the accompanying script. □

Remark AF.28 (Candidate-domain size)**.** *At bound B, the search domain has size*

$$|\Theta(B)| = \min(B, V_{\max}) \cdot (2B)^2.$$

At $B = 20$ and $V_{\max} = 20$, this is $|\Theta| = 20 \cdot 40^2 = 32000$ candidates.

Audit context. Candidate-domain size, best/second-best mismatch context, and distribution quantiles are recorded in Appendix AE (Tables 70–71). Counterfactual baseline comparisons are recorded in Table 74.

B	minimizer	max abs. log mismatch	sum abs. log mismatch
1	$(d, k_{23}, k_{13}) = (1, 2, 2)$	5.055363	9.234257
2	$(d, k_{23}, k_{13}) = (2, 4, 4)$	4.574151	7.925260
3	$(d, k_{23}, k_{13}) = (3, 6, 6)$	4.092939	6.760103
4	$(d, k_{23}, k_{13}) = (4, 8, 8)$	3.611727	5.653839
5	$(d, k_{23}, k_{13}) = (5, 10, 10)$	3.130515	4.579843
6	$(d, k_{23}, k_{13}) = (6, 12, 12)$	2.649304	3.526259
7	$(d, k_{23}, k_{13}) = (7, 13, 14)$	2.168092	2.727366
8	$(d, k_{23}, k_{13}) = (8, 13, 16)$	1.686880	2.179388
9	$(d, k_{23}, k_{13}) = (9, 13, 18)$	1.205668	1.639285
10	$(d, k_{23}, k_{13}) = (10, 13, 20)$	0.724456	1.105393
11	$(d, k_{23}, k_{13}) = (11, 13, 22)$	0.295823	0.576526
12	$(d, k_{23}, k_{13}) = (12, 13, 23)$	0.252318	0.292414
13	$(d, k_{23}, k_{13}) = (13, 13, 23)$	0.212296	0.252393
14	$(d, k_{23}, k_{13}) = (14, 13, 23)$	0.175242	0.215339
15	$(d, k_{23}, k_{13}) = (15, 13, 23)$	0.140746	0.180842
16	$(d, k_{23}, k_{13}) = (16, 13, 23)$	0.108476	0.148573
17	$(d, k_{23}, k_{13}) = (17, 13, 23)$	0.078164	0.118261
18	$(d, k_{23}, k_{13}) = (18, 13, 23)$	0.049585	0.089682
19	$(d, k_{23}, k_{13}) = (19, 13, 23)$	0.037458	0.062648
20	$(d, k_{23}, k_{13}) = (20, 13, 23)$	0.037458	0.043192

Table 82: Bounded-complexity minimax search for CKM magnitudes within the candidate family (88) at $(m, n) = (6, 3)$. Each row reports the unique minimizer in the domain $1 \le d \le \min(B, V_{\max})$ and $1 \le k_{23}, k_{13} \le 2B$ under the objective and tie-break rules of Proposition AF.27. Rows are reproduced by the deterministic script `scripts/exp_ckm_mixing_depth_rigidity.py`.

AF.5 CKM matrix closure from three magnitudes and a Jarlskog anchor

To turn the magnitude closure of Table 83 into a fully specified 3×3 mixing matrix, we use the PDG standard CKM parameterization by three angles and one CP phase [2]. In this convention,

$$|V_{ub}| = s_{13}, \qquad |V_{us}| = s_{12}c_{13}, \qquad |V_{cb}| = s_{23}c_{13},$$

and the Jarlskog invariant is

$$J = s_{12}s_{23}s_{13}c_{12}c_{23}c_{13}^2 \sin\delta.$$

We therefore (i) extract (s_{12}, s_{23}, s_{13}) from the magnitude triplet, (ii) solve for δ using a chosen J normalization, and (iii) reconstruct the full CKM matrix.

Reference reconstruction. To avoid mixing incompatible PDG conventions for different entries, we define a single "PDG reference reconstruction" by taking the PDG central values of $|V_{us}|$, $|V_{cb}|$, $|V_{ub}|$, and J used elsewhere in this paper, extracting $(s_{12}, s_{23}, s_{13}, \delta)$ via the above identities, and then generating all $|V_{ij}|$ from the PDG parameterization. The closed prediction uses the bounded-complexity minimizer for $(|V_{us}|, |V_{cb}|, |V_{ub}|)$ and the rigid J_{geo} value (85).

This section extends the bounded-complexity closure program to the lepton sector. We record a minimal, auditable closure for the PMNS mixing angles and provide a corresponding matrix reconstruction in the PDG standard parameterization. Majorana phases do not affect oscillation probabilities and are not constrained by this minimal closure, so we ignore them here [2].

parameter	PDG ref. value	predicted form	predicted value	r_{mix}	log(pred/ref)
$\lvert V_{us}\rvert$	0.2243	$1/\sqrt{20}$	0.223606798	3.113	-0.003095
$\lvert V_{cb}\rvert$	0.0422	$\varphi^{-13/2}$	0.0438107147	6.500	0.037458
$\lvert V_{ub}\rvert$	0.00394	$\varphi^{-23/2}$	0.00395040968	11.500	0.002639

Table 83: CKM-magnitude closure in the golden resolution coordinate (87) at $(m, n) = (6, 3)$, using the bounded-complexity minimizer at $B = 20$ in Proposition AF.27.

parameter	PDG recon. value	closed value	mismatch
s_{12}	0.224301741	0.223608543	-0.003095
s_{23}	0.0422003276	0.0438110566	0.037458
s_{13}	0.00394	0.00395040968	0.002639
δ [deg]	55.709284	53.010101	-2.699183
J	3×10^{-5}	3.00994×10^{-5}	0.003309

Table 84: Extraction of CKM angles and CP phase in the PDG standard parameterization from a magnitude triplet and a Jarlskog anchor. For s_{ij} and J the mismatch is log(closed/ref); for δ the mismatch is $\Delta\delta$ in degrees.

AF.6 PMNS angles as bounded-complexity amplitudes

We use the same golden resolution coordinate for dimensionless amplitudes as in (87):

$$r_{\mathrm{mix}}(x) := -\frac{\log x}{\log \varphi} \qquad (x > 0).$$

Candidate-family status (audit). [Audit]As in the CKM closure (Section AF.4), all "rigidity" and "uniqueness" statements below are conditional: they hold within the explicitly declared finite candidate family and bound, with deterministic tie-break rules (Definition H.1). The family is chosen to encode protocol-native motifs (normalization/equipartition and golden depth) while keeping the search space discrete, finite, and reproducible.

Forcing rationale (normalization and depth). As in the CKM closure of Section AF.4, we restrict to a bounded candidate family fixed by two protocol-native mechanisms: (i) normalization/equipartition at the amplitude level. For Haar-uniform unitary mixing in an effective d-dimensional subspace, $\mathbb{E}|U_{ij}|^2 = 1/d$, so the minimal-description overlap scale is $|U_{ij}| \sim 1/\sqrt{d}$ [124,125]. (ii) discrete golden-branch depth costs yield exponentially small weights with base φ; taking square roots at the amplitude level yields half-depth factors $\varphi^{-k/2}$. We treat the resulting PMNS hierarchies as a bounded-complexity closure problem rather than as free continuous inputs [2, 60]. For definiteness, the reference targets used by the accompanying scripts are taken as representative normal-ordering global-fit central values under the PDG convention [2, 60].

We define a simple candidate family for the three sines (s_{12}, s_{23}, s_{13}) of the PMNS mixing angles:

$$s_{12} = \sqrt{\frac{p_{12}}{q_{12}}}, \qquad s_{23} = \sqrt{\frac{p_{23}}{q_{23}}}, \qquad s_{13} = \varphi^{-k_{13}/2},$$

with a bounded-complexity box

$$1 \le q_{12}, q_{23} \le B, \qquad 1 \le p_{12} \le q_{12} - 1, \qquad 1 \le p_{23} \le q_{23} - 1,$$
$$\gcd(p_{ij}, q_{ij}) = 1, \qquad 1 \le k_{13} \le 2B,$$

element	PDG recon. $\lvert V_{ij}\rvert$	closed $\lvert V_{ij}\rvert$	log(closed/ref)
$\lvert V_{ud}\rvert$	0.974512179	0.974671429	0.000163
$\lvert V_{us}\rvert$	0.2243	0.223606798	-0.003095
$\lvert V_{ub}\rvert$	0.00394	0.00395040968	0.002639
$\lvert V_{cd}\rvert$	0.224193254	0.223495378	-0.003118
$\lvert V_{cs}\rvert$	0.9736306	0.973719897	0.000092
$\lvert V_{cb}\rvert$	0.0422	0.0438107147	0.037458
$\lvert V_{td}\rvert$	0.00796231328	0.00808837153	0.015708
$\lvert V_{ts}\rvert$	0.0416288982	0.0432384402	0.037935
$\lvert V_{tb}\rvert$	0.999101414	0.999032039	-0.000069

Table 85: Full CKM magnitude table induced by the magnitude closure and the Jarlskog anchor, compared to a PDG-consistent reference reconstruction (see text). Rows are reproduced by the deterministic script `scripts/exp_ckm_matrix_closure.py`.

unitarity check	PDG recon. value	closed value
row 1	-1.110e-16	-1.110e-16
row 2	+0.000e+00	-2.220e-16
row 3	+0.000e+00	+0.000e+00
col 1	-1.110e-16	-1.110e-16
col 2	+0.000e+00	-2.220e-16
col 3	+0.000e+00	+0.000e+00

Table 86: Row/column unitarity diagnostics: $\sum_j |V_{ij}|^2 - 1$ (rows) and $\sum_i |V_{ij}|^2 - 1$ (columns) for the reconstructed and closed CKM matrices.

and we select the unique minimizer by lexicographic minimization of the maximum absolute log mismatch and then the sum mismatch (as in Definition H.1).

Remark AF.29 (Why the PMNS candidate box uses reduced rationals and $k_{13} \le 2B$)**.** *The square-root rational forms $s = \sqrt{p/q}$ encode the normalization motif directly at the amplitude level while keeping the candidate family discrete and closed under bounded denominator. For the depth exponent, writing $s_{13} = \varphi^{-k_{13}/2}$ makes the half-depth structure explicit in the same r_{mix} coordinate as in the CKM closure. Bounding k_{13} by $2B$ keeps the half-depth exponent budget commensurate with the rational-denominator budget B without introducing higher-denominator freedom.*

Proposition AF.30 (Bounded-complexity rigidity for PMNS mixing sines)**.** *Fix representative global-fit reference values for (s_{12}, s_{23}, s_{13}) under PDG conventions [2, 60]. For each $B \in \{2, \dots, 20\}$, minimize the minimax log-mismatch objective over the candidate box described above, using the same deterministic tie-break rules as in Definition H.1. At $B = 20$ the unique minimizer is*

$$(p_{12}/q_{12}, p_{23}/q_{23}, k_{13}) = (4/13, 6/11, 8),$$

and, within the tested range $B = 2, \dots, 20$, the minimizer stabilizes at $B = 13$ and remains constant for all B with $13 \le B \le 20$ (Table 87).

Proof. Finite exhaustive enumeration with deterministic tie-break rules; reproduced by the accompanying script. □

B	minimizer	max abs. log mismatch	sum abs. log mismatch
2	$(p_{12}/q_{12}, p_{23}/q_{23}, k_{13}) = (1/2, 1/2, 4)$	0.950499	1.237468
3	$(p_{12}/q_{12}, p_{23}/q_{23}, k_{13}) = (1/3, 1/2, 6)$	0.469287	0.553524
4	$(p_{12}/q_{12}, p_{23}/q_{23}, k_{13}) = (1/3, 1/2, 8)$	0.043089	0.096161
5	$(p_{12}/q_{12}, p_{23}/q_{23}, k_{13}) = (1/3, 1/2, 8)$	0.043089	0.096161
6	$(p_{12}/q_{12}, p_{23}/q_{23}, k_{13}) = (1/3, 1/2, 8)$	0.043089	0.096161
7	$(p_{12}/q_{12}, p_{23}/q_{23}, k_{13}) = (2/7, 4/7, 8)$	0.035928	0.071529
8	$(p_{12}/q_{12}, p_{23}/q_{23}, k_{13}) = (2/7, 4/7, 8)$	0.035928	0.071529
9	$(p_{12}/q_{12}, p_{23}/q_{23}, k_{13}) = (2/7, 5/9, 8)$	0.035928	0.057444
10	$(p_{12}/q_{12}, p_{23}/q_{23}, k_{13}) = (3/10, 5/9, 8)$	0.011925	0.033049
11	$(p_{12}/q_{12}, p_{23}/q_{23}, k_{13}) = (3/10, 6/11, 8)$	0.011925	0.023874
12	$(p_{12}/q_{12}, p_{23}/q_{23}, k_{13}) = (3/10, 6/11, 8)$	0.011925	0.023874
13	$(p_{12}/q_{12}, p_{23}/q_{23}, k_{13}) = (4/13, 6/11, 8)$	0.011925	0.013468
14	$(p_{12}/q_{12}, p_{23}/q_{23}, k_{13}) = (4/13, 6/11, 8)$	0.011925	0.013468
15	$(p_{12}/q_{12}, p_{23}/q_{23}, k_{13}) = (4/13, 6/11, 8)$	0.011925	0.013468
16	$(p_{12}/q_{12}, p_{23}/q_{23}, k_{13}) = (4/13, 6/11, 8)$	0.011925	0.013468
17	$(p_{12}/q_{12}, p_{23}/q_{23}, k_{13}) = (4/13, 6/11, 8)$	0.011925	0.013468
18	$(p_{12}/q_{12}, p_{23}/q_{23}, k_{13}) = (4/13, 6/11, 8)$	0.011925	0.013468
19	$(p_{12}/q_{12}, p_{23}/q_{23}, k_{13}) = (4/13, 6/11, 8)$	0.011925	0.013468
20	$(p_{12}/q_{12}, p_{23}/q_{23}, k_{13}) = (4/13, 6/11, 8)$	0.011925	0.013468

Table 87: Bounded-complexity minimax search for PMNS mixing sines in the candidate family described in the text. Rows are reproduced by the deterministic script `scripts/exp_pmns_mixing_depth_rigidity.py`. Reference targets use representative global-fit central values under PDG conventions [2, 60].

Remark AF.31 (Candidate-domain size)**.** *Let $R(B)$ be the set of reduced fractions p/q with $1 \le q \le B$, $1 \le p \le q-1$, and $\gcd(p,q) = 1$. Then $|R(B)| = \sum_{q=2}^{B} \varphi_E(q)$, where φ_E is Euler's totient function [27]. The PMNS candidate box has size*

$$|\Theta(B)| = |R(B)|^2 \cdot (2B),$$

corresponding to independent choices for (p_{12}/q_{12}), (p_{23}/q_{23}), and $k_{13} \in \{1, \dots, 2B\}$. At $B = 20$, one has $|R(20)| = 127$ and therefore $|\Theta(20)| = 127^2 \cdot 40 = 645160$.

Normal vs. inverted ordering (NO/IO) diagnostic. The PMNS closure above uses representative normal-ordering (NO) reference targets. To assess sensitivity to the ordering choice, we repeat the same bounded-complexity closure against a representative inverted-ordering (IO) target triple and record the selected minimizers and mismatch metrics. This diagnostic is not used as a premise; it is included only as an auditable robustness check.

Audit context. Candidate-domain size, best/second-best mismatch context, and distribution quantiles for the PMNS-sine closure (and the bounded-denominator δ closure below) are recorded in Appendix AE (Tables 70–71); uncertainty-robustness stress tests are recorded in Table 72, and counterfactual baseline comparisons in Table 74.

AF.7 Matrix reconstruction and a discrete CP-phase closure

To reconstruct a full 3×3 mixing matrix, we use the PDG standard parameterization (three angles plus one Dirac CP phase) [2]. We compare a single reference reconstruction (from repre-

parameter	reference	predicted form	predicted value	r_{mix}	log(pred/ref)
s_{12}	0.554076	$\sqrt{4/13}$	0.554700196	1.225	0.001126
s_{23}	0.738241	$\sqrt{6/11}$	0.738548946	0.630	0.000417
s_{13}	0.147648	$\varphi^{-8/2}$	0.145898034	4.000	-0.011925

Table 88: PMNS mixing-angle closure in the golden resolution coordinate at $(m, n) = (6, 3)$, using the bounded-complexity minimizer at $B = 20$. Rows are reproduced by the deterministic script `scripts/exp_pmns_mixing_depth_rigidity.py`.

ordering	$(\sin^2\theta_{12}, \sin^2\theta_{23}, \sin^2\theta_{13})_{\mathrm{ref}}$	minimizer $(p_{12}/q_{12}, p_{23}/q_{23}, k_{13})$	max abs. log mismatch	δ minimizer $(Q = 12)$	$E_\infty(\lvert U\rvert)$
NO	$(0.307, 0.545, 0.0218)$	$(4/13, 6/11, 8)$	0.0119	$\delta = 13\pi/12$ [195.0°]	0.012
IO	$(0.307, 0.551, 0.0220)$	$(4/13, 11/20, 8)$	0.0165	$\delta = 13\pi/12$ [195.0°]	0.016

Table 89: NO/IO robustness diagnostic for the PMNS closures at $(m, n) = (6, 3)$: we rerun the bounded-complexity minimizers at $B = 20$ (angles) and $Q = 12$ (phase) against representative normal- and inverted-ordering reference targets (PDG conventions). Rows are reproduced by the deterministic script `scripts/exp_pmns_no_io_stability.py`.

sentative global-fit central values) to a closed prediction obtained from the bounded-complexity angle minimizer together with a discrete protocol-level closure for the Dirac phase δ [60]. Because the PMNS *magnitudes* depend on $\cos\delta$ while the CP-odd invariant depends on $\sin\delta$, we use a bounded-denominator rational-angle candidate family

$$\delta = \frac{k\pi}{q}, \qquad 1 \le q \le Q, \qquad 1 \le k \le 2q - 1, \qquad \gcd(k, q) = 1,$$

and we select a unique minimizer by a CP-odd anchor rule: first require $\mathrm{sgn}(J_\ell) = \mathrm{sgn}(\chi)$ as the chirality-anchored CP-sign convention (Definition 7.7), then minimize the mismatch $|\log(|J_\ell|/|J_{\ell,\mathrm{ref}}|)|$, and finally break the remaining $\delta \leftrightarrow \pi - \delta$ quadrant ambiguity (since magnitudes depend on $\cos\delta$) by minimizing the maximum absolute log mismatch of the induced PMNS magnitudes $|U_{ij}|$ against the same reference reconstruction. Ties are broken by bounded-complexity order (q, k). Table 90 records the resulting bounded-denominator sweep $Q = 1, \ldots, 12$ and the stabilized minimizer.

Remark AF.32 (Status of the CP-sign anchor in the PMNS closure)**.** *The chirality-anchored sign rule fixes a deterministic convention for selecting a quadrant of δ within a finite rational candidate family. It does not introduce additional continuous freedom, and it is not used to tune the angle magnitudes: the angle minimizer is selected independently by Proposition AF.30, while the sign anchor only resolves the remaining $\delta \leftrightarrow \pi - \delta$ ambiguity in a protocol-consistent way (Remark 7.8).*

AG Mass-depth rigidity audits and matching-layer details (supplement)

This appendix collects audit tables and matching-layer bookkeeping details that support the mass-spectrum closure of Section 13. The main text records the closed template and the spectrum table; the material below provides bounded-complexity evidence and quantized matching summaries.

Q	minimizer	δ [deg]	$\mathrm{sgn}(J_\ell)$ vs. $\mathrm{sgn}(\chi)$	$E_\infty(\lvert U\rvert)$	J_ℓ (closed)	$\lvert\log(\lvert J_\ell\rvert/\lvert J_{\ell,\mathrm{ref}}\rvert)\rvert$
1	$\delta = 1\pi/1$	180.0	FLIP	0.012	+4.01876e-18	35.298
2	$\delta = 3\pi/2$	270.0	OK	0.292	-0.0328156	1.341
3	$\delta = 4\pi/3$	240.0	OK	0.164	-0.0284192	1.197
4	$\delta = 5\pi/4$	225.0	OK	0.099	-0.0232042	0.994
5	$\delta = 6\pi/5$	216.0	OK	0.064	-0.0192886	0.809
6	$\delta = 7\pi/6$	210.0	OK	0.043	-0.0164078	0.648
7	$\delta = 8\pi/7$	205.7	OK	0.030	-0.0142382	0.506
8	$\delta = 9\pi/8$	202.5	OK	0.021	-0.012558	0.380
9	$\delta = 10\pi/9$	200.0	OK	0.015	-0.0112236	0.268
10	$\delta = 11\pi/10$	198.0	OK	0.012	-0.0101406	0.166
11	$\delta = 12\pi/11$	196.4	OK	0.012	-0.00924524	0.074
12	$\delta = 13\pi/12$	195.0	OK	0.012	-0.00849331	0.011

Table 90: Bounded-denominator closure for the PMNS Dirac phase δ using a chirality-anchored CP-sign convention (Definition 7.7) and a deterministic bounded-complexity tie-break. Here $E_\infty(|U|) := \max_{i,j} |\log(|U_{ij}|_{\mathrm{closed}}/|U_{ij}|_{\mathrm{ref}})||$ is the max abs. log mismatch of the induced PMNS magnitudes against the reference reconstruction. Rows are reproduced by the deterministic script `scripts/exp_pmns_matrix_closure.py`.

parameter	reference value	closed value	mismatch
s_{12}	0.554075807	0.554700196	0.001126
s_{23}	0.738241153	0.738548946	0.000417
s_{13}	0.147648231	0.145898034	-0.011925
δ [deg]	195.000000	195.000000	0.000000
J_ℓ	-0.00858602	-0.00849331	-0.010856

Table 91: PMNS angle/phase extraction and the induced leptonic Jarlskog invariant J_ℓ under the chosen conventions. Rows are reproduced by the deterministic script `scripts/exp_pmns_matrix_closure.py`.

Audit note (finite exhaustive searches). Whenever this appendix reports a rigidity "winner" inside a bounded coefficient box, it is obtained by an exhaustive enumeration over that finite integer domain with deterministic tie-break rules (as stated near each table). The scripts referenced in captions reproduce these finite enumerations and write LaTeX fragments.

AG.1 Rigidity of the depth formula at bounded coefficient complexity

To make the integer depth assignment auditable as a low-complexity closure, we test a bounded-coefficient ansatz for the depth map. Write the stable-type differences relative to the electron reference w_e as

$$\Delta V := V(w) - V(w_e), \qquad \Delta g := g(w) - g(w_e), \qquad \Delta|w|_1 := |w|_1 - |w_e|_1.$$

Consider the integer ansatz

$$\widehat{r}(w) = a\,\Delta V + b\,\Delta g + c\,\Delta|w|_1, \qquad a, b, c \in \mathbb{Z}, \tag{89}$$

and measure its mismatch on the scheme-stable charged-lepton anchor set $\{\mu, \tau\}$ by the depth deviation in the resolution coordinate $r(\mu)$. As a diagnostic, we also record the same metrics on

element	reference $\lvert U_{ij}\rvert$	closed $\lvert U_{ij}\rvert$	log(closed/ref)
$\lvert U_{e1}\rvert$	0.823342335	0.823147051	-0.000237
$\lvert U_{e2}\rvert$	0.548003102	0.548764701	0.001389
$\lvert U_{e3}\rvert$	0.147648231	0.145898034	-0.011925
$\lvert U_{\mu 1}\rvert$	0.287059885	0.28831328	0.004357
$\lvert U_{\mu 2}\rvert$	0.620062595	0.618895453	-0.001884
$\lvert U_{\mu 3}\rvert$	0.730149985	0.730646201	0.000679
$\lvert U_{\tau 1}\rvert$	0.489595774	0.489187475	-0.000834
$\lvert U_{\tau 2}\rvert$	0.561440093	0.561983738	0.000968
$\lvert U_{\tau 3}\rvert$	0.667143913	0.666985676	-0.000237

Table 92: PMNS magnitude table induced by the bounded-complexity angle closure and the discrete phase choice. Rows are reproduced by the deterministic script `scripts/exp_pmns_matrix_closure.py`.

unitarity check	reference value	closed value
row 1	+0.000e+00	+2.220e-16
row 2	-1.110e-16	+2.220e-16
row 3	+0.000e+00	+2.220e-16
col 1	+0.000e+00	+2.220e-16
col 2	+0.000e+00	+2.220e-16
col 3	-1.110e-16	+0.000e+00

Table 93: Row/column unitarity diagnostics: $\sum_j |U_{ij}|^2 - 1$ (rows) and $\sum_i |U_{ij}|^2 - 1$ (columns) for the reconstructed and closed PMNS matrices.

an extended fermion set including quark reference masses (scheme-dependent by convention). Table 94 records the selected minimizers in the coefficient box $|a|, |b|, |c| \le B$ for $B = 1, \dots, 20$ under a lexicographic minimization rule: first minimize the leptonic minimax deviation, then the leptonic sum deviation, then the extended-set minimax and sum deviations, and finally coefficient complexity.

Proposition AG.1 (Rigidity of the $(2, 5, 1)$ coefficients at bounded complexity)**.** *In the bounded search domain $|a|, |b|, |c| \le 20$, the unique minimizer of the leptonic objective (as defined above) satisfies*

$$(a, b, c) = (2, 5, 1).$$

Moreover, within the tested range $B = 1, \dots, 20$, the minimizer stabilizes at $B = 5$ and remains constant for all B with $5 \le B \le 20$.

Proof. This is a finite exhaustive enumeration over integer triples in the stated box with deterministic tie-break rules; the resulting minimizers are listed in Table 94 and reproduced by the accompanying script. □

Leave-one-out stability of the coefficient choice. As an additional audit, we repeat the $B = 20$ coefficient search while leaving out one anchor at a time from the finite anchor set $\{u, d, s, c, b, t, \mu, \tau\}$ used by the rigidity script, and record whether the selected minimizer changes under the same lexicographic objective. Table 95 reports the resulting leave-one-out sweep.

B	(a,b,c)	$\max_{\mu,\tau}$	$\mathrm{sum}_{\mu,\tau}$	$\max_{\mathrm{ext}}$	$\mathrm{sum}_{\mathrm{ext}}$
1	$(1,-1,1)$	5.079526	6.024227	10.246816	24.792808
2	$(2,2,-2)$	3.079526	6.134824	7.277571	31.990963
3	$(2,3,-1)$	2.079526	4.134824	6.277571	25.990963
4	$(2,4,0)$	1.079526	2.134824	5.277571	19.990963
5	$(2,5,1)$	0.079526	0.134824	4.277571	14.795234
6	$(2,5,1)$	0.079526	0.134824	4.277571	14.795234
7	$(2,5,1)$	0.079526	0.134824	4.277571	14.795234
8	$(2,5,1)$	0.079526	0.134824	4.277571	14.795234
9	$(2,5,1)$	0.079526	0.134824	4.277571	14.795234
10	$(2,5,1)$	0.079526	0.134824	4.277571	14.795234
11	$(2,5,1)$	0.079526	0.134824	4.277571	14.795234
12	$(2,5,1)$	0.079526	0.134824	4.277571	14.795234
13	$(2,5,1)$	0.079526	0.134824	4.277571	14.795234
14	$(2,5,1)$	0.079526	0.134824	4.277571	14.795234
15	$(2,5,1)$	0.079526	0.134824	4.277571	14.795234
16	$(2,5,1)$	0.079526	0.134824	4.277571	14.795234
17	$(2,5,1)$	0.079526	0.134824	4.277571	14.795234
18	$(2,5,1)$	0.079526	0.134824	4.277571	14.795234
19	$(2,5,1)$	0.079526	0.134824	4.277571	14.795234
20	$(2,5,1)$	0.079526	0.134824	4.277571	14.795234

Table 94: Bounded-coefficient rigidity search for the depth ansatz (89) over $B = 1, \ldots, 20$. The primary anchor set is $\{\mu, \tau\}$; the extended set includes quark reference masses as a diagnostic. Rows are generated by `scripts/exp_mass_depth_rigidity.py`.

Audit context. Candidate-domain size, best/second-best mismatch context, and distribution quantiles for the mass-depth closure are recorded in Appendix AE (Tables 70–71); uncertainty-robustness stress tests are recorded in Table 72, and counterfactual baseline comparisons in Table 74.

AG.2 A minimal matching layer: quantized depth shifts

In effective field theory, scheme and threshold conventions enter as multiplicative matching factors. In the resolution coordinate, a matching factor is an additive shift: if μ_{ref} is a reference mass and μ_{pred} is a closed template value, then

$$\Delta r := r(\mu_{\mathrm{ref}}) - \widehat{r} = \log_{\varphi}\left(\frac{\mu_{\mathrm{ref}}}{\mu_{\mathrm{pred}}}\right), \qquad \frac{\mu_{\mathrm{ref}}}{\mu_{\mathrm{pred}}} = \varphi^{\Delta r}.$$

To make the matching layer auditable at bounded complexity, we record a minimal dyadic quantization convention: matching shifts are summarized on the quarter-depth lattice $\Delta r \approx k/4$. Table 97 reports Δr, the nearest $k/4$, the residual $\Delta r - k/4$, and the implied quantized matching factor $\varphi^{k/4}$. Table 98 summarizes the residual sizes across the same rows. This does not change the closed depth formula; it makes the scheme/matching correction explicit in the same discrete language as the rest of the paper.

Remark AG.2 (Why a quarter-depth lattice is the minimal dyadic choice)**.** *Two structural features of the present paper single out dyadic denominators as the protocol-native low-complexity family for matching-layer summaries. First, phases are treated as dyadic registers $\mathbb{Z}_{2^p}$ and the*

leave-out	(a,b,c)	$\max_{\mu,\tau}$	$\mathrm{sum}_{\mu,\tau}$	$\max_{\mathrm{ext}}$	$\mathrm{sum}_{\mathrm{ext}}$	status
`none`	$(2,5,1)$	0.079526	0.134824	4.277571	14.795234	SAME
`-u`	$(2,5,1)$	0.079526	0.134824	4.277571	11.790788	SAME
`-d`	$(2,5,1)$	0.079526	0.134824	4.277571	14.393098	SAME
`-s`	$(2,5,1)$	0.079526	0.134824	4.277571	13.609571	SAME
`-c`	$(1,1,6)$	0.079526	0.134824	3.402135	8.177093	DIFF
`-b`	$(2,5,1)$	0.079526	0.134824	4.246816	10.517663	SAME
`-t`	$(2,5,1)$	0.079526	0.134824	4.277571	13.251455	SAME
`-mu`	$(2,5,1)$	0.055298	0.055298	4.277571	14.715708	SAME
`-tau`	$(2,6,1)$	0.079526	0.079526	4.246816	11.281053	DIFF

Table 95: Leave-one-out robustness diagnostic for the depth-coefficient search at $B = 20$. Each row removes one anchor from the finite anchor set and recomputes the selected minimizer under the same lexicographic objective as in Table 94. Rows are generated by `scripts/exp_mass_depth_leave_one_out.py`.

tested leave-outs	SAME	DIFF	fraction SAME	DIFF cases
8	6	2	`-c`, `-tau`	

Table 96: Compact summary of the leave-one-out robustness sweep in Table 95. The baseline is $(a,b,c) = (2,5,1)$ at $B = 20$ (Proposition AG.1). Rows are generated by `scripts/exp_mass_depth_leave_one_out.py`.

holonomy diagnostics treat denominators of the form denom $= 2^p$ *in CAP audit form (Remark 6.11); thus dyadic refinement is the protocol-native notion of "one more bit" of resolution. Second, several candidate families used for mixing amplitudes are square-root structured (e.g.* $\varphi^{-k/2}$ *and* $1/\sqrt{d}$ *in* (88) *and the analogous PMNS family), so half-depth exponents appear already at the amplitude level. When such half-depth normalizations are composed with a logarithmic matching dictionary (as in* (19)*), quarter-depth steps arise as the smallest dyadic lattice that can express the resulting corrections without introducing higher-denominator freedom. Accordingly,* $k/4$ *is used here as the* minimal *dyadic reporting lattice; finer dyadic lattices* $k/2^s$ *(*$s > 2$*) can be adopted at higher complexity if one wishes to audit smaller residual structure. We emphasize that we do not optimize the lattice denominator in this paper:* $1/4$ *is chosen as the minimal dyadic reporting convention, and the residuals in Tables 97–98 make the remaining mismatch explicit.*

AH Scalar-sector interface audits (supplement)

This appendix records scalar-sector interface audits used as supporting certificates for the main-text scalar-sector closure statements (Section 8.4).

Audit note (bounded families and deterministic tie-breaks). All scalar-sector "rigidity" statements in this appendix are formulated as deterministic selections from explicit bounded rational/integer candidate families, with a fully specified tie-break rule. The accompanying scripts reproduce the same finite sweeps and write LaTeX fragments; they are not additional premises beyond the stated bounded families and tie-breaks.

field	$r(\mu)$	$\widehat{r}$	Δr	nearest	residual	$\varphi^{k/4}$
e	0.000	0	+0.000	0/4	+0.000	1
μ	11.080	11	+0.080	0/4	+0.080	1
τ	16.945	17	-0.055	0/4	-0.055	1
u	2.996	6	-3.004	−12/4	-0.004	0.236068
d	4.598	5	-0.402	−2/4	+0.098	0.786151
s	10.814	12	-1.186	−5/4	+0.064	0.547981
c	16.247	12	+4.247	17/4	-0.003	7.73032
b	18.722	23	-4.278	−17/4	-0.028	0.129361
t	26.456	28	-1.544	−6/4	-0.044	0.485868
W	24.866	25	-0.134	−1/4	+0.116	0.886652
Z	25.128	25	+0.128	1/4	-0.122	1.12784
H	25.788	26	-0.212	−1/4	+0.038	0.886652

Table 97: Minimal matching-layer summary in the resolution coordinate. The "nearest" column reports the closest quarter-step $k/4$ to the observed Δr. Rows are generated by `scripts/exp_mass_matching_layer.py`.

statistic	value
entries	12
median $\lvert\Delta r - k/4\rvert$	0.050
p90 $\lvert\Delta r - k/4\rvert$	0.116
max $\lvert\Delta r - k/4\rvert$	0.122
$N_{\lvert\cdot\rvert\le 0.01}$	3
$N_{\lvert\cdot\rvert\le 0.05}$	6

Table 98: Residual-size summary for the quarter-step matching lattice in Table 97. Rows are generated by `scripts/exp_mass_matching_layer.py`.

AH.1 Higgs–Z depth-offset rigidity at bounded denominator

Proposition AH.1 (Higgs–Z depth-offset rigidity at bounded denominator)**.** *Let m_Z and m_H denote the PDG reference masses used elsewhere in this paper (Table 18). Define the resolution-depth offset*

$$\Delta r_{HZ} := \log_\varphi\left(\frac{m_H}{m_Z}\right).$$

Within the bounded candidate family of reduced rationals $\Delta r = p/q$ with $1 \le q \le 20$ and $0 \le p \le q$, selecting the unique minimizer of the absolute log mismatch

$$e(p/q) := \left|\log\left(\frac{m_Z\,\varphi^{p/q}}{m_H}\right)\right|$$

by deterministic tie-break rules yields the stabilized minimizer $\Delta r = 2/3$ (Table 99). Concretely, we minimize e and then break ties by choosing the smallest denominator q and then the smallest numerator p (equivalently: lexicographic minimization of (e, q, p)), matching the generator script `scripts/exp_higgs_z_offset_rigidity.py`. Equivalently, the Higgs scale is captured at low complexity by the closed relation

$$m_H \approx m_Z\,\varphi^{2/3}.$$

Q	minimizer	Δr	$m_Z\,\varphi^{\Delta r}$ [GeV]	$\log(\text{pred}/m_H)$	$\lvert\cdot\rvert$
1	$\Delta r = 1/1$	1.000000	147.545	+0.163819	0.163819
2	$\Delta r = 1/2$	0.500000	115.992	-0.076787	0.076787
3	$\Delta r = 2/3$	**0.666667**	**125.678**	**+0.003415**	**0.003415**
4	$\Delta r = 2/3$	0.666667	125.678	+0.003415	0.003415
5	$\Delta r = 2/3$	0.666667	125.678	+0.003415	0.003415
6	$\Delta r = 2/3$	0.666667	125.678	+0.003415	0.003415
7	$\Delta r = 2/3$	0.666667	125.678	+0.003415	0.003415
8	$\Delta r = 2/3$	0.666667	125.678	+0.003415	0.003415
9	$\Delta r = 2/3$	0.666667	125.678	+0.003415	0.003415
10	$\Delta r = 2/3$	0.666667	125.678	+0.003415	0.003415
11	$\Delta r = 2/3$	0.666667	125.678	+0.003415	0.003415
12	$\Delta r = 2/3$	0.666667	125.678	+0.003415	0.003415
13	$\Delta r = 2/3$	0.666667	125.678	+0.003415	0.003415
14	$\Delta r = 2/3$	0.666667	125.678	+0.003415	0.003415
15	$\Delta r = 2/3$	0.666667	125.678	+0.003415	0.003415
16	$\Delta r = 2/3$	0.666667	125.678	+0.003415	0.003415
17	$\Delta r = 2/3$	0.666667	125.678	+0.003415	0.003415
18	$\Delta r = 2/3$	0.666667	125.678	+0.003415	0.003415
19	$\Delta r = 2/3$	0.666667	125.678	+0.003415	0.003415
20	$\Delta r = 2/3$	0.666667	125.678	+0.003415	0.003415

Table 99: Bounded-denominator rigidity sweep for the Higgs–Z depth offset in the φ-resolution coordinate: for each Q we minimize $e(p/q) = |\log((m_Z\varphi^{p/q})/m_H)|$ over reduced rationals p/q with $1 \le q \le Q$ and deterministic tie-break rules. Rows are generated by `scripts/exp_higgs_z_offset_rigidity.py`.

AH.2 A minimal parity contrast by coarse graining at the anchor

AI Gauge-factor complexity-label sensitivity (supplement)

Proposition 8.2 closes the non-abelian gauge factors by CAP within an explicit compact-factor candidate family. One audit concern is whether the output depends on a particular choice of "intrinsic complexity label" (e.g. using $\dim(\mathfrak{g})$ rather than rank or representation size). This appendix (i) records a bounded sensitivity sweep across several natural discrete complexity labels and (ii) notes a short theorem-level reason why the same minimizer persists for these labels.

AI.1 Candidate family and selection rule

We enumerate compact, connected, non-abelian simple Lie groups through their Lie algebras within a bounded audit window, using the classical families together with low-dimensional exceptional cases. Within this finite list, we select a pair (G_2, G_3) of non-isomorphic simple factors by the same CAP form used in Proposition 8.2: choose the lexicographically minimal pair under a given factor complexity label, with a deterministic tie-break that refines by $(\dim, \text{rank}, \text{name})$.

We compare the following factor labels:

- $\dim(\mathfrak{g})$ (dimension-as-complexity, used in the main text);
- $\text{rank}(\mathfrak{g})$;
- $\dim(\mathfrak{g}) + \text{rank}(\mathfrak{g})$;
- $d_{\min}$, the minimal dimension of a faithful complex representation (up to finite quotients).

Rows are generated by `scripts/exp_gauge_complexity_sensitivity.py`. This script performs the stated bounded enumeration inside the declared audit window and writes the resulting

observable	canonical	reflected
χ (chirality index)	-2	2
$\overline{\lvert w\rvert_1}^{(2\times 2)}$	$\mu = 1.671875,\ \mathrm{Var} = 0.177490$	$\mu = 1.671875,\ \mathrm{Var} = 0.177490$
$\overline{V(w)}^{(2\times 2)}$	$\mu = 8.343750,\ \mathrm{Var} = 21.967773$	$\mu = 8.343750,\ \mathrm{Var} = 21.967773$
$\overline{D_\pi(w)}^{(2\times 2)}$	$\mu = 0.093750,\ \mathrm{Var} = 0.030273$	$\mu = 0.093750,\ \mathrm{Var} = 0.030273$

Table 100: A minimal parity contrast at $(m, n) = (6, 3)$ on the $n = 3$ Hilbert grid: the chirality index χ flips sign under reflection (parity-odd), while coarse-grained scalar summaries built from intrinsic stable-type functionals are invariant under reflection up to pullback (parity-even). Rows are generated by `scripts/exp_scalar_coarse_grain.py`.

LaTeX fragment; it does not introduce additional modeling freedom beyond the finite list and tie-break rule described above.

factor complexity label	CAP-minimizer (G_2, G_3)	key (k_2, k_3)	tie-break / notes
$\dim(\mathfrak{g})$	$SU(2)$, $SU(3)$	$(3, 8)$	lex by (dim, rank, name)
$\mathrm{rank}(\mathfrak{g})$	$SU(2)$, $SU(3)$	$(1, 2)$	lex by (rank, dim, name)
$\dim(\mathfrak{g}) + \mathrm{rank}(\mathfrak{g})$	$SU(2)$, $SU(3)$	$(4, 10)$	lex by (dim+rank, dim, name)
$d_{\min}$	$SU(2)$, $SU(3)$	$(2, 3)$	lex by (d_min, dim, name)

Table 101: Sensitivity of the CAP-minimal two-factor non-abelian closure across several discrete complexity labels, within the bounded audit window described above. In all rows, k_i denotes the label value of the selected factor G_i. The main text uses $\dim(\mathfrak{g})$ as the factor label; this appendix records that the same minimizer persists under alternative labels in the tested window.

AI.2 A short robustness proof for common labels

Proposition AI.1 (Robustness of the $SU(2) \times SU(3)$ minimizer across common labels)**.** *Consider the CAP selection rule in Proposition 8.2, but replace the primary factor label* $\dim(\mathfrak{g})$ *by any one of the following labels on compact simple Lie algebras:*

$$k \in \Big\{\dim(\mathfrak{g}),\ \mathrm{rank}(\mathfrak{g}),\ \dim(\mathfrak{g}) + \mathrm{rank}(\mathfrak{g}),\ d_{\min}\Big\},$$

where $d_{\min}$ *denotes the minimal dimension of a nontrivial complex representation of* $\mathfrak{g}$ *(equivalently: a faithful complex representation, since* $\mathfrak{g}$ *is simple). Assume the same deterministic tie-break refinement used in the sweep (refining by* $(\dim, \mathrm{rank}, \mathit{name})$*). Then the unique lexicographic minimizer of* $(k(\mathfrak{g}_2), k(\mathfrak{g}_3))$ *over pairs of non-isomorphic compact simple factors is* $(\mathfrak{su}(2), \mathfrak{su}(3))$*.*

Proof. **(1) First factor is always** $\mathfrak{su}(2)$**.** Among non-abelian compact simple Lie algebras, the minimal possible values of

$$\dim(\mathfrak{g}), \qquad \mathrm{rank}(\mathfrak{g}), \qquad d_{\min}(\mathfrak{g})$$

are attained uniquely at $\mathfrak{su}(2)$:

- $\dim(\mathfrak{g}) \geq 3$ with equality iff $\mathfrak{g} \cong \mathfrak{su}(2)$ (Lemma 9.4);
- $\mathrm{rank}(\mathfrak{g}) \geq 1$ with equality iff $\mathfrak{g} \cong \mathfrak{su}(2)$ (classification: rank-1 simple is A_1; see, e.g., [18]);
- $d_{\min}(\mathfrak{g}) \geq 2$ with equality iff $\mathfrak{g} \cong \mathfrak{su}(2)$ (the fundamental 2-dimensional representation of A_1; see, e.g., [55]).

Therefore, regardless of whether k is dim, rank, dim +rank, or $d_{\min}$, the lexicographically minimal first factor is $\mathfrak{su}(2)$.

(2) Second factor is always $\mathfrak{su}(3)$. The second factor must be non-isomorphic to $\mathfrak{su}(2)$. We check each label:

- If $k = \dim$, then the minimal non-abelian simple dimension strictly larger than 3 is 8, attained uniquely at $\mathfrak{su}(3)$ (Lemma 9.4).
- If $k = \text{rank}$, then the minimal rank strictly larger than 1 is 2. The compact simple rank-2 Lie algebras are A_2, $B_2 \cong C_2$, and G_2. Their dimensions are 8, 10, and 14, respectively, so the tie-break by dim selects $A_2 = \mathfrak{su}(3)$.
- If $k = \dim + \text{rank}$, then for any $\mathfrak{g} \ncong \mathfrak{su}(2)$ one has $\dim(\mathfrak{g}) \geq 8$ and $\text{rank}(\mathfrak{g}) \geq 2$, hence $k(\mathfrak{g}) \geq 10$. Equality $k = 10$ is attained by $\mathfrak{su}(3)$ (dimension 8, rank 2). For the other rank-2 cases, B_2 has $k = 12$ and G_2 has $k = 16$, and higher ranks only increase k. Thus $\mathfrak{su}(3)$ is the unique minimizer.
- If $k = d_{\min}$, then $d_{\min}(\mathfrak{su}(3)) = 3$ (the defining representation), while every other compact simple Lie algebra not isomorphic to $\mathfrak{su}(2)$ has $d_{\min} \geq 4$: for $B_2 \cong C_2$ one has $d_{\min} = 4$ (the defining representation of C_2), and for G_2 one has $d_{\min} = 7$; higher ranks only increase the minimal nontrivial representation dimension in the classical families. Hence $d_{\min}$ selects $\mathfrak{su}(3)$.

This proves that for each listed label, the unique minimizer is $(\mathfrak{su}(2), \mathfrak{su}(3))$. □

Relation to the sweep. Table 101 remains an audit artifact: it verifies by explicit enumeration (within a bounded window) that no implementation detail of the sweep changes the minimizer under the tested labels. Proposition AI.1 explains why this stability is expected already from low-rank classification facts.

AJ Reproducibility

This paper includes auditable scripts that reproduce the finite combinatorics, folding statistics, and the Hilbert chirality-index checks. All scripts are written in Python and live under:

`docs/papers/2025_z128_standard_model_stable_sector_hpa_omega/scripts/`.

Some extended audit and plotting utilities use a small scientific stack recorded in `requirements.txt`.

AJ.1 What is reproduced

The scripts reproduce:

- enumeration of X_6 and verification $|X_6| = 21$ (Lemma 4.5);
- Hamming-weight distribution of X_6 and the $18 \oplus 3$ cyclic/boundary split (Proposition 4.9);
- computation of $\text{Fold}_6(N)$ for $N = 0, \ldots, 63$, including surjectivity and the degeneracy histogram (Theorem 4.18);
- generation of a complete Fold_6 table (Appendix AE.2);
- a bounded counterfactual fold-family sensitivity sweep at $m = 6$ (Appendix Q).

- computation of the Hilbert chirality index χ at order $n = 3$ and its sign flips under reflection and traversal reversal (Proposition 5.4).
- an addressing-basis audit (Hilbert vs. a row-major counterfactual) that makes the tick-first locality choice explicit at the minimal anchor (Table 5).
- a bounded sensitivity sweep for gauge-factor selection under alternative complexity labels (Appendix AI).
- a coarse-grained scalar parity check on the $n = 3$ Hilbert grid that contrasts the parity-odd chirality index with parity-even block-averaged intrinsic observables (Table 100).
- reproduction of the closed 21 $\to$SM labeling table (Table 15), whose underlying labeling map is uniquely fixed by Theorem 9.17 once the declared ordering keys are chosen (Remark 9.20);
- generation of the mass-spectrum closure table (Table 18).
- bounded-coefficient rigidity search for the depth ansatz (Table 94).
- generation of a PMNS mixing-angle closure and its induced matrix tables (Section 12).
- generation of a resolution-threshold staircase table for Fibonacci-structured uplifts (Section 14.2.1).
- generation of a discrete cosmology energy-budget fit fragment and its visualization (Appendix AD.12).
- generation of finite-resolution connection/holonomy audit tables on the $n = 3$ Hilbert grid (Section 6).
- generation of uncertainty-robustness audit tables (Appendix AE.7).
- generation of counterfactual baseline audit tables (Appendix AE.9).
- generation of systematic aggregation/multiplicity baselines for the $\alpha_{\mathrm{em}}^{-1}$ and J normalization dictionaries (Section AF.1 and Section AF.3).
- generation of the quantitative rigidity-target summary table used in the main text (Table 16).

AJ.2 Main entry points

- `scripts/run_all.py`: runs the full deterministic pipeline in a fixed order and checks that the expected generated fragments exist.
- `scripts/exp_x6_enumeration.py`: enumerates X_6 and writes `sections/generated/x6_*.tex`.
- `scripts/exp_xm_enumeration.py`: enumerates X_m for an m-sweep and writes:
  - `sections/generated/xm_sweep_rows.tex`
- `scripts/exp_fold6_stats.py`: computes Fold_6 statistics and writes `sections/generated/fold6_*.tex`.
- `scripts/exp_fold_family_sensitivity.py`: generates a bounded counterfactual fold-family sensitivity fragment:

  - `sections/generated/fold_family_sensitivity_rows.tex`

- `scripts/exp_foldm_stats.py`: computes Fold_m statistics for an m-sweep and writes:
  - `sections/generated/foldm_sweep_rows.tex`
- `scripts/exp_hilbert_chirality_index.py`: computes χ on the $n = 3$ Hilbert path and writes `sections/generated/hilbert_chi_summary.tex`.
- `scripts/exp_addressing_selection.py`: compares Hilbert addressing to a row-major counterfactual by protocol-internal locality and computability metrics and writes:
  - `sections/generated/addressing_selection_rows.tex`
- `scripts/exp_gauge_complexity_sensitivity.py`: generates a bounded sensitivity sweep for gauge-factor complexity-label choices and writes:
  - `sections/generated/gauge_complexity_sensitivity_rows.tex`
- `scripts/exp_hilbert_chi_sweep.py`: sweeps χ across multiple Hilbert orders and writes:
  - `sections/generated/hilbert_chi_sweep_rows.tex`
- `scripts/exp_scalar_coarse_grain.py`: generates a coarse-grained scalar parity table fragment and writes:
  - `sections/generated/scalar_coarse_grain_rows.tex`
- `scripts/exp_resolution_thresholds.py`: generates a resolution-threshold staircase table fragment and (optionally) a plot:
  - `sections/generated/resolution_thresholds_rows.tex`
  - `figures/resolution_thresholds_staircase.png` (optional)
- `scripts/exp_cosmology_energy_budget_fit.py`: generates the discrete energy-budget fit fragment and the mandatory figure used in Appendix AD.12:
  - `sections/generated/cosmology_energy_budget_fit_equation.tex`
  - `figures/cosmology_energy_budget_fit.png`
- `scripts/exp_edge_mismatch_decomposition.py`: generates edge-connection audit fragments:
  - `sections/generated/edge_mismatch_deg_pair_rows.tex`
  - `sections/generated/edge_mismatch_cost_quantiles_rows.tex`
- `scripts/exp_holonomy_loops.py`: generates a plaquette-holonomy distribution fragment:
  - `sections/generated/holonomy_cycle_type_rows.tex`
- `scripts/exp_sm_labeling_solver.py`: implements the deterministic rank-matching construction of Theorem 9.17 and writes `sections/generated/sm_labeling_rows.tex` (Remark 9.20).
- `scripts/exp_labeling_lift_consistency.py`: audits a functorial label lift under the prefix projection $\pi_{m\to 6}$ and writes:

  - sections/generated/label_lift_rows.tex

- scripts/exp_mass_spectrum.py: generates the mass-spectrum table fragments:
  - sections/generated/mass_spectrum_anchor_rows.tex
  - sections/generated/mass_spectrum_quark_rows.tex
  - sections/generated/mass_spectrum_neutrino_rows.tex
  - sections/generated/mass_spectrum_rows.tex (combined)
- scripts/exp_higgs_z_offset_rigidity.py: generates a bounded-denominator rigidity sweep for the Higgs–Z depth offset and writes:
  - sections/generated/higgs_z_offset_sweep_rows.tex
- scripts/exp_mass_matching_layer.py: computes a minimal quantized matching-layer summary for the mass-spectrum closure and writes:
  - sections/generated/mass_matching_layer_rows.tex
  - sections/generated/mass_matching_layer_summary_rows.tex
- scripts/exp_mass_depth_rigidity.py: runs a bounded-coefficient search (20 iterations) and writes sections/generated/mass_depth_rigidity_rows.tex.
- scripts/exp_mass_depth_leave_one_out.py: runs a leave-one-out robustness sweep for the mass-depth coefficient search and writes:
  - sections/generated/mass_depth_leave_one_out_rows.tex
  - sections/generated/mass_depth_leave_one_out_summary_rows.tex
- scripts/exp_ckm_mixing_depth_rigidity.py: runs a bounded-complexity minimax search for CKM magnitudes (20 iterations) and writes sections/generated/ckm_mixing_*.tex.
- scripts/exp_ckm_matrix_closure.py: reconstructs a full CKM matrix from three magnitudes and a Jarlskog anchor (both a PDG-consistent reference reconstruction and the closed prediction) and writes:
  - sections/generated/ckm_angles_rows.tex
  - sections/generated/ckm_matrix_rows.tex
  - sections/generated/ckm_unitarity_rows.tex
- scripts/exp_pmns_mixing_depth_rigidity.py: runs a bounded-complexity minimax search for PMNS mixing sines and writes:
  - sections/generated/pmns_mixing_rigidity_rows.tex
  - sections/generated/pmns_mixing_rows.tex
- scripts/exp_pmns_matrix_closure.py: reconstructs a PMNS matrix from the bounded-complexity angles and a discrete CP-phase closure and writes:
  - sections/generated/pmns_delta_sweep_rows.tex
  - sections/generated/pmns_angles_rows.tex
  - sections/generated/pmns_matrix_rows.tex
  - sections/generated/pmns_unitarity_rows.tex

- `scripts/exp_pmns_no_io_stability.py`: runs a NO/IO robustness diagnostic for the PMNS closures and writes:
  - `sections/generated/pmns_no_io_stability_rows.tex`
- `scripts/exp_neutrino_mass_interface.py`: generates a minimal neutrino mass-scale interface table fragment:
  - `sections/generated/neutrino_mass_interface_rows.tex`
- `scripts/exp_inverse_hypercharge_fit.py`: generates the inverse diagnostic fragment:
  - `sections/generated/inverse_hypercharge_fit_rows.tex`
- `scripts/exp_inverse_hypercharge_sign_fit.py`: generates the inverse diagnostic fragment:
  - `sections/generated/inverse_hypercharge_sign_fit_rows.tex`
- `scripts/exp_inverse_hypercharge_full_fit.py`: generates the inverse diagnostic fragment:
  - `sections/generated/inverse_hypercharge_full_fit_rows.tex`
- `scripts/exp_inverse_rep_dim_fit.py`: generates the inverse diagnostic fragment:
  - `sections/generated/inverse_rep_dim_fit_rows.tex`
- `scripts/exp_inverse_generation_fit.py`: generates the inverse diagnostic fragment:
  - `sections/generated/inverse_generation_fit_rows.tex`
- `scripts/exp_inverse_diag_summary.py`: aggregates a compact main-text summary across inverse diagnostics and writes:
  - `sections/generated/inverse_diag_summary_rows.tex`
- `scripts/exp_labeling_order_sensitivity.py`: measures SM-side ordering-key sensitivity of the induced cyclic labeling and writes:
  - `sections/generated/labeling_order_sensitivity_rows.tex`
- `scripts/exp_audit_closure_metrics.py`: generates bounded-complexity audit metrics (domain sizes, uniqueness gaps, quantiles) and writes:
  - `sections/generated/audit_closure_metrics_rows.tex`
  - `sections/generated/audit_closure_quantiles_rows.tex`
- `scripts/exp_audit_uncertainty_robustness.py`: generates minimizer stability rates under sampled target perturbations and writes:
  - `sections/generated/audit_uncertainty_robustness_rows.tex`
- `scripts/exp_audit_counterfactual_baselines.py`: generates counterfactual baseline comparisons and writes:
  - `sections/generated/audit_counterfactual_rows.tex`
- `scripts/exp_audit_pi_polynomial_null.py`: generates a broader π-polynomial null baseline sweep for α^{-1} and writes:

  - sections/generated/audit_pi_poly_null_rows.tex

- scripts/exp_alpha_coeff_rigidity.py: runs the bounded simplex search for the α^{-1} coefficient rigidity statement and writes:
  - sections/generated/alpha_coeff_rigidity_rows.tex
- scripts/exp_aggregation_baselines.py: generates systematic aggregation and multiplicity baseline fragments and writes:
  - sections/generated/alpha_aggregation_baselines_rows.tex
  - sections/generated/j_multiplicity_baselines_rows.tex
- scripts/exp_ew_rigidity.py: runs finite searches for the electroweak Z-scale rigidity statements and writes:
  - sections/generated/ew_alpha_pi2_rigidity_rows.tex
  - sections/generated/ew_sin2_rational_rigidity_rows.tex
- scripts/exp_jarlskog_pi_rigidity.py: runs the bounded (a, n) search for the $J = 1/(a\pi^n)$ rigidity statement and writes:
  - sections/generated/jarlskog_pi_rigidity_rows.tex
- scripts/exp_quant_summary.py: generates the quantitative summary fragment used in Table 16 and writes:
  - sections/generated/quant_summary_rows.tex
- scripts/exp_sigma_summary.py: generates a sigma-normalized mismatch summary fragment (using the explicit audit sigma scales in scripts/common_constants.py) and writes:
  - sections/generated/sigma_summary_rows.tex
- scripts/exp_audit_summary.py: generates the audit summary fragment:
  - sections/generated/audit_summary_rows.tex

AJ.3 How to run (examples)

- cd docs/papers/2025_z128_standard_model_stable_sector_hpa_omega
- python3 -m pip install -r requirements.txt
- python3 scripts/run_all.py
- python3 scripts/exp_x6_enumeration.py
- python3 scripts/exp_fold6_stats.py
- python3 scripts/exp_hilbert_chirality_index.py
- python3 scripts/exp_sm_labeling_solver.py
- python3 scripts/exp_mass_spectrum.py
- python3 scripts/exp_mass_depth_rigidity.py
- python3 scripts/exp_ckm_mixing_depth_rigidity.py
- python3 scripts/exp_audit_summary.py
- latexmk -pdf -interaction=nonstopmode -halt-on-error main.tex

AJ.4 Generated LaTeX fragments

The scripts write small LaTeX fragments into:

`docs/papers/2025_z128_standard_model_stable_sector_hpa_omega/sections/generated/`

These fragments are generated outputs and should not be edited by hand; re-run the scripts to regenerate them deterministically from the stated constructions and bounded sweeps. This repository includes the generated fragments so the paper can compile out of the box, but they can be regenerated at any time.

AK Closed computable work packages (interface deliverables)

This appendix summarizes the interface work packages that are realized *within this paper* as explicit computable deliverables. They are not premises for any theorem-level folding statement; they are protocol-layer closures and audit objects with deterministic scripts and generated tables.

AK.1 Functorial refinement of the field-level labeling map

The labeling map $\mathcal{L}_{\mathrm{SM}}$ at $(m, n) = (6, 3)$ is closed in Section 9. Its canonical uplift/refinement under window growth is made explicit by prefix projection and deterministic refinement indices in Appendix V, together with generated lift-multiplicity and refinement-audit tables.

AK.2 Mixing matrices as holonomy of protocol connections

Finite protocol connections and holonomy diagnostics are constructed explicitly in Section 6. The resulting bounded-complexity closures for CKM/PMNS magnitudes and their induced matrix reconstructions are recorded in Sections 11 and 12, with unitarity and CP-odd invariants reported in generated tables.

AK.3 Resolution flow and running couplings

The discrete uplift/coarse-graining flow is fixed as the protocol flow law in Definition 8.16. Its scale dictionary is provided by the Fibonacci resolution coordinate and the RG conversion rule in Proposition 8.17, while the thresholded staircase $m_{\mathrm{eff}}(\mu)$ is fixed by Corollary 14.2.

AK.4 Mass/inertia as protocol cost and latency (interface)

The closed mass-spectrum template in Section 13 is complemented by a matching-layer delay and lapse dictionary in Section Y, including Wigner–Smith delay as an operational proxy and standard GR/SR reference relations used only at the interface layer.

AK.5 Protocol-to-continuum error control (interface)

The $\chi(x)$ reconstruction protocol in Appendix AD.8 and the overhead-to-gravity weak-field dictionary in Appendix AD.7 together define a concrete pipeline from discrete protocol statistics to continuum representative fields such as Φ and ρ_{eff}. To make this pipeline auditable as a quantitative interface deliverable, Appendix AD.9 records explicit error-control bounds and propagation formulas: concentration bounds for bounded folding-derived statistics, log-ratio perturbation bounds for $\widehat{\chi}$, and truncation/noise-amplification bounds for the finite-difference operators (needed for χ' and $\Delta\chi$), together with the resulting uncertainty propagation to $\widehat{\gamma}$ and $\widehat{\rho}_{\mathrm{eff}}$.

References

[1] Michael E. Peskin and Daniel V. Schroeder. *An Introduction to Quantum Field Theory*. Westview Press, Boulder, CO, 1995.

[2] Particle Data Group. Review of particle physics. *Physical Review D*, 110:030001, 2024.

[3] Haobo Ma. Holographic polar arithmetic: A finite-resolution scan algebra for the hpa–ω program. Companion manuscript in the `docs/papers` repository, 2025.

[4] Haobo Ma. Computational action principle: Least-discrepancy dynamics and field unification in hpa–ω. Companion manuscript in the `docs/papers` repository, 2025.

[5] Haobo Ma. Computational action principle ii: Dynamical einstein gravity and quantum interfaces from routing overhead in hpa–ω. Companion manuscript in the `docs/papers` repository, 2025.

[6] Haobo Ma. The holographic hilbert universe: Constructive spacetime, computational-lapse gravity, and a conditional riemann critical-line rigidity theorem in hpa–ω. Companion manuscript in the `docs/papers` repository, 2025.

[7] Haobo Ma. Holographic phase thermodynamics: Arithmetic statistical mechanics, computational lapse, and the geometric origin of intelligence in hpa–ω. Companion manuscript in the `docs/papers` repository, 2025.

[8] Haobo Ma. The geometry of physical constants in hpa–ω: From the fine-structure constant to particle spectra and black-hole/cosmological invariants. Companion constants-geometry manuscript in the `docs/papers` repository, 2025.

[9] Haobo Ma. Resolution folding under φ–π–e triple-operator constraints: A zeckendorf–hilbert–abel framework for the $64 \to 21$ projection and recursive uplift. Companion finite-resolution folding manuscript in the `docs/papers` repository, 2025.

[10] Haobo Ma. Holographic polar omega theory. Axiomatic interface manuscript in the `docs/papers` repository, 2025.

[11] Haobo Ma. Omega theory: Axiomatic foundations of holographic spacetime and interactive evolution. Companion physics manuscript in the `docs/papers` repository, 2025.

[12] Richard P. Feynman. The theory of positrons. *Physical Review*, 76(6):749–759, 1949.

[13] Richard P. Feynman. The development of the space-time view of quantum electrodynamics. Nobel Lecture, 1965. Nobel Prize in Physics 1965.

[14] Karl Johan Åström and Richard M. Murray. *Feedback Systems: An Introduction for Scientists and Engineers*. Princeton University Press, Princeton, NJ, 2008.

[15] Rolf Landauer. Irreversibility and heat generation in the computing process. *IBM Journal of Research and Development*, 5(3):183–191, 1961.

[16] Robert M. Gray and David L. Neuhoff. Quantization. *IEEE Transactions on Information Theory*, 44(6):2325–2383, 1998.

[17] Thomas M. Cover and Joy A. Thomas. *Elements of Information Theory*. Wiley, Hoboken, NJ, 2 edition, 2006.

[18] Brian C. Hall. *Lie Groups, Lie Algebras, and Representations: An Elementary Introduction*. Springer, Cham, 2 edition, 2015.

[19] Hermann Weyl. *The Theory of Groups and Quantum Mechanics*. Dover Publications, New York, 1931. Reprint editions available; original German edition 1928.

[20] Eugene P. Wigner. Lower limit for the energy derivative of the scattering phase shift. *Physical Review*, 98(1):145–147, 1955.

[21] F. T. Smith. Lifetime matrix in collision theory. *Physical Review*, 118(1):349–356, 1960.

[22] M. Lothaire. *Algebraic Combinatorics on Words*. Cambridge University Press, Cambridge, 2002.

[23] Douglas Lind and Brian Marcus. *An Introduction to Symbolic Dynamics and Coding*. Cambridge University Press, Cambridge, 1995.

[24] Michael A. Nielsen and Isaac L. Chuang. *Quantum Computation and Quantum Information*. Cambridge University Press, Cambridge, 10th anniversary edition edition, 2010.

[25] E. Zeckendorf. Représentation des nombres naturels par une somme de nombres de Fibonacci ou de nombres de Lucas. *Bulletin de la Société Royale des Sciences de Liège*, 41:179–182, 1972.

[26] Jean-Paul Allouche and Jeffrey Shallit. *Automatic Sequences: Theory, Applications, Generalizations*. Cambridge University Press, Cambridge, 2003.

[27] G. H. Hardy and E. M. Wright. *An Introduction to the Theory of Numbers*. Oxford University Press, Oxford, 6 edition, 2008.

[28] L. Kuipers and Harald Niederreiter. *Uniform Distribution of Sequences*. Wiley, New York, 1974.

[29] J. W. S. Cassels. *An Introduction to Diophantine Approximation*. Cambridge University Press, Cambridge, 1957.

[30] Michael Artin and Barry Mazur. On periodic points. *Annals of Mathematics*, 81(1):82–99, 1965.

[31] William Parry and Mark Pollicott. *Zeta Functions and the Periodic Orbit Structure of Hyperbolic Dynamics*, volume 187–188 of *Astérisque*. Société Mathématique de France, Paris, 1990.

[32] David Ruelle. *Thermodynamic Formalism: The Mathematical Structures of Classical Equilibrium Statistical Mechanics*. Addison-Wesley, Reading, MA, 1978.

[33] Philippe Demontigny, Thao Do, Archit Kulkarni, Steven J. Miller, David Moon, and Umang Varma. Generalizing zeckendorf's theorem to f-decompositions. 2013. arXiv:1309.5599.

[34] Iddo Ben-Ari and Steven J. Miller. A probabilistic approach to generalized zeckendorf decompositions. 2014. arXiv:1405.2379.

[35] Michel Dekking. The structure of zeckendorf expansions. 2020. arXiv:2006.06970.

[36] David Hilbert. über die stetige abbildung einer linie auf ein flächenstück. *Mathematische Annalen*, 38:459–460, 1891.

[37] Hans Sagan. *Space-Filling Curves*. Springer, New York, 1994.

[38] Bongki Moon, H. V. Jagadish, Christos Faloutsos, and Joel H. Saltz. Analysis of the clustering properties of the hilbert space-filling curve. *IEEE Transactions on Knowledge and Data Engineering*, 13(1):124–141, 2001.

[39] Gerard ́t Hooft. Dimensional reduction in quantum gravity. In *Salamfestschrift: A Collection of Talks*, 1993. arXiv:gr-qc/9310026.

[40] Leonard Susskind. The world as a hologram. *Journal of Mathematical Physics*, 36(11):6377–6396, 1995. arXiv:hep-th/9409089.

[41] Raphael Bousso. The holographic principle. *Reviews of Modern Physics*, 74:825–874, 2002.

[42] Kenneth G. Wilson. Confinement of quarks. *Physical Review D*, 10:2445–2459, 1974.

[43] Heinz J. Rothe. *Lattice Gauge Theories: An Introduction*. World Scientific, Singapore, 4 edition, 2012.

[44] Jean-Pierre Serre. *Linear Representations of Finite Groups*. Springer, New York, 1977. Translated from the French by Leonard L. Scott.

[45] Cecilia Jarlskog. Commutator of the quark mass matrices in the standard electroweak model and a measure of maximal CP nonconservation. *Physical Review Letters*, 55(10):1039–1042, 1985.

[46] M. V. Berry. Quantal phase factors accompanying adiabatic changes. *Proceedings of the Royal Society of London. Series A*, 392(1802):45–57, 1984.

[47] Mikio Nakahara. *Geometry, Topology and Physics*. CRC Press, Boca Raton, 2 edition, 2003.

[48] Steven Weinberg. *The Quantum Theory of Fields. Volume I: Foundations*. Cambridge University Press, Cambridge, 1995.

[49] R. F. Streater and A. S. Wightman. *PCT, Spin and Statistics, and All That*. Princeton University Press, Princeton, 1989.

[50] Hermann Weyl. Elektron und gravitation. i. *Zeitschrift für Physik*, 56:330–352, 1929.

[51] Chen Ning Yang and Robert L. Mills. Conservation of isotopic spin and isotopic gauge invariance. *Physical Review*, 96(1):191–195, 1954.

[52] Roberto Contino. The higgs as a composite nambu–goldstone boson. 2011. TASI lecture notes; arXiv:1005.4269.

[53] Giuliano Panico and Andrea Wulzer. *The Composite Nambu–Goldstone Higgs*, volume 913 of *Lecture Notes in Physics*. Springer, Cham, 2016.

[54] John B. Kogut and Leonard Susskind. Hamiltonian formulation of wilson's lattice gauge theories. *Physical Review D*, 11:395–408, 1975.

[55] William Fulton and Joe Harris. *Representation Theory: A First Course*, volume 129 of *Graduate Texts in Mathematics*. Springer, New York, 1991.

[56] C. Bouchiat, J. Iliopoulos, and Ph. Meyer. Anomaly-free version of weinberg's model. *Physics Letters B*, 38:519–523, 1972.

[57] Edward Witten. An SU(2) anomaly. *Physics Letters B*, 117:324–328, 1982.

[58] Albert Einstein. Zur elektrodynamik bewegter körper. *Annalen der Physik*, 322(10):891–921, 1905.

[59] Peter J. Mohr, David B. Newell, Barry N. Taylor, and Eite Tiesinga. Codata recommended values of the fundamental physical constants: 2022. *Reviews of Modern Physics*, 97:025002, 2025.

[60] Ivan Esteban, Maria C. Gonzalez-Garcia, Michele Maltoni, Thomas Schwetz, and José W. F. Tórtola. The fate of hints: updated global analysis of three-flavor neutrino oscillations. *Journal of High Energy Physics*, 09:178, 2020. NuFIT global analysis reference used for representative PMNS targets.

[61] Claude E. Shannon. A mathematical theory of communication. *Bell System Technical Journal*, 27(3):379–423, 1948.

[62] Steven Weinberg. Baryon- and lepton-nonconserving processes. *Physical Review Letters*, 43:1566–1570, 1979.

[63] Peter Minkowski. Mu $\rightarrow$ e gamma at a rate of one out of 10^9 muon decays? *Physics Letters B*, 67:421–428, 1977.

[64] Alexander Vilenkin and E. P. S. Shellard. *Cosmic Strings and Other Topological Defects*. Cambridge University Press, Cambridge, 1994.

[65] Ya. B. Zeldovich, I. Yu. Kobzarev, and L. B. Okun. Cosmological consequences of the spontaneous breakdown of discrete symmetry. *Zh. Eksp. Teor. Fiz.*, 67:3–11, 1974. English translation: Sov. Phys. JETP 40 (1975) 1.

[66] Matias Zaldarriaga and Uroš Seljak. All-sky analysis of polarization in the microwave background. *Physical Review D*, 55(4):1830–1840, 1997.

[67] Marc Kamionkowski, Arthur Kosowsky, and Albert Stebbins. Statistics of cosmic microwave background polarization. *Physical Review D*, 55(12):7368–7388, 1997.

[68] Arthur Lue, Li-Min Wang, and Marc Kamionkowski. Cosmological signature of new parity-violating interactions. *Physical Review Letters*, 83(8):1506–1509, 1999.

[69] Yuto Minami and Eiichiro Komatsu. New extraction of the cosmic birefringence from the Planck 2018 polarization data. *Physical Review Letters*, 125(22):221301, 2020.

[70] Stephen W. Hawking. Particle creation by black holes. *Communications in Mathematical Physics*, 43:199–220, 1975.

[71] Robert M. Wald. *General Relativity*. University of Chicago Press, Chicago, 1984.

[72] Randall J. LeVeque. *Finite Difference Methods for Ordinary and Partial Differential Equations: Steady-State and Time-Dependent Problems*. SIAM, Philadelphia, 2007.

[73] Stéphane Boucheron, Gábor Lugosi, and Pascal Massart. *Concentration Inequalities: A Nonasymptotic Theory of Independence*. Oxford University Press, Oxford, 2013.

[74] A. W. van der Vaart. *Asymptotic Statistics*. Cambridge University Press, Cambridge, 1998.

[75] Iwo Białynicki-Birula. Weyl, dirac, and maxwell equations on a lattice as quantum cellular automata. *Physical Review D*, 49(12):6920–6927, 1994.

[76] Luca Bombelli, Joohan Lee, David Meyer, and Rafael D. Sorkin. Space-time as a causal set. *Physical Review Letters*, 59(5):521–524, 1987.

[77] Guifré Vidal. Entanglement renormalization. *Physical Review Letters*, 99:220405, 2007.

[78] Brian Swingle. Entanglement renormalization and holography. *Physical Review D*, 86:065007, 2012.

[79] Fernando Pastawski, Beni Yoshida, Daniel Harlow, and John Preskill. Holographic quantum error-correcting codes: Toy models for the bulk/boundary correspondence. *Journal of High Energy Physics*, 06:149, 2015.

[80] Stephen P. Martin and David G. Robertson. Standard model parameters in the tadpole-free pure $\overline{\text{ms}}$ scheme. *Physical Review D*, 100:073004, 2019. arXiv:1907.02500.

[81] Takeshi Fukuyama. Searching for new physics beyond the standard model in electric dipole moment. 2013. arXiv:1201.4252 (latest revision 2013).

[82] E. L. F. de Lima and C. C. Nishi. Flavor invariants for the SM with one singlet vector-like quark. 2024. arXiv:2408.10325.

[83] Howard Georgi and Sheldon L. Glashow. Unity of all elementary-particle forces. *Physical Review Letters*, 32(8):438–441, 1974.

[84] Paul Langacker. Grand unified theories and proton decay. *Physics Reports*, 72(4):185–385, 1981.

[85] G. H. Hardy. *Divergent Series*. Oxford University Press, Oxford, 1949.

[86] Ricardo Estrada and Ram P. Kanwal. *A Distributional Approach to Asymptotics: Theory and Applications*. Birkhäuser, Boston, 2 edition, 2002.

[87] Eugene P. Wigner. *Gruppentheorie und ihre Anwendung auf die Quantenmechanik der Atomspektren*. Friedr. Vieweg & Sohn, Braunschweig, 1931. English translation and expanded edition: Academic Press (1959); standard source for Wigner's theorem.

[88] Jacob D. Bekenstein. Black holes and entropy. *Physical Review D*, 7(8):2333–2346, 1973.

[89] James M. Bardeen, Brandon Carter, and Stephen W. Hawking. The four laws of black hole mechanics. *Communications in Mathematical Physics*, 31:161–170, 1973.

[90] Robert M. Wald. Black hole entropy is the noether charge. *Physical Review D*, 48(8):R3427–R3431, 1993.

[91] Albert Einstein and Nathan Rosen. The particle problem in the general theory of relativity. *Physical Review*, 48(1):73–77, 1935.

[92] Martin D. Kruskal. Maximal extension of schwarzschild metric. *Physical Review*, 119(5):1743–1745, 1960.

[93] Juan Maldacena and Leonard Susskind. Cool horizons for entangled black holes. *Fortschritte der Physik*, 61(9):781–811, 2013. arXiv:1306.0533.

[94] Michael S. Morris and Kip S. Thorne. Wormholes in spacetime and their use for interstellar travel: A tool for teaching general relativity. *American Journal of Physics*, 56(5):395–412, 1988.

[95] Matt Visser. *Lorentzian Wormholes: From Einstein to Hawking*. AIP Press, New York, 1995.

[96] Jacob D. Bekenstein. Universal upper bound on the entropy-to-energy ratio for bounded systems. *Physical Review D*, 23(2):287–298, 1981.

[97] John L. Friedman, Kristin Schleich, and Donald M. Witt. Topological censorship. *Physical Review Letters*, 71(10):1486–1489, 1993. arXiv:gr-qc/9305017.

[98] Gregory J. Galloway, Kristin Schleich, Donald M. Witt, and Eric Woolgar. Topological censorship and higher genus black holes. *Physical Review D*, 60:104039, 1999. arXiv:gr-qc/9902061.

[99] Clifford M. Will. *Theory and Experiment in Gravitational Physics*. Cambridge University Press, Cambridge, 2 edition, 1993.

[100] Irwin I. Shapiro. Fourth test of general relativity. *Physical Review Letters*, 13(26):789–791, 1964.

[101] Wolfgang Rindler. *Relativity: Special, General, and Cosmological*. Oxford University Press, Oxford, 2 edition, 2006.

[102] Caroline Series. The modular surface and continued fractions. *Journal of the London Mathematical Society*, 31(1):69–80, 1985.

[103] Anatole Katok and Boris Hasselblatt. *Introduction to the Modern Theory of Dynamical Systems*, volume 54 of *Encyclopedia of Mathematics and its Applications*. Cambridge University Press, Cambridge, 1995.

[104] Marius Iosifescu and Cor Kraaikamp. *Metrical Theory of Continued Fractions*. Kluwer Academic Publishers, Dordrecht, 2002.

[105] Marc A. Rieffel. c^*-algebras associated with irrational rotations. *Pacific Journal of Mathematics*, 93(2):415–429, 1981.

[106] Marc A. Rieffel. Projective modules over higher-dimensional noncommutative tori. *Canadian Journal of Mathematics*, 40(2):257–338, 1988.

[107] Alain Connes. *Noncommutative Geometry*. Academic Press, San Diego, 1994.

[108] Tom M. Apostol. *Modular Functions and Dirichlet Series in Number Theory*. Springer, New York, 2 edition, 1990.

[109] Fred Diamond and Jerry Shurman. *A First Course in Modular Forms*, volume 228 of *Graduate Texts in Mathematics*. Springer, New York, 2005.

[110] David Lovelock. The Einstein tensor and its generalizations. *Journal of Mathematical Physics*, 12(3):498–501, 1971.

[111] N. N. Cencov. *Statistical Decision Rules and Optimal Inference*. American Mathematical Society, Providence, RI, 1982. English translation of the Russian monograph; standard reference for Cěncov's theorem on monotone metrics.

[112] Wassily Hoeffding. Probability inequalities for sums of bounded random variables. *Journal of the American Statistical Association*, 58(301):13–30, 1963.

[113] M. A. Naimark. Spectral functions of a symmetric operator. *Izvestiya Akademii Nauk SSSR, Seriya Matematicheskaya*, 4:277–318, 1940. Naimark dilation theorem (original Russian source).

[114] W. Forrest Stinespring. Positive functions on c^*-algebras. *Proceedings of the American Mathematical Society*, 6(2):211–216, 1955.

[115] Karl Kraus. *States, Effects, and Operations: Fundamental Notions of Quantum Theory.* Springer, Berlin, 1983.

[116] Michael A. Nielsen and Isaac L. Chuang. *Quantum Computation and Quantum Information.* Cambridge University Press, Cambridge, 2000.

[117] Andrew M. Gleason. Measures on the closed subspaces of a Hilbert space. *Journal of Mathematics and Mechanics*, 6(6):885–893, 1957.

[118] Paul Busch. Quantum states and generalized observables: A simple proof of Gleason's theorem. *Physical Review Letters*, 91(12):120403, 2003.

[119] Sheldon L. Glashow. Partial-symmetries of weak interactions. *Nuclear Physics*, 22(4):579–588, 1961.

[120] Steven Weinberg. A model of leptons. *Physical Review Letters*, 19(21):1264–1266, 1967.

[121] Abdus Salam. Weak and electromagnetic interactions. In Nils Svartholm, editor, *Elementary Particle Theory: Relativistic Groups and Analyticity*, pages 367–377. Almqvist & Wiksell, Stockholm, 1968. Proceedings of the Eighth Nobel Symposium.

[122] Nicola Cabibbo. Unitary symmetry and leptonic decays. *Physical Review Letters*, 10(12):531–533, 1963.

[123] Makoto Kobayashi and Toshihide Maskawa. CP-violation in the renormalizable theory of weak interaction. *Progress of Theoretical Physics*, 49(2):652–657, 1973.

[124] Francesco Mezzadri. How to generate random matrices from the classical compact groups. *Notices of the American Mathematical Society*, 54(5):592–604, 2007.

[125] Benoit Collins and Piotr Sniady. Integration with respect to the haar measure on unitary, orthogonal and symplectic group. *Communications in Mathematical Physics*, 264(3):773–795, 2006.